University of Southampton

Faculty of Sciences

Southampton Oceanography Centre

School of Ocean and Earth Sciences

The Dynamics of Rotating Two-Layer Exchange Flows – An Analytical and Numerical Modelling Study

by

Ulrike Riemenschneider

Thesis for the degree of Doctor of Philosophy

February 2004

Graduate School of the
Southampton Oceanography Centre

This PhD dissertation by

Ulrike Riemenschneider

has been produced under the supervision of the following persons:

Supervisors:

Prof. Peter D. Killworth

Dr. David A. Smeed

Chair of Advisory Panel:

Prof. Harry L. Bryden

Member of Advisory Panel:

Dr. Tim J. Henstock

"I mentioned to your Majesty at the beginning of my discourse that my intention in embarking on these travels was not only to contemplate and observe these natural motions which are purely visual, but also to investigate those which are more concealed but just as marvelous to the human mind, and encourage one to discover, for the public good, the reasons. Embolded by the observations of the surface motion of our channel, happily I was able to prepare myself as best I could, for greater and nobler research, more fruitful since it was more difficult and new, and consequently worth of Your Majesty's spirited genius."

"So, in the Channel, as I have demonstrated, there are two currents, one opposed to the other, and one above the other (leaving the lateral currents contrary to the Superior which I have explained well enough). The reason, to my mind, may be founded on the principle that the heaviest expels the lighter, therefore my Subject having two densities, one lighter than the other, as Your Majesty will see from the Saltiness."

Count Luigi Ferdinando Marsigli (1681) -
corresponding with Queen Christina of Sweden

To my parents

Susanne & Helmut

University of Southampton

Abstract

Faculty of Science
School of Ocean and Earth Science
Southampton Oceanography Centre

Doctor of Philosophy

The Dynamics of Rotating Two-Layer Exchange Flows – An Analytical and Numerical Modelling Study

by Ulrike Riemenschneider

February 2004

Two-layer hydraulic exchange flows with zero potential vorticity and zero net flux are modelled analytically for rectangular channels with a constriction, a sill and a combination of the two. Controlled flows are determined for a range of non-dimensional channel widths L, scaled by the Rossby radius, and Bernoulli potentials ΔE; and these are traced along the channels. The interface between the two layers is linear and may separate from either side wall of the channel, all possible flow regimes are considered when tracing the solutions.

The flows are traced using a method analogous to the Froude number plane developed by Armi (1986), for channels with $L \propto \sqrt{D}$, where D is the non dimensional channel depth. Flow along other geometries is traced using the Gill functional approach (Gill, 1977). Maximal and submaximal flows are derived and discussed for a variety of channel geometries.

Analogous to the non-rotating case, most flows through a flat bottom channel are traceable. Flow through a channel with a sill is traceable only for a limited range of Bernoulli potentials, which depend on the width of the channel at the control. It is shown that the virtual control of a maximal flow over a sill does not need to coincide with the entrance of the channel, as has been assumed in most previous studies of hydraulically controlled flows over a sill. The controlled fluxes are derived for a comprehensive range of Bernoulli potentials as well as channel widths L. A method for determining the long wave-speeds in the channel is outlined.

In the second part of this thesis two-layer exchange flows are modelled numerically using MICOM (Miami Isopycnic Coordinate Ocean Model) in an idealised set up with two rectangular basins separated by a rectangular channel with a sill. A comprehensive set of 71 experiments is run varying the rotation rate f, the density difference between the two layers $\Delta\rho$, and the interface level in the dense reservoir, ΔH.

The flow features in the top and bottom layer are described for two experiments and compared to the theoretical results in the thesis, as well as observations and laboratory experiments. The typical 'crossing-over' of the bottom layer at the top of the sill is found and a boundary current forms on the left-hand side looking upstream. The majority of the transport in the top layer is confined to a boundary current on the left-hand side of the channel, a feature that has never been described before, but which is also predicted by the theory. It is shown that all flows exhibit inherent time variability, which is disregarded in the steady hydraulic theory.

The flux results confirm that as rotation and therefore L increases the non-dimensional flux reaches a maximum, and so rotation imposes an upper limit on the flow. An empirical parameterisation for two-layer exchange flows is derived using the MICOM results. The transport across the sill is found to depend on $\Delta H^{3/2}$ a result expected for non-rotating flows, but that does not derive from the scaling of the rotating theory.

Idealised models of the Faroe-Bank-Channel and the Denmark Strait are run and transport results are compared to observations in these straits. The Denmark Strait is only poorly modelled by a two-layer exchange while agreements for the Faroe-Bank-Channel is somewhat better.

Contents

List of Figures

List of Tables

Acknowledgements

First and foremost and without reservations I would like to acknowledge my appreciation and gratitude for the guidance, advice and support from my supervisors Peter Killworth and David Smeed. They made my journey through this PhD and the learning experience in Oceanography a truly enjoyable one.

Secondly I want to thank Jeff Blundell for his continuous presence and willingness to solve many of my computing problems and show me the tricks and quirks of Fortran programming.

In addition there were many people who helped me get started with MICOM, Matlab and other computing tools, and others who took the time to discuss hydraulic theory with me until the penny dropped, or who gave me much valued feedback and suggestions on my work in terms of science and presentation. These are in alphabetical order: Steve Alderson, Robin Hanking, Andrew Hogg, Mai-Man Lee, Alex Megann, Larry Pratt, Ben Rabe, Andrew Shaw and Mark Siddall.

I would also like to thank Diane Buckley and Wayne Baddams for taking care of the administration and the money-matters involving the PhD with complete efficiency.

I also want to mention three lecturers and mentors I have had over the past eight years as a student, whose active encouragement and faith in my abilities have given me the strength and determination to get this far. They are: Pat O'Leary, Ted Hurley and Douglas Heggie.

Life in Southampton and at SOC was made easy and enjoyable by the large and diverse postgraduate community, many of whom became good friends, house mates and office mates, and so a big thank you has to go to: Andrey Akhmetzhanov, Roberta Boscolo, Sergio Cappucci, Steffen Dransfeld, Riccardo Farneti, Laura Font, Ivailo Grigorov, Dave Gunn, Ana Hilario, Babette Hoogakker, Taro Hosoe, Dave Lamkin, Angela Landolfi, Juan Cruz Larrasoaña, Marisa da Motta, Silvia Nascimento, Luciano Pezzi, Anna Pirani, Cesar Riberio, Oliver Ross, Ana Silva, Sinhue Torres, Susanne Ufermann, Michael Winkelhofer and so many more. They have become my Southampton family.

And finally I would like to thank my family, my parents and my brothers and sisters, for supporting me and my studies all the way despite never quite knowing what I was actually doing.

The project was funded by the Southampton University Alumni Fund and a maintenance grant from funds of the James-Rennell-Division (NERC).

Chapter 1

Introduction

The subject of the thesis, which is hydraulic theory with particular emphasis on the effects of rotation, found its way into oceanography as a means of describing the flow between ocean basins separated by landmasses or deep sea ridges and connected only by relatively narrow and shallow channels. These flows, although not observable from land, are analogous to flow over weirs, dams or waterfalls, which have been studied long before the oceanic phenomenon since they are much easier to observe.

The existence of exchange flows in the oceans was first described in an extensive scientific work undertaken by Marsigli (1681) which was far ahead of its time. He described the surface current in the Bosphorus Strait which enters the Sea of Marmara from the Black Sea and the deep current which flows in the opposite direction towards the Black Sea. The subject of Oceanography and with it the continued interest in exchange flows did not flourish until about 150 years later. Since then interest in the study of exchange flows has grown steadily and the added complexity of rotation entered the picture due to the much larger scales in size and time of the oceanic flows in comparison with the counterparts on land.

As an introduction to the thesis, we will outline the motivations which lead to this work being undertaken in section 1 of this chapter and try to give the reader a feeling for why there continues to be a great interest in studying exchange flows and associated overflows. Then in section 2 we will move on to outline previous research on the topic, covering theoretical and modelling studies as well as work carried out in the field and the laboratory. Finally an outline for the chapters that follow will be given and the core findings will be previewed in section 3.

1.1 Background and motivation

We have already alluded to the fact that exchange flows occur where topographic constraints, such as land masses or deep sea ridges, prevent the free flow of water masses between large ocean basins. In many such cases the flow has to make its way through relatively small, narrow channels which limit the transport that can be exchanged. In addition many of these channels are topographically quite complex. They usually consist

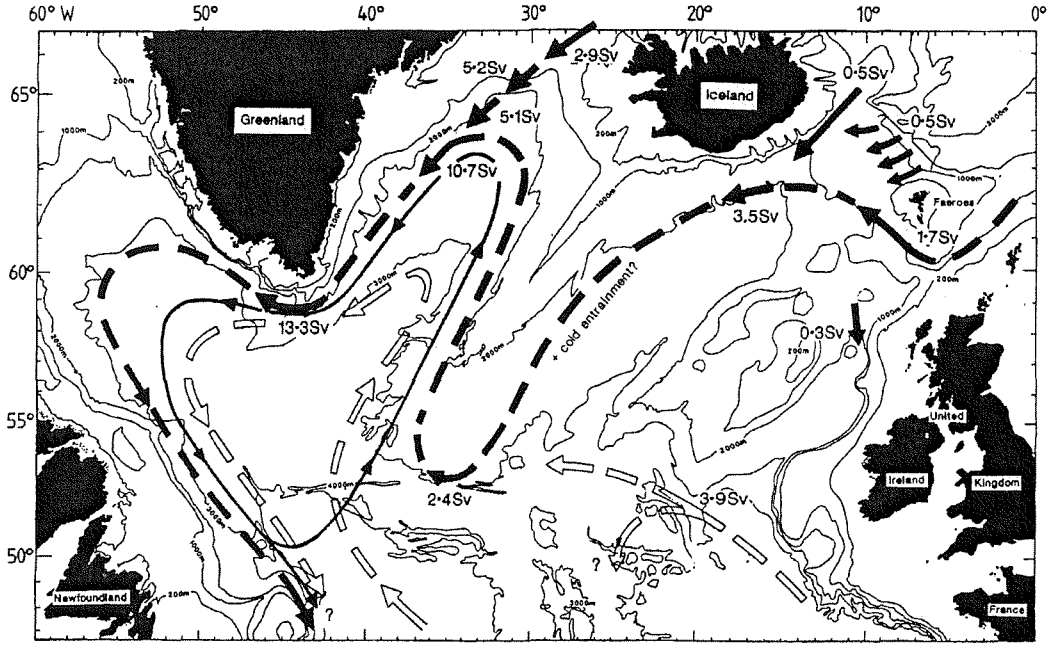

Figure 1.1: Proposed transport scheme in the North Atlantic resulting from the overflows at the GIS Ridge. Figure reproduced from Dickson and Brown (1994).

of at least one constriction, the narrowest points along the channel, and one or more sills, the shallowest or saddle points. Away from these extrema in the topography the channels widen and deepen and eventually enter into large adjacent ocean basins.

The word *strait* is generally used for constrictions between land masses, such as the Strait of Gibraltar, the Denmark Strait or the Strait of Sicily, amongst many others. Channels which transect deep sea ridges are usually referred to as *deep sea channels.* We shall limit our studies in this thesis to straits.

The flow through these bottlenecks of the ocean is driven by the density differences between the water masses on either side of the channels. One of the basins will contain denser water than the other one and it will overflow as a gravity current into the depths of the basin which contains predominantly lighter water masses. In return those lighter waters are 'sucked' into the denser basin along the surface to balance the volume loss through the overflow. The amount of transport exchanged is determined largely by the surrounding topography via a mechanism referred to as *hydraulic control.*

The overflows can pick up spectacular speeds as they descend down the slope into the lighter basin. Along the way they entrain surrounding fluid through the large shear which develops along the outer edge of the overflowing water mass, thus growing steadily in transport. By this entrainment process they form deep waters which play a major role in driving the thermohaline circulation (sometimes referred to as the meridional overturning circulation) and thus determine the development of global climate.

An important example of a region which is well known for its overflows and resulting deep water formation is the Greenland-Iceland-Scotland (GIS) Ridge. Through cooling of the surface waters in the Greenland-Iceland-Norwegian (GIN) Seas deep dense water

of the surface waters in the Greenland-Iceland-Norwegian (GIN) Seas deep dense water downwells and piles up behind the ridge, it then overflows predominantly through the two deepest channels along the ridge: the Faroe Bank Channel and the Denmark Strait. Using available observations Dickson and Brown (1994) put together a proposed transport scheme in the North Atlantic resulting from these overflows and the schematic is reproduced in figure 1.1. The Denmark Strait is located between Greenland and Iceland, while the Faroe Bank Channel lies south-west of the Faroe Islands as seen in the figure. Estimates suggest that roughly 2.9 Sv of Denmark Strait Overflow enter the North Atlantic and then entrain enough ambient water to form a 5.2 Sv strong deep boundary current. The flow through the Faroe Bank Channel is estimated to be somewhat weaker at 1.7 Sv, however it too entrains a substantial amount of ambient water and grows in transport to an estimated 3.5 Sv. It follows the topography of the Reykjanes ridge, growing further in transport, and joins the Denmark Strait overflow to form a combined deep water current of 10.7 Sv, which drives the circulation in the entire North Atlantic

The effects rotation has on overflows such as the one through the Faroe Bank Channel are clearly seen in figure 1.2, which has been reproduced from Duncan et al. (2003) and shows three temperature and velocity sections of the flow through the Faroe Bank Channel at the sill (top) and at two sections further downstream. In the top panel the overflow is concentrated right at the bottom of the channel and the contour of zero velocity is almost horizontal across the channel. Further downstream however, in the middle panel, the overflow current is banked up against the right-hand wall due to rotational effects and continues travelling along the slope as it moves further downstream as seen in the bottom panel. In wider channels such as the Denmark Strait the concentration of the flow along the right-hand side[1] of the channel and the tilt in density (or temperature) interfaces is still more obvious. It is assumed that rotation limits the flow through straits, especially in channels wider than a Rossby radius, and provides an upper limit for the transport; it is therefore imperative to include this condition when studying the mechanisms determining controlled flows.

Because of their important role in determining and driving the thermohaline circulation it is vital to get exchange flows and overflows right in global climate models. This is difficult however, since most climate models employ quite a coarse resolution to permit them to be run over long time periods. Often the resolution is so coarse that a channel like the Denmark Strait is represented by only 2 or 3 grid boxes, which makes an accurate reproduction of the physical processes in the Strait impossible.

The effects a misrepresentation of the overflows can have on basin wide circulation patterns has been effectively shown by Roberts and Wood (1997). They carried out tests with four different topographic representations of the GIS Ridge, shown in figure 1.3, using a typical Bryan-Cox type climate model with vertical levels describing the topography. They found that small changes in the topography can give significantly different transports

[1] In the Southern Hemisphere it will bank up on the left-hand side

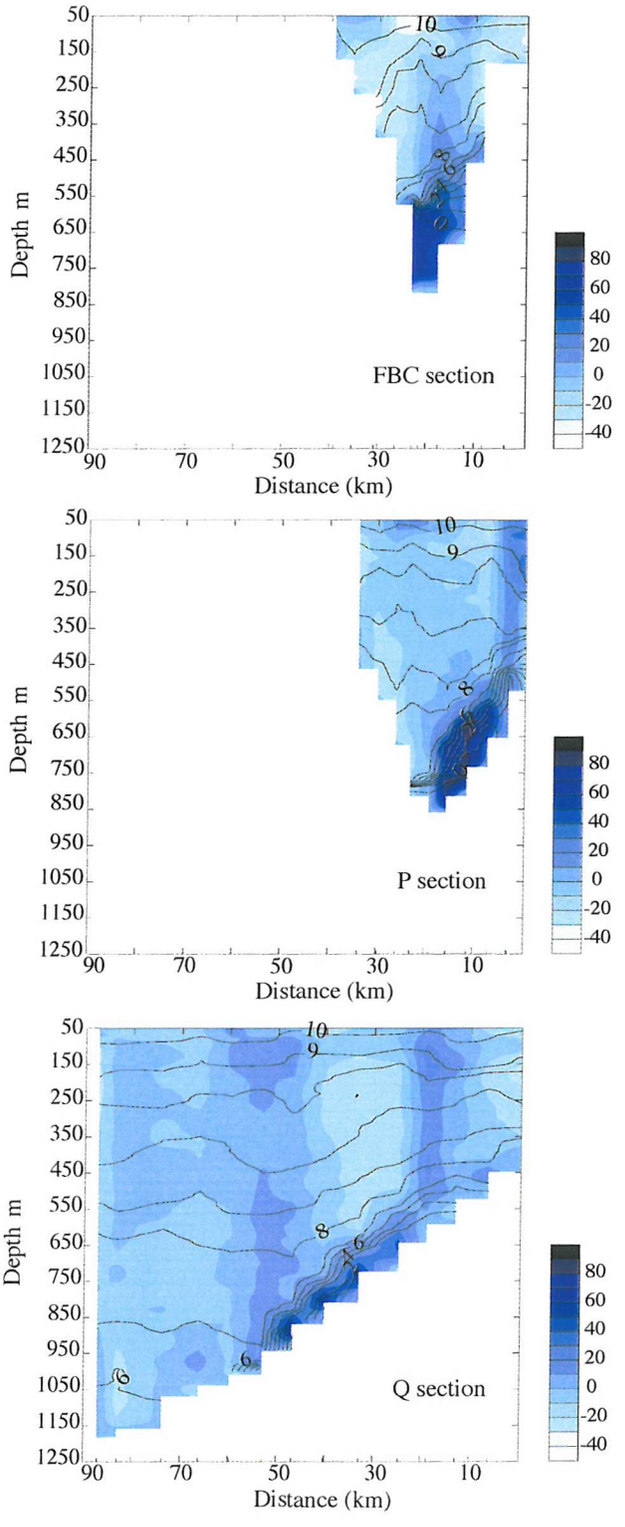

Figure 1.2: Velocity shading (cm/s) and temperature contours (^{o}C) for a section at the Faroe Bank Channel (top) and two sections some distance downstream of the channel (middle and bottom). The plot is reproduced from Duncan et al. (2003).

across the ridge which in turn alters the circulation in the adjacent basins appreciably.

As can be seen in the figure 1.3, the flux can range from 0 Sv to 12 Sv and Roberts and Wood (1997) found that in the two cases with little or no dense overflow, the overturning circulation and hence deep water formation in the GIN Seas ceased, while it was up to 10 Sv in the experiments with large overflows which is an overestimation of the observed values. The overturning circulation in the North Atlantic increases by up to 50% in the experiments with large overflow transport compared to those with little overflow. This increase in zonal mass transport also enhances the heat transport by about 50% which is a major change that needs to be considered when using such models to study climate.

Additional demonstration of the importance of continuing studies of overflows, was given by Hansen et al. (2001). They link a decrease in the upstream interface height of the overflow water at an Ocean Weather Station north of the Faroe Bank Channel to the decrease in the transport through the channel observed in historical data between 1950 to 2000. In regions such as the North Atlantic these kinds of changes can have significant effects on the formation of deep water as well as the development of the meridional overturning circulation.

Generally the way to improve the representation of overflows in OGCMs has been seen to be the parameterisation of the overflows and it is to this end that we propose to study and deepen our understanding of these flows. The first attempt at implementing and testing a parameterisation of overflows in a z-coordinate Ocean-General-Circulation-Model (OGCM) was done by Price and Yang (1998). They combined transport estimates as well as a formulation for the entrainment into a Marginal Sea Boundary Condition (MSBC) to prescribe the flow in an OGCM. We will briefly discuss more details of this work at the end of section 2.

Now, before we outline the layout and content of the thesis, let us briefly review some of the work that has been done in the field of rotating hydraulics to date and is still currently being carried out.

1.2 Review of previous research

Let us first of all consider some of the analytical work involving hydraulic theory to date. This is by no means a complete review of all related studies to date but gives just an overview of what we feel have been the most important contributions to the field. Many other references can be found within the cited papers as well as further on in this thesis.

1.2.1 Hydraulic theory

Non-rotating flows

A large body of work already existed for non-rotating hydraulics before the more complex effects of rotation were included. Most notably Wood (1970) studied single layer flow

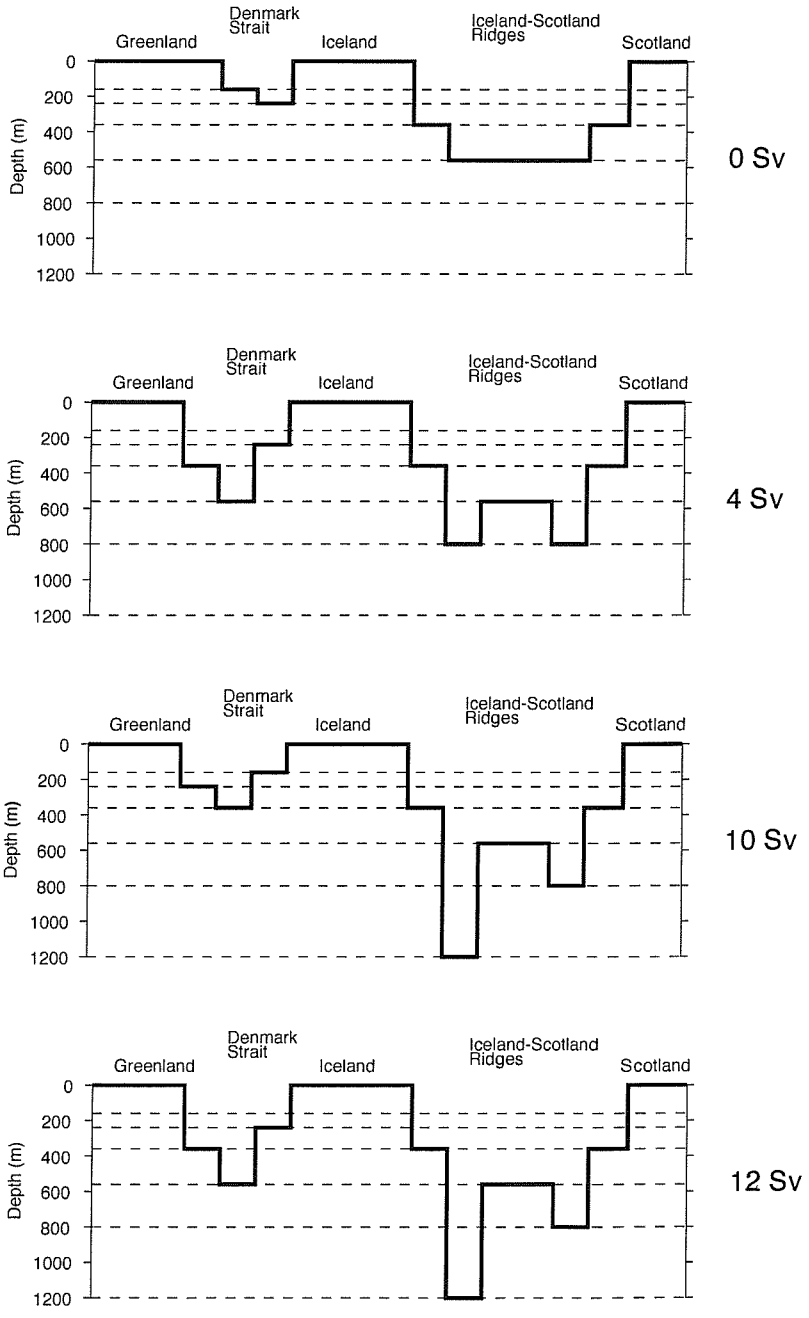

Figure 1.3: Different topographic cross-section of the GIS Ridge tested by Roberts and Wood (1997) in a Bryan-Cox type model. The numbers indicate the total transport across the ridge.

through a contraction, as well as the flow of a single layer underneath a stagnant layer and the exchange of two layers through a contraction.

Subsequently Armi and Farmer contributed a significant body of work to the understanding of two-layer exchange without rotation; in particular, Armi and Farmer (1986) study the maximal two-layer exchange through a contraction with barotropic net flow, and Farmer and Armi (1986) outline the same sort of investigation for flow over a sill and through the combination of a sill and contraction with barotropic flow. The latter type of exchange flow, they found, is fundamentally different from the former. In the case of the sill the control at the crest acts primarily through the deeper layer into which the sill projects and only indirectly controls the surface layer.

Armi and Farmer developed the representation of the flow solutions on a Froude number plane and used it to show clear distinctions between maximal and submaximal flows. Dalziel (1991) continued the study of the non-rotating case by adapting the functional approach developed by Gill (1977), however he primarily focused on the maximal solutions of such flows.

Rotating flows

The study of rotating hydraulics gained momentum with a small theoretical and practical study by Whitehead et al. (1974), for zero potential vorticity flows. They found transport estimates for both a single layer and a two-layer rotating flow, which are given by $\frac{1}{2}\frac{h_u^2 g'}{f}$ and $\frac{1}{6}\frac{H_0^2 g'}{f}$ respectively, where h_u is the height of the surface of the dense water in the upstream basin above sill level, g' is the reduced gravity, f the Coriolis parameter and H_0 the depth of the channel at the shallowest point. To this day the first expression for the transport is still the most effective and widely used and has been shown by Killworth and McDonald (1993) to be an upper bound of the single-layer flux.

Gill (1977) formulated the single layer rotating problem in terms of a functional for constant potential vorticity, and Dalziel (1988) and Dalziel (1990) adapted this approach for two-layers with rotation for zero and constant potential vorticity and also supported his finding with laboratory experiments.

All of the studies mentioned so far were limited to idealised rectangular channels.

Topgraphy

The next complexity added to the study of hydraulics after rotation was that of a more realistic topography than the simple rectangular sections. Dalziel (1992) outlined properties of two-layer non-rotating flow through a variety of non-rectangular sections, such as parabolas and v-shapes, and Killworth and McDonald (1993) showed that the flux estimate in the single-layer case was also an upper bound for channel cross-sections which did not necessarily have a flat bottom. Killworth (1994) continued the work on maximal flux estimates by showing that the zero potential vorticity flow in a rectangular channel is an upper bound for all possible potential vorticity distributions, which is true for all

bottom shapes.

Stratification

Due to the mathematical complexity of the problem progress beyond this point has been slow and only few studies have been done for flows with more than two layers. Smeed (2000) outlined a non-rotating theory for three layers, based on Dalziel (1991), which was inspired by the desire of the author to build a theoretical understanding of the seasonal variations observed in the Bab al Mandab. Bab al Mandab connects the Red Sea to the Gulf of Aden and it exhibits a three layer exchange flow during the summer months. This work lead on to the extension of that theory for multiple layers by Lane-Serff et al. (2000).

Killworth (1992b) has been one of the very few to touch upon the problem of continuous stratification without rotation and Killworth (1995) briefly attempts to outline the behaviour of continuously stratified rotating flow.

Mixing, friction and time dependence

Other aspects of exchange flows and overflows which have also attracted a lot of attention are the effects of mixing and time dependence on the transport through channels. Field observations have often shown the theory to overestimate actual observed flows (Killworth (1992a); Whitehead (1998)) and effects other than topographic control and rotation, such as diapycnal mixing, friction and time dependence, are believed to play a key role in limiting the flux. Helfrich (1995) looks at time dependent aspects of two-layer non-rotating flows while Pratt et al. (2000) analyse the time dependent hydraulic adjustment of single-layer flow in a rotating channel. Hogg et al. (2001) look at the effects of mixing in a two-layer non-rotating flow, while Pratt (1986) investigated the effect of friction on the flow.

1.2.2 Numerical modelling of exchange flows

To overcome the hurdle imposed by the complexity of the problem when studying the effects of rotation, mixing or more complex topography on exchange flows, one way forward might be to use primitive equation models to simulate those effects.

There are two kinds of numerical modelling approaches, which have been used to study overflows. One is the process-model approach, that is a primitive equation model is set up with a simplified and idealised domain to study very specific aspects of exchange flows. This is the approach we will take in the second part of the thesis to investigate the dependence of the transport on a variety of external parameters in a very idealised setting.

The second approach is to study a specific strait with realistic topography at high resolution and compare results with those from observations to 'fill in' the aspect of the flow missed in the limited scope of any observational work.

Käse and Oschlies (2000) carried out a modelling study of the flow through the Strait of Denmark using SPEM (S-coordinate Primitive Equation Model). First an idealised topographic setting was taken to test the model and subsequently realistic topography was introduced to investigate the response of the overflow to the irregular features of the real ocean floor. They found that downstream of the sill a string of eddies forms which agrees with observations and they also tested the response of the overflow to different magnitudes of bottom friction. Following this work Käse et al. (2003) compared a comprehensive set of observations taken over three years 1996 - 1998 with the results from further runs using SPEM with a very similar set-up as in Käse and Oschlies (2000).

Another example of a detailed modelling study is that by Ferron et al. (2000). Its principal goal was to find the best topographical representation of the Romanche Fracture Zone in climate models that captures the control section accurately, in order to achieve the right amount of transport of Antarctic Bottom Water from the Brazil Basin into the Sierra Leone and Guinea Basins. Results from a primitive equation model and a reduced gravity model were used to identify the crucial sections and were compared with field observations along the Fracture Zone with great success.

Numerical models can equally be an effective tool to investigate the effects of exchange flows on the adjacent basins. Herbaut et al. (1996) used a z-coordinate primitive equation model to study the effects of the density forcing through the Strait of Gibraltar and the Strait of Sicily on the general circulation of the Western Mediterranean Sea.

As part of this thesis, we will be working with MICOM (the Miami Isopycnic Coordinate Ocean Model) to carry out an idealised process study of two-layer exchange flows. In this context a modelling study by Willebrand et al. (2001) is of specific interest to our work. They carried out an intercomparison between a Bryan-Cox type (BC) ocean model, using geopotential levels to represent the topography, an isopycnic coordinate ocean model and a model using terrain-following (sigma) coordinates, by modelling the circulation in the North Atlantic. Similarly to Roberts and Wood (1997), they found that a major factor determining whether the overturning circulation is realistic or not depends crucially on the accuracy of the representation of the overflows. The isopycnic model (MICOM), they used was found to be the most reliable in its representation of these flow, thus justifying our choice for using MICOM in this particular study.

Another difference between the BC model and MICOM is the limited representation of topography in the BC model, while isopycnic models allow for more realistic representation of the topography.

All types of process studies of idealised or specific exchange-flow models outlined above are very useful. Not only do they allow us to study the detailed processes of the flows which observations might miss, but they also allow us to validate the results of the models through the comparison with the data and improve the representation of certain processes in the large scale global models. Furthermore they can help to identify regions of particular interest in terms of specific flow features or important localised processes and thus lead to better informed and targeted observational initiatives.

1.2.3 Observational and laboratory studies

Observational work is, by its nature and the locations of some of the most interesting overflows, long and expensive in the planning and often dependent on the weather conditions one finds at the time of the cruise. For this reason observational data especially in the Northern Atlantic are still scarce. Continued efforts are being made however to gain in situ data for comparison with model results and quantify the effects of topographic control and the limiting factors such as mixing and friction.

The observational studies carried out in the Denmark Strait in 1997 and 1998, mentioned in section 1.2.2, are described by Girton and Sandford (2001, 2003) and the analysis focuses on the modifications of the flow due to bottom friction and entrainment. Nikolopoulos et al. (2003) apply the hydraulic single-layer theory by Killworth (1994) with realistic topography to the flow in the Strait of Denmark. Their estimates are based on a subset of the observations described by Girton and Sandford (2003) and show good agreement with the observed flows of about 2.5 Sv.

The Faroe Bank Channel, although it is deeper than the Denmark Strait, has been found to carry slightly less transport across the GIS Ridge. Saunders (1990) estimated a transport of about 1.9±0.4 Sv. These results were obtained from observations in the region in 1987 and 1988. CTD and ADCP sections from these cruises provided cross-sectional profiles of the density and flow field in the channel and the characteristic tilting of the interface across the channel due to the influence of rotation is evident. More recent work on the Faroe Bank Channel has been published by Duncan et al. (2003) and involves the analysis of observations from RRS *Discovery* cruise 242 which was undertaken in autumn of 1999. The specific focus of this work was on the effects of friction and mixing in the channel. A similar study was undertaken by Mauritzen et al. (2004), which also deals with the importance of mixing in the region around the Faroe Bank Channel .

However, the probably most studied strait, from an historical point of view, is the Strait of Gibraltar connecting the Mediterranean to the North Atlantic. A comprehensive report of the flow through this strait was put together by Lacombe and Richez (1982) and Armi and Farmer (1985) analysed the data in the context of two-layer hydraulic exchange. They found that the exchange flow is controlled at three sections along the channel whose locations depend only on the local topography. In particular they found that the Mediterranean outflow is primarily controlled at the Spartel sill, which lies west of the narrowest point of the Strait, while the inflowing Atlantic surface water is mainly controlled at the Tarifa Narrows. A third control at the Camarinal sill, situated between the Spartel sill and the Tarifa Narrows, is highly time dependent and only acts on the overflowing bottom layer.

Bryden and Kinder (1991) review a traditional method based of salt and mass conservation to determine the in and outflow through the Strait of Gibraltar using the Knudsen relations:

$$Q_1 = \frac{S_2 E}{S_2 - S_1} \tag{1.1}$$

$$Q_2 = -\frac{S_1 E}{S_2 - S_1} \tag{1.2}$$

Here S_1 and Q_1 denote the salinity and volume flux of Atlantic surface waters into the Mediterranean, while subscript 2 denotes the same variables for the Mediterranean water and E is the amount of evaporation over the Mediterranean. Bryden and Kinder (1991) also apply a steady non-rotating hydraulic control model to determine the flux. The effects of rotation on the surface flow of Atlantic water through the Strait has been investigated by Bormans and Garrett (1991)

In the context of the Mediterranean the Sicily Strait has also been studied observationally in recent years, as well as being modelled numerically. A comprehensive comparison of observational an numerical results is currently being published by Béranger et al. (2004).

Besides comparison with observational results, laboratory work often comes in support with some of the theoretical work mentioned earlier. Both Whitehead et al. (1974) and Dalziel (1988) supported and compared their analytical work with laboratory experiments. Laboratory studies are very useful for studying particular qualitative features and processes of the flow, but are often less useful for direct quantitative comparisons.

Borenäs and Whitehead (1998) carried out an experiment in a rotating tank to test the nature of the upstream separation in a single layer flow and compared the results to two different theories they developed. One assumed the separated region to be stagnant and the other assumed it to be recirculating. They found that the observations from the experiments resembled the theory postulating a stagnant region more closely than that postulating a recirculation region, but the comparison was not conclusive. In a similar fashion Pratt (1987) concentrated on the behaviour of hydraulic jumps in a rotating channel with a single layer.

Recent novel experiments carried out by Rabe et al. (2002) investigate the effects of an island in a flat bottom channel on the exchange flow through that channel.

1.2.4 Parameterising overflows

We have already mentioned in section 1 that the aspect of greatest interest in connection with overflows is to represent them correctly and efficiently in OGCM. Where this is not possible due to the lack of resolution a workable parameterisation is needed to emulate their effects correctly.

Price and Yang first attempted to parameterise overflows in 1998 (Price and Yang (1998)). Their proposed parameterisation is based on transport estimates from the Bryden and Kinder model (Bryden and Kinder (1991)), outlined in section 1.2.3 earlier, for channels narrower than a deformation radius. Transport through channels wider than one Rossby radius are represented by the estimate of Whitehead et al. (1974) for maximum single layer flow. Finally the entrainment model used is that of Price and Baringer (1994)

which doubles, in some cases even triples, the transport down the slope. All of these conditions are collapsed into a Marginal Sea Boundary Condition (MSBC), parameterising both the transport and the subsequent entrainment of the exchange. This parameterisation is then tested for two specific cases, the Mediterranean Sea and the Nordic Sea overflows, consisting of the flows through the Denmark Strait and the Faroe Bank Channel.

Some of the limitations of these parameterisations are outlined in the paper and are related to the particular implementation used in the model. In addition, the success of the parameterisation also continues to be limited by the yet unrefined representation of both the transport and the entrainment of the overflow.

1.2.5 Summary

The above references are just a selection of the kind of analytical and numerical modelling work that has been done, and is still continuing, to study hydraulic processes in idealised settings as well as the exchange flows and overflows through specific straits. We have also shown the considerable efforts to obtain field observations and model representative flows in the laboratory.

For a complete summary of the recent progress on the effects of rotation on models of sea straits, from a theoretical, modelling and observational point of view, see Pratt (2003c) as well as the review by Pratt and Lundberg (1991). A generalised and accessible introduction to the theoretical characteristics of non-rotating hydraulic flows is given by Pratt (2003a).

In addition there is a collection of short papers in the volume of proceedings from 'The second Meeting on the Physical Oceanography of Sea Straits' (2001) which are available to download from http://www.soc.soton.ac.uk/JRD/PROC/STRAIT/. From these it is evident that the importance of studying exchange flows has not diminished in recent years. A lot of research is currently being carried out in the field and many questions still await answers.

1.3 Goals and outline for the thesis work

It is our aim in this thesis to review and extend existing two-layer rotating hydraulic theory in order to refine our understanding of how hydraulic control processes work in flows influenced considerably by the rotation of the earth. We will work with the approach of Gill (1977) and Dalziel (1988) as well as that of Armi (1986), Armi and Farmer (1986) and Farmer and Armi (1986), and show that the two can be equally used to determine maximal as well as submaximal solutions of rotating flows. We will assume that the flow has zero potential vorticity (in the analytical modelling) and the topography is limited to a rectangular cross-section. However we will look at flat-bottom channels with a constriction as well as straight channels with a sill and combinations of the two.

The work will be new especially because it will deal extensively with submaximal

flows, whereas prior work such as Dalziel (1988) has often been limited to finding an upper bound to the flow. We feel that this approach is limiting, especially since we argue that it is difficult to actually observe maximal flows in the ocean and we will see that also numerical simulations of such flows are predominantly submaximal and only approach the maximal solutions.

We will focus on studying the dependence of the transport through straits on external parameters such as the Coriolis parameter or flow-specific conditions such as the density difference between the two main water masses or the availability of dense overflow water in the source basin.

Apart from studying the two-layer exchange flows analytically we will use MICOM (Miami Isopycnic Coordinate Ocean Model) with an idealised setup of a rectangular channel of constant width to model exchange flows over a sill at the centre of the channel. We will investigate how the transport through the channel responds to changes in rotation rate, density difference between the two water masses and the change in upstream interface height. This type of study has not been done previously. From the results we will derive an empirical estimate of the flow through the channel which we hope will be of use in future improved parameterisations of exchange flows. We will see from the modelling results that the time variability of two-layer exchange flow can be quite considerable, a fact often ignored by the theoretical models which are usually steady. Some of the time dependence we find seems to correspond to the pulsating phenomenon observed in the transport through the Denmark Strait and we will discuss the features giving rise to these pulsations.

The thesis is divided into eight chapters as follows:

Chapter 2, after this introduction, constitutes a background chapter on the principles of hydraulic theory. Many important concepts will be introduced which will be taken as known in the subsequent chapters and will not be explained again in detail.

Chapter 3 outlines our work on the rotating two-layer zero potential vorticity exchange theory expressed using two variables; details of what this means will become clear in chapter 2. We will show that for a very specific topography the flow can be represented and traced in a pseudo-Froude-number plane as used by Armi (1986) to trace non-rotating flow along a channel. In order to make the study comprehensive, we consider all possible configurations of how the interface between the two layers may be separated from the sidewalls and we will also discuss examples of maximal and submaximal flows as well as flows that cannot be traced. At the end we will derive the long-wave speeds for a few flows and show how they correspond to the controls we find using hydraulic theory.

Chapter 4 will outline a method of reducing the case studied in chapter 3 to a single variable, which allows us to find the controlled flow solutions using a single functional analogous to the method developed by Gill (1977). This case has been looked at by Dalziel (1988) but he only concentrated on maximal flows, while we will focus on submaximal flows and show maximal flows as a natural limit of the submaximal solutions. Results for controlled maximal and submaximal fluxes will be given for a comprehensive parameter

domain spanning a range of widths and Bernoulli potentials.

In Chapter 5 we move on to the numerical modelling part of the work. We will describe MICOM and present several test runs to determine the optimal resolution and topography for the rotating runs. Several non-rotating runs are presented and the results are compared to the well established theory by Armi (1986).

In Chapter 6 the rotating experiments are presented. Firstly we will discuss the flow structures observed in two selected experiments, one with a shallow channel (500 m) and one with a deep channel (900 m), where we find considerable time variability. Then the results from all experiments carried out in an idealised domain to establish the dependence of the transport through the channel on the upstream interface height, as well as on the rotating rate and the reduced gravity, are drawn together and an empirical estimate for the observed fluxes is derived. Finally we will outline a method of finding the control sections in the rotating flow, based on the long wave speeds derived from the model output. The results are indicative but not conclusive.

Chapter 7 will be a brief discussion of model runs carried out with a topography resembling approximately that of the Denmark Strait and the Faroe Bank Channel. As far as possible comparisons will be made between the model and observations as well as the theory.

In Chapter 8 we will briefly discuss our achievements and conclude with suggestions and ideas for future work.

The appendices of which there are 5 contain details of analytical methods and results and will be reference where appropriate. In appendix E lists of variables and parameters are given as we define them and use them throughout this thesis.

Chapter 2

Principles of hydraulic theory

The aim of this chapter is to give an overview of the principles of hydraulics as they have been developed and used previously for a wide variety of applications in many of the works already referenced in the introduction. We will summarise fundamental aspects of the theory that will reoccur throughout the thesis and knowledge of which will be taken as given later on.

In the past the route to determining critical solutions of hydraulic flows has come from two different angles, distinguished by the presentation of the solutions, but essentially based to the same assumption made about the flows. The first route, referred to as the 'functional approach', was formulated by Gill (1977) for the single layer rotating case with uniform potential vorticity and has since been adapted by Dalziel (1988) for the twolayer non-rotating and rotating cases, and used by Lane-Serff et al. (2000) to determine multiple layer controlled solutions. It generalises the hydraulic problem and sets up a framework within which a variety of problems can be solved.

Armi (1986), Armi and Farmer (1986) and Farmer and Armi (1986) on the other hand have approached the solutions by arguing an asymmetry of the flow over a channel or through a constriction, which is also an assumption made in the functional approach, and describing it in terms of Froude numbers. It will become clear in this chapter, and in chapter 3, that both approaches rely on the same principles to find the solutions and that the problem solved by Armi (1986) is just one case of a class of problems solvable using the functional approach.

Pratt (2003a) has summarised the general conditions for hydraulic criticality for a variety of examples and his work shows nicely the link between the work by Armi (1986) and the functional approach. We will review the most important aspect of his work here which will also be at the centre of the work we present in chapters 3 and 4.

2.1 Single variable problem

A fundamental characteristic of hydraulic flows are the conserved properties they exhibit over the entire flow, such as volume or mass transport, potential vorticity or energy. They are the core upon which the solvability of the problems is based. These quantities are

functions of the flow structure such as velocities and layer thicknesses, as well as the geometry of the channels and obstacles which the flow encounters. The flow can therefore be described using functionals, we will denote these by G, which are expressions of the conserved quantities in terms of variables describing the flow structure and geometry at a given section of the channel such as its width $L(x)$, and its depth $D(x)$.

Throughout these first three chapters we will use x as the along channel axis, y as the across channel direction and z as the vertical axis. Additionally we choose a topography that only changes with x but remains constant across the channel. Therefore L and D above only depend on x.

In its simplest form, in a single layer flow for example, the hydraulic problem can be described by one functional with one unknown such as the depth of the layer, $h(x)$. Solving for this unknown determines the flow structure at a given section, where $L(x)$, $D(x)$, and external parameters such as the Bernoulli potential, E are also known:

$$G(h(x); L(x), D(x); E, Q, ...) = \text{constant}. \tag{2.1}$$

We have chosen $h(x)$ as an example, but it could be any other variable describing the flow. By definition

$$\frac{dG}{dx} = \frac{\partial G}{\partial h}\frac{dh}{dx} + \frac{\partial G}{\partial L}\frac{dL}{dx} + \frac{\partial G}{\partial D}\frac{dD}{dx} + \cdots = 0 \tag{2.2}$$

To derive the condition under which critical flow occurs we need to think about the conditions in which free, stationary long-waves of small amplitude can exist in the flow. The requisite for such a stationary wave is that at some section along the channel it must be possible to alter the steady flow in such a way that the conserved quantities such as flux and energy are still conserved, this is the critical section. In other words, a small disturbance dh can exist at the control section that is independent of variations in L and D and preserves G:

$$(dG)_{L,D,...} = \frac{\partial G}{\partial h}dh = 0 \tag{2.3}$$

or

$$\frac{\partial G}{\partial h} = 0 \tag{2.4}$$

This is equivalent to saying that the flow is asymmetric about the controlled point, because as a result $\frac{dh}{dx}$ can take a finite value at the control. In this case the structure of the flow is different on either side of the control, with distinct velocity and interface profiles; this applies at every controlled section. If $\frac{\partial G}{\partial h} \neq 0$ then $\frac{dh}{dx}$ would have to be equal to zero for equation (2.2) to hold, and the flow would be symmetric about the proposed control and thus not critically controlled.

In order for (2.2) to hold, the following also has to hold true at all control sections

$$\left(\frac{\partial G}{\partial L}\frac{\partial L}{\partial x} + \frac{\partial G}{\partial D}\frac{\partial D}{\partial x} + \ldots\right)_{x=x_c} = 0. \tag{2.5}$$

This condition is often referred to as the 'regularity' condition. Sections at which both $\frac{\partial D}{\partial x}$ and $\frac{\partial L}{\partial x}$ are zero, are *primary*, or topographic controls. In a constant width channel they lie at the crest of the sill, and in a channel of constant depth they coincide with the narrowest point of the topography.

It is also possible for controls to occur at points away from sections which exhibit a topographic extremum. The location of these is determined by evaluating $\frac{\partial G}{\partial L} = 0$ or $\frac{\partial G}{\partial D} = 0$, depending on whether the set topography is constant in depth or width respectively. If both depth and width vary all terms in equation (2.5) need to be considered. We refer to these controls as *secondary*, or virtual controls.

Knowing the channel geometry and flow structure of the primary control x_c (c indicates values at the primary control) in theory allows us to find the position of the secondary control x_v (v indicates values at the secondary control) for channels of relatively simple geometry, by following a few steps.

Let us assume a channel of constant width L with a simple sill. Furthermore let us assume that, for a given Bernoulli potential G, we determined the flow features at the primary control which, as we know, occurs at the top of the sill.

1. We know G_c which, by definition, is the same for the entire flow and thus equal to $G(x_v) = G_v = G_c$.

2. We then solve $\frac{\partial G}{\partial D} = 0$, since D is the only varying parameter in the problem, and we find an expression for the one unknown, $h(x)$, in terms of the depth at the secondary control, D_v, which we are trying to find. (All other variables in the function such as L and G are known.)

3. Since G_v is dependent only on $h(x_v)$ and D_v, since all other parameters are known, we can substitute for $h(x_v) = f(D_v)$ into the functional G and solve for D_v.

4. We have therefore found D_v at the secondary control, which allows us to find $h(x_v)$ and thus determine the flow conditions at the virtual control.

Of course this procedure can only be used if either D or L is constant and if the location of the primary control is known.

In the rotating case this method of finding the second control is further complicated by the fact that the interface separating the two layers may be tilted so much that it outcrops at the surface of the flow or grounds at the bottom of the channel. In such cases G may vary along the channel as the flow regimes change and each case needs to be considered separately.

Dalziel (1988) developed a more general procedure to find both controls for a rotating channel with more complex topographies, even if the primary control is not known for certain. These added complexities mean that the controls can only be solved for numerically, as done by Dalziel (1988). Finding the second control in the non-rotating as well as the rotating cases is fundamental to Dalziel's work since he explicitly concentrates on

finding maximal flows, which are flows that pass through two controls and result in the maximum possible flux through a given topography.

We will not dwell on a method to find the second control position, but rather describe maximal flows as a natural limit to flows through channels where we always know the position of the primary control. A more detailed description and discussion of maximal and submaximal flows follows in section (2.4).

Pratt (2003a) summarises various cases for which the functional approach is applicable. An example for a hydraulic problem which can be formulated with a single unknown and one functional is the single-layer non rotating case. Solving $\frac{dG}{dh} = 0$ in this case leads to the familiar condition that at the control section $u = \sqrt{g'h}$, meaning the speed of the flow u is equal to the speed of propagation of a typical long-wave $\sqrt{g'h}$ and as a result the wave is arrested. This suggests the definition of criticality in terms of the Froude number:

$$F = \frac{u}{\sqrt{g'h}} = 1 \tag{2.6}$$

However if complexity is added to the problem, such as a second, dynamically important layer or rotation for example, the problem may not reduce to a single functional any longer and two or more such equations need to be formulated and treated separately. The next section will outline the general characteristics of such a flow.

2.2 Two-variable problem

Instead of one functional G the flow is now described by two such expressions G_1 and G_2, each depending on two unknowns which we shall denote by h_1 and h_2 denoting layer thicknesses in a two-layer problem,

$$G_1(h_1(x), h_2(x); L(x), D(x); E_1, Q_1 ...) = \text{constant} \tag{2.7}$$

and

$$G_2(h_1(x), h_2(x); L(x), D(x); E_2, Q_2 ...) = \text{constant}, \tag{2.8}$$

as before, these unknowns may be chosen to be other variables describing the flow. The condition for solvability at the control is that the Jacobian of these two functions vanishes, meaning that they are tangent in the (h_1, h_2) plane:

$$\nabla G_1 \times \nabla G_2 = \frac{\partial G_1}{\partial h_1}\frac{\partial G_1}{\partial h_2} - \frac{\partial G_1}{\partial h_2}\frac{\partial G_2}{\partial h_1} = 0, \tag{2.9}$$

where $\nabla = \frac{\partial}{\partial h_1} i + \frac{\partial}{\partial h_2} j$.

The regularity condition as described by Pratt (2003a) becomes:

$$\frac{\partial G_1}{\partial h_i}\left(\frac{\partial G_2}{\partial x}\right)_{h_1,h_2} - \frac{\partial G_2}{\partial h_i}\left(\frac{\partial G_1}{\partial x}\right)_{h_1,h_2} = 0 \qquad (i = 1 \text{ or } i = 2). \tag{2.10}$$

Here the subscripts denote parameters which are being held constant.

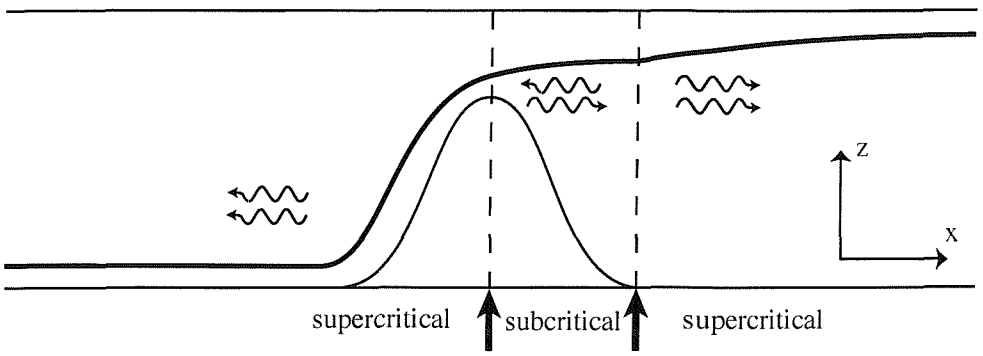

Figure 2.1: Sketch to illustrate the separation of super- and subcritical regions of flow by the control point indicated by arrows and dashed vertical lines. The wavy arrows indicate the direction in which the waves are able to propagate along the channel. Notice that the information is always propagates away from the subcritical region in the centre. The regime shown is maximal, for submaximal flows the supercritical region upstream becomes subcritical.

An example of a problem formulated using two functionals, given by Pratt (2003a), is two layer non-rotating flow. This problem reduces to a similar condition as the single-layer flow where the composite Froude number, $F_1^2 + F_2^2 = \frac{u_1^2}{g'h_1} + \frac{u_2^2}{g'h_2}$, equals unity.

Armi and Farmer (Armi (1986); Armi and Farmer (1986); Farmer and Armi (1986)) have created a significant body of work for the non-rotating two-layer case, using Froude number planes to describe the solutions space. This approach is a variant of the functional approach. Although it does not use functionals explicitly it makes the same fundamental assumption about conservation of certain quantities within the flow. Armi and Farmer assume that both the Bernoulli potential and the flux along the channel are conserved and tangential at the control and these two quantities are the functionals.

Pratt (2003a) goes on to describe an analogous method for multiple functionals in multiple unknowns. This may be useful for flows which have more than two dynamically important layers, such as the exchange flow in Bab al Mandab, which is made up of three layers in the summer. Multi-layer theory has also been developed by Lane-Serff et al. (2000), with particular application to Bab al Mandab.

2.3 Super- and subcritical flow

So far we have established that the points at which $\frac{\partial G}{\partial h} = 0$ are critical for describing hydraulic flows, but using a functional also allows us to make important statements about the regions of flow separating the control points. Here $\frac{\partial G}{\partial h}$ is either > 0 or < 0, the former is referred to as *supercritical* flow and the latter as *subcritical* flow. Both regions are distinctive not only because of the different gradients of the functional but also because the free long-waves are able to travel in different directions depending on whether the flow is super- or subcritical.

In a two-layer flow with a rigid lid, there is one internal wavemode which has two wave speeds associated with it. If the two phase speeds have opposite signs, the internal waves

can propagate both upstream and downstream and the mode is subcritical. If the two phase speeds have the same sign then the internal waves of that mode can propagate in one direction only, the mode is supercritical. When one of the phase speeds is equal to zero then that mode is critical. We could therefore determine whether a flow is controlled by solving an eigenvalue problem for the wave speeds, but using the functional gives us direct access to this information without solving for the waves. A sketch of the behaviour of the wavemodes at different points along the channel is shown in figure 2.1.

Depending on how many controls a flow encounters and what type of regions it exhibits the flow solutions along the channel are referred to as maximal and submaximal which will be described briefly.

2.4 Maximal and submaximal solutions

In figure 2.2 the different types of flows are indicated for a simple non-rotating sill. The two controls are indicated by thick arrows below the topography. The supercritical regions are indicated by solid lines and the subcritical regions by dashed lines. The diagram is redrawn from Dalziel (1988, 1990), and shows the solutions of the interface height above the topography for a non-rotating flow. We have already alluded to the fact that the interface in rotating flow is slanted across the channel and so cannot be represented with a single line along the channel, however the regional division between the supercritical and subcritical flow stays the same with the possible controls occurring at the top of the sill and at the entrance upstream. This fact has been observed by Dalziel (1988).

Maximal flows pass through two controls and are made up of two supercritical regions separated by a subcritical region. In the supercritical regions information is carried away from the subcritical region by internal waves and as a result changes in the supercritical regions do not affect or change the flow in the subcritical region. Changes in the subcritical region on the other hand are carried into the supercritical regions and the flow here adjusts itself to match the changes. It has been described by Armi and Farmer (1986) as well as by Dalziel (1988), that maximal flows are not influenced by any changes in the upstream and downstream basins.

Submaximal flows (marked with thin lines in figure 2.2) only pass through one control at the sill that separates one supercritical region, downstream, from one subcritical region, upstream. Therefore changes in the subcritical upstream basin may affect and change the flow at the control and in the supercritical region.

Figure 2.2 shows that for flow over a simple sill the controls are separated by some distance. For zero net flow through a flat-bottom channel the controls actually coincide at the narrowest point of the channel and as a result the subcritical region separating the two supercritical regions vanishes, according to Armi (1986) and Armi and Farmer (1986).

Maximal flows (marked with thick lines in figure 2.2), as the name suggests, give the maximum flow possible through a given geometry, and previous studies have often

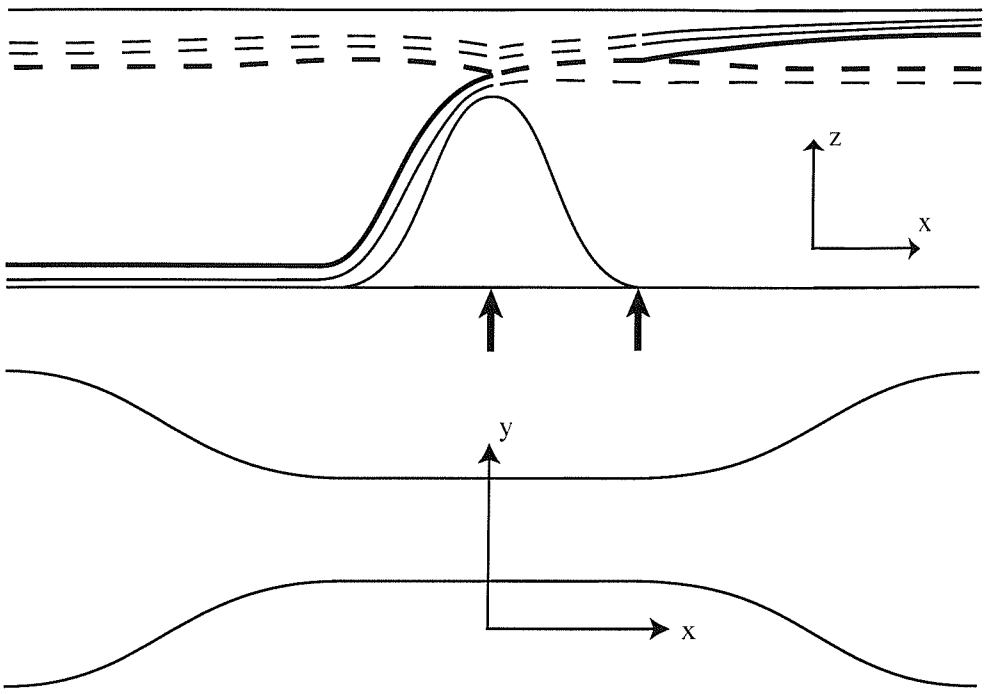

Figure 2.2: In the top panel an along channel section shows the types of flows possible over a simple sill. The thick lines indicate maximal flow and the thin lines submaximal flows, while the dashed lines mark subcritical flow and the solid lines supercritical flow. The primary control at the top of the sill and the secondary control at the entrance of the channel from the upstream basin are marked by the big arrows. Note that only in the maximal flow does the second control separate a subcritical from a supercritical region. In this case there is an alternative flow of the same flux but with a subcritical region upstream. In the bottom panel a planar view of the channel is shown. The second control is only possible because at the entrance the channel becomes flat and widens towards the upstream basin. This sketch is reproduced from Dalziel (1990).

focused on finding maximal flows for specific topographies independent on conditions in the basins. Examples as mentioned before are Whitehead et al. (1974) and Dalziel (1988) in the two-layer case. In the study of single-layer flows on the other hand variations in the upstream conditions have already been largely taken into account in the theory, by Whitehead et al. (1974) and Killworth and McDonald (1993), amongst others.

In reality however, two-layer flows can also be highly variable on daily timescales, due to tides, on yearly timescales, due to the seasons, and even on decadal timescales, due to climatic variability. Such variability has been observed in all major straits such as the Strait of Gibraltar, the Denmark Strait and most notably the Faroe Bank Channel, for which Hansen et al. (2001) discovered a marked decrease in transport over the last 5 decades since 1950. This leads us to conclude that many actual overflows are not necessarily maximal. It has been shown by Whitehead (1998) and Killworth (1992a) that maximal transport estimates often result in much larger transport than actually observed and it is therefore worth studying, in more detail, the submaximal flows in two-layer flows which may be more helpful in estimating fluxes while taking into account variable external conditions.

By their very nature, maximal flows do not 'care' what is happening in the upstream basin, since they are bounded by two supercritical regions and changes in those do not affect the flow. Maximal flows are purely determined by the geometry of the channel in the subcritical region and two controls along it, a primary and a secondary control. Submaximal flows on the other hand, again by definition, are determined by one control only and by the reservoir conditions; they therefore respond to changes in the upstream basin, such as a lowering in the interface height.

A note of caution is in order here: of course if the characteristics of the overflowing watermass itself change, for example if it becomes denser or lighter, then the overflow has to adjust. In such a case the transport through the channel will be altered even if the flow was maximal to begin with. Maximal flows are however insensitive to small changes in the topography in the supercritical regions, if all other properties stay the same.

A knowledge of how the flux varies considering the variability of such factors is of significant importance in understanding and modelling overflow variability. We will attempt to do so first from an analytical modelling point of view and subsequently from a numerical modelling point of view.

Chapter 3

Theory of two-layer rotating hydraulics

In this chapter we will present two-layer rotating theory and its expression in terms of two variables and hence use two functionals to find the relevant solutions. We will show the results in Armi-Farmer 'pseudo-Froude-number' like planes and argue that in the rotating case these plots are useful and enlightening in terms of tracing flows along channels of a very specific topography.

3.1 Semigeostrophic two-layer shallow water theory

Consider a channel of rectangular cross-section, aligned in the x-direction, rotating at a constant angular speed $f/2$, and containing two layers of a shallow, inviscid, homogeneous fluid; y denotes the across channel direction and z the vertical direction. The bottom layer is denser than the top layer and the depth of the channel is $D(x)$, which only varies in the along channel direction. At its shallowest point the depth is D_0 and for a flat bottom channel the depth is D_0 everywhere. Its width is denoted by $W(x)$, and at the narrowest section it is given as W_0. In figure 3.1 the details of the co-ordinate system and the variables used to describe the flow are shown. The interface separating the two layers may ground at some point across the channel or outcrop at the surface allowing either the bottom or top layer to vanish in some regions of the channel.

The following two-dimensional shallow-water equations govern the hydrostatic flow along the channel:

$$\frac{\partial u_1}{\partial t} + u_1\frac{\partial u_1}{\partial x} + v_1\frac{\partial u_1}{\partial y} - fv_1 = -\frac{1}{\rho_0}\frac{\partial P}{\partial x} - g'\left(\frac{\partial h_1}{\partial x} + \frac{\partial D}{\partial x}\right) \tag{3.1}$$

$$\frac{\partial v_1}{\partial t} + u_1\frac{\partial v_1}{\partial x} + v_1\frac{\partial v_1}{\partial y} + fu_1 = -\frac{1}{\rho_0}\frac{\partial P}{\partial y} - g'\frac{\partial h_1}{\partial y} \tag{3.2}$$

$$\frac{\partial h_1}{\partial t} + \frac{\partial (u_1 h_1)}{\partial x} + \frac{\partial (v_1 h_1)}{\partial y} = 0 \tag{3.3}$$

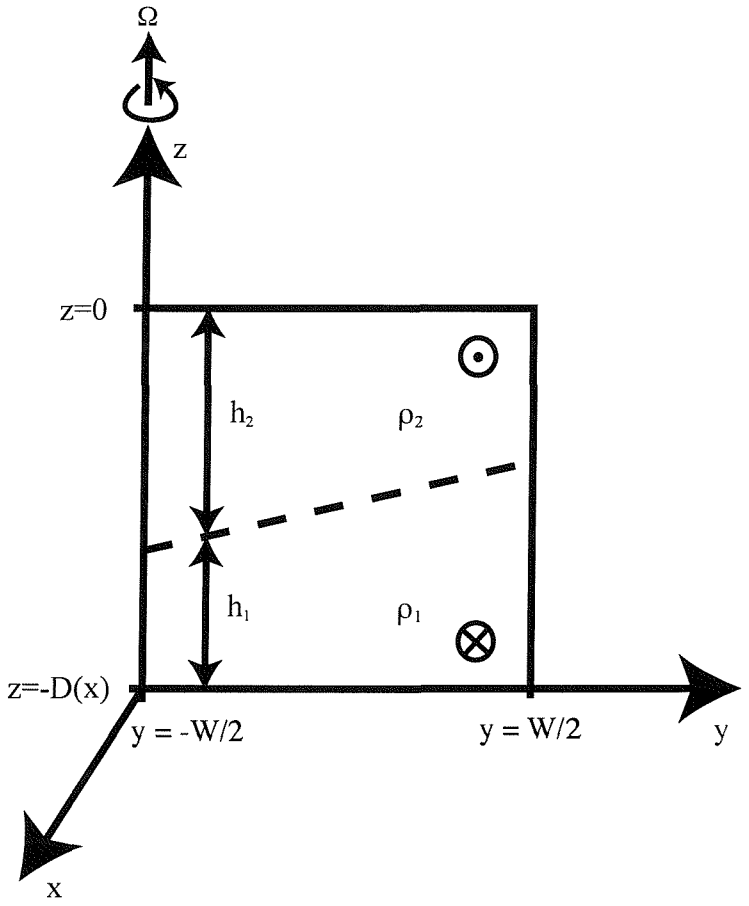

Figure 3.1: Sketch of the cross-section through a rectangular channel with two layers. h_1 and h_2 are the thickness of the bottom and top layer respectively. Their densities are ρ_1 and ρ_2 with $\rho_1 > \rho_2$. The total depth of the channel is $D(x)$ and its width $W(x)$, both width and depth are dependent only on x. The dashed line indicates the interface separating the two layers, which in the case of zero potential vorticity is linear. The net flow in the bottom layer is in the negative x direction and that in the top layer in the positive x direction. The dense reservoir lies at the positive end of the x-axis while the lighter reservoir lies at the negative end.

$$\frac{\partial u_2}{\partial t} + u_2\frac{\partial u_2}{\partial x} + v_2\frac{\partial u_2}{\partial y} - fv_2 = -\frac{1}{\rho_0}\frac{\partial P}{\partial x} \tag{3.4}$$

$$\frac{\partial v_2}{\partial t} + u_2\frac{\partial v_1}{\partial x} + v_2\frac{\partial v_2}{\partial y} + fu_2 = -\frac{1}{\rho_0}\frac{\partial P}{\partial y} \tag{3.5}$$

$$\frac{\partial h_2}{\partial t} + \frac{\partial (u_2 h_2)}{\partial x} + \frac{\partial (v_2 h_2)}{\partial y} = 0 \tag{3.6}$$

and

$$h_1 + h_2 = D \tag{3.7}$$

Equations (3.1), (3.2), (3.4) and (3.5) are the momentum equations for the two layers, and (3.3) and (3.6) are the continuity equations. The pressure at a reference level in the top layer, taken to be $z = 0$, is denoted by P and u_i and v_i are the flow velocities in the x and y direction respectively, where $i = 1$ denotes the bottom layer and $i = 2$ the top layer. The reference density is denoted by ρ_0 and g' is the reduced gravity.

This study is only concerned with steady flows and therefore all the time derivatives in the above equations can be set to zero. For each layer it can be proven that the potential vorticity

$$q_i = \frac{f + \frac{\partial v_i}{\partial x} - \frac{\partial u_i}{\partial y}}{h_i} \tag{3.8}$$

is conserved along stream lines. We will assume the potential vorticity to be zero throughout the first two chapters, which present the theoretical part of the thesis. Limitations of this assumption will become clear as we develop the theory, but note that Dalziel (1988) did an extensive study of the two layer rotating problem for zero and constant potential vorticity, and results were shown to differ only slightly. We therefore give up the small improvement of the constant potential vorticity theory in favour of the mathematically more tangible problem of zero potential vorticity and investigate it in more depth than Dalziel (1988).

If the potential vorticity is set to zero equation (3.8) reduces to:

$$\frac{\partial v_i}{\partial x} - \frac{\partial u_i}{\partial y} + f = 0. \tag{3.9}$$

It is known that flows of uniform potential vorticity have a boundary layer structure, where the width of the boundary layer is given by $a = \frac{\sqrt{g'D_0}}{f}$, the Rossby radius of deformation, based on D_0, the depth of the water column at the shallowest part of the channel. This boundary structure is less obvious in the zero potential vorticity theory, as the velocities vary linearly across the channel, however as the flow moves downstream, over a sill or past a constriction, it flows fastest along the left-hand[1] wall of the channel

[1] *'Left-hand side'* will from now on refer to the left side of the channel when looking in the direction of the mean flow in the top layer, i.e. in towards the upstream basin. Usually the bottom layer is taken as the reference, but in order to avoid confusion with the way we have plotted the results we reverse this convention. Therefore on all diagrams showing a planar view of the channel the left-hand side is also the left-hand side of the diagram.

and turns into a confined boundary current.

We will thus use the Rossby radius as a scaling of the flow in the across channel direction y, and so the momentum and continuity equations are non-dimensionalised using the following scales:

$$\begin{aligned} (D, h_i, z) &= (D, h_i, z)^* D_0 \\ x &= x^* R \\ (W, y) &= (W, y)^* a \\ u_i &= u_i^* \sqrt{g' D_0} \\ v_i &= v_i^* \sqrt{g' D_0} \left(\frac{a}{R}\right) \end{aligned} \tag{3.10}$$

where R is a scaling of the typical along channel distance and the asterisk (*) marks the non-dimensional variables. From now all equations will be expressed non-dimensionally unless stated otherwise and we will drop the (*). The non-dimensional width W^* will be denoted by L, i.e. $W/a = W^* = L$.

If used in the continuity expressions for the two layers the first four scales suggest a scaling of v by $\sqrt{g'D_0}(a/R)$. Assuming the traditional sill approximation, that the along-channel length-scale is significantly larger than the across channel length-scale, the horizontal aspect ratio $\epsilon = a/R \ll 1$, and hence the flow is nearly parallel ($v \ll u$). In general variations of flow and topography are more gradual in the downstream direction ($\frac{\partial}{\partial x} \ll \frac{\partial}{\partial y}$). Under these conditions the non-dimensionalised equations (3.1 - 3.7) can be reduced and it can be shown that u_i in both layers is in geostrophic balance:

$$u_1 = -\frac{\partial P}{\partial y} - \frac{\partial h_1}{\partial y} \tag{3.11}$$

$$u_2 = -\frac{\partial P}{\partial y}. \tag{3.12}$$

It follows that

$$u_2 - u_1 = \frac{\partial h_1}{\partial y}. \tag{3.13}$$

The same approximation is used to simplify the vorticity equation (3.8) and after non-dimensionalising it for both layers we find:

$$\frac{\partial u_1}{\partial y} = 1 \tag{3.14}$$

and

$$\frac{\partial u_2}{\partial y} = 1, \tag{3.15}$$

while (3.7) remains unchanged: $h_1 + h_2 = D$. Therefore the velocity fields in the bottom and top layer are linear:

$$u_1 = u_{10} + y \tag{3.16}$$

and

$$u_2 = u_{20} + y \tag{3.17}$$

and hence, from (3.13), h_1 is also linear across the channel:

$$h_1 = (u_{20} - u_{10})y + h_{10}. \tag{3.18}$$

Here u_{10}, u_{20} and h_{10} are constants of integration and represent the velocities and layer thickness at the centre of the channel, $y = 0$. Equation (3.18) suggests an obvious definition of the slope of the interface as $h_s = u_{20} - u_{10}$, this definition will become central later on in chapter 4.

The theory described thus far has formed the basis of many previous studies including Whitehead et al. (1974) and Dalziel (1988, 1990), who equally noted the linearity of the velocity fields and interface height. It applies only for the zero potential vorticity two-layer case. For a single layer flowing underneath a deep and stagnant upper layer, a case also treated by Whitehead et al. (1974) the velocity profile is also linear, but the interface height is quadratic. For cases of constant potential vorticity, both the velocity and the interface height profiles are non-linear for single layer and two layer flows.

With the expressions for the layer thickness and velocities, the fluxes through the channel can now be calculated by integrating across the channel and the resulting expression will depend on the three constants of integration u_{10}, u_{20} and h_{10}, as well as D and L describing the channel geometry. To reduce the dependence to two constants it is assumed that zero net flux passes though the channel, i.e.

$$Q_1 + Q_2 = \int_{L(x)/2}^{-L(x)/2} u_1 h_1 dy + \int_{L(x)/2}^{-L(x)/2} u_2 h_2 dy = 0. \tag{3.19}$$

From this equation an expression for h_{10} can be found in terms of u_{10} and u_{20}, which will be different depending on whether the flow is separated, with the interface intersecting the bottom or the surface or both, or is fully attached, with the two layers present across the whole channel. The details of the computations for the different cases are discussed more in section 3.1.2 and also in appendix A.

The theory presented here would open a whole new spectrum of results if the net flux were assumed to be constant rather than zero, thus introducing another constant which can be chosen as desired in equation 3.19; this analysis however is beyond the scope of the thesis. Results for such a non zero net flow have been described by Armi and Farmer (1986) and Farmer and Armi (1986) for the non-rotating case, and by Dalziel (1988) for the rotating case.

The flux, because it is a conserved quantity, will be taken as the first functional in terms of the two variables u_{10} and u_{20}. Generally we will use expressions for the flux in the bottom layer Q_1 given by the first integral in equation (3.19). Alternatively expressions for the flux in the top layer Q_2 could be used without loss of generality. The second functional needed comes from the assumption that the Bernoulli potential is conserved along the entire flow.

3.1.1 Bernoulli's potential

So far the along channel momentum equations (3.1) and (3.4) have not been used to describe the flow. Integrating these with respect to x we find

$$\frac{1}{2}u_1^2 + (P + h_1 - D) = E_1 \tag{3.20}$$

and

$$\frac{1}{2}u_2^2 + P = E_2. \tag{3.21}$$

On subtracting them we get

$$E_1 - E_2 = \frac{1}{2}(u_1^2 - u_2^2) + h_1 - D \tag{3.22}$$

where E_1 and E_2 are the Bernoulli constants for the bottom and top layer respectively. They are independent of both x and y, and hence constants that are conserved over the entire flow, unless a hydraulic jump occurs.

Substituting the linear expressions for u_1, u_2, and h_1 into (3.22) results in the following expression

$$\Delta E = E_1 - E_2 = \frac{1}{2}(u_{10}^2 - u_{20}^2) + h_{10} - D. \tag{3.23}$$

Note that $(u_{10}^2 - u_{20}^2)$ can be rewritten as $(u_{10} - u_{20})(u_{10} + u_{20}) = -h_s(u_{10} + u_{20})$ which will become important later when the two functionals will be reduced to one.

Ideally we would like to take ΔE as a measure of the flow conditions in the upstream basin, in particular the interface height far away from the controlled flow at the sill. It would allow us to directly work with the dependence of the flow on upstream basin conditions. This is common practice and works very well in non-rotating flows, however, the simplifying assumption of zero potential vorticity, and the resulting linear velocity fields make this comparison difficult. Before we move on to develop the theory further and describe specific solutions, we will take a moment to discuss the disadvantages of using zero potential vorticity.

Drawbacks of zero potential vorticity

In non-rotating flows where the problem is essentially one-dimensional and the velocity field is constant across the channel, a sluggish deep upstream flow is easily approached as the bottom layer in the upstream basin increases in thickness. Therefore the value of the Bernoulli potential is generally used as a descriptor of the stratification in the basins.

The simplification of zero potential vorticity in the rotating case is based upon the assumption that the basin upstream is infinitely deep. However, because the velocity fields in both layers are linear across the channel the wider the channel becomes the larger the velocities will become, and so the solutions do not tend towards the limit of stagnant reservoirs.

In a rotating channel of constant width and increasing depth the conditions of the basin are approached in a roundabout way by the flow in the channel. In the description of the solution over a sill in chapter 4, it will be seen that upstream the interface slope goes to zero in a constant width channel, and so $h_{10} \rightarrow \Delta E + D$ and thus $h_{20} \rightarrow -\Delta E$, figure 4.13 will illustrate this nicely. This supports the assumption that ΔE can be seen as a measure of the interface height in the upstream basin although the flow may not be sluggish. In a channel of increasing width though, the velocities will inevitably start to increase and the interface to tilt more strongly, compromising our assumption that ΔE can be used to describe of the stratification in the basins.

It should also be noted that by increasing the depth of the channel such that it approaches the depth of the basin the assumption of zero potential vorticity is compromised and in this case single layer reduced gravity theory might be more applicable.

These are some of the main concerns when using zero potential vorticity theory. So there seems to be an inherent problem in trying to link the solution in the channel to the state of flow in the upstream basin in the case of zero potential vorticity and two active layers. There will have to be a transition from a two layer flow in the channel to a single layer flow above and below an infinitely deep stagnant layer in the upstream and downstream basins respectively. Pratt (2003b) and Timmermans (2004, personal communication) have attempted to connect controlled two layer solutions at the sill to conditions in the upstream basin, where the lower layer is deep and stagnant and only the top layer is dynamically important. They determined solutions at the sill, and to find a link to the basin flow they tested whether a supercritical solution exists upstream that has the same properties in terms of the Bernoulli constant and flux, which need to be preserved. However no continuous link is established between the solutions at the sill and the basin (if they exist) and it is assumed also that the basins are infinitely deep.

For the purpose of this study we assume $\Delta E = -h_{20}$ in the upstream basin far from the channel, even though it is not possible to directly link the channel and the basin using the presented theory.

3.1.2 Attached and separated cases

In order to do a comprehensive study of all possible flow regimes within a rectangular channel, seven different scenarios for the position of the interface are considered, these are shown in figure 3.2. As a result the intervals over which the zero net flux expression (3.19) is integrated changes for each case and therefore leads to different expressions for h_{10} in terms of u_{10} and u_{20} (or h_s in the single variable case) for each regime. Details of the different regimes and the respective expressions for h_{10} are given in appendix A.

For the fully attached case the interface and velocity profiles are well defined for both layers across the entire channel. This is not the case for semi-attached or fully separated flows and for these the profiles need to be redefined.

In regime 7, a sketch of which is shown in figure 3.3, the flow is separated from both

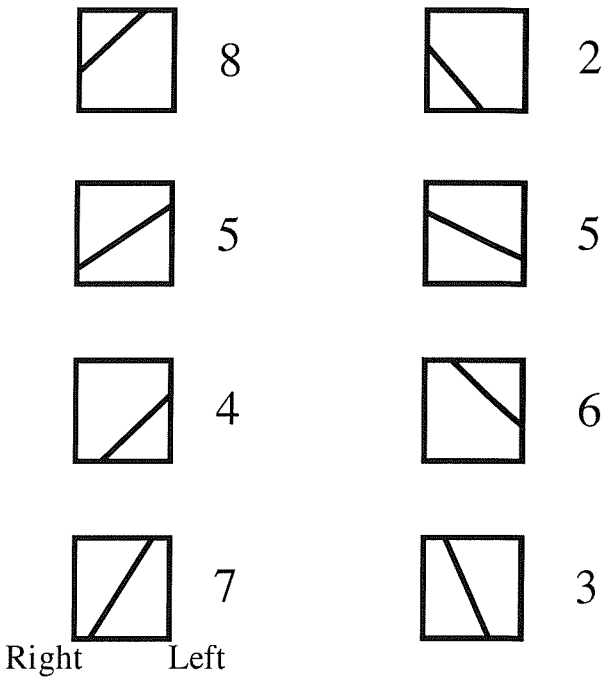

Figure 3.2: Sketches of the flow regimes considered in the analysis. Regime 5 is *fully attached*, regimes, 2, 4, 6 and 8 are *semi-separated* and regimes 3 and 7 are *fully separated*. In the presentation of the results only regimes with a positive slope (4, 5, 7 and 8) are considered. 'Left-hand' wall refers to the left-hand side of the channel when looking from the lighter towards the denser reservoir in the direction of the net flow of the top layer.

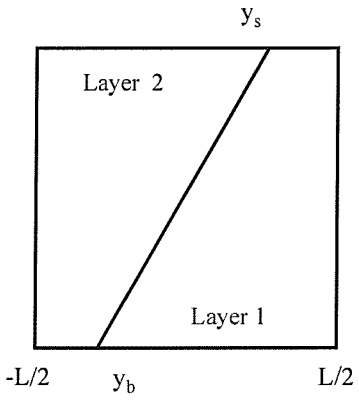

Figure 3.3: Schematic of regime 7. The interface grounds at y_b and outcrops at y_s.

the right-hand and left-hand side of the channel and so the interface height is defined as follows:

$$h_1 = \begin{cases} 0 & \text{for } -L/2 \leq y \leq y_b \\ (u_{20} - u_{10})y + h_{10} & \text{for } y_b \leq y \leq y_s \\ D & \text{for } y_s \leq y \leq L/2 \end{cases}$$

where y_b denotes the point across the channel where the interface intersects with the bottom, similarly y_s denotes the point at which the interface outcrops at the surface.

The vorticity equation applies in the regions where both layers are present as well as where only one of the layers is present and as a result the linearity of the velocity profiles is maintained. By assuming that at y_b and y_s the velocity profiles in both layers are continuous the transition between the regions is smooth. Therefore the velocities in the bottom and top layer are given as follows

$$u_1 = \begin{cases} \text{undefined} & \text{for } -L/2 \leq y \leq y_b \\ y + u_{10} & \text{for } y_b \leq y \leq L/2 \end{cases}$$

and

$$u_2 = \begin{cases} y + u_{20} & \text{for } -L/2 \leq y \leq y_s \\ \text{undefined} & \text{for } y_s \leq y \leq L/2. \end{cases}$$

Similarly the interface and velocity profiles are set up for all the other regimes.

As mentioned before, for each regime an expression for h_{10} can be derived assuming the zero net flux condition. We will derive h_{10} for regime 7 as an example; the results for all the other regimes are given in appendix A.

For regime 7 the integrals for the fluxes read:

$$Q_1 = \int_{y_b}^{y_s} u_1 h_1 dy + D \int_{y_s}^{L(x)/2} u_1 dy \tag{3.24}$$

and

$$Q_2 = D \int_{-L(x)/2}^{y_b} u_2 dy + \int_{y_b}^{y_s} u_2 h_2 dy \tag{3.25}$$

Applying the zero net flux condition $Q_1 + Q_2 = 0$ we can derive and expression for h_{10}:

$$h_{10} = \frac{Du_{10}(y_s - L/2) - Du_{20}(y_s + L/2) - 1/2(u_{20} - u_{10})^2(y_b^2 - y_s^2)}{(u_{20} - u_{10})(y_b - y_s)} \tag{3.26}$$

From equation (3.18), we find expressions involving y_s and y_b:

$$h_1(y_b) = (u_{20} - u_{10})y_b + h_{10} = 0 \tag{3.27}$$

$$h_1(y_s) = (u_{20} - u_{10})y_s + h_{10} = D \tag{3.28}$$

and solving for y_s and y_b:

$$y_b = \frac{-D - u_{10}L - u_{20}L}{2(u_{20} - u_{10})} = -\frac{h_{10}}{u_{20} - u_{10}} \tag{3.29}$$

$$y_s = \frac{D - u_{10}L - u_{20}L}{2(u_{20} - u_{10})} = \frac{D - h_{10}}{u_{20} - u_{10}} = \frac{D}{u_{20} - u_{10}} + y_b. \tag{3.30}$$

Replacing y_s in equation (3.26), h_{10} simply reduces to:

$$h_{10} = \frac{1}{2}(D + u_{10}L + u_{20}L) \tag{3.31}$$

The analytical formula for the flux in the bottom layer for regime 7 was found to be the following:

$$Q_1 = \frac{(D - h_{10})^3 + h_{10}^3}{3(u_{20} - u_{10})^2} + \frac{u_{10}(u_{20} - u_{10}) + h_{10}}{2(u_{20} - u_{10})}[(D - h_{10})^2 - h_{10}^2] + \frac{h_{10}u_{10}D}{u_{20} - u_{10}} + \frac{1}{2}\left[\frac{L^2}{4} - \left(\frac{D - h_{10}}{u_{20} - u_{10}}\right)^2\right] + u_{10}\left[\frac{L}{2} - \frac{D - h_{10}}{u_{20} - u_{10}}\right]. \tag{3.32}$$

Equation (3.31) can be substituted for h_{10} in this equation to find the flux purely in terms of u_{10} and u_{20} and the geometry variables, L and D.

We can do similar (but clearly not identical) computations for all the other regimes. However, when we actually compute the fluxes in the numerical code we have done so only numerically without deriving each individual flux expression. The reason for this is the complexity of the resulting equations, which easily leads to algebraic errors.

3.1.3 Summary

We have, in the last two sections, defined the two functionals we will be working with:

$$\frac{1}{2}(u_{10}^2 - u_{20}^2) + h_{10} - D = \Delta E \tag{3.33}$$

and

$$\int_{L(x)/2}^{-L(x)/2} u_1 h_1 dy = Q_1. \tag{3.34}$$

depending on u_{10} and u_{20}, as well as h_{10} which can be found as a function of the former two by assuming zero net flux. The expression for h_{10} will differ for each regime considered.

We now have all the tools to determine the controlled solutions of the flow and describe its features along a channel of any geometry. Several examples using an Armi-Farmer type 'pseudo-Froude-number' diagram will be presented for the analysis in two variables, in section 3.2. We label it 'pseudo' because in rotating hydraulics the velocity variations across the channel add an extra dimension to the problem and the definition of a Froude number is not as clear. Thus the Froude number plane presentation of solutions has only limited use in the rotating case. It does however give us a valuable initial insight into the behaviour of rotating flows and for a small subset of channel topographies we are actually able to trace the flow using a diagram, just like in the non-rotating case.

Before we get on to describe the solutions however there is a very important aspect of the flow which needs to be discussed before proceeding any further and that is the issue of reversed flow (or backflow) within a layer; by that we mean regions of the flow-field where the velocity is reversed with respect to the mean flow of the given layer.

3.1.4 Backflow

The presence of backflow is an inherent source of ambiguity in the rotating zero potential vorticity theory. Due to the linearity of the velocity profile, regions of backflow may occur anywhere along the channel, in either layer. If the flow is semi-separated (regime 4) at the control then the top-layer will contain a considerable region of backflow along the entire length of the channel. The bottom layer never exhibits backflow at the control in this case but may do further upstream.

The problem with such regions is that the origin of the water is ambiguous. In the case of the top layer it may either have come from the downstream basin and then turned around at some point to flow back in the downstream direction, it may be trapped in a region of re-circulation, or it may have come from the upstream basin. In the final case it is not clear what the mechanism is by which information is propagated in the downstream direction, if the flow in part of the region is directed downstream.

In previous two-layer studies the problem of backflow has been dealt with in two ways. Dalziel (1988) removed it by assuming that in the region where the velocities change sign and flow is directed in the opposite direction to the mean flow within a given layer the fluid is stagnant. This method relies on the fact that backflow occurs only in parts of the channel where just one layer is present. Whitehead et al. (1974) on the other hand assumed that all regions containing only one layer are stagnant and the main flow is concentrated in a small region of the channel cross-section containing two layers. This assumption led to his formulation of the maximum flow being given by $Q = \frac{1}{6}\frac{g'D_0^2}{f}$. The problem with this assumption is that it necessarily leads to pronounced and most likely unrealistic shear layers where the flow meets the stagnant regions.

Similarly for single layer constant potential vorticity flow under an infinitely deep and stagnant upper layer Killworth (1994) eliminated backflow by adjusting the interface above the backflow region to be horizontal and assuming the flow in this region to be stagnant. This is not possible in the two layer case since both layers are dynamically involved in the flow and changing the interface will affect both flows.

In field observations back-flows are rarely seen in the deep overflows, which is consistent with the theory. Backflow in the surface layers may well occur in the ocean but these are probably not due to the hydraulic process but due to other forcing mechanisms, such as wind stresses.

Laboratory experiments by Dalziel (1988) for two layers and Whitehead and Salzig (2001) and Borenäs and Whitehead (1998) for one and a half layers have shown that there are regions upstream of the sill where the bottom layer seems stagnant rather then

re-circulating, but these regions do not come in contact with the sill, and this again agrees with theoretical findings. Dalziel (1988) does not describe the circulation in the top layer, like all other laboratory studies we reviewed the main focus is on the circulation in the bottom layer.

Because it is still unclear how to treat the problem of backflow we have opted to include backflow in the presented theory to give us an idea of where it occurs and how it influences the controls. The theory can easily be adapted in the future to exclude velocities which are directed against the mean flow in each layer and a comparison will no doubt be valuable.

So with the formulation detailed in the previous section and including reverse flow we will now present some novel solutions and results of this theory. Although the approach used by Dalziel (1988) is in many ways quite similar to our approach there are some crucial differences. We will develop a new way to look at two-layer rotating flows which we hope will highlight some aspects of the theory which have been obscured in previous studies. Such as the importance of the second virtual control and how it arises in some cases as a natural extension to otherwise non-traceable submaximal flows.

3.2 Solutions in terms of two variables

The two variables in terms of which the flow is being described are u_{10} and u_{20}, and as outlined in section 3.1.3 both the flux in the bottom and top layer and the Bernoulli potential can be expressed in terms of these for a specified cross-section. So we essentially have two unknowns and two functionals to solve for the flow.

In figures 3.4, 3.6 and 3.9 the results for Q_1 (thin dashed lines) and ΔE (thin solid lines) are contoured in the ($\bar{u}$,Δu) plane for widths, $L = 1$, 0.5 and 1.5 respectively, while the depth is unity in all plots, i.e. $D = 1$. Here $\bar{u} = \frac{1}{2}(u_{10} + u_{20})$ and $\Delta u = \frac{1}{2}(u_{10} - u_{20})$. The asterisks indicate points where a pair of contours ΔE and Q_1 are tangential and the values of $\bar{u}$ and Δu at this point therefore describe a controlled flow. Notice that in all four plots the dashed lines are not labelled for clarity of the figures, however the controlled fluxes corresponding to each of the ΔE-contours plotted are given in figures 3.5, 3.7 and 3.11.

The thick solid lines indicate transitions from fully attached to semi-separated to fully separated flows, and the small inset in figure 3.4 shows precisely which regimes apply in the different regions of the plot.

Formally the location of the controlled flows can be found by applying the condition outlined in chapter 2 for two variables, equation (2.9) in this case becomes

$$\nabla Q_1 \times \nabla \Delta E = \frac{\partial Q_1}{\partial u_{10}} \frac{\partial \Delta E}{\partial u_{20}} - \frac{\partial Q_1}{\partial u_{20}} \frac{\partial \Delta E}{\partial u_{10}} = 0, \tag{3.35}$$

by replacing G_1 by Q_1, G_2 by ΔE, h_1 by u_{10} and h_2 by u_{20}.

In figure 3.4 all the controlled flows lie in regimes 4 and 8. The plot closely resembles

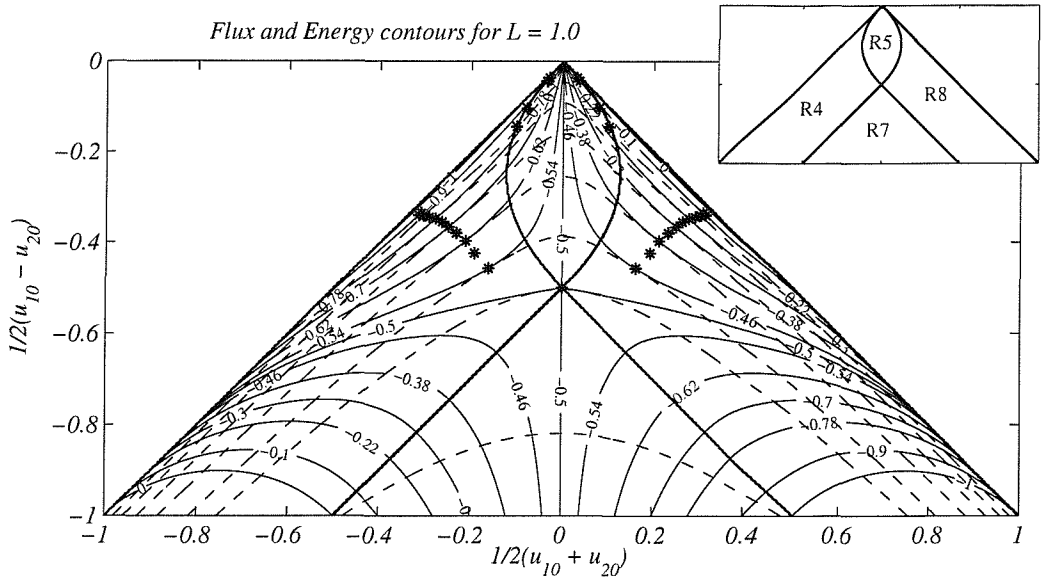

Figure 3.4: Solutions for the flux per unit width (dashed lines) and the Bernoulli function (thin solid lines) for a range of u_{10} and u_{20} in a channel of width $L = 1.0$, with a maximal flux $Q_1 = -0.168$. Note that $1/2(u_{10} - u_{20}) = \Delta u$ and $1/2(u_{10} + u_{20}) = \bar{u}$. The thick solid lines indicate points of separation and the plot inset at the top of the figure shows which regime occurs in the respective regions, where R stands for 'regime'. At some points the flux and energy lines are tangential and the pairs of ΔE and Q_1 at those points make up the controlled flows; they are indicated by small asterisks. Figure 3.5 shows the range of selected pairs of controlled solutions, plotting ΔE and the corresponding Q_1.

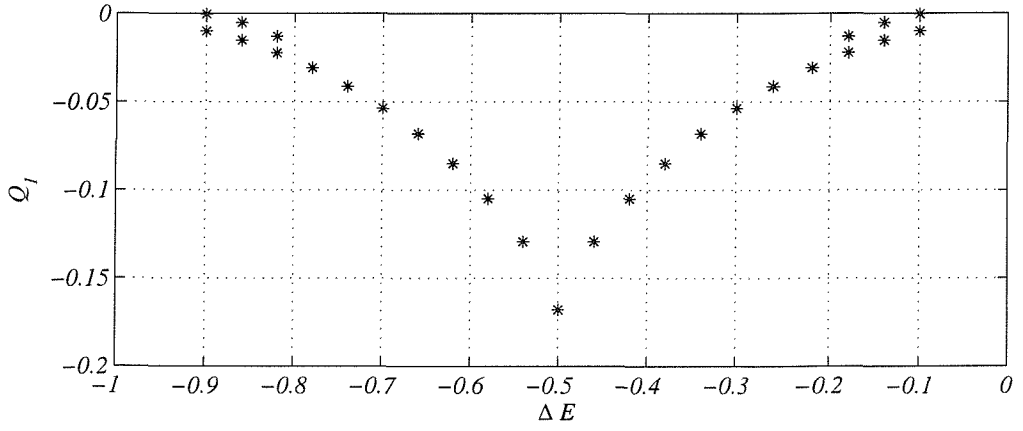

Figure 3.5: Plot of the controlled fluxes Q_1, for a range of ΔE for a channel of width $L = 1.0$, corresponding to the asterisks marked in figure 3.4. Note that there are three controlled fluxes for $|\Delta E| < 0.2$ and > 0.8, and the maximum flux occurs at $\Delta E = -0.5$ where $Q_1 = -0.168$.

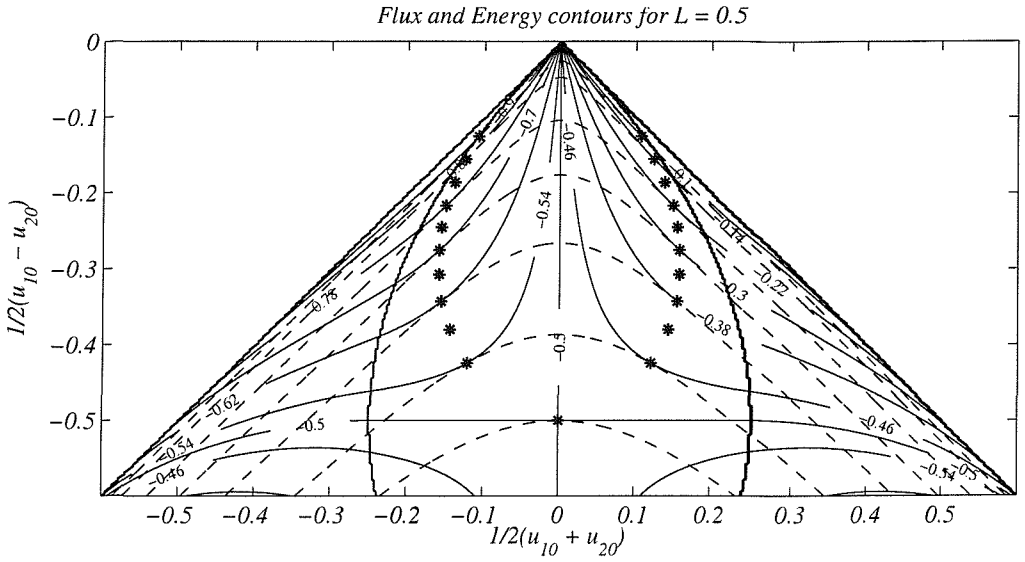

Figure 3.6: Same as figure 3.4, but for a section with $L = 0.5$. The maximum possible controlled flow is here roughly $Q_1 = -0.115$. Most controlled flows lie within the fully attached region.

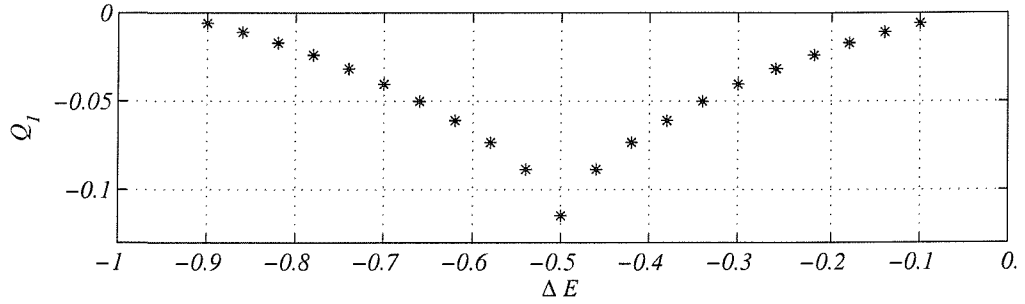

Figure 3.7: Plot of the controlled fluxes Q_1, for a range of ΔE for a channel of width $L = 0.5$, corresponding to the asterisks marked in figure 3.6. The maximum flux occurs at $\Delta E = -0.5$ where $Q_1 = -0.115$.

a rotated version of the Froude number plane, reproduced in figure 3.8, used by Armi (1986) to present their results. Though instead of using the squared Froude numbers, F_1^2 and F_2^2, to plot the results, we simply use the velocities of the solutions at the centre of the channel, $y = 0$.

However, because we non-dimensionsalise the velocities using $\sqrt{g'D_0}$, u_{10} and u_{20} essentially correspond to the Froude numbers in the two layers at the centre of the channel, $F_{10} = \frac{u_{10}}{\sqrt{g'D_0}}$ and $F_{20} = \frac{u_{20}}{\sqrt{g'D_0}}$ (in these particular expressions u_{10} and u_{20} are dimensional). The solid line in figure 3.4 extending from (-1, -1) to (0, 0) is the axis u_{10} (i.e. $u_{20} = 0$) and the line from (0, 0) to (1, -1) the axis u_{20} (i.e. $u_{10} = 0$).

The contours of the Bernoulli function are the same in figures 3.8 and 3.4 since equation (3.22) is identical in the non-rotating case and the zero potential vorticity rotating case. A small difference between the description by Armi (1986) and our results is that we use a more general non-dimensionalisation, expressing the wave speeds in terms of D_0 rather

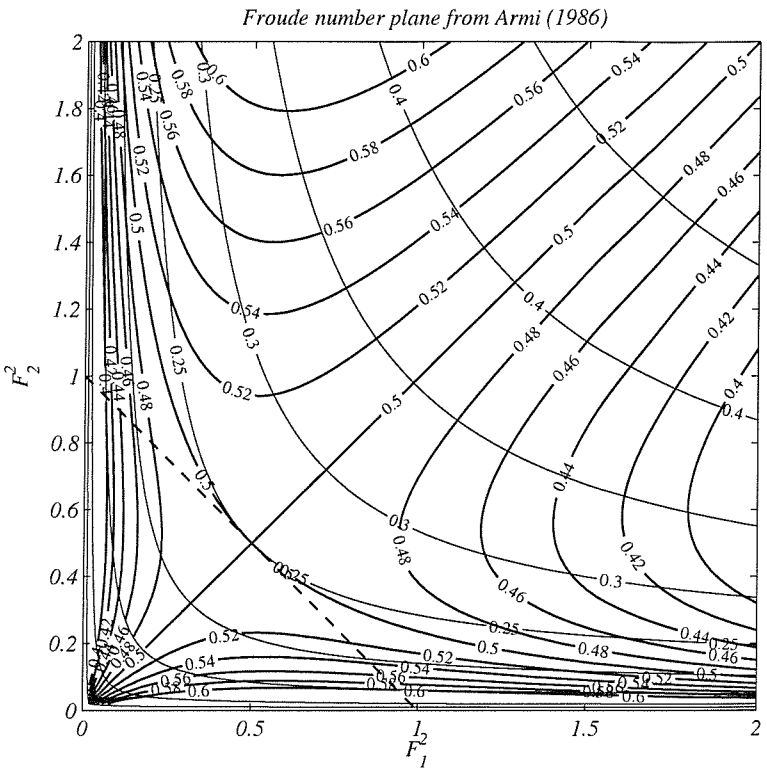

Figure 3.8: A Froude number plane diagram from Armi (1986) showing the results for a rectangular non-rotating channel with a flat bottom. The thick solid lines are the contours of the Bernoulli potential along which the flow can be traced, while the thin solid lines are the flux contours. The points at which a pair of $(Q, \Delta E)$ contours is tangential fall on the line where the composite Froude number $F_1^2 + F_2^2$ equals 1 indicated by the thick dashed line.

than the individual layer thickness.

The flux contours are different however; they follow the same shape but the values in the rotating case are much lower. This is the point at which the non-rotating theory developed by Armi (1986) and the theory including rotation, presented here, exhibit inherent differences.

What is interesting to point out in these pseudo-Froude-number diagrams is that the controlled fluxes are equal for values of ΔE and the corresponding value $-(1 + \Delta E)$, a point also true in the non-rotating case as described by Armi and Farmer (1986). A result that is very different from the non-rotating case is that for a small range of ΔE there are two associated controlled fluxes, as can be seen in figures 3.4 and 3.9. The second controls, with the smaller fluxes, lie in the fully attached region, where another set of asterisks can be made out.

Zooming in on the small region at the tip of plot 3.9, which is shown in figure 3.10, it can be seen that the flux contours become steeper in slope around $\frac{1}{2}(u_{10} + u_{20}) = 0$ to form a 'nose' in shape, and thus another Bernoulli contour will be tangential to some of the flux contours. One example in figure 3.10 is the $\Delta E = -0.7$ line which is tangential to $Q_1 = -0.0065$ as well as $Q_1 = -0.0888$. We will encounter these second controls again

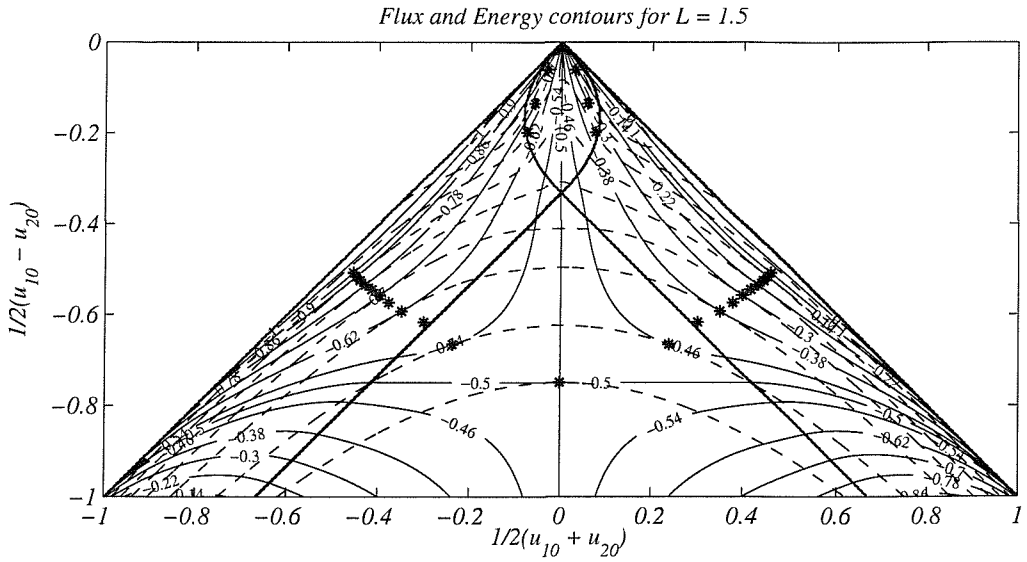

Figure 3.9: Same as figure 3.4, but for a section with $L = 1.5$. The maximum possible controlled flux is here roughly $Q_1 = -0.3$. Most of the controlled flows here lie in the fully or semi-separated region.

in the next chapter and discuss their importance in more detail.

Notice also, that as in the non-rotating case, controlled flows are not possible below the line $\Delta E = -0.5$ as the contours of energy and flux cross but are never tangential. As the channel gets wider the horizontal part of the $\Delta E = -0.5$ contour moves down and thus the largest possible controlled flux for a given width increases.

The maximum controlled flux for a channel of width $L = 1$ is $Q_1 = -0.168$ with $\Delta E = -0.5$ while it is about $Q_1 = -0.3$ for $L = 1.5$, but only $Q_1 = -0.115$ for $L = 0.5$. For both $L = 1.5$ and $L = 1$, the controlled flows are mainly semi-separated or fully separated, as opposed to fully attached for the channel of width 0.5.

Another significant difference between the rotating and the non-rotating theory is that Armi and Farmer could use the Froude number planes to trace their flows along the channel from the upstream basin towards the downstream basin. This is generally not possible for the rotating theory. However we found a very special case for which it is possible which we shall now outline, after reviewing how Armi and Farmer trace the solutions along a constant depth channel.

3.2.1 Special traceable case

In the Froude number planes by Armi and Farmer, figure 3.8, all fluxes are plotted as non-dimensional volume flow per unit width, since the volume transport is just a multiple of the width: $Q_1 = h_1 u_1 L$. This is not the case in the rotating theory; on the contrary it is quadratic in L, as can be seen in equation 3.32. This means that diagrams such as 3.4 cannot generally be used to trace flows along the channel, in contrast to the non-rotating case where this is easily done.

In the non-rotating case we can pick a line of constant ΔE in figure 3.8, also referred

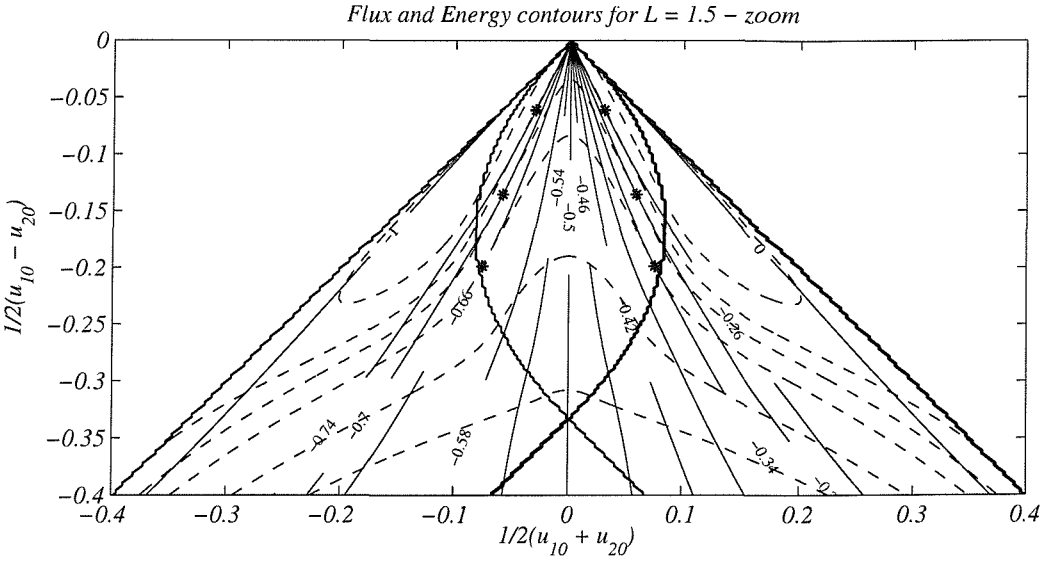

Figure 3.10: Enlargement of the region at the tip of figure 3.9. The flux lines form a 'nose' around $u_{10} + u_{20} = 0$. The energy contours (solution lines) meet another flux line indicating the possibility of a second control.

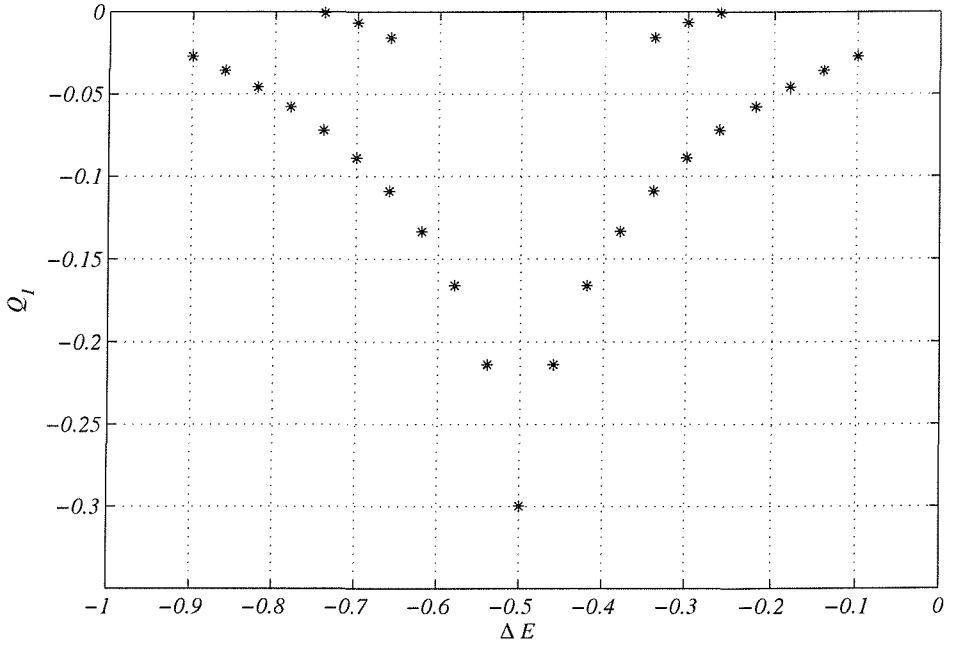

Figure 3.11: Plot of the controlled fluxes Q_1, for a range of ΔE for a channel of width $L = 1.5$, corresponding to the asterisks marked in figure 3.9. The maximum flux occurs at $\Delta E = -0.5$ where $Q_1 = -0.3$.

to as the solutions line, and follow it to give us the solutions of the flow along a flat bottom channel. Starting at large F_1^2 or F_2^2 we trace the solutions line and find that it crosses flux lines of increasing value, so the channel becomes narrower at a rate such that the width multiplied by the value of the flux per unit width remains constant. The location of the solution line in the Froude number space give us the speeds of the flow in the top and bottom layer. At the point where it is tangential to a flux line, the channel is narrowest and the flow is controlled. In the non-rotating case these points all fall onto one line where $G = F_1^2 + F_2^2 = 1$. The channel then widens again as the flux lines decrease in value along the solution line we are tracing.

In the rotating case this neat way of tracing the flow is not applicable for the reasons mentioned earlier. However, there is one exception for a very specific topography. Since each plot has a fixed L (width of the channel in terms of Rossby radii) if this ratio of width to Rossby radius remains constant along the channel, i.e. the width and depth both change such that $\frac{W}{D^{1/2}} = const.$, these plots can be used in the same way as those for the non-rotating case. Let us go through the steps of tracing such flows.

First of all, if we want to find the solution of the flow along the channel in a single diagram we need to consider that the flow is non-dimensionalised locally. By that we mean that at any point along the channel the flow is scaled by the local depth and hence the local Rossby radius. So to be precise it is not L (non-dimensionalised using D_0) that is constant in each plot but rather $L/\sqrt{D} =$ constant, where D is the depth at any section along the channel which may not necessarily be equal to 1. Take for example figure 3.12, at the sill $L_0 = \frac{f}{\sqrt{g'D_0}}W_0$ while an arbitrary distance away from the sill $L^{(1)} = \frac{f}{\sqrt{g'D^{(1)}}}W^{(1)}$ which is also equal to L_0 if the flow is to be traced in one plot, (here the superscripts and subscripts refer to positions along the channel, 0 for the control section and 1 for some other arbitrary point along the channel). Usually, however, we are interested in the variation of the topography and flow with a non-dimensionalisation using the scales of just one cross-section, usually the sill. Hence what we are really after is $L^{(1)} = \frac{f}{\sqrt{g'D_0}}W^{(1)}$. If we substitute $W^{(1)} = \frac{L_0\sqrt{g'D^{(1)}}}{f}$ into this expression we find:

$$L^{(1)} = L_0\sqrt{\frac{D^{(1)}}{D_0}}. \tag{3.36}$$

So if the width is non-dimensionalised using the depth of the channel at the sill, we find that $L^{(1)}$ goes like $L_0\sqrt{D^{(1)}}$ (remember $D_0 = 1$ always).

Analogous to Armi (1986) we want to trace the flow along the energy lines (solution lines), but again, if we use a single diagram the scaling of the energies will change along the channel. The Bernoulli potential scales like the square of the velocities, $\Delta E_0 \sim g'D_0$, and further along the channel $\Delta E^{(1)} \sim g'D^{(1)}$; in other words, as the channel deepens the Bernoulli potential scaled locally will change and thus we cannot simply use one of the ΔE contours to trace the flow. However, by taking the ratio of the two Bernoulli potentials, we find that $\Delta E^{(1)} = \frac{D^{(1)}}{D_0}\Delta E_0$. Using an analogous argument involving the scaling of the fluxes, we find that $Q_1^{(1)} = \frac{D^{(1)2}}{D_0^2}Q_0$. Finally, this leads us to conclude that

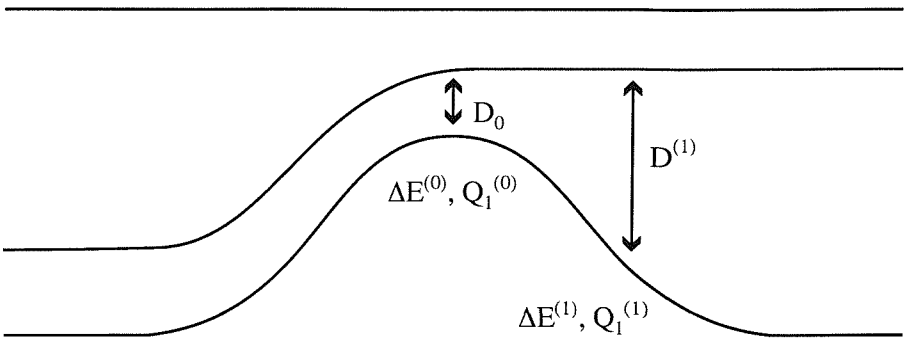

Figure 3.12: The flow in each of the pseudo-Froude-number diagrams is scaled using the local variables of the topography. If the flow is to be followed along the channel the results along these solution lines need to be 'tuned' to the scales at the top of the sill, the primary control section, indicated by 0.

$\frac{\Delta E}{\sqrt{\lvert Q_1\rvert}}$	Flux Q_1	ΔE
-3	-0.0550	-0.7036
-2	-0.0918	-0.6060
-1.4	-0.1400	-0.5238
-1.3035	-0.1545	-0.5124
-1.225	-0.1667	-0.5002
0	nd	0

Table 3.1: Table of the values of the controlled flows contoured in figure 3.13. Column one contains the value of the solutions lines, column two the corresponding controlled flux and column three the Bernoulli potential.

the ratio $\frac{\Delta E^{(1)}}{\sqrt{Q_1^{(1)}|}} = \frac{\Delta E_0}{\sqrt{|Q_0|}}$ = constant. So the flow through a channel of constant $L/\sqrt{D}$ can be traced along contour $\frac{\Delta E}{\sqrt{|Q_1|}}$ = constant.

In figure 3.13 the contours of flux, Q_1, and $\frac{\Delta E}{\sqrt{|Q_1|}}$ are plotted with thin dashed and solid lines respectively. As before, the thick solid lines present points of separation. In table 3.1 the values of the contoured solution lines are listed together with the corresponding value of the controlled flux and ΔE.

In a channel whose depth and width are changing as described earlier, the flow with $\Delta E = -0.5$ corresponds to the flow along contour, $\frac{\Delta E}{\sqrt{|Q_1|}} = -1.225$ which is not traceable anymore as can be seen in figure 3.13. This has equally been shown to be true in the non-rotating case, see Farmer and Armi (1986).

The first traceable flow in figure 3.13 is that along solution line -1.3035. It is this one that is the maximal flux for the given geometry. Other flows along solution lines such as -1.4 are also traceable, but they are submaximal. We will now outline the tracing process and then give the details of a few of the traced flows.

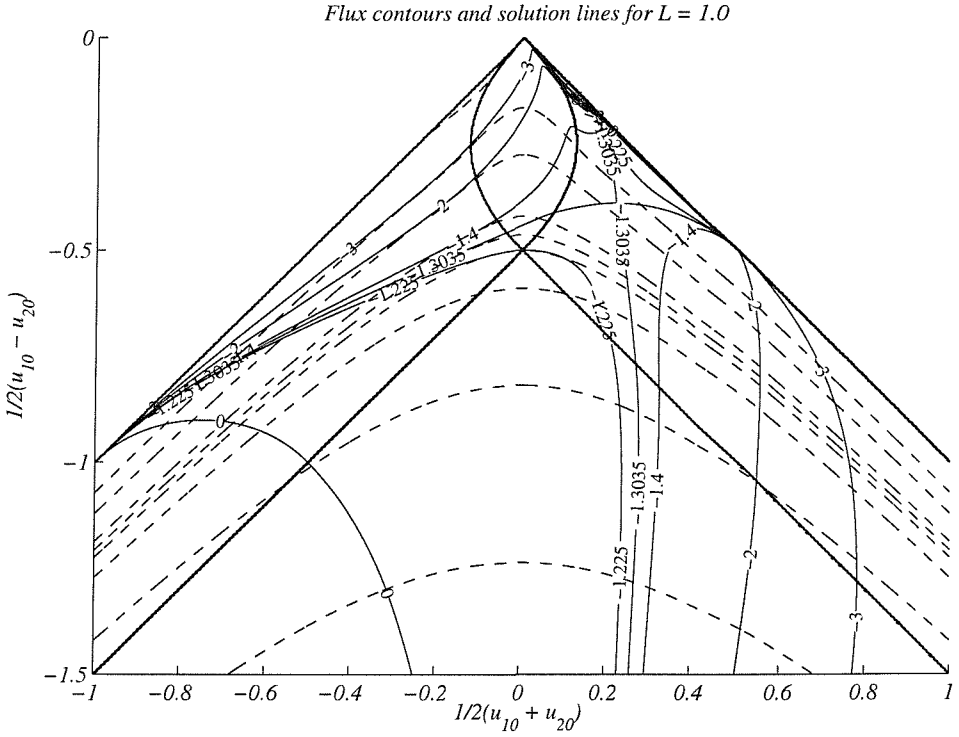

Figure 3.13: Plot showing the flux contours - thin dashed lines, and the solutions lines, $\frac{\Delta E}{\sqrt{|Q_1|}}$ - thin solid lines, for a rectangular rotating channel whose depth is changing like the square-root of its width. For this particular case the flow can be traced along the channel using the solution lines in a single diagram, similarly to the non-rotating case. The thick solid lines mark points of transition from one regime to another as in figure 3.4. Again the controlled solutions are indicated by tangential flux contours and solutions lines. Only the solutions lines are labelled and the corresponding flux-values are listed in table 3.1.

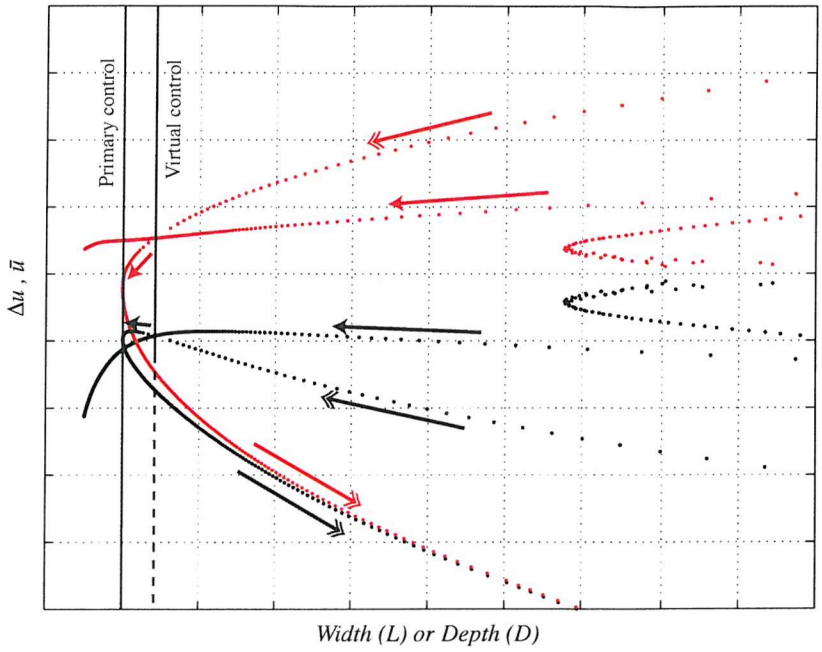

Figure 3.14: Sketch outlining the general behaviour of the solution for a rotating two-layer flow along a channel with a varying along channel geometry. The variables Δu and $\bar{u}$ are plotted in black and red respectively. The arrows indicate the net flow direction of the bottom layer, while the double-headed arrow head marks a supercritical branch and the single-headed arrow head a subcritical branch. At the virtual control a sub and a supercritical branch merge. The primary control is located at a minimum in the topography, either depth, width or both. Downstream there is no virtual control, hence the virtual control line is dashed where it passes over the downstream solutions.

Tracing the flow

The tracing of the flows along the solution lines was undertaken numerically, by scanning the data file containing $\frac{\Delta E}{\sqrt{|Q_1|}}$ across the entire domain of $\bar{u}$ and Δu to find intervals containing the desired contour value of the solution line, for example -2. By linear interpolation we found the position of the contour, i.e. the values of $\bar{u}$ and Δu. At the same locations of the interval containing the solution line we pick the corresponding values of the flux, and again linearly interpolate to determine the flux along the solution line to greater accuracy.

We thus arrive at a set of points describing the location, in terms of $\bar{u}$ and Δu, of the solution line and the corresponding flux values. But again we need to note that these values are scaled using the local geometry and therefore all these parameters describing the flow along the channel need to be 'tuned' to the scaling at the control.

Firstly we need to find the local depth in terms of the depth at the sill, D_0, since in the diagram 3.13 D is assumed to be 1 everywhere. Using previous simple scaling arguments we find that $D^{(1)} = D_0\sqrt{\frac{Q_0}{Q^{(1)}}}$. Similarly $\bar{u}$ and Δu need to be re-scaled, giving $\bar{u}^{(1)} = \bar{u}_0\sqrt{\frac{D^{(1)}}{D_0}}$ and similarly $\Delta u^{(1)} = \Delta u_0\sqrt{\frac{D^{(1)}}{D_0}}$. We can now present these rescaled parameters in a plot of $\bar{u}$ and Δu against D.

An example of how the results of traced flow will be presented throughout the thesis is shown in figure 3.14 for a maximal solution which we will shortly discuss in more

detail. In general the flows will consist of three solution branches, described equally well by Δu (black) or $\bar{u}$ (red), two supercritical (marked with a double-headed arrow) and one subcritical (single-headed arrow), as shown in the figure. The general features of the solutions in terms of Δu and $\bar{u}$ are the same and the following description thus applies to both variables.

The direction of the arrows indicates the direction of the net flow in the bottom layer. Those that point to the left lie along the upstream solution branches for which there are two, one supercritical and one subcritical. These two meet at a virtual control marked by a vertical line. The flow then approaches the primary control at the top of the sill or at the contraction (marked by a second vertical line). Between the virtual and primary control the flow passes briefly through a region where the flow can only be subcritical. After the primary control the solution line turns back on itself and moves downstream as a supercritical flow (marked by a double-headed arrow pointing right).

These types of plots give some valuable insight into the flow along the channel and we shall now pick three such flows and follow them.

Maximal flow

As mentioned before, the case where $\frac{\Delta E}{\sqrt{|Q_1|}} = -1.3035$ is the first one traceable for $L_0 = 1$ in diagram 3.13. After determining the solutions upstream and downstream using the method described in the previous section, the results are plotted in diagram 3.15, which shows $\bar{u}$ and Δu as a function of the depth away from the sill. All the information needed to describe the flow is contained within such a diagram.

The red dots represent $\bar{u}$ and the black dots Δu. Notice that $\Delta u = -\frac{1}{2}h_s$ is always less than 0 as it should be. All the branches on the diagram can be identified with sections of the contours on figure 3.13. The part of the -1.3035 contour that extends from (-1, -1) to the point where it is tangential to the flux contour, $Q_1 = -0.1545$, corresponds to the flow downstream of the sill. In 3.15 the downstream flow is presented by dotted lines commencing at $D^{(1)} = 7$ where both $\bar{u}$ and Δu are equal to -2.5.

What does this tell us about the flow far downstream? Since $\bar{u} = \Delta u$, $\bar{u} - \Delta u = u_{20} = 0$. The top-layer therefore has approximately zero velocity at the centre of the channel and on either side of the zero velocity line significant flow will be directed in opposite directions. Similarly, $\bar{u} + \Delta u = u_{10} = -5$ which leads us to conclude that the velocities in the bottom layer are unidirectional, since $u_1 = y + u_{10}$ and y has a maximum value of $L/2 = \sqrt{D}/2 = \sqrt{7}/2 = 1.32$, hence u_1 will be negative across the whole channel. We also know from figure 3.13 that the flow downstream including the control is semi-separated in regime 4.

Where the flux and solution contours are tangential in figure 3.13 we are at the top of the sill. This point corresponds to the point at which the dotted curves of $\bar{u}$ and Δu touch the line $D^{(1)} = 1$ in figure 3.15.

As we move past the control point on figure 3.13 the -1.3035 contour passes through

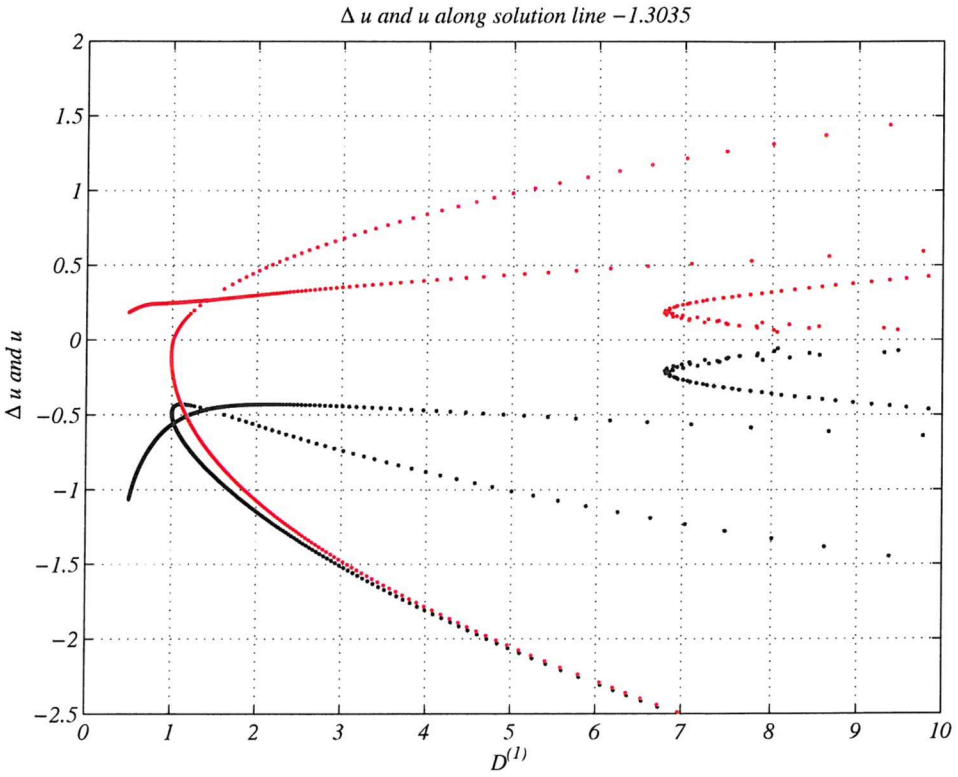

Figure 3.15: Plot of Δu in black, and $\bar{u}$ in red, against the depth of the channel, for a flow with $\frac{\Delta E}{\sqrt{|Q_1|}} = -1.3035$ and minimum width $L_0 = 1$. The primary control is at $D^{(1)} = 1$ where for both Δu and $\bar{u}$ there are two values (roots). The secondary control occurs at $D^{(1)} \sim 1.4$, where again only two of the values coincide. The two lines approaching the point where $D^{(1)} = 7$ and $\bar{u} = \Delta u = -2.5$ are the downstream solutions of the flow upstream the flow is briefly subcritical until it encounters the second control, from here the flow can follow either supercritical branch, which is the one that links smoothly to the second control, or a subcritical branch which exhibits a discontinuity in the gradient of the solutions at the virtual control.

a brief region of fully attached flow, before is comes to a point where it crosses another solution line of the same value. The line that leads straight on and approaches the $u_{10} = 0$ axis corresponds to the dotted lines that connect with a continuous gradient to the control section. As $D^{(1)}$ increases $\bar{u}$ approaches $-\Delta u$, meaning that $u_{10} = 0$ and u_{20} will be a large positive value. This means that the bottom layer will now have a significant region of backflow upstream and the top layer will also still have some backflow, however not as significant as downstream.

Apart from the dotted lines in figure 3.15 that link up smoothly, there are two more lines, one for $\bar{u}$ and one for Δu, which extend into the space where $D^{(1)} < 1$. These two correspond to values along the solution line that is crossed by the one we just followed and extends from about (0.25, -1.5) and up towards the tip of diagram 3.13. At the point where the -1.3035 contours cross, it is possible for the flow to follow two paths, one described earlier to the right of the point of intersection, alternatively the flow could continue upwards along the contour approaching the tip of the plot. This connection is characterised by a discontinuity in the gradient of both $\bar{u}$ and Δu at the virtual control in plot 3.15. Armi (1986) postulates that following the contour straight on leads to the maximal flux solution which is also fully controlled, with a supercritical region upstream, while following the contour upwards would also result in a flow with the maximum flux, but having submaximal flow features, i.e. the flow is subcritical everywhere upstream.

This is in fact confirmed also in our case. Some explanation might enlighten the scenario here. Notice that for each $D^{(1)}$ we have several values for both $\bar{u}$ and Δu, for most part as can be seen in figure 3.15 there are three values for both of these parameters, with two important exceptions. On the line $D = 1$ there are only two and on the line $D \sim 1.43$ there are only two. These are the two controls. The former one is the primary control at the top of the sill and the latter one the virtual control. Essentially each value corresponds to a root of the functional, if two coincide, we are encountering a control point! After each control the flow has the potential to follow a super- or a subcritical path. At the primary control the flow splits into the downstream flow, which is always supercritical, and the upstream flow, which briefly moves along a subcritical path. It then encounters the secondary or virtual control and again it has the possibility to follow either a supercritical path, the one that links to the subcritical regions continuously, or the subcritical path, which exhibits a discontinuity. Both of these are valid paths of the flow and both can carry the same, maximal, amount of flow.

As soon as the value of the solution line is increased by a small amount the flow no longer exhibits a second control and no second branching is observed. We shall now describe an example of such a purely submaximal flow.

A submaximal case

As an example of a submaximal flow we choose to trace $\frac{\Delta E}{\sqrt{|Q_1|}} = -1.400$. As opposed to the maximal case, in the submaximal case the subcritical branch of the upstream solution

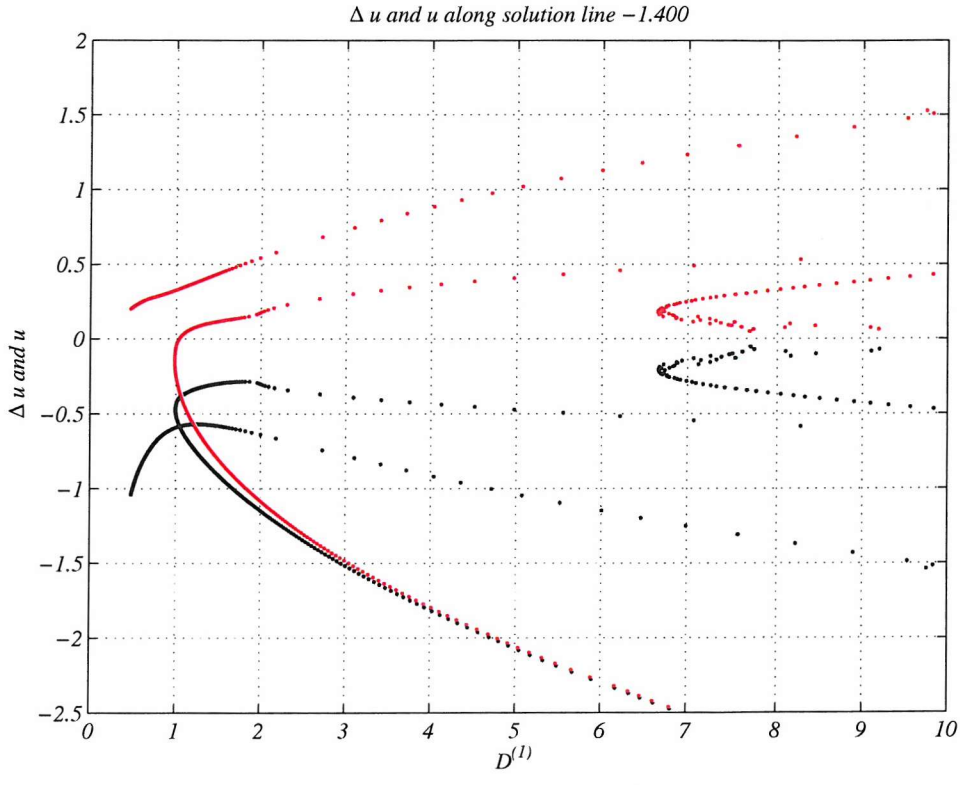

Figure 3.16: Along channel results of a flow with $\frac{\Delta E}{\sqrt{|Q_1|}} = -1.400$ and $L_0 = 1$. The colour scheme is the same as in figure 3.15, and the controlled flow is $Q_1 = -0.14$ in this case. The particular flow is submaximal, as there is no point beyond the primary control were the supercritical and subcritical branches meet upstream to allow for a secondary control.

never intersects with the supercritical solution to allow the flow to change into a different regime. The roots at each cross-section of this submaximal flow are shown in figure 3.16.

Again the dotted lines in figure can be identified with certain sections of the solution line -1.400. The downstream features are very similar to those we have encountered in the maximal flow case with $\bar{u} = \Delta u$, and hence $\bar{u} - \Delta u = u_{20} = 0$ leading to the same conclusions regarding the flow features. The contour for the downstream flow is that lying to the left of the tangential point of flux and solutions line in figure 3.13. Beyond the control the contour moves up into the fully attached region and then into the region where regime 8 occurs.

The interface height between the two layers and the velocity fields of both are plotted in figure 3.17, and a three dimensional plot in figure 3.18 shows the position of the interface over the topography. The formation of the separated boundary current in the top-layer can be seen in the second panel which also shows that the back flow does not extend across the sill. In panel three the boundary current in the top layer is featured upstream of the sill and in contrast to the bottom layer there is a region of back flow on the right-hand side all along the channel.

The remaining two smooth dotted lines of solutions for $\bar{u}$ and Δu in figure 3.16 correspond to the contour extending upwards from $\bar{u} \sim 0.3$ towards $\Delta u \sim -0.5$ where it curves to the right slightly. There is also a patch of seemingly randomly arranged points which correspond to small and unconnected contour pieces at the very tip of plot 3.13; they have no significance for any of the flows discussed here.

In addition to the traceable cases there are two types of flow which are not traceable. One is 'almost' traceable, in the sense that both upstream and downstream branches can be discerned on a diagram like 3.16 but there is a jump in one branch which renders the flow discontinuous and thus non-traceable. In the second case the upstream branch of the flow is missing completely indicating that there is only one root for most of the cross-sections and the downstream flow cannot be connected to any kind of flow upstream. We shall briefly show an example of both types of flows.

An untraceable case - I

Following the contour of $\frac{\Delta E}{\sqrt{|Q_1|}} = -2$ will give a flow that is submaximal with a flux, $Q_1 = -0.0918$, that is less than that achieved by the flow previously described. Again the flow features are determined upstream and downstream using the same method as before and the results are plotted in diagram 3.19.

The downstream flow features are again almost identical to those we encountered in the maximal and submaximal flow cases with $\bar{u} = \Delta u$, and hence $\bar{u} - \Delta u = u_{20} = 0$. The contour for the downstream flow is that lying to the left of the tangential point of flux and solutions line in figure 3.13. Beyond the control the contour moves up into the fully attached region and then doubles back on itself twice. As it does so a second time a discontinuity occurs in the flow features evident through a jump in the dotted lines in

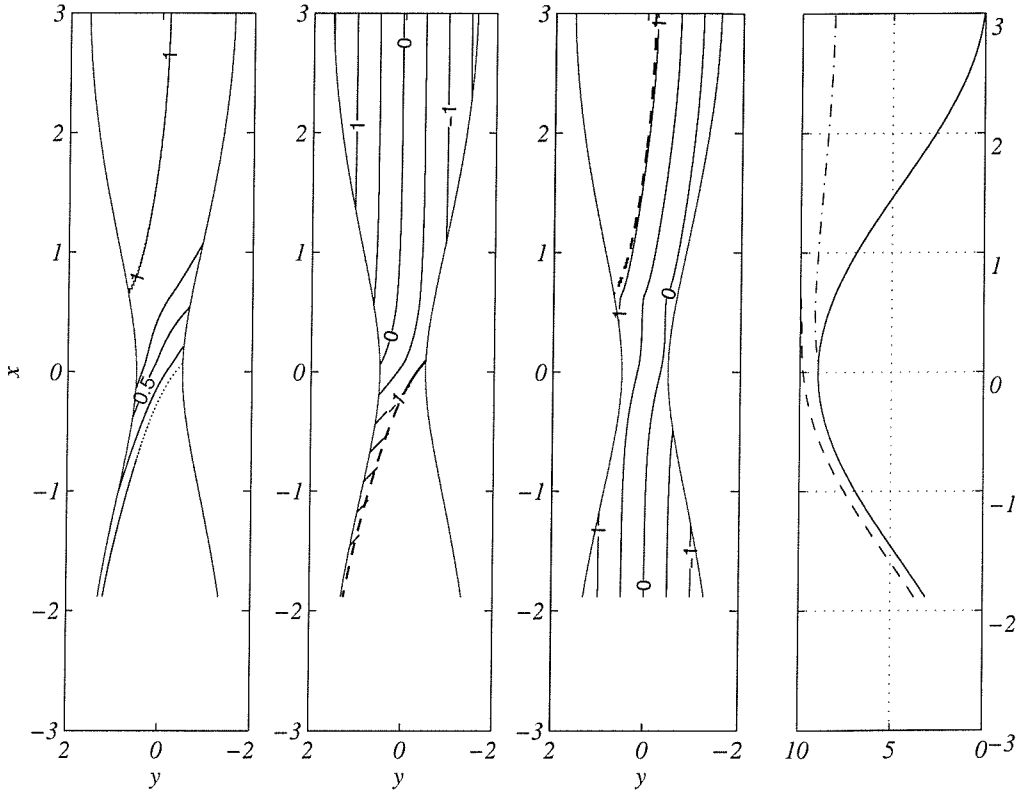

Figure 3.17: A contour plot of the bottom layer thickness is shown in the left-hand panel as a fraction of the channel depth, hence to the left of contour 1 the top layer vanishes. Here $L_0 = D_0 = 1$ and $\frac{\Delta E}{\sqrt{|Q_1|}} = -1.40$. The second panel shows the velocity field in the bottom layer which separates from the right-hand wall just before the sill and remains separated as a boundary current indicated by the thick dashed line. Panel three shows the velocity field in the top-layer which vanishes upstream to the left of the thick dashed contour (as in the first panel). Notice the back flow in the top layer does not reach the sill, while it is present in the top layer along the right-hand of the whole channel. The plot on the far right shows as a dashed line the intersection of the interface with the left-hand wall and as a dashed-dotted line the intersection with the right-hand wall above the topography (solid line). All of these figures show the submaximal case described in the text for a channel with $L = \sqrt{D}$.

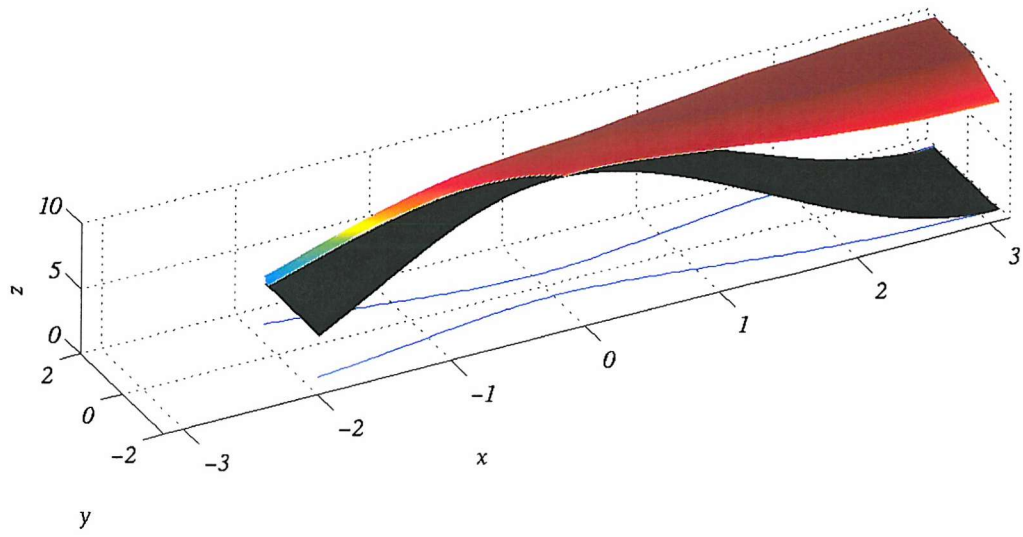

Figure 3.18: Three dimensional surface plot of the interface height (coloured surface) above the topography (black surface) for the submaximal case with $L = \sqrt{D}$, $L_0 = D_0 = 1$ and $\frac{\Delta E}{\sqrt{|Q_1|}} = -1.40$.

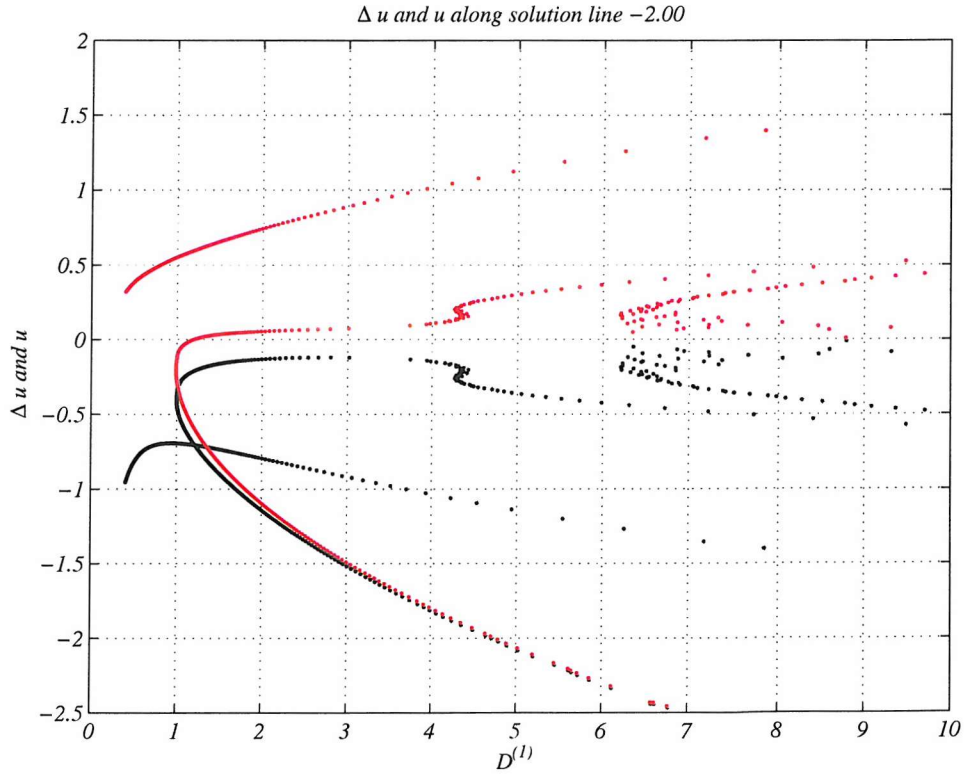

Figure 3.19: Untraceable case number one, traced along solutions line -2.00, is one for which a solution ceases to exist beyond the secondary control. At the point where $D^{(1)} \sim 4.3$ a third root develops for a small region, which continues to exist as the channel deepens while the root that was being traced from the control ceases to exist. The colour scheme is as in 3.15.

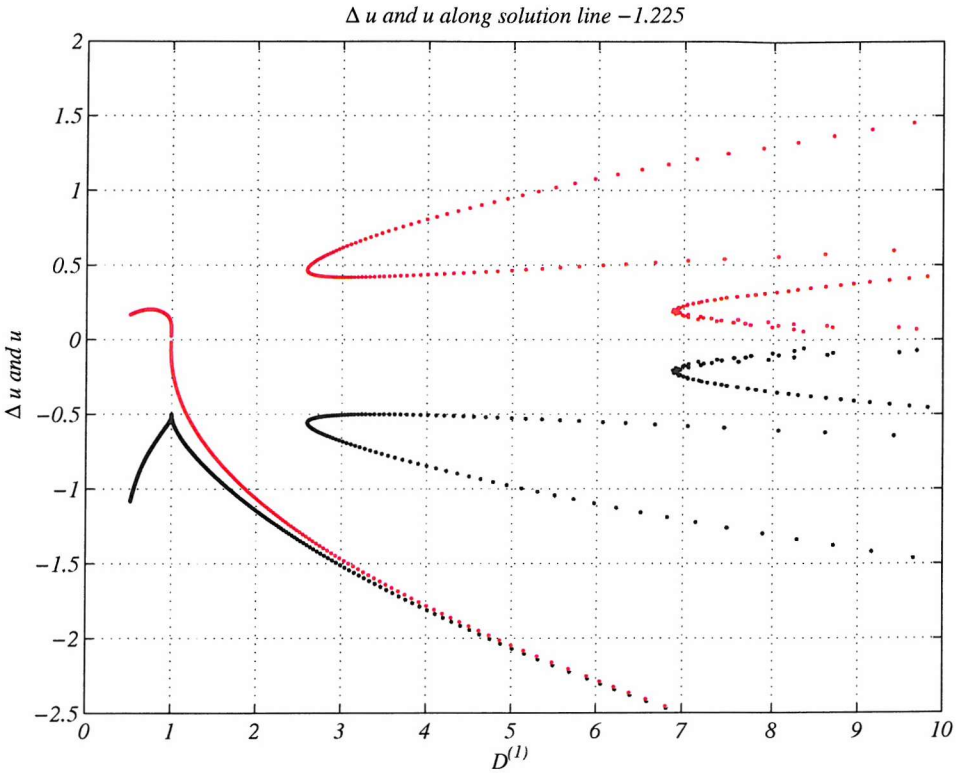

Figure 3.20: Untraceable case number two, traced along solution line 1.225 is not even traceable beyond its primary control. From figure 3.13 it can be seen that along this particular solution line there is no flux maximum. Although the solution line is tangential to the flux contour 0.167 the flux contours it intersects continue to increase leaving this flow untraceable.

figure 3.19. Beyond this point the flow ceases to connect smoothly to the sill conditions.

The remaining two smooth dotted lines of solutions for $\bar{u}$ and Δu correspond to the contour extending upwards from $(\bar{u}, \Delta u) = (0.55, 0)$. As before there is a patch of somewhat randomly arranged points (roots) which can be ignored.

An untraceable case - II

For completeness and for illustration purposes figure 3.20 is included to show what a flow looks like that is not traceable at all past the primary control. This is the flow which corresponds to $\Delta E = -0.5$ and should be traceable in a flat-bottom channel but is not when the depth increases away from a contraction. The downstream features are as before and here the flow is traceable, but as soon as the control point is passed the traceability is lost, as the flux lines crossing the solution line continue to increase instead of decrease, a prerequisite for traceability.

3.3 Long-waves

So far we have described how to determine control sections using two functionals. Another way to locate the control is by computing the long-wave speeds at each cross-section along

the channel, and find those sections where one of the wave speeds becomes zero. This type of analysis should confirm that the flow is controlled at the top of the sill and also show up locations along the channel where the flow might approach a virtual control.

Gill (1977) has shown, that when using a functional to solve for controlled flows ($\frac{\partial G}{\partial h} = 0$), regions where $\frac{\partial G}{\partial h} < 0$ and $\frac{\partial G}{\partial h} > 0$ are equivalent to subcritical and supercritical regions respectively, where internal waves travel in two or just one direction.

When dealing with observed flows or results from models, determining the locations of the controls is of course not possible by simply solving a functional, but rather they need to be determined from the available observations at a selection of sections across the channel. If rotation is deemed not to be important then the controls can be determined by simply computing the Froude number from the observation. If rotation is important however a more rigourous method is to compute the wave modes using the mean flow field and density stratification. In appendix B we outline the details of a method to find the wave-speeds in the analytical solution of the flow, by formulating it as an eigenvalue problem. We will use an analogous method later on to determine the locations of the controls in the MICOM results.

In brief the analysis involves the following steps: into the non-dimensionalised equations of motion the expressions for u_i, v_i, h_i and P are substituted, in terms of a mean value and perturbation, such as: $u_i = \bar{u}_i + u_i'$. The perturbations in turn are replaced by a wave-like expression, for example $u_i'(x, y) = u_i'(y)e^{ik(x-ct)}$, where c is the wavespeed and k the wave number. The resulting expressions are four homogeneous equations in four unknowns, which may be reduced to three and written in matrix from. The determinant of the matrix forms the characteristic equation for c, which we can then solve for.

As with the derivation of the flow fields of the two-layer rotating problem the characteristic equation will be different for each regime. All of them are described in appendix B.

We will now discuss some examples of the behaviour of the waves along a channel for which $L = \sqrt{D}$, which we have been working with so far. At the top of the sill, $D_0 = 1$ and $L_0 = 1$. Let us look at a submaximal and a maximal example of the flow in such a channel.

Submaximal flow

Figure 3.21 shows the wave speeds along the contour $\frac{\Delta E}{\sqrt{|Q_1|}} = -1.40$ in figure 3.13 which is a submaximal flow. The blue dots represent wave speeds, in the semi-separated flow of regimes 4, which is for the most part supercritical. At $D_0 = 1$, at the top of the sill, one of the wave speed passes through zero which is where the primary control is located. Beyond this point the flow becomes subcritical with one wave speed being positive and for a small region it becomes fully attached (regime 5), which is indicated by the red dots. At $D \sim 2$ the flow separates again from the side wall and enters regime 8, marked in green. It is at the transition between regime 5 and regime 8 that the negative wave speed

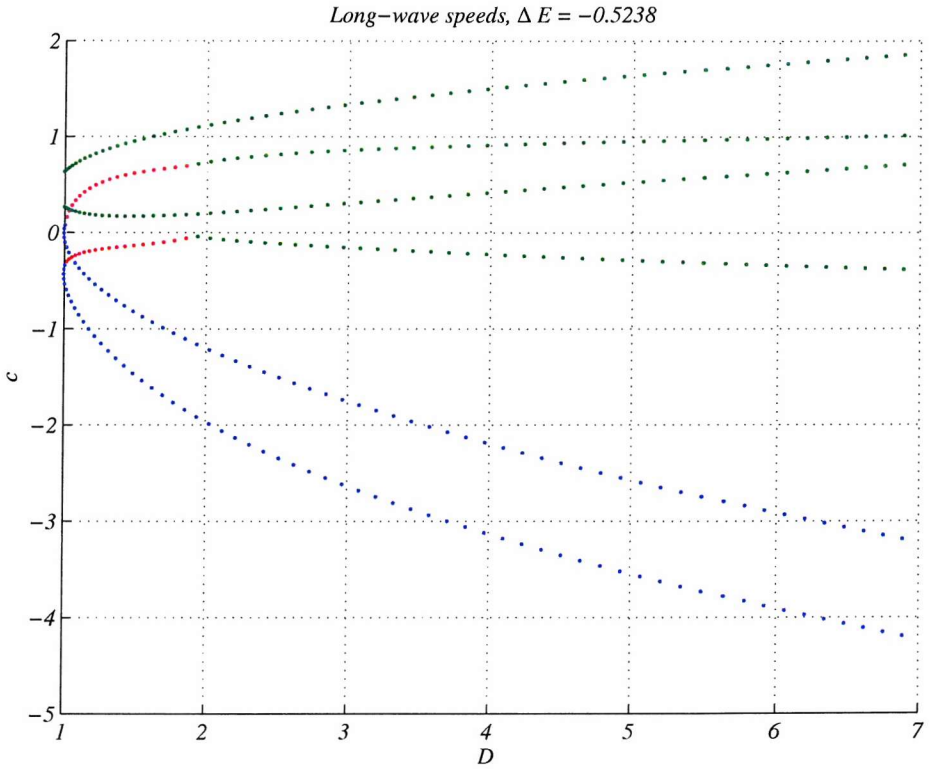

Figure 3.21: Wave speeds plotted against the depth of a channel with $L = \sqrt{D}$. Blue denotes flow in regime 4, red - regime 5 and green - regime 8. The flow is submaximal with $\Delta E = -0.5238$ ($\frac{\Delta E}{\sqrt{|Q_1|}} = -1.40$). The primary control is located at section $D = 1$ at the top of the sill. At $D \sim 2$ one of the wave speeds approaches zero, but the sub- and supercritical branches of the upstream flow never actually meet.

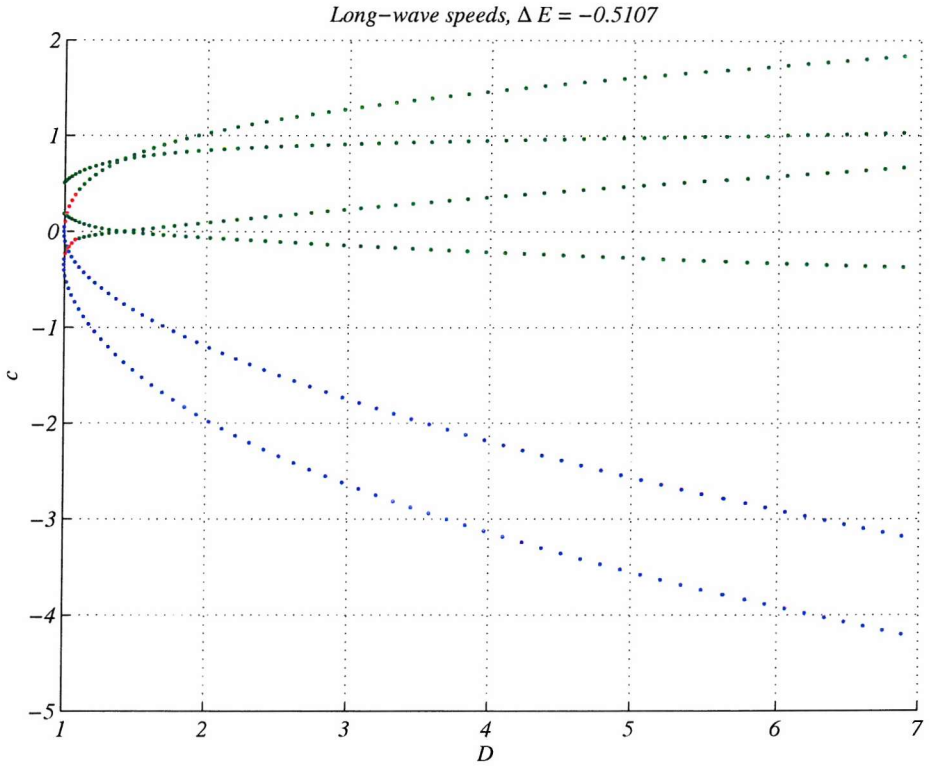

Figure 3.22: Plot of the wave speed for a maximal flow with $\Delta E = -0.5107$, $L_0 = D_0 = 1$. The topography is as for the flow in figure 3.21 and the colour scheme of the dots is also the same. Primarily control again occurs at section $D = 1$ at the top of the sill. At $D \sim 1.5$ the sub- and supercritical branches upstream merge and one crosses the line $c = 0$, this indicates the location of the virtual control.

almost approaches zero but then becomes increasingly negative again further upstream and therefore the flow remains subcritical. The supercritical branch of the upstream solution lies entirely within regime 8, but never merges with the subcritical branch so that a transition to a different flow state upstream of the sill does not occur.

Maximal flow

In contrast, figure 3.22, shows the wave speeds for $\Delta E = -0.5107$ which is the maximal flow shown in figure 3.13. It can be seen clearly that the two branches of the semi-separated flow in regime 8 (green) merge at a depth a little less than 1.5 and one of the negative wave speeds crosses $c = 0$ and become positive; this is the virtual control and coincides with the point at which the contours of $\frac{\Delta E}{\sqrt{|Q_1|}} = -1.3035$ cross. Beyond this point the flow can follow either a positive or a negative branch and thus become supercritical or remain subcritical respectively.

Non-traceable flow

Any flow for which $|\Delta E| < 0.5107$ will not be traceable. Similar to the non-traceable solutions for a channel with a pure sill and no contraction, the super- and subcritical

branches will separate in the horizontal, similar to what we saw in figure 4.15, and in the gap between them no solutions exist, rendering the flow untraceable.

3.4 Conclusions

In this chapter the rotating two-layer exchange flow theory with zero potential vorticity, which has been used by Dalziel (1988) and Whitehead et al. (1974) amongst others, was adapted and significantly extended to include all possible separated and attached flow regimes. It allows us to trace a larger variety of possible flows along channels of different topographies.

The main achievement in redeveloping the theory has been the presentation of the two-layer rotating hydraulic theory results in a way that is analogous to the presentation of the non-rotating results by Armi (1986) and Armi and Farmer (1986). We found that also in the rotating problem the pseudo-Froude-number representation of the solutions can give valuable insight into the behaviour of the controlled flows.

We found that it is possible for a special topography with $L \propto \sqrt{D}$ to trace the flow along the channel using one of these pseudo-Froude-number diagrams and we have used this tracing method to discuss maximal as well as submaximal and non-traceable flows. This again presents an extension to the work by Dalziel (1988), who concentrated only on maximal flows. We have shown that for a channel with a varying depth and width the maximal flux occurs for a $|\Delta E| > 0.5$ and for a channel with $L_0 = D_0 = 1$ the maximal flow occurs at $|\Delta E| \sim 0.5107$.

We find that the maximal flux for any given topographic cross-section occurs for $\Delta E = -0.5$ which also agrees with the findings by Armi and Farmer (1986) for the non-rotating case. As L_0 increases, while D stays constant, so does the maximum controlled flux. This means that in a flat bottom channel the maximal flow along the solution line $\Delta E = -0.5$ will always be traceable, and the two controls coincide at the narrowest point of the channel, just as in the non-rotating case. We will discuss a traced maximal flow in a flat bottom channel in the next chapter.

Furthermore we have seen that for some ΔE there are two controlled flow solutions; one consistently exists for all ΔE while the other one is centred around very small values of both Δu and $\bar{u}$ and seems to only occurs predominantly for values of ΔE close to 0 and -1. We will see more evidence of this control in the next chapter and build a more complete picture of what is means for the flow.

Finally we set up an eigenvalue problem for the two-layer rotating flows that allows us to find the wave speeds along the channel and used them to find the control sections. This is a very useful method that can be adapted to determine control sections of observed flows in the ocean or in the laboratory where rotation is important. In fact we will apply this analysis in chapter 6 and 7 to examples of flows modelled numerically, with promising results.

Chapter 4

Solution space for a single variable

In the previous chapter we discussed a neat and simple way to trace a flow and determine its velocity and interface heights anywhere along a channel of a geometry with $L \propto \sqrt{D}$.

However, we are also interested in channels with other geometries, such as constant depth and varying width, constant width and varying depth, or alternatively a channel whose width and depth change at some arbitrary ratio. Dalziel (1988) focused on channels of constant depth and varying width, and on constant width channels containing a sill connected to a channel with flat bottom and varying width. These geometries where equally considered by Armi (1986) and Armi and Farmer (1986) in the non-rotating case, while Farmer and Armi (1986) also studied channels whose width and depth were changing simultaneously.

The previous analysis could be adapted for other geometries, although it would not be possible to trace such flows on one diagram. One could imagine a three dimensional figure in which plots such as figure 3.4 are stacked side by side with the geometry changing by small amounts from plot to plot. We would get a three dimensional picture with distance along the channel, having a changing geometric variable such as depth as the third dimension. Control points would be found as previously described, by determining a pair of ΔE and Q_1 which are tangential at a particular control section. The solutions away from the control are determined by the points at which a desired solution surface of given ΔE, intersects with the controlled flux surface, in the plots away from the control section.

Another way of representing and tracing the hydraulically controlled flows, which we will adopt and discuss further here, involves reducing the dependence of the flux to one variable and use a Gill-like functional approach to trace the solutions along the channel.

The reason for doing so is twofold. First of all, it links nicely the two different ways that have been used in the past to study hydraulic problems. On the one hand the non-rotating theory by Armi (1986), Armi and Farmer (1986) and Farmer and Armi (1986) utilising the Froude number plane to describe the solutions and on the other hand the non-rotating analysis carried out by Dalziel (1991) who follows the functional representation. Secondly, we feel it is neater and easier to think about the problem as a collection of functionals, the roots of which we are tracing, rather than a three dimensional representation where

we need to trace the solutions along surfaces rather than contours.

So in the following section we will first of all discuss the reduction of the problem to a single variable functional and then trace flows along channels of constant depth and varying width and constant width and varying depth. For both types of channels we will discuss maximal, submaximal and non-traceable solutions.

4.1 Single variable reduction

The aim here is to reduce the two functionals used in the previous chapter to one, with only one unknown. The choice of functionals is between Q_1 and ΔE. For the purposes of this analysis we will use the flux Q_1 as the functional, and the interface slope h_s as the unknown in terms of which it will be written:

$$Q_1 = (D, L, \Delta E; h_s) = \text{constant}. \tag{4.1}$$

Dalziel (1988) uses the Bernoulli functional instead, and on page 27 of his thesis he justifies this by observing that "the conservation of the Bernoulli potential introduces roots of a quadratic [when solving for u_1 and u_2] which may cause some ambiguity in the definition of J [G]", if the flux Q_1 were taken to be the functional G. We avoid this problem by choosing variables $\Delta u = \frac{1}{2}(u_{10} - u_{20}) = -\frac{1}{2}h_s$ and $\bar{u} = \frac{1}{2}(u_{10} + u_{20})$ instead of u_1 and u_2 to describe the flow. The Bernoulli function (3.23), may then be written as

$$\Delta E = E_1 - E_2 = -\frac{1}{2}h_s(u_{10} + u_{20}) + h_{10} - D = -2\Delta u\bar{u} + h_{10} - D. \tag{4.2}$$

From (4.2) and using $h_s = u_{20} - u_{10}$ the following expressions for u_{10} and u_{20} can be derived:

$$u_{10} = \frac{h_{10} - \Delta E - D}{h_s} - \frac{h_s}{2} \tag{4.3}$$

$$u_{20} = \frac{h_{10} - \Delta E - D}{h_s} + \frac{h_s}{2}. \tag{4.4}$$

These are then substituted into the flux integral, the form of which depends upon which regime we assume the flow to be in, and by assuming zero net flux $Q_1 + Q_2 = 0$ an expression for h_{10} is found, again different for each regime (see appendix A). In the fully attached regime 5 h_{10} is given by:

$$h_{10} = \frac{D(2\Delta E + 2D - h_s^2)}{2(D - h_s^2)} \tag{4.5}$$

and in the fully separated case with a positive slope, regime 7, h_{10} is given by:

$$h_{10} = \frac{2L(\Delta E + D) - Dh_s}{2(L - h_s)}. \tag{4.6}$$

Note the peculiarity in the dependence of these expressions. The fully attached case is independent of L, while the fully separated case is not.

For the semi-separated cases, h_{10} is the solution of a quadratic, which suggests two possible solutions. However it turns out that one of the roots gives rise to an answer that is not physically consistent and has therefore been ignored. Appendix A outlines an algorithm used to compute h_{10} and to test whether it is consistent with the assumptions made in computing it.

Now we know u_{10}, u_{20} and h_{10} purely in terms of the geometric parameters L and D, ΔE, and the variable describing the flow, h_s. Integrating across the bottom layer for the fully attached regime, we find the flux to be given by:

$$Q_1 = \frac{L^3 h_s}{12} - \frac{LDh_s}{4}\left[1 - \left(\frac{D + 2\Delta E}{D - h_s^2}\right)^2\right]. \tag{4.7}$$

Similar equations can be derived for the other regimes, but they are a lot more complex. We have not derived each flux equation but rather determine the fluxes numerically.

Notice that if $D + 2\Delta E = 0$ the flux of regime 5 is linear in h_s. This also applies for all other regimes. Since we always choose $D_0 = 1$ at the control, this means that the functional for $\Delta E = -0.5$ will always be linear. This is because for $\Delta E = -0.5$ the controlled flow will have $\bar{u} = 0$ as we have seen in the previous chapter. Equation (4.2) will therefore reduce to $\Delta E = h_{10} - D$ and thus lose its dependence on h_s. The implications of this will become clear in the next section where we describe and use the concept of criticality and aim to derive the controlled flows. With an equation for each flow regime we can now compute Q_1 for a range of h_s, fixing D, L and ΔE as desired.

Figure 4.1 shows the result of such a computation, with the different line-styles indicating the regime of the flow. The figure presents results for a range of h_s from -5 to 5, given $L_0 = 0.5$, $D_0 = 1$ and $\Delta E = -0.6$. The fluxes can be seen to be anti-symmetric about the point at which the slope as well as the flux are zero. Although the analysis is set up in such a way that it gives results for negative as well as positive slopes, we will only consider negative ffuxes, which are generally associated with a positive slope. All other flows, despite being accurate solutions to the equations, are not physical, considering the assumptions regarding topography and the location of the dense and the light reservoirs. Note that we made the same assumptions in figures 3.4, 3.6, 3.9 and 3.10 by only working with $u_{10} - u_{20}(= -\frac{1}{2}h_s) < 0$.

Each pair (h_s, Q_1) on one of the lines in figure 4.1 represents a physically realisable flow that may occur at a cross-section with $D = 1$, $L = 0.5$ (or $L/\sqrt{D} = 0.5$) and a Bernoulli potential $\Delta E = -0.6$. The features of this flow can be derived just by knowing h_s and the regime it lies in; from these h_{10}, u_{10} and u_{20} can be found and thus the flow fields of top and bottom layer and the position of the interface.

In relation to figure 3.6, the fluxes plotted in figure 4.1 are those along the contour $\Delta E = -0.6$ and our primary point of interest lies in finding the control point which coincides with the point marked by an asterisk in figure 3.6.

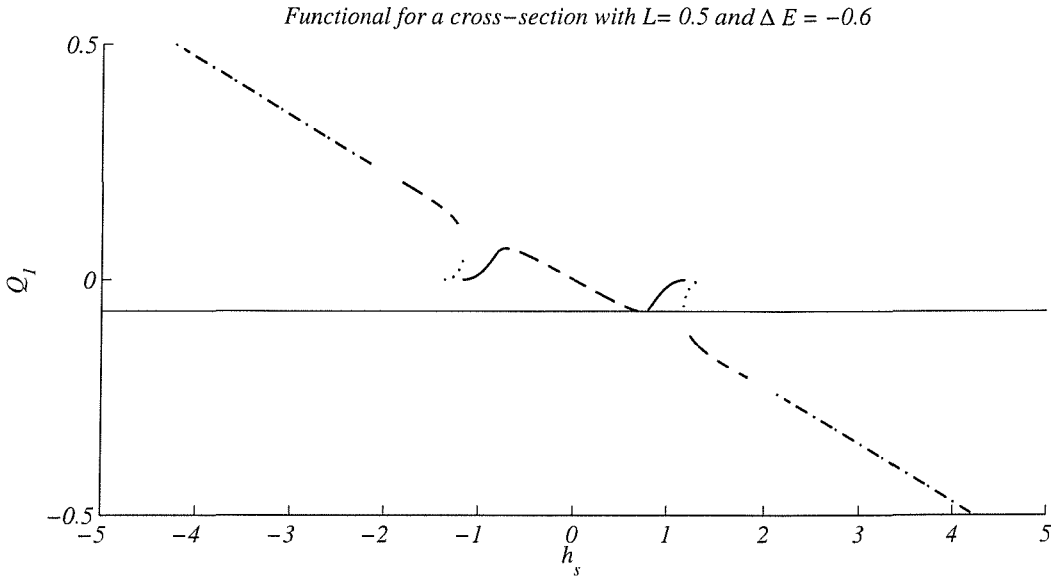

Figure 4.1: Typical plot of the flux as a function of the slope. Here $L = 0.5$, $D = 1.0$ and $\Delta E = -0.6$. The regimes can be distinguished by the different line-styles: regime 5 - dashed, 4 and 2 - solid, 8 and 6 - dotted, and 7 and 3 - dashed-dotted. Regimes 2, 6, 3 and some of 5 have a negative slope and thus lie in the left half of the plot, where as the others lie to the right of $h_s = 0$. The solid horizontal line marks the controlled flux which occurs at the local minimum of the functional, where the slopes are positive.

4.1.1 Determining and tracing the controlled flows

The conditions for criticality have been discussed in general in chapter 2. In the single-variable notation the equivalent of equation (2.2) is:

$$\left(\frac{dQ_1}{dh_s}\right)\frac{dh_s}{dx} + \left(\frac{dQ_1}{dL}\right)\frac{dL}{dx} + \left(\frac{dQ_1}{dD}\right)\frac{dD}{dx} = 0 \tag{4.8}$$

and by previous arguments the condition for control to occur is $\frac{\partial Q_1}{\partial h_s} = 0$. As outlined in chapter 2, between the controls, if $\frac{\partial Q_1}{\partial h_s} > 0$, the flow is said to be *supercritical*, if $\frac{\partial Q_1}{\partial h_s} < 0$ the flow is said to be *subcritical*. In figure 4.1 therefore a control point occurs where regime 5 (dashed line) has a minimum just to the right of $h_s = 0$. All solutions on the functional immediately to the left of the control point are subcritical and those to the right are supercritical.

By computing the functional for a section a small distance away from the control with different, slightly larger, values for D and/or L, the roots linking to the control are found to be the points at which the new functional intersects the controlled flow determined from the functional at the control section. Whether the flow is traceable or not will depend on whether at that channel cross section there exist roots of the functional with the desired controlled flux.

Figure 4.2 illustrates the process of tracing the flow upstream and downstream away from the control section in the case of a flat bottom channel, with $D_0 = 1$, $L_0 = 0.3$ and $\Delta E = -0.7$. The curve labelled 0.30, which is tangential to the horizontal line, is the functional for the controlled section with a maximum flux of $Q_1 = -0.0265$. In this case

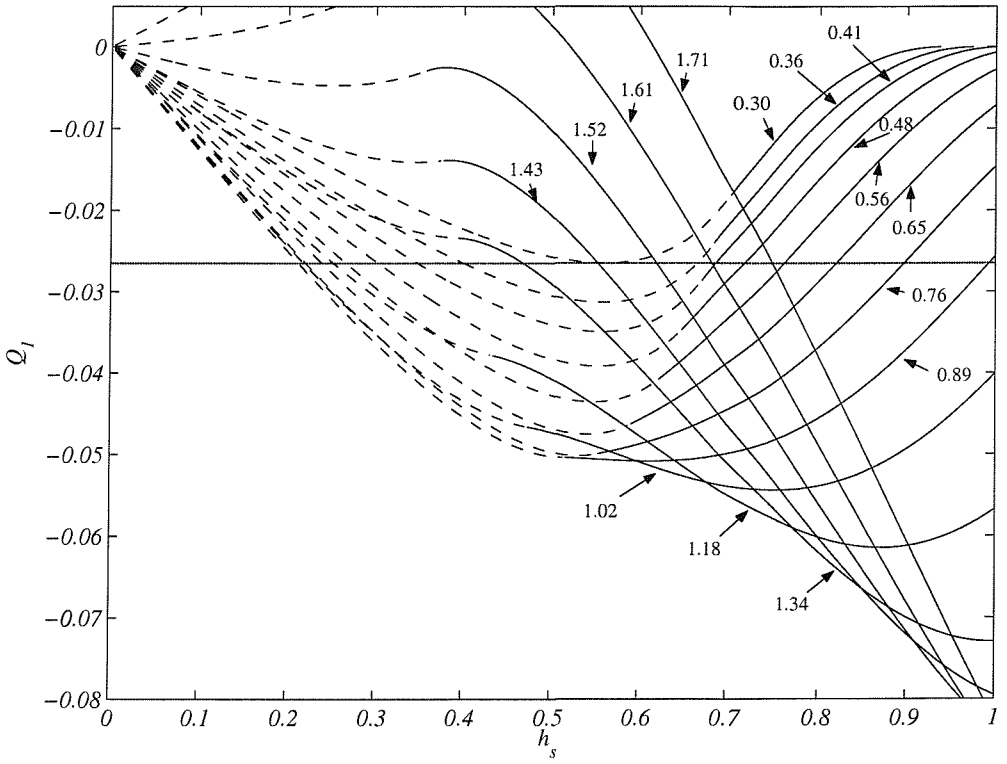

Figure 4.2: Plot of the flux as a function of h_s for a variety of cross-sections with increasing width. Each functional is labelled with the width of the channel. The thick horizontal line is the controlled flow $Q_1 = -0.0265$ for a section with $D_0 = 1$, $L_0 = 0.3$ and $\Delta E = -0.7$. As the width is increased the minimum of the curves move down and the points where the horizontal line intersects the subsequent curves are the solutions of the flow up and downstream. Functionals for sections with $L < 0.3$ will have a minimum above the dotted line. A second minimum develops for curves with $L > 1.43$, which lies above the marked controlled flux.

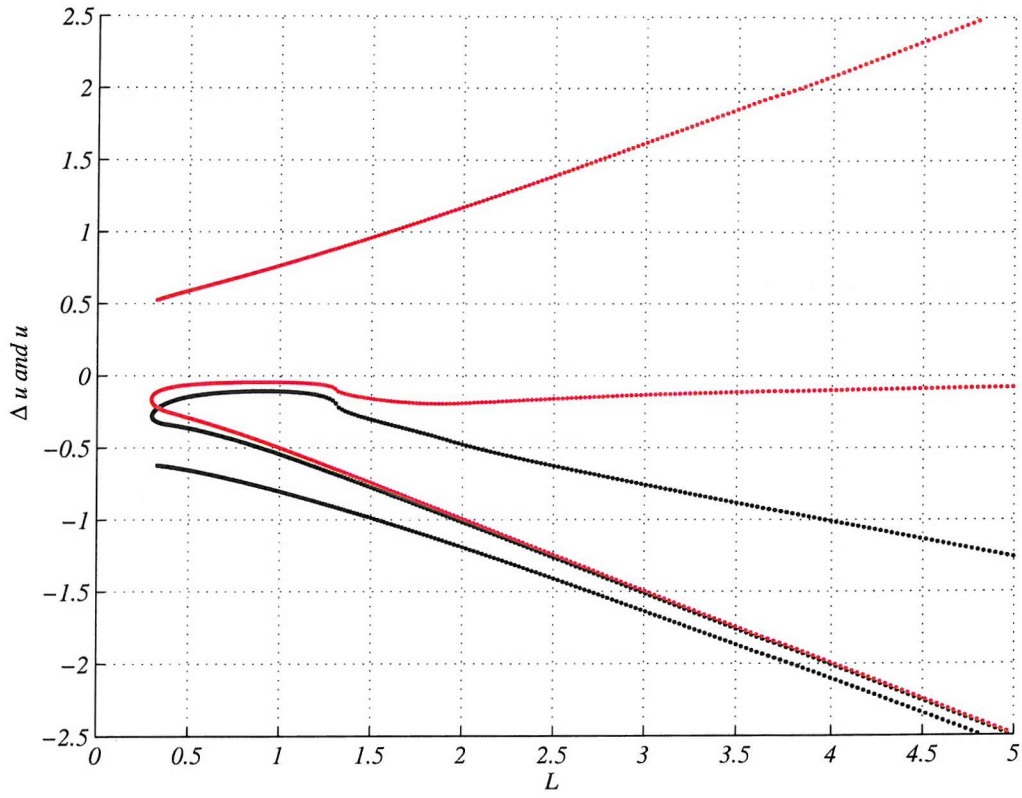

Figure 4.3: Plot of $\bar{u}$ (red) and Δu (black) as a function of width along a channel of constant depth, $D_0 = 1$, $L_0 = 0.3$ and $\Delta E = -0.7$. Along the entire channel there are three values for both variables indicating that it does not pass through a second control at any point.

the controlled flow is fully attached. From the plot the slope for this particular control can be determined, here $h_s \sim 0.56$ and from it all other variables to describe the flow (h_{10}, u_{10}, u_{20}, etc.) may be found.

The next curve, the minimum of which lies somewhat below the horizontal line, is for a channel cross-section a small distance Δx away from the control, where $L = 0.36 > L_0$ ($D = 1, \Delta E = -0.7$). The points of intersection of this curve with the horizontal line marking the controlled flux give the solution of the flow for the cross-sections just up- and downstream of the contraction.

With the widening of the channel the minimum of subsequent curves continues to move down. Beyond the point where the controlled flux has reached $Q_1 \sim -0.051$ it ceases to move straight down but instead the slopes of the controlled flow start increasing, along with their fluxes and the minima move of the plot. For $h_s < 0.4$ the flux is drawn upwards and a second control develops at about $h_s \sim 0.3$ for functionals with $L \gtrsim 1.43$.

If this minimum develops below the flux that is to be traced (if its absolute value is larger than the horizontal flux line), the traced flow will pass through this control and traceability will cease beyond it. If the minimum develops above the controlled flux, the flow will 'almost' feel it, but not directly encounter it and therefore remain traceable.

Just to reiterate, each of the curves in figure 4.2 is a functional for the flow at a specific cross-section and their intersections with the horizontal line are the roots of the

functional. Having found all the roots for the example above, in which the depth remains constant and the width increases from $L_0 = 0.3$, the results are shown in figure 4.3. This plot can be interpreted similarly to figures like 3.15 shown in chapter 3.

The primary control where two roots coincide lies on the line $L = 0.3$, from there the downstream flow moves of to the bottom right of the plot again with $u_{10} = 0$ as a result. Upstream $\bar{u}$ approaches zero, while Δu becomes increasingly negative therefore $u_{10} \sim \Delta u$ and $u_{20} \sim -\Delta u$ far upstream. At no point is there another location at which two roots coincide and therefore there is no virtual control in this flow, the flow is submaximal. The dip in the curves as $L \sim 1.3$ is where the flow 'feels' the presence of a second control but does not actually pass through it.

This process of tracing the flow is equally applicable for any shape of channel and we will now first of all discuss flows in flat bottom channels in more detail, and then the slightly more complex case of flows over a sill.

4.2 Flows through a flat bottom channel

Having outlined the process of tracing a controlled flow along a channel of arbitrary topography using a single functional, we will now present three different types of flows through a flat bottom channel in more detail: a maximal, a submaximal and a non-traceable flow.

Maximal flow

We have seen in chapter 3 that the maximal flux for any given cross-section is determined by the flux contour that is tangential to the solution line $\Delta E = -0.5$. This point coincides with the intersection of the two contours of $\Delta E = -0.5$ in the pseudo-Froude-number plane and here three roots coincide, making the flow maximal.

We have mentioned earlier that if we express the flow in terms of a functional Q_1 then for $D = 1$ and $\Delta E = -0.5$, this functional is going to be linear with h_s which means it has no extremum points. As a result we are not be able to determine the controlled flux for such a geometry using the functional. In order to be able to trace this maximal flow we have to return to the representation of the solutions in terms of two variables as discussed in the previous chapter.

When we look at the three figures 3.6, 3.4 and 3.9 we observe that the intersection of $\Delta E = -0.5$ moves steadily downwards, as the channel widens, while the flux contours move up. This means that as the channel widens the contour of the controlled flux will intersect $\Delta E = -0.5$ in three places giving two supercritical roots and one subcritical root.

The two supercritical roots move away to the right and left of the intersection, from the diagrams it is obvious that Δu will be equal for both, while $\bar{u}$ at one root will be $-\bar{u}$ at the other root. The third root (the subcritical one) follows the vertical line $\bar{u} = 0$

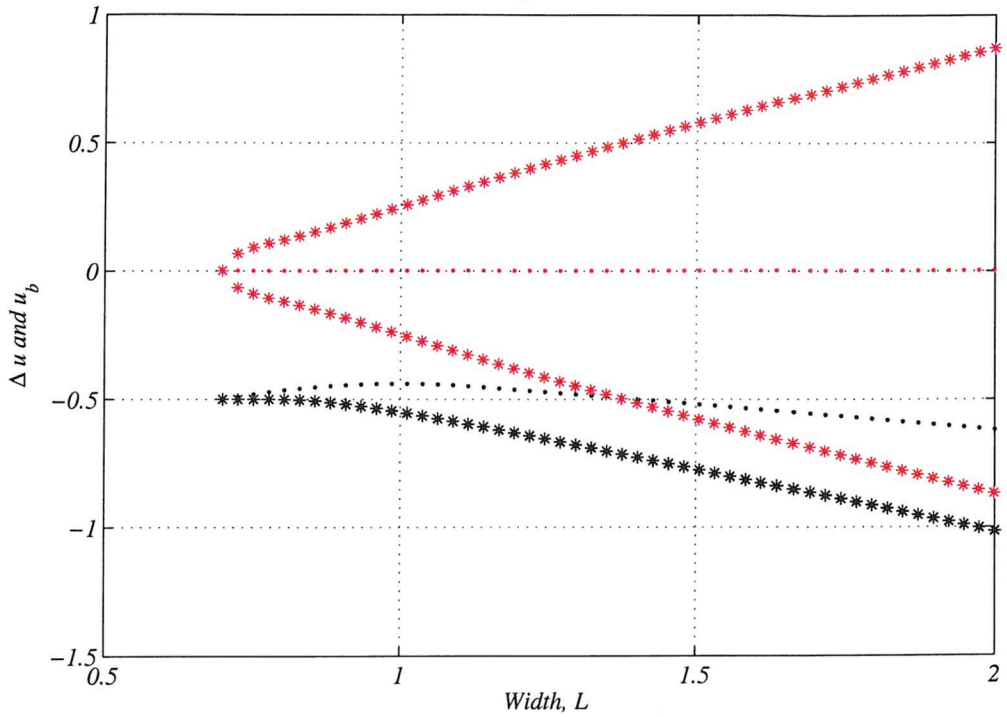

Figure 4.4: Plot of $\bar{u}$ in red and Δu in black for a channel with $L_0 = 0.7$, $\Delta E = -0.5$ and $D_0 = 1$. The supercritical branches are marked with asterisks and the subcritical ones with dots. All three branches merge smoothly at the primary control indicating that the three roots coincide at one point and primary and secondary control are both located at the central control section. The controlled flux is $Q_1 = -0.1464$.

upwards, as Δu also approaches a small value less than 0.

A plot of Δu and $\bar{u}$ against the width of the channel is shown in figure 4.4 for a channel with $L_0 = 0.7$ ($D_0 = 1$ and $\Delta E = -0.5$). The supercritical branches of $\bar{u}$ are the two red branches (marked with asterisks) moving symmetrically away from the primary control, while on the subcritical branch $\bar{u} = 0$. For Δu the supercritical branches, again marked by asterisks, lie on top of one another and extend downwards from the control. The respective subcritical branches are marked with dots.

All these observations lead to the conclusion that the flow is symmetric about the central control section. While downstream the bottom layer will separate from the right-hand wall and form a boundary current on the left-hand side of the channel, upstream the top layer will exhibit the same features only as a mirror image and rotated by 180 degrees about the horizontal, i.e. it will also separate, but from the left-hand wall and form a boundary current along the right (regime 8).

Submaximal case

All flows with $\Delta E \neq -0.5$ which are traceable are submaximal; we have briefly seen one example when we outlined how to trace solutions in section 4.1.1. Another typical example of a submaximal flow occurs in a channel with $L_0 = D_0 = 1$ at the control and $\Delta E = -0.7$.

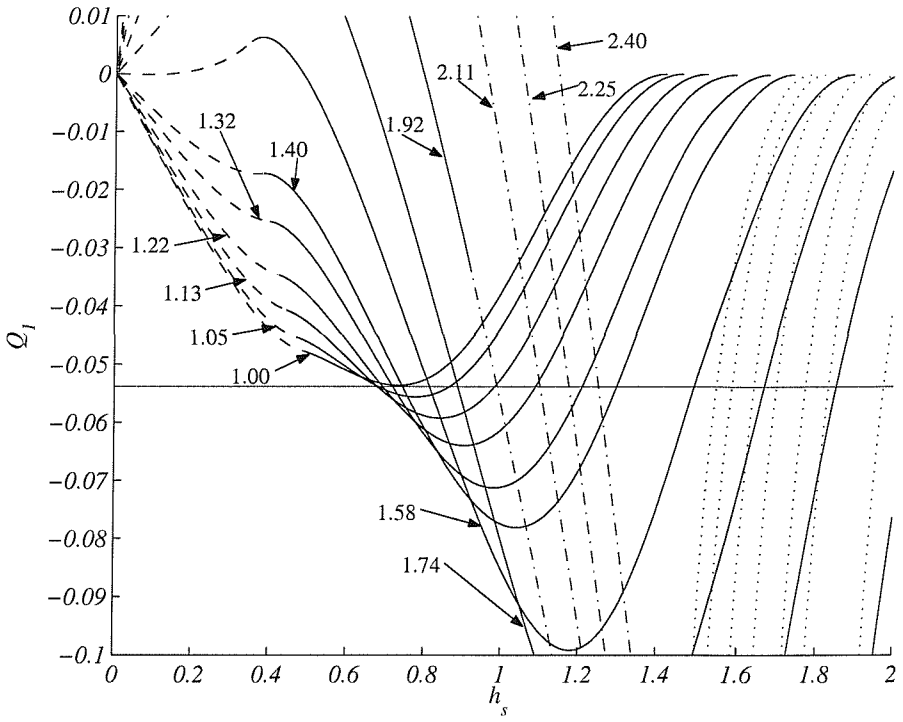

Figure 4.5: Flux lines for $D_0 = 1$, $L_0 = 1.0$ and $\Delta E = -0.7$. The controlled flux is $Q_1 = -0.054$.

Figure 4.5 shows the functionals at consecutive sections along the channel. The functional marked 1.00 is that of the control section and it can be seen that the flow is separated (regime 4) at the control, where the curve has a minimum. The controlled flux is determined to be $Q_1 = -0.0536$. As before, the roots of the subsequent functionals can be plotted against the varying geometric variable, in this case width, presented in figure 4.6. The control as usual is at $L = 1$ where two roots coincide and the super and subcritical branches move away from this point. The unconnected branches are the supercritical upstream solutions which do not link to the controlled flow at the sill and so there is no secondary control beyond which the flow could become supercritical.

We can see in figure 4.5 that a second control does develop for channels wider than $L = 1.40$ but the flux of this second control is much smaller than the controlled flux we are tracing and thus the flow does not 'feel' this control and is not limited by it.

In figure 4.7 the contours of the bottom layer thickness are shown in the right-hand panel, where we observe that the flow is separated from the right-hand wall all along the channel. Upstream the interface is almost vertical and positioned at the centre of the channel so that the left half contains only dense bottom water, while the right half contains the lighter surface water. The velocity contours in the bottom and top layer are plotted in the middle and right panel respectively. It can be seen that there is no recirculation in the bottom layer at the control. The region of backflow in the bottom layer is confined to a region upstream of the contraction on the left-hand side of the channel. In the top layer backflow occurs all along the right-hand side of the channel

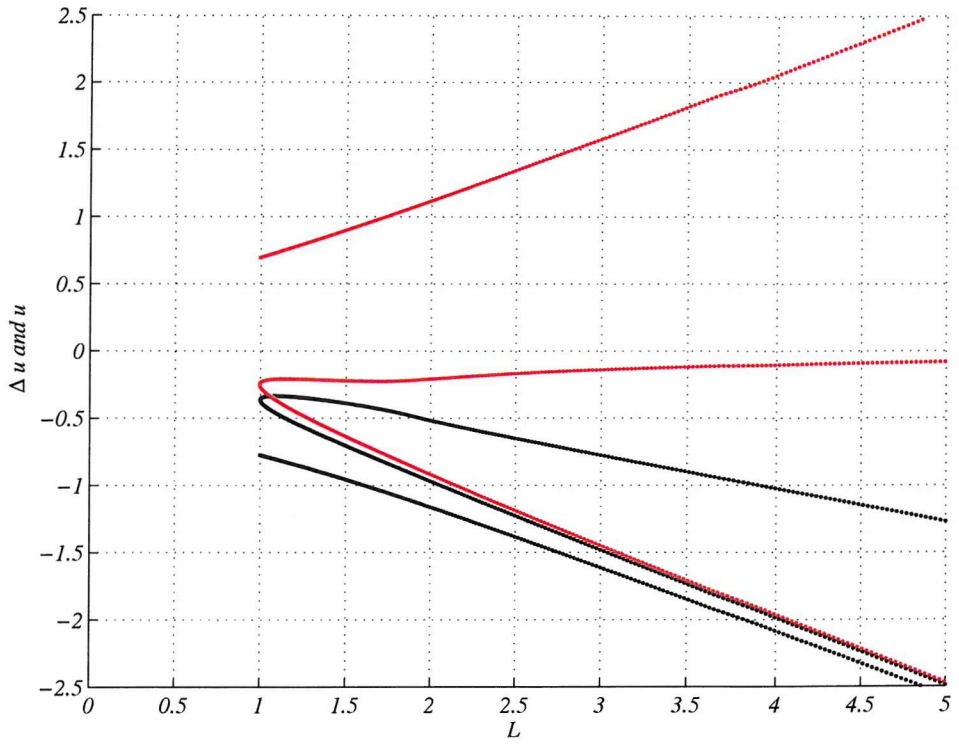

Figure 4.6: Δu and $\bar{u}$ are plotted as a function of width in a flat bottom channel with $\Delta E = -0.7$. At the control $L_0 = D_0 = 1$; the controlled flux is $Q_1 = -0.0536$. The flow is submaximal, as the subcritical and supercritical solution branches upstream never meet, so no second control is possible.

including at the control, while the flow towards the upstream basin is actually confined to the left-hand side of the channel and although it separates from the left-hand wall and turns somewhat right as the channel widens the upstream velocities become fastest at at the centre of the channel.

Non-traceable case

Let us briefly show an example of a flow that encounters a second control and subsequently becomes untraceable.

The functionals of a flow with $\Delta E = -0.9$ and width $L_0 = 0.4$ are plotted in figure 4.8. The control section has a controlled flux of $Q_1 = -0.0054$ and for a small range of L lager than L_0 the minimum of the curve moves down and roots can be found with the subsequent functionals. At $L = 0.65$ however the functional has developed a second minimum which coincides with the controlled flow. So the flow passes through this point, beyond which the the flow becomes untraceable as the absolute value of the minimum decreases for wider channels.

Figure 4.9 illustrates the peculiarity of the second control well. It shows the roots of the functional for each width along the channel, but only those that link directly to the control; the third supercritical upstream branch is not shown. At $L \sim 0.64$ four roots can be seen in the plot (plus one that is not shown), so two new roots have developed due to the second minimum in the functional. Further along the channel these roots disappears

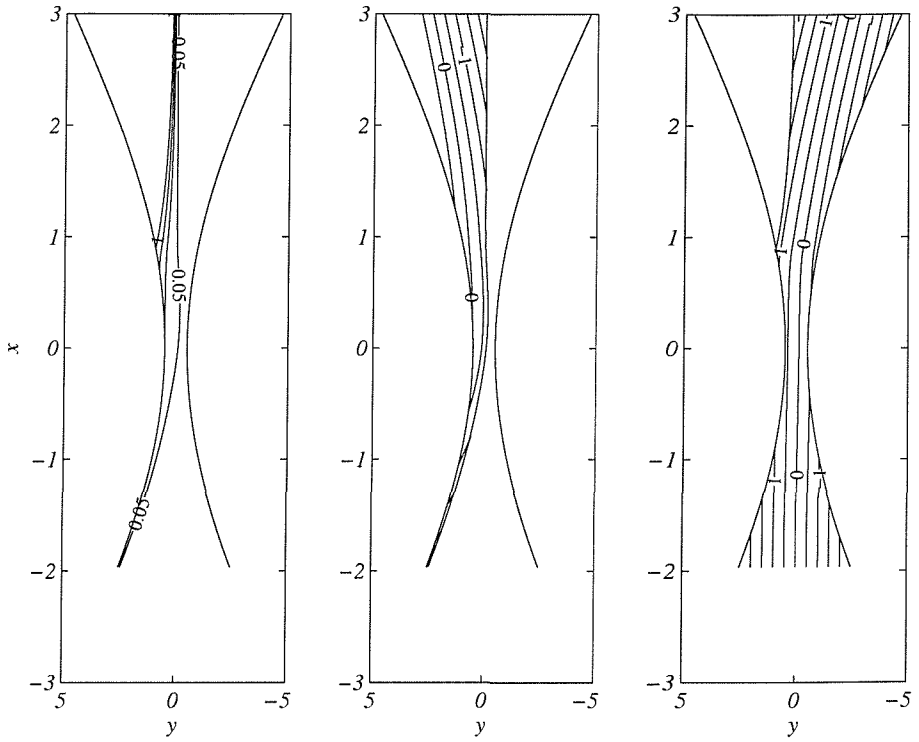

Figure 4.7: The panel on the left shows the contours of interface height above the bottom in a channel with $D_0 = 1$, $L_0 = 1.0$ and $\Delta E = -0.7$. (The line where the interface grounds at the bottom is marked by contour 0.05 for reasons related to the plotting program.) In the panel in the middle the velocity contours of the bottom-layer are shown, along with the line at which the interface grounds along the channel. On the right we have the contours of the top-layer velocity field as well as the line where the interface outcrops at the surface.

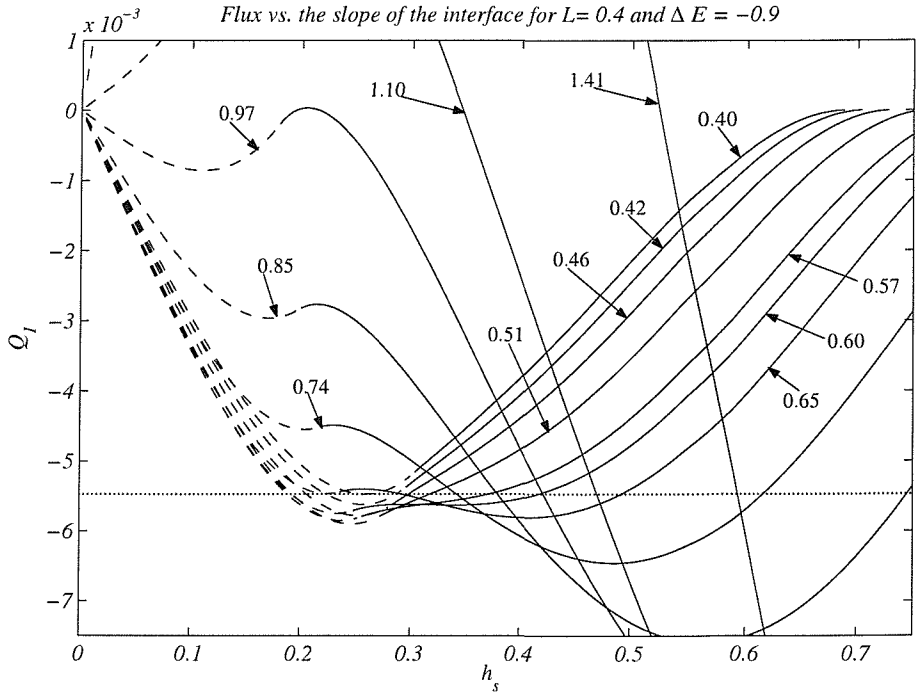

Figure 4.8: Functionals for the flow through a channel of width $L_0 = 0.4$, $D_0 = 1.0$ and $\Delta E = -0.9$. The controlled flux is $Q_1 = -0.0054$, however it is not traceable.

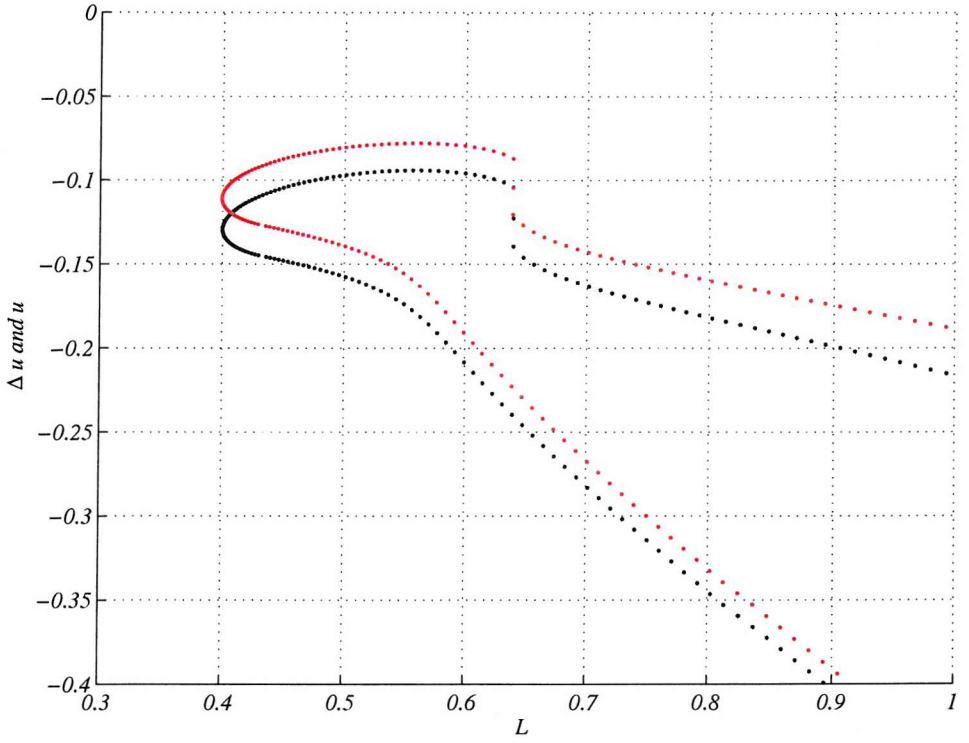

Figure 4.9: Δu (red) and $\bar{u}$ (black) for a flat-bottom channel whose solution is not traceable beyond a second control upstream. Again a second turning point develops around $L \sim 0.64$ and the flow develops a fourth root, the solution linking to the control section ceases to exist, while the new root continues to exist, but does not link smoothly to the control. Here $L_0 = 0.4$, $D = 1$ and $\Delta E = -0.9$. The controlled flow is $Q_1 = -0.00547$.

again and only three are retained, however they do not link smoothly to the control, since they have been offset by the 'disturbance' of the second minimum in the functional. This second control only affects the flow if it is larger than the flow we are trying to trace.

4.3 Flows through a channel with a sill

In the previous section it has been shown that tracing a flow in a flat bottom channel is relatively easy in the sense that almost all flows for any given ΔE and any geometry are traceable.

If the channel is set up to include a sill on the other hand we find that the flow is only traceable for a limited range of ΔE. We have seen an indication of this in the previous chapter when tracing a solution for a channel with simultaneously varying widths and depths, and this fact has also been observed by Farmer and Armi (1986) for the non-rotating case. Finding the maximal flow in a channel with a sill is also more tricky than for a purely width-changing channel.

We will firstly show an example of a submaximal flow, which is easily traceable, and then show how to find a maximal solution in a channel of width $L_0 = 1$. Further we will show untraceable cases in a channel that is purely depth-changing, which can however be

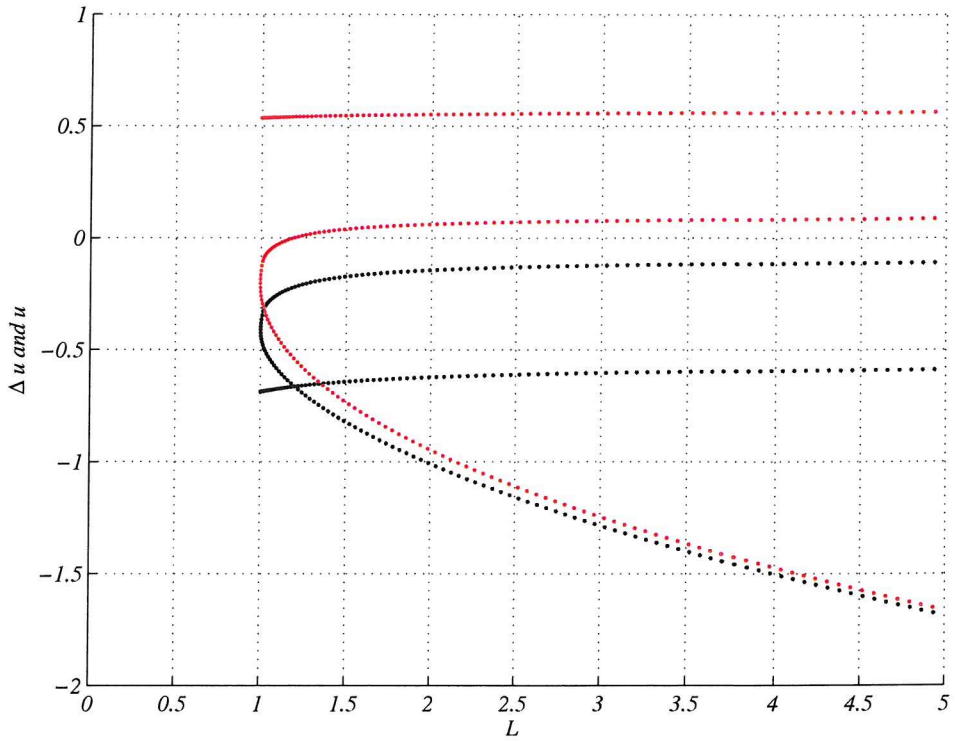

Figure 4.10: Solutions along a channel of constant width and varying depth, where $\Delta E = -0.6$ and $L_0 = D_0 = 1$. The controlled flux is $Q_1 = -0.0946$.

traced if the second control is located at the entrance of the channel.

A submaximal case

The example presented here is that of a channel with constant $L_0 = 1$, $D_0 = 1$ and $\Delta E = -0.6$. The depth away from the sill increases with a sinusoidal shape. Figure 4.10 shows Δu and $\bar{u}$ as a function of depth for this particular flow and indicates that it is traceable both upstream and downstream at least for the range of depths shown here. Velocity fields and interface heights along the channel are plotted in figure 4.11. In the panel of the left the thickness of the bottom layer is contoured. Upstream of the sill at $x = 0$ the interface is almost horizontal and here there is a significant region of back flow in the bottom layer confined to the left-hand side of the channel. This region can be discerned in the middle panel where the bottom layer velocity field is contoured. The stagnation point on the left-hand side of the channel occurs just before the control, and so the back flow in the bottom layer never reaches the sill. Separation of the bottom layer also occurs just before the sill and the overflow becomes the characteristic boundary current.

The velocity field in the top layer, contoured in the right panel, shows back flow along the whole right-hand side of the channel while the fastest flow towards the upstream basin is confined to the left-hand side of the channel. This is not the clear crossing over feature one might expect from rotation, there is only a small turning of the contours to the right as the flow approaches the sill along with an intensification of the velocities on the left

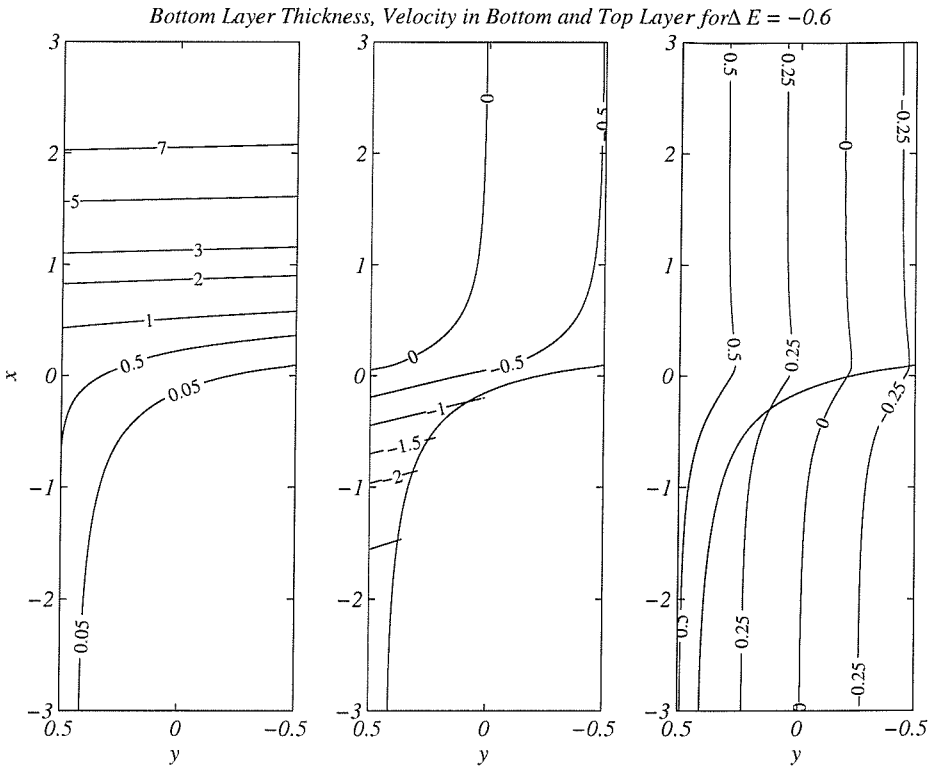

Figure 4.11: Left-hand panel shows contours of the thickness of the bottom layer for a flow with $\Delta E = -0.6$ and $L_0 = D_0 = 1$. and it can be seen that the flow separates from the right-hand side of the channel just before the control. In the middle the velocity field of the bottom layer is contoured and similarly the panel on the right contains the contours of the top layer.

hand side of the channel. These top layer features have never been described in this form in any previous studies and we will see in the numerical studies presented in chapter 6 that some of the feature also remerge in the model.

In figure 4.12 the interface height is shown in three dimensions (coloured surface) above the topography (black). This is essentially a more visual representation of the data in the left panel of figure 4.11.

The line of intersection with the right-hand wall (dash-dotted), the intersection with the left-hand wall (dashed) and the height of the interface at the centre of the channel (dotted) are shown in figure 4.13, and it becomes clear that as the flow approaches the upstream basin the thickness of the top-layer approaches $-\Delta E$, in this case $h_{20} = -\Delta E = 0.6$. This characteristic is unique to channels of constant width and we have discussed its importance in section 3.1.1.

Another example of a submaximal flow is shown in figure 4.14, for which $\Delta E = -0.516$. Here it can be seen that the supercritical branch which in the earlier example still lay quite far from the subcritical upstream branch approaches it and at $D \sim 1.7$ two root almost coincide. The features of this flow will in general be very similar to those we described for the previous example of a submaximal flow.

As we decrease ΔE by only a very small amount, to -0.515 in the same geometric

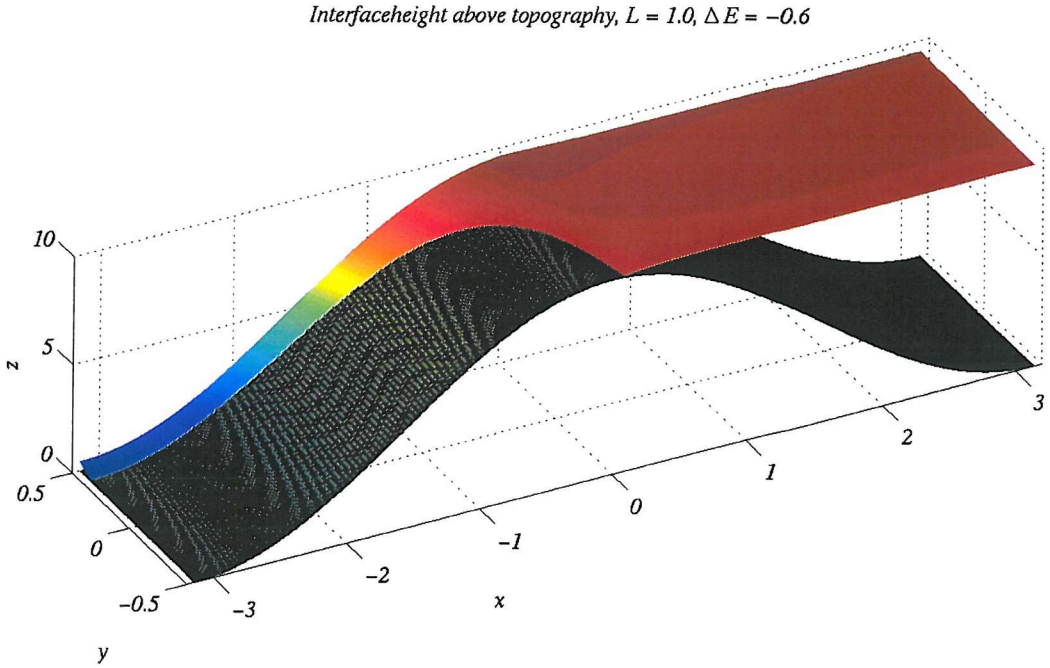

Figure 4.12: Three dimensional plot of the interface (coloured surface) separating top and bottom layer in the channel trace using figure 4.10. The black surface is the topography.

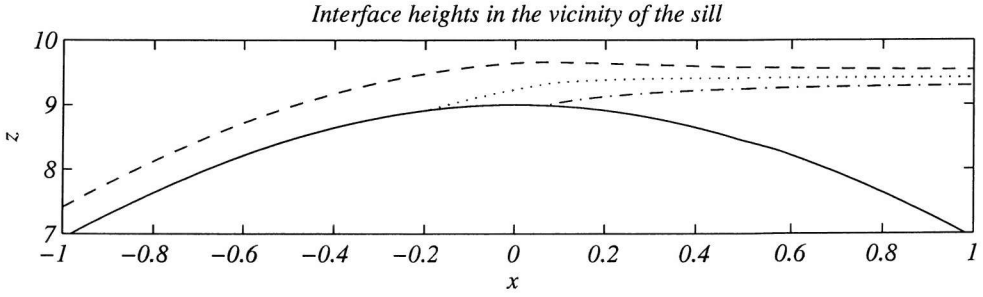

Figure 4.13: Plot of the interface height at the left-hand wall (dashed) the right-hand wall (dash-dotted) and in the centre of the channel (dotted) close to the top of the sill at $x = 0$. The flow is the same as presented in figure 4.10. Notice that as the flow moves towards the upstream basin the slope of the interface decreases steadily towards a value close to zero and the thickness of the top layer approaches $-\Delta E = 0.6$ at the centre of the channel.

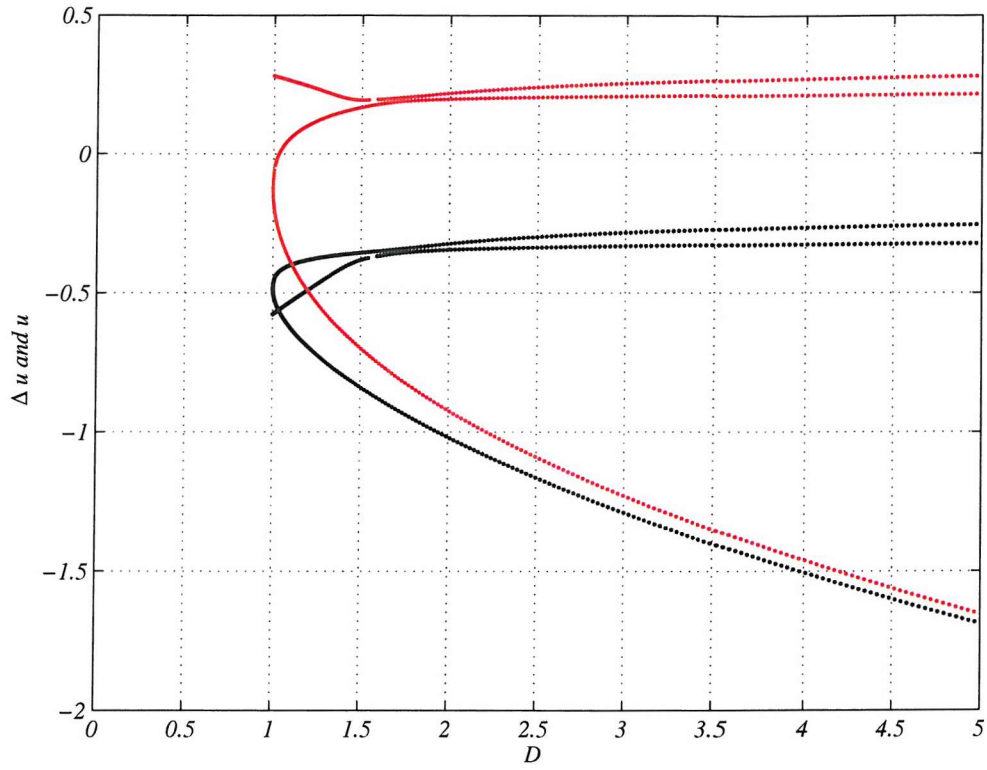

Figure 4.14: Solutions along a channel of constant width and varying depth, where $\Delta E = -0.516$. The flow is submaximal, whoever the supercritical and subcritical solution branch upstream come very close and a second control is almost achieved at $D^{(1)} \sim 1.7$. The controlled flux is $Q_1 = -0.1483$.

setup the flow becomes non-traceable as can be seen from the roots plotted in figure 4.15 for this particular example. For some ΔE between -0.516 and -0.515 there will be two roots coincide exactly at some D and a maximal solution will be achieved. (For reasons related to the resolution of our numerical code, we did not determine the exact position of the second control.) This is another quite novel results, in that it have never been shown before that a channel with a sill can have a virtual control that is not located at the entrance to the channel and become maximal in a channel whose depth continues to increase beyond the control and whose width remains constant.

A non-traceable case

As already mentioned, in figure 4.15 the roots of a flow along a channel with $L_0 = 1.0$, $D_0 = 1$ and $\Delta E = -0.515$ are shown in terms of Δu and $\bar{u}$. It can be seen that the flow is fully traceable in the downstream direction, however upstream two roots coincide at $D \sim 1.343$, form a second control and beyond it the flow ceases to be traceable.

Comparing an untraceable flow in a flat bottom channel, see figure 4.9, with an untraceable flow in a constant width channel, described here, we can see that there are distinct differences in the way the become untraceable. In the flat bottom case a second minimum and hence another controlled flow occurs in functionals for widening channels, as a results two new roots may develop. If the flow passes through this second control

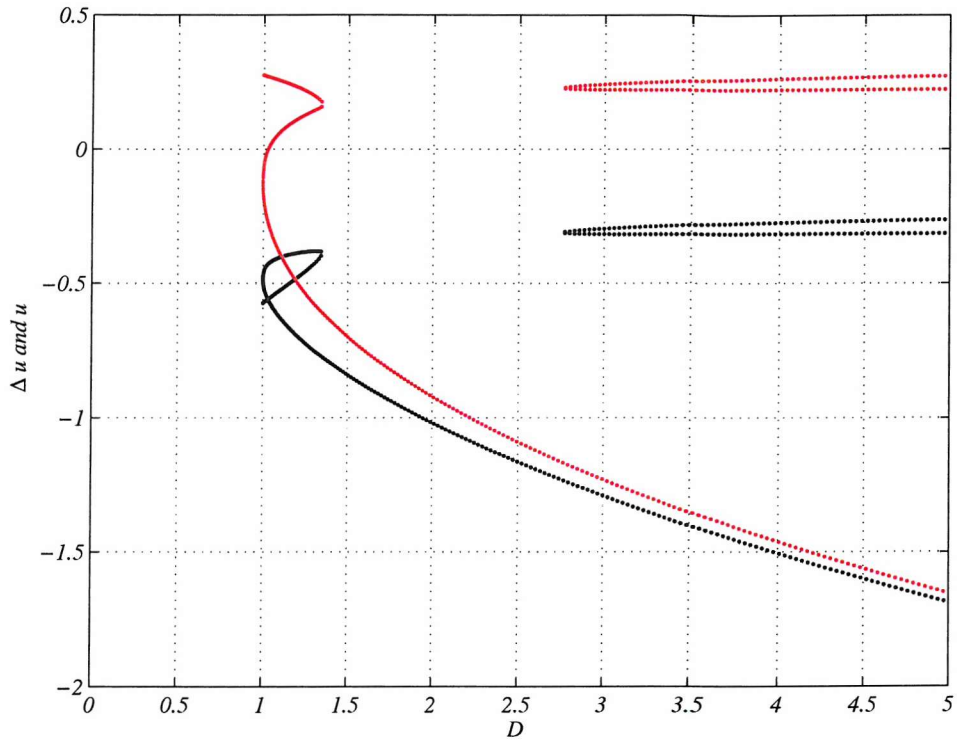

Figure 4.15: Solutions for $\Delta E = -0.515$. Two roots coincide at $D^{(1)} \sim 1.3$ and a second control occurs, beyond which the solutions cease. The controlled flux is $Q_1 = -0.1493$.

it becomes untraceable. In a depth varying channel on the other hand the funcionals only have one minimum and the flow ceases to be traceable when it passes through that minimum a second time. Beyond this point only one root remains, as can be seen in figure 4.15.

As ΔE is decreased further, to -0.510 say, the point at which the second control is encountered by the flow will move closer towards the sill, shown in figure 4.16.

Our analysis of traced flows so far has shown that the minima of the functionals of increasing L increase. This fact suggests that if the channel geometry of a depth varying channel is chosen, such that beyond the second control the depth is kept constant and the width is being increased the flow should be traceable after passing through the second control. In this case the flow is maximal with a virtual control at the entrance of the channel. This is the maximal flow that has been shown to exist previously for channels with a sill by Farmer and Armi (1986) in the non-rotating case and by Dalziel (1988) for the rotating case.

We will show this is indeed the case for both of the non-traceable cases shown here.

A maximal flow

In order to make the first untraceable flow with $\Delta E = -0.515$ traceable, we keep the geometry of the channel constant at $D = 1.343$ once it has encountered the virtual control, while the width is gradually increased. In figure 4.17 the results of Δu are plotted against

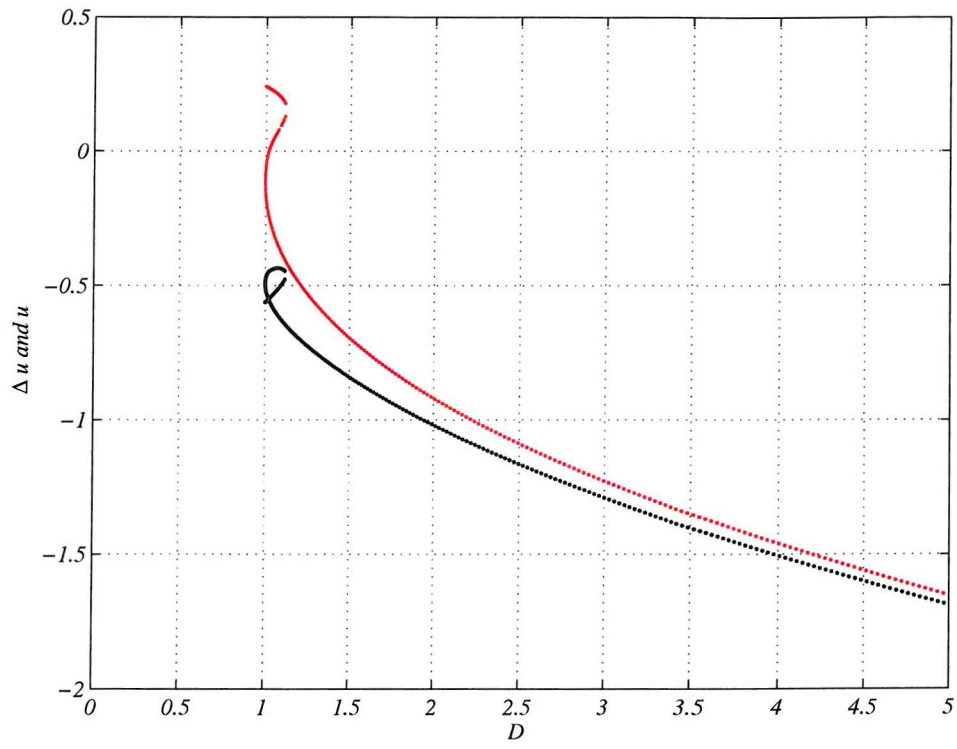

Figure 4.16: Solutions for $\Delta E = -0.510$. As ΔE approaches -0.5 the location of the second control moves closer to the sill. Here its location is at $D^{(1)} \sim 1.2$. The controlled flow is $Q_1 = -0.1542$.

$-\cos(x)$, where x is the distance along the channel. At $-\cos(x) \sim -0.92$ the channel ceases to deepen but starts to widen instead and the subsequent super- and subcritical branches are marked. The maximal flow will follow the supercritical branch after passing through the control. We have only shown the roots in terms of Δu here for the clarity of the plot.

The same principle applies for the second example of a non-traceable flow over a sill with $L_0 = 1$, $D_0 = 1$ and $\Delta E = -0.510$. If beyond the virtual control the depth is kept constant at $D = 1.2$ and the channel is widened the flow becomes traceable again and the roots of the functionals are shown in figure 4.18. Here both Δu and $\bar{u}$ are plotted. Note that there seem to be discontinuities in the solution branches, however these are purely due to a lack of resolution used along the channel.

If we were to decrease ΔE even further the upstream control would continue to approach the top of the sill, and we would eventually arrive at the flat bottom result for $\Delta E = -0.5$.

Notice that in the two examples above we have made the channel symmetric in the sense that both up and downstream the bottom become flat and the width increases, however the downstream basin could have any shape and the flow would still be realised.

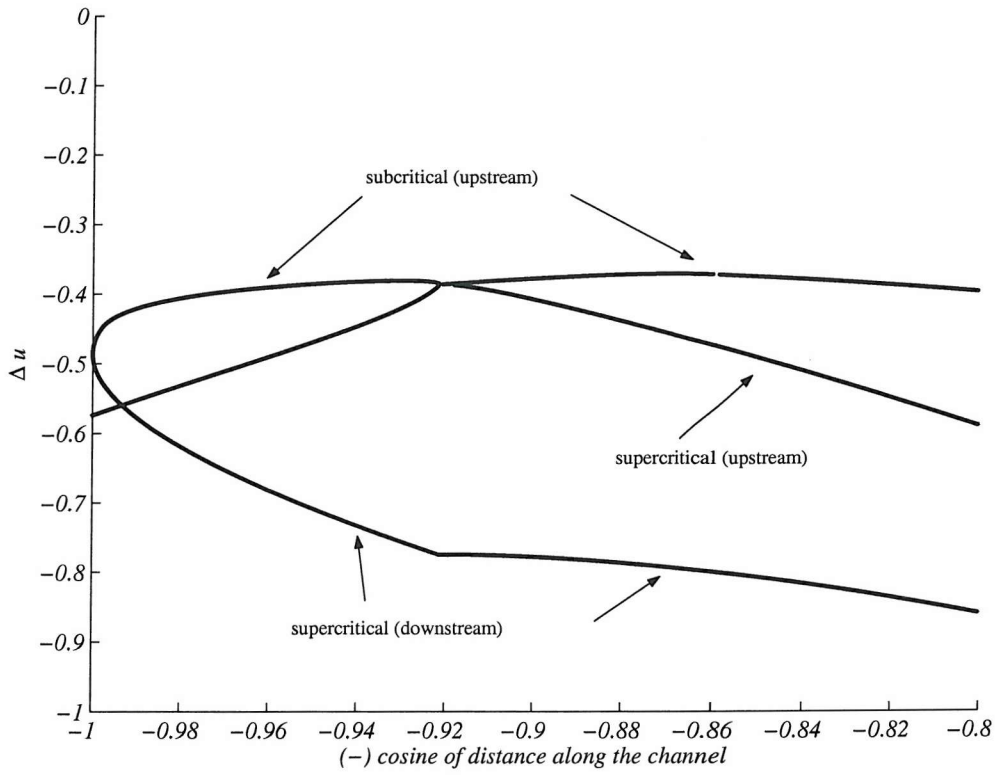

Figure 4.17: Variable Δu describing the flow plotted against -cosine of the distance along the channel, here $\Delta E = -0.515$. These are solutions for a maximal flow along a channel with a sill which becomes a flat bottom channel after the second control. The sub- and supercritical branches are labelled.

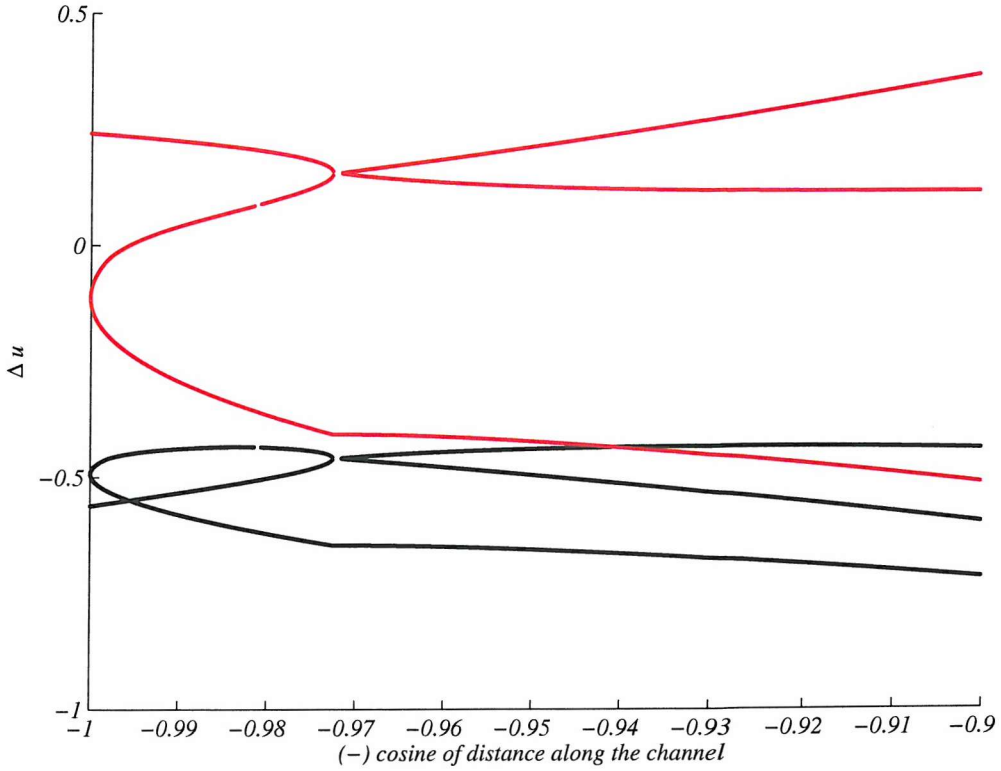

Figure 4.18: Δu and $\bar{u}$ for a flow with $\Delta E = -0.510$; the branches will be equivalent to those in figure 4.17.

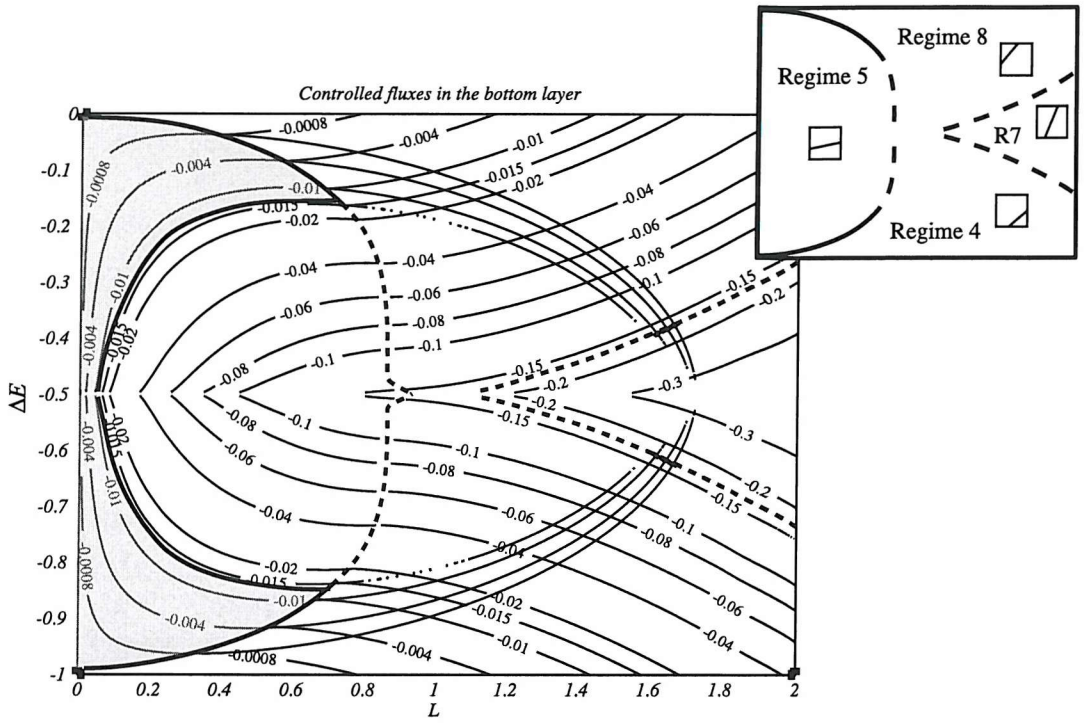

Figure 4.19: Contour plot (thin solid lines) of the flux of the controlled flows over a domain spanning $\Delta E = [-1, 0]$ and $L = (0, 2]$. The thicker solid lines indicate points at which the interface separates from one or both of the walls. The inset plot at the top right indicates which regime the controlled flows are in. Extending from regime 5 there are two small regions with two possible controlled flows (two sets of contours overlap. Those contours that show an increasing flux as L increases are separated, while those that decrease remain fully attached, they do however exhibit a region of recirculation at the control, which is not present in the separated solutions in regime 4. The separated solutions in regime 8 also exhibit substantial recirculation. The grey shaded regions contain controlled flows which encounter a second control and are subsequently not traceable in the upstream direction. (All controlled flows plotted have a positive slope, h_s.)

4.4 Controlled flows and traceability

We have used the conditions for control described in section 4.1.1 to determine the controlled fluxes from the functional Q_1 for a range covering $\Delta E = [-1, 0]$, $L = [0.01, 2.0]$ and slopes $h_s = [-5.0, 5.0]$. Basically, for each curve of Q_1 in terms of h_s the controlled flow solution was determined by finding the minima in the flux curves with positive slopes. The resulting controlled fluxes are contoured in figure 4.19.

The thick continuous lines mark the points of separations from one or both of the walls and the little inset plot at the top right illustrates which regime the controlled flows are in. Beyond the separation point of the fully attached flow two controlled flows are possible for a small region of pairs of ΔE and L - which we alluded to in the previous section. The second controlled flux arises from the fact that the function of flux in terms of h_s develops another turning point.

The main controls to the right of the region containing the fully attached cases are semi-separated. For $\Delta E \in [-1.0, -0.5)$ the separation is from the right-hand wall and the interface grounds across the channel (regime 4), whereas for $\Delta E \in [0, -0.5)$ the interface outcrops at the surface and therefore separates from the left-hand wall (regime 8). The contours of the controlled fluxes for the separated flows in this region increase as the channel becomes wider.

Along the line $\Delta E = -0.5$ no controlled flows exist, as the flux curve is linear in h_s and thus contains no turning points. That is not to say however that these flows are not physically possible. We outlined one such maximal flow which occurs as $\Delta E = -0.5$ in section 4.2 when tracing a the flow along a flat-bottomed channel.

The second controlled flow possible in this region is one that stays attached to both walls and the contours of these flows curve in towards the central line of the diagram ($\Delta E = -0.5$), indicating that as the channel widens the flow decreases. These fully attached solutions develop a region of significant backflow within the cross-sectional flow-field in both layers. Solutions separating and moving into regime 4 never develop any recirculation regions in the bottom layer while those moving into regime 8 do. At this point it may also be worth noting that the top and bottom layers are symmetric in the sense that if the flow we are tracing in the bottom layer has a value of $\Delta E = -0.6$, for example, the flow in the top layer will look like the flow in the bottom layer if ΔE were -0.4. This tells us that although the bottom layer does not develop backflow for any of the controlled solutions, the top layer flow associated with that controlled flow will contain a region of reversed flow.

Various options of how and why to eliminate regions of backflow have been discussed in section 3.1.4. We have opted to retain them to give a more fundamental picture of zero potential vorticity flow which has not been described like this before.

Furthermore in figure 4.19 another two lines of separation occur fanning away from the central line of the plot at $L \sim 1.0$. In the region to the right of these lines lie the fully separated controlled flows.

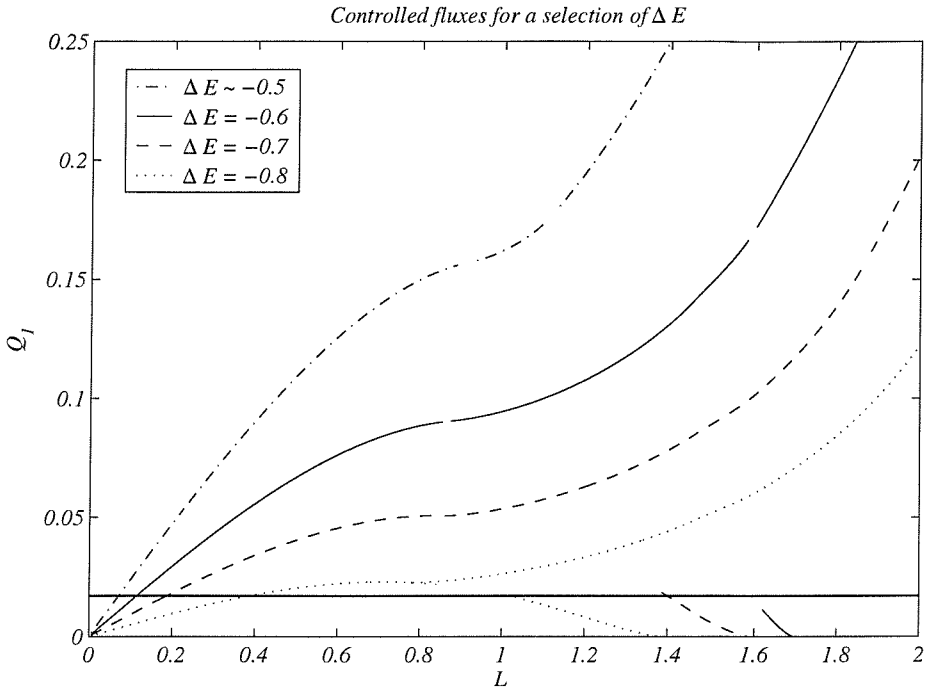

Figure 4.20: An alternative way of presenting the fluxes for four constant values of $\Delta E = [-0.5, -0.6, -0.7$ and $-0.8]$. At $L \sim 0.8$ the flows separate from the right-hand wall, this separation is indicated by the first gap in the curves, and subsequently the fluxes continue increasing. At the second gap the flow becomes completely separated. Below the horizontal line $Q_1 = -0.015$ the flow a second control occurs for some ΔE, which prevent flow with a flux less than 0.015 to be traceable beyond this second control.

In figure 4.20 we show the fluxes for four different values of ΔE as a function of the width of the channel L. It is clear that $\Delta E \sim -0.5$ gives the largest fluxes, and that at $L \sim 0.8$ the fluxes tend to level off. But after separation from the right-hand wall occurs (indicated by the first gap in the curves), the flux increases again. This is analogous to the findings by Dalziel (1988), however he argues that if backflow were to be excluded the flux would level off. (After the second gap in the curves the flow is completely separated.)

4.4.1 Traceability

Figure 4.19 not only gives a comprehensive picture of all the controlled flows possible for a range of variables, it actually also allows us to determine whether a flow is traceable in a channel with a flat bottom, without having to plot the functional for every cross-section. To do so, a point on the contour plot 4.19 is chosen, for example $\Delta E = -0.8$ and $L = 0.3$, where the flux is given to be $Q_1 = -0.014$. To trace a flux upstream and downstream the assumption that ΔE is constant along the channel is used.

If we look along the line of constant ΔE for a slightly wider channel, say $L = 0.4$, it can be seen that the controlled flow is larger, indicating that the minimum of the functional moves down in relation to the minimum of the functional at the previous section, and thus the flow is traceable. At $L \sim 1.05$ the line of constant $\Delta E = -0.8$ passes through

two contours, one with a flux of ~ 0.03 ($\gg 0.014$) and one equal to ~ 0.014, this means that this particular flow passes through a second control upstream beyond which the flow is not traceable anymore since on this solution branch the flux is now decreasing.

For flows with a flux greater than ~ 0.015 no second control arises. Take for example a channel of width $L_0 = 0.6$ and $\Delta E = -0.6$, here $Q_1 \sim -0.08$. As the channel widens the controlled flow increases and this solution exists everywhere up- and downstream of the control section. It too passes through the region where a second control may be possible, but all these flows have $|Q_1| \ll 0.08$ and thus this particular flow does not feel a second control.

Figure 4.20 illustrates the points we have just made in a different way. Here the fluxes for a selection of ΔE are plotted against L. We can observe that the dominant trend of the flux is to increase with increasing L, which means all the flows are traceable. There are a small number of second controls though, which lie generally below the line $Q_1 = -0.015$. Flows with a flux at the primary control which is less than the largest flux of the second control will encounter this control and cease to be traceable beyond it as the flux decreases with L along this solution branch. As ΔE approaches -0.5 the range of flows exhibiting a second control and thus not being traceable becomes smaller.

We can therefore identify regions in plot 4.19, in which the controlled fluxes are either traceable or not. The regions where the flow encounters a second control and no solutions exist beyond this control are shaded grey. For channels of width $L \lesssim 0.8$ there therefore exists a minimal flux of $Q_1 \sim -0.015$, smaller flows are not traceable towards the upstream basin.

For a channel with a sill figure 4.19 is less conclusive in terms of the traceability of the flow. It does tell us the controlled fluxes for a given cross-section but cannot be used in the same way as for a flat bottom channel to determine whether the flow is traceable. We have determined in section 4.3 that for $|\Delta E| > 0.515$, $L_0 = 1.0$ and $D_0 = 1.0$ all flows over a sill are traceable until the exit/entrance of a channel and are submaximal. Any flow with $|\Delta E| \lesssim 0.515$ ceases to be traceable as it encounters a second control, but can be traced if beyond this point the channel ceases to deepen and instead widens into the basin upstream. In this case the second control is located at the entrance to the channel.

For channels of width $L_0 = 0.8$ and 0.6 we have also determined the approximate conditions for maximal flow and these are listed in table 4.1. These data points suggest that as the channel widens the ΔE for which maximal flow occurs decreases as does the depth of the section at which the virtual control is located D_v. So as L decreases the virtual control seems to move further away from the top of the sill. This limit is analogous to the non-rotating limit, i.e. as rotation becomes less important (L decreases) the control would move towards the limit of an infinitely deep channel/basin.

L_0	ΔE	Q_1	D_v
1.0	~ -0.516	~ -0.1483	~ 1.7
0.8	~ -0.51750	~ -0.1356	~ 2.5
0.6	~ -0.52135	~ -0.1120	~ 4.0

Table 4.1: Maximal flows for a range of L_0 are listed, giving the corresponding ΔE, Q_1 and D_v, the depth of the channel at the virtual control.

4.5 Conclusions

We have in this chapter presented a way to trace controlled flows along channels with constant depth and varying width as well as constant width and varying depth using a single functional, which we chose to be the flux in the bottom layer Q_1. Dalziel (1988) refrained from taking the flux as a functional noting that an ambiguity may arise when solving for either u_1 or u_2. We have avoided this problem by choosing different variables: Δu and $\bar{u}$.

There is however another drawback in using the flux as a functional and $h_s = -2\Delta u$ as the unknown, that is that the expressions for the flux will be linear in h_s for $\Delta E = -0.5$ thus making it impossible to derive the controlled flows for $\Delta E = -0.5$. As we have discussed, for flat bottom channels the maximal flow occurs as $\Delta E = -0.5$ and thus for Dalziel's study of maximal exchange flows, which he focused on, using Q_1 would indeed not give any conclusive results.

For this reason we returned to the analysis with two functionals in chapter 3, to describe the maximal flow in a flat bottom channel. However for all submaximal flows and maximal flows in a channel with a sill, using the flux-functional works very well, and we have shown examples for such flows in this chapter.

For submaximal flows in a flat bottom channel we found that some flows with a flux $Q_1 \lesssim -0.015$ are not traceable along the channel and this values presents a minimum flux possible through certain channel geometries. It is not completely clear what the significance of this minimal flux is. If we were to hazard an explanation for this phenomenon then it would be that for certain flows, even though the interface is above channel depth, the pressure in the reservoir is not enough to actually push the fluid through the contraction. As soon as the pressure is enough to cause a through flow the transport will increase from zero to the minimum flux in a transient adjustment and settle to the minimum flow in a steady state. Similarly if the pressure in the upstream basin is gradually reduced, then as soon as the flow falls below the minimum it cannot maintain this flow in steady state and thus the flow ceases completely. Of course this minimal flux could also simply be a quirk of the mathematics that does not have a physically relevant explanation.

The second control that gives rise to the minimal flux over a sill has not previously been described. Although Dalziel (1988) considered essentially the same analytical problem, he excluded reverse flow, which means he would have never been able to solve for any of

these second controls, as they contain a significant amount of back flow in both layers.

We have shown that a maximal flow is possible in a channel that is purely depth varying and the virtual control does not need to be associated with the entrance of the channel. This is certainly true for three channel widths we tested ($L_0 = 0.6$, 0.8 and 1.0). For each of these widths there is a unique $|\Delta E|$ for which the maximal flow occurs and it increases as L decreases. In past studies such as Farmer and Armi (1986) and Dalziel (1988) it has always been argued that the virtual control in a depth varying channel has to be located at the entrance of the channel.

If for the sill channels $|\Delta E|$ becomes less than the maximal case the flow ceases to be traceable along a purely depth varying channel. If however the channel depth is kept constant beyond this point and the width is increased the flow will be traceable further upstream.

By the same method outlined in this chapter for flat bottom channels and channels of constant width, zero potential vorticity flow can be traced along channels of any other topography provided the cross-section is rectangular. We have shown one example of a flow along a channel of simultaneously varying width and depth in chapter 3.

Finally we have produced a comprehensive picture of the controlled fluxes possible through the primary control section of a rectangular channel shown in figure 4.19. For every $L_0 \in [0.01, 2]$ and $\Delta E \in [-1, 0]$ the controlled fluxes can be read of this picture for any topography, however, only for flat bottom channels is it also possible to tell whether the flow is actually traceable or not.

Analogous to Dalziel (1988) the non-dimensional flux increases initially as the channel becomes wider and keeps rising if the backflow is not excluded. Our numerically simulations in the second half of the thesis and the laboratory experiments by Dalziel (1988) clearly do not support this result. This is believed to be a limitation of zero potential vorticity theory, which leads to a linear dependence of the velocities on y and results in large velocities and fluxes for very wide channels. The general perception is that as the channel widens rotation will affect the flux in such a way as to impose an upper limit on the flow regardless of its physical width, which is confirmed in the numerical experiments presented in chapter 6 and the laboratory work by Dalziel (1988). Dalziel (1988) shows that if the backflow is excluded from the analysis then the controlled fluxes should level off and become independent of the width of the channel. This is something we have started to look at, but at this point is beyond the scope of the thesis.

This concludes our analytical study of two-layer rotating exchange flows.

Chapter 5

Numerical simulations of sill flows

In order to complement the analytical work presented in the first two chapters our goal was to carry out a modelling study of pure two-layer exchange flows in a widely used ocean model with an idealised set up, in order to see how well the flow structures and transport results from the model compare with the theory and to identify important features that the analytical solutions are missing.

To do so we used the well established ocean circulation model MICOM, the Miami Isopycnic Co-ordinate Ocean Model. As before we shall concentrate on the effects of rotation on the exchange flows. The motivation, which was also discussed in the introduction, is mainly the limited scope of representing these types of flows in coarse resolution global ocean and climate models and the subsequent need for parameterising them in such models. Ideally a parameterisation is desirable that will allow the flow though straits and over sills to be expressed in terms of topographic variables, such as width and depth of the channel, in terms of flow-specific parameters, such as the reduced gravity and the upstream interface height, and in terms of external parameters, such as the Coriolis parameter. We will work towards such a parameterisation in this and the following chapter for an idealised two-layer flow scenario through a rectangular channel.

In the first section of this chapter we will briefly outline the features of the model used. Then a few test runs will be described with which we investigated the effects of resolution and different domain set ups on the model results.

In order to test the ability of the model to reproduce results from a case the theory of which is well understood, a few runs are carried out with no rotation and compared with the theoretical work of Armi and Farmer (Armi, 1986; Armi and Farmer, 1986; Farmer and Armi, 1986). These will be outlined in section 5.2.

5.1 The model - MICOM

MICOM is an isopycnic co-ordinate model, in which the ocean is viewed as a stack of immiscible layers, each characterised by a constant value of density. It is governed by dynamic equations resembling the shallow-water equations, and the layers interact through hydrostatically transmitted pressure forces.

There are several reasons for choosing this type of model rather than a model with the conventional vertical z-coordinate representation. Firstly it is less restrictive on the bottom topography which can be used. Isopycnic models in general provide a piecewise linear representation of the ocean topography which can be specified simply by defining a pressure at the bottom of the lowest layer in each grid box, thus smoothly prescribing the bottom boundary of the domain. A model using z as the vertical co-ordinate and in which vertical levels represent the topography does not allow the same flexibility unless one uses the 'partial cell' representation of the topography as described by Griffies et al. (2000) and originally developed by Adcroft et al. (1997).

Another advantage of an isopycnic model is the low vertical resolution needed for the proposed experiments. To effectively resolve two-layer flows two points in the vertical suffice. In a z-coordinate model two grid points in the vertical would not be enough to resolve the overflow. A positive side-effect of the low vertical resolution needed is that it allows us to employ a higher horizontal resolutions to fully resolve the mesoscale features of the flow.

Griffies et al. (2000) outline comprehensively the differences between the z-coordinate models and isopycnic models and note that overflows are naturally represented in ρ-coordinates. In addition detailed information about MICOM can be found in various papers by the authors of the model such as Bleck and Boudra (1986), Bleck and Smith (1990) and references therein, as well as in the MICOM user manuals available at http://www.acl.lanl.gov/CHAMMP/micom/docs.html.

We use version MICOM 2.7 for this study and to model the exchange flows in an idealised configuration, we exclude features and processes such as diapycnal mixing, the mixed layer, wind or thermal forcing and convection. Certain aspects however, in particular diapycnal mixing, are known to have significant effects on the flow across the sills and especially the downslope gravity currents the overflows give rise to, and this topic has attracted a lot of attention by other researchers. It is however a different aspect of exchange flows the study of which is not the aim of this thesis.

MICOM is a primitive equation model solving the following, layer-integrated nonlinear momentum equation:

$$\frac{\partial \mathbf{v}}{\partial t} + \nabla\left(\frac{\mathbf{v}^2}{2}\right) + (\zeta + f)\mathbf{k} \times \mathbf{v} = -\nabla M + \frac{1}{\Delta p}[g\Delta\tau_{\mathbf{x},\mathbf{y}} + \nabla \cdot (\nu \Delta p \nabla \mathbf{v})]. \tag{5.1}$$

This is formulated in x, y, α coordinates, where $\alpha = \frac{1}{\rho}$ is the specific volume, and the variables are defined as follows: u and v are the horizontal velocity components of the velocity vector $\mathbf{v}$, $\zeta = (\partial v/\partial x)_\alpha - (\partial u/\partial y)_\alpha$ is the relative vorticity, $M \equiv gz + p\alpha$ is the Bernoulli function or Montgomery potential, Δp is the pressure thickness of the isopycnic layer, (τ_x, τ_y) are the bottom drag-related stresses, in the x and y direction and ν is an eddy viscosity coefficient. There is no vertical friction in the model, this means the interaction between the two layers is frictionless, and the bottom drag acts like a

Parameter	Value	Dimensions	Description
g	980.6	$\frac{cm}{s^2}$	graviational constant
λ	0.2	-	Smagorinsky constant
C_D	0.003	-	Drag coefficient
u_d	1.0	$\frac{cm}{s}$	diffusive velocity for momentum dissipation
$\bar{c}$	10	$\frac{cm}{s}$	residual bottom layer velocity
s_L	1	-	variable setting the boundary conditions to *slip*

Table 5.1: List of numerical parameters used in MICOM.

horizontal friction on the layers occupying the bottom 10 m of the water column, which is just the bottom layer in most of our experiments.

The nonlinear continuity equation, in terms of the density coordinate, is given by

$$\frac{\partial}{\partial t}\left(\frac{\partial p}{\partial \alpha}\right)+\frac{\partial}{\partial x}\left(u\frac{\partial p}{\partial \alpha}\right)+\frac{\partial}{\partial y}\left(v\frac{\partial p}{\partial \alpha}\right)=0. \tag{5.2}$$

In MICOM dissipation of momentum near the bottom (bottom stress/friction) is modelled by the standard bulk method as

$$(\tau_x,\tau_y)=-C_D\bar{\mathbf{v}}(|\bar{\mathbf{v}}|+\bar{c})=-C_D\bar{\mathbf{v}}\left(\sqrt{\bar{u}^2+\bar{v}^2}+\bar{c}\right), \tag{5.3}$$

where $\bar{\mathbf{v}}=(\bar{u},\bar{v})$ is the average horizontal velocity of all layers in the bottom boundary layer (10 m), and a residual velocity $\bar{c}$ is introduced in case the velocities become very small.

The turbulent viscosity in the model is defined by

$$\nu=\max\{u_d\Delta x,\lambda\left[\left(\frac{\partial u}{\partial x}-\frac{\partial v}{\partial y}\right)^2+\left(\frac{\partial v}{\partial x}-\frac{\partial u}{\partial y}\right)^2\right]^{1/2}\Delta x^2\}, \tag{5.4}$$

where λ is a dimensionless scaling parameter sometimes referred to as the Smagorinsky constant since this viscosity scheme was developed by Smagorinsky (1963). This biharmonic friction scheme often used in large-scale eddy-permitting ocean models is described in more detail by Griffies and Hallberg (2000).

Parameters such as the viscosity are essential for the numerical stability of the model, however they are in part also a physical parameterisation of the influence of unresolved (sub-grid) spatial scales on resolved scales. Ideally we would like the flow to be inviscid and not be influenced by friction or viscosity, just like an ideal fluid, in order to match the assumption in the theory as closely as possible, however for numerical stability this is not possible.

We carried out a series of four experiments using the non-rotating setup described in section 5.2, in which we gradually lowered the bottom-drag to $C_D = 0.003, 0.002, 0.001$ and 0.0. At $C_D = 0.002$ an increase in flux of about 5% was observed compared to the flux at $C_D = 0.003$, while the flow remained stable with flux fluctuations $< 0.1Sv$. When decreasing C_D further to 0.001, the flux increase was 8% compared to the flux at

$C_D = 0.003$, but fluctuations of $> 0.5Sv$ started to occur. Finally setting $C_D = 0.0$ in a final test-run resulted in oscillations of $> 1.0Sv$ in the bottom layer and even more unstable flux in the top-layer with fluctuations of up to $3Sv$. It was decided to keep the bottom-drag at the value most commonly used in ocean models, $C_D = 0.003$, especially since the change in flux was small compared to the loss in stability of the flow.

The lowest value of the viscosity which results from equation (5.4) is $\nu \sim 3.5 \times 10^5$ cm^2/s for the gridsize of $\Delta x \sim 3.5$ km, which we use for the rotating experiments discussed in the next chapter. A typical velocity at the top of the sill can be taken to be about $U = 100$ cm/s and a typical Rossby radius is $a = 22$ km, which is about 0.4 times the channel width. So a typical estimate of the Reynolds number at the top of the sill is $Re = \frac{Ua}{\nu} \sim 630$. In regions where the velocity gradients are larger the viscosity maybe up to 5 times that value, but in such regions the velocities will also be larger, balancing the effects of viscocity. In general the Reynolds number will lie between 100 and 1000 which are typical values for the highly turbulent flows in the ocean. We can therefore say that the inviscid effects dominate the flow.

Both viscosity and bottom drag will act to take energy out of the system and thus decrease the transport, so we to expect flows that have smaller fluxes than predicted by the theory. In addition MICOM, in the way we have set it up, uses non-zero potential vorticity and it has been proven using hydraulic theory that flows with non-zero potential vorticity fields tend to have smaller fluxes than those for zero potential vorticity (see Dalziel (1988)). This will be another source of discrepancy between the MICOM results and the analytical solutions.

The boundary condition at the side walls is set to free-slip allowing tangential velocities at the channel and basin walls to be non-zero. See table 5.1 for a list of the parameters as they are set in the model.

5.1.1 Model domain

Since the study is intended to be an idealised process study, we adopt an idealised domain, consisting of two large rectangular box oceans separated by a rectangular channel with a sinusoidal sill at the centre. A sketch of the topography is shown in figure 5.1.

The channel is aligned in the east-west direction, with the upstream basin (the dense reservoir) in the east and the downstream basin (the light reservoir) in the west. This setup was chosen to be analogous to the Strait of Gibraltar, where the source of the overflow water lies east of the strait in the Mediterranean Sea, while the North Atlantic, west of the strait, is the downstream basin. For all experiments the Coriolis parameter is kept constant over the entire domain, meaning that it does not vary with latitude and we only look at the flow on an f-plane. We argue that the possible variation in f in the regions of interest such as the channel are negligible considering that the horizontal scales are never more than 50 - 100 km in the channel.

The projection used in the model is the conventional Mercator projection with the

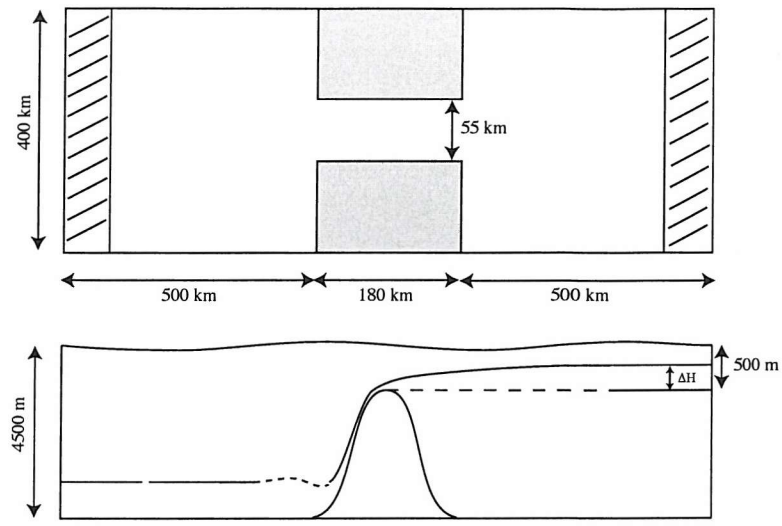

Figure 5.1: Sketch of the model domain. In the top panel a planar view of the two basins and the channel separating them is shown. The dashed areas are the sponge zones at the far ends of the basins. The bottom panel shows a side view of the flat bottom basins and the sinusoidal sill at the centre of the channel. The interface is indicated by a solid line starting close to the surface in the dense eastern reservoir (right) and overflowing to a lower level in the predominantly light western reservoir (left). The dimensions given in the sketch are only approximate and change somewhat for different experiments. ΔH is the interface height above the sill in the up-stream basin. The model has a free surface.

i-direction pointing south, and j east. The basins are approximately 400 km wide and 500 km long and separated by a 180 km long channel which is roughly 55 km wide. The minimum depth of the sill was set to 500 m or 900 m depending on the experiment and located exactly at the centre of the channel. Both basins are kept at the same depth of 4500 m or 3000 m for most experiments.

As a reminder, we will as in the theory refer to the light reservoir as the downstream basin and to the dense reservoir as the upstream basin. The *right-hand wall* will be the wall that lies to the right of the net direction of the top layer flow, hence the southern wall of the channel, while the northern wall will be referred to as the *left-hand wall* regardless of whether we are talking about the top or bottom layer.

5.1.2 Relaxation

Just as in the theory we are interested in reproducing flows through the channel which remain constant over long periods of time. To this end the lower layer requires a continuous source of water in the upstream basin and a sink in the downstream basin, and vice versa in the upper layer. We have opted to relax the interface between the two layers to a fixed value at the western and eastern walls of the two basins to achieve a constant throughflow. Of course this does not necessarily mean that the flow is actually steady on small time scales. We will see in the next chapter that there are a variety of oscillatory features on time scales of a few days which have direct effects on the overflows, we shall therefore refer to the flows as pseudo-steady.

The process of relaxation involves the interface between the two layers being pushed

Degree resolution	i	j	nrelax	baclin	batrop	Δx (km)	Flux (Sv)
0.1	40	120	10	300	10	9.2	6.769
0.05	81	241	20	150	5	5.3	7.0519
0.04	101	301	25	120	4	3.4	7.3418
0.025	161	481	40	75	2.5	2.3	7.2715

Table 5.2: Details of the setup of the resolution test runs. Listed are the resolution in degrees, the number of boxes in the i and j-directions, the number of gridboxes relaxed along the far walls in both basins (nrelax), the baroclinic timestep (baclin) and the barotropic timestep (batrop) in seconds, and the resulting flux at the top of the sill.

towards a fixed target value over a specified number of gridboxes, while in the remainder of the domain the interface is left unaltered from its natural solution state. In both basins we choose the relaxation to act on one fifth of the number of gridboxes constituting the length of the basins. A target value was specified for both basins and the timescale of relaxation was chosen to be one day so that it is comparable with the timescale for the propagation of Kelvin waves across the basin.

Another important role of the relaxation mechanism is to dampen out waves that might travel around the basin and return into the channel to influence the flow there. Ideally we would like to have two infinitely large basins on either side of the channel so that waves travelling out of the channel and into the basins move off to infinity and never return to influence the flow in the channel, this is emulated by the presence of the 'sponge' zone at either end of the basins, as marked in figure 5.1.

The following equation describes the process of relaxation:

$$\frac{\partial p}{\partial t} = \frac{\beta}{\tau}(p_T - p_o) \tag{5.5}$$

where β describes the strength of the relaxation, decreasing linearly from 1 to 0 away from the walls, p_T denotes the target height in pressure units, p_o the old interface height resulting from the model and τ the timescale of relaxation.

Next we will discuss several test runs carried out to determine the best resolution for the proposed experiments.

5.1.3 Resolution

Three different resolutions: 0.1, 0.05 and 0.025 degrees, were tested to find an optimum compromise between the resolution of small scale features of the flow and computational feasibility of the simulations. A list of the details of the setup of the different resolutions is given in table 5.2 including the resolution finally chosen as the most efficient: 0.04 degrees.

For all the tests the basins were 1500 m deep and the channel at its shallowest point was 900 m. The density of the bottom and top layer were chosen as 26.0 and 25.0 in sigma units respectively. In MICOM the reduced gravity is defined as follows: $g' = \frac{\Delta\rho}{\rho_0}g$, where

$\rho_0 = 1000$, hence in this case it is equal to $9.806 \times 10^{-3}\ m/s^2$. The Coriolis parameter was set to $8.531 \times 10^{-5}\ s^{-1}$ as it is at the latitude of Gibraltar. The target value for the downstream relaxation was set to $\Delta H_D = 500$ m, below sill depth, and upstream to $\Delta H = 500$ m above sill depth.

Lowest Resolution

At the lowest resolution of 0.1 degrees the domain was represented by a 40×120 grid with the channel extending from 17 to 22 in the i-direction and from 50 to 70 in the j-direction. In this setup the experiment was run for 400 days.

The top panel in figure 5.2 shows the flux in the top and bottom layer, indicated by dashed and solid lines respectively, over those 400 days. After about 70 days the flow has adjusted and settles to a uniform flow with an average flux over day 100 to 400 of 6.769 Sv.

In figure 5.3(B) the velocities in the in the top and bottom layers are presented in the right and left-hand panel respectively, the arrows indicate the direction of the flow and the contours the magnitude of the speed[1]. The bottom layer exhibits the characteristic crossing over at the top of the sill which we expect in rotating flows and subsequently flows as a boundary current along the left-hand wall into the downstream basin. The top layer on the other hand only shows a relatively weak crossing over at the exit of the channel and it then forms a boundary current along the left-hand side of the channel with a mild re-circulation upstream.

In figure 5.3(A) the thickness of the bottom layer is contoured on the left and the concentration of the flow as a boundary current on the left-hand side of the channel is clear. In the surface plot on the right a dip in the interface is noticeable at $y \sim -70$, which is indicative of an hydraulic jump, of which we shall see clearer evidence at higher resolutions. To the right of the boundary current the bottom layer is less dynamically active and the interface is almost flat, however it never vanishes as we might expect in rotating flows of this kind. The minimum thickness never falls much below 50 m.

Medium Resolution

The medium resolution tested was 0.05 degrees and the domain consisted of 81×241 gridboxes, with the channel extending from 34 to 44 in the i-direction and from 100 to 140 in the j-direction. At this gridsize the length of the channel was 212 km along the centre line and the basins were 532 km long and 426 km wide, the width of the channel was 53 km. Again the model was run for 400 days and the resulting fluxes in the top and bottom layer are shown in the middle panel of figure 5.2 as a function of time. The flux seems to adjust to a more or less steady state after 50 days, however at day 230 there is a small step in the function increasing it slightly. The averaged flow over day 100 to 400

[1]The upstream basin lies at the top end of the plots, at the positive end of the y-axis, and the downstream basin at the negative end.

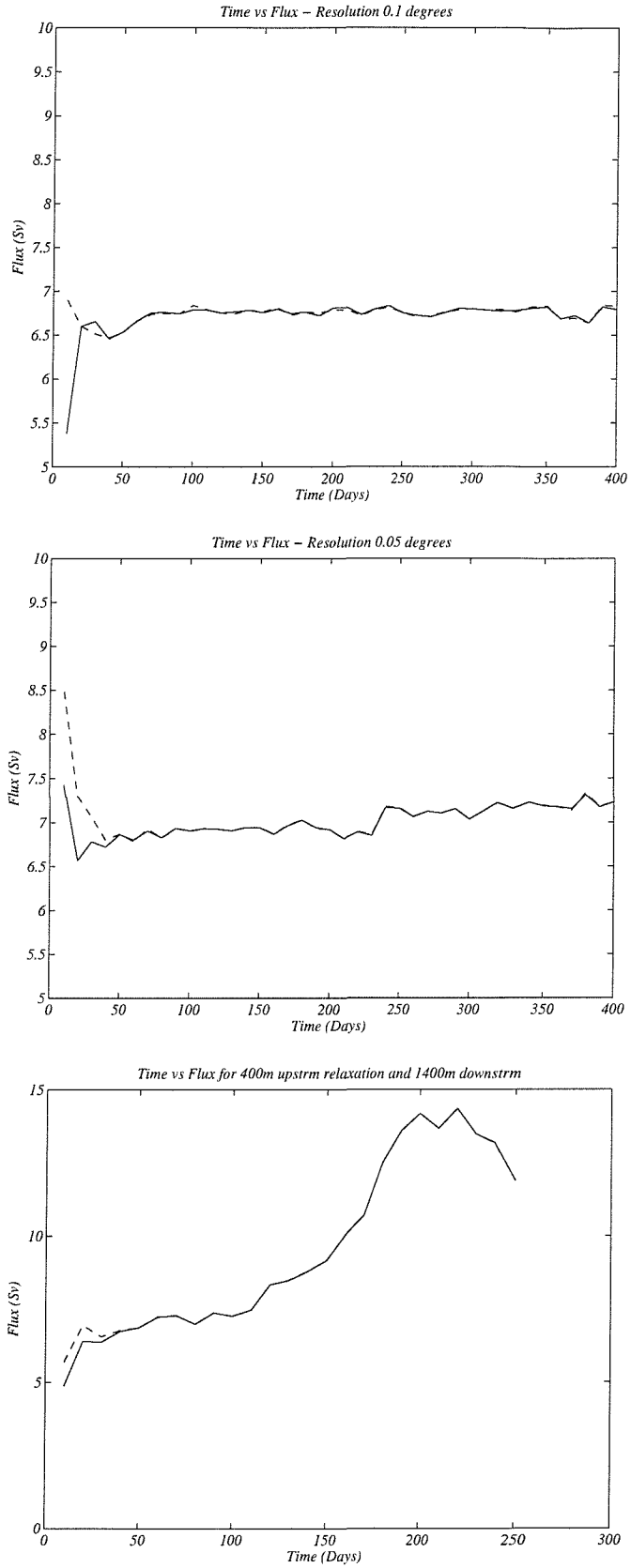

Figure 5.2: Flux as a function of time for a 0.1 (top), 0.05 (middle) and 0.025 (bottom) degree resolution. The dashed line is the flow in the top-layer and the solid line the flow in the bottom layer. The typical fluxes for these experiments are listed in table 5.2.

(A)

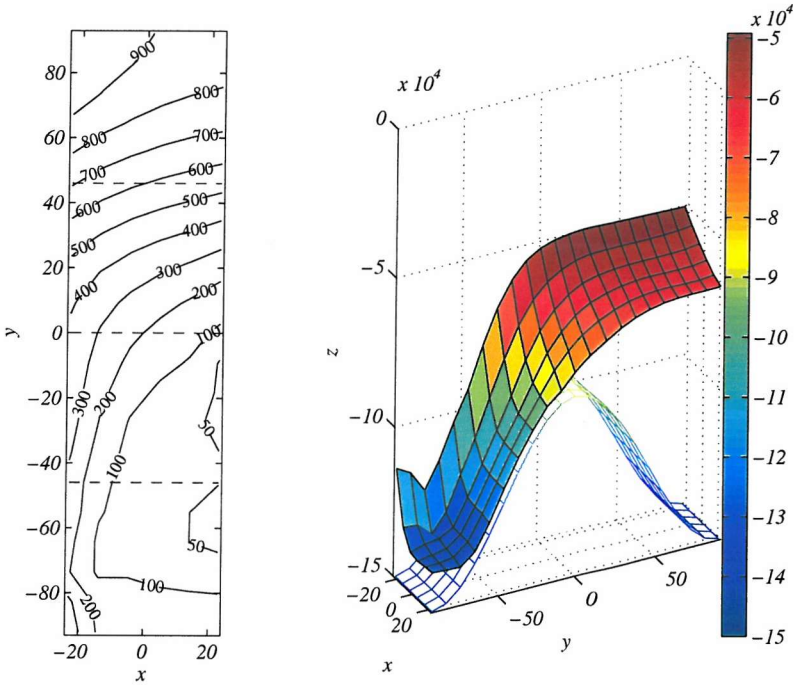

(B)

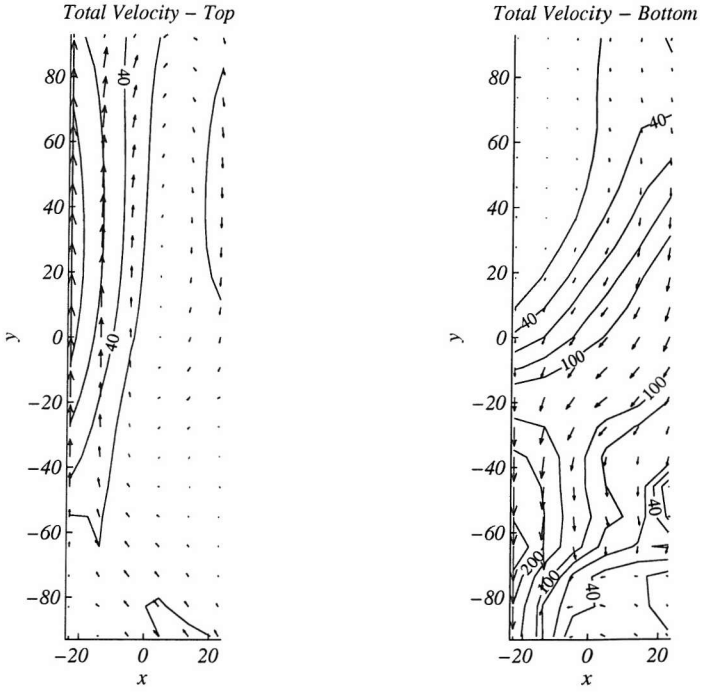

Figure 5.3: **(A)** *Left:* The thickness of the bottom layer is contoured for the lowest resolution of 0.1 degree (D_0 = 900 m, ΔH = 500 m, ΔH_d = 500 m and g' = 9.8060 × 10^{-3} m/s^2, f = 8.5319 × 10^{-4} s^{-1}, W = 55.416 km). The dashed lines indicate the top of the sill at $y = 0$ and the point at which the channel is half its height from the bottom. *Right:* The interface and sill in the channel are plotted as meshed surfaces. The x and y axis are scaled in kilometres, while values in the vertical are in centimetres and $z = 0$ is at the surface. **(B)** The total velocity in the top-layer and bottom-layer are shown on the left and right respectively. The arrows indicate the direction of the flow, and the contours the magnitude. Note that the size of the arrows does not indicate the strength of the currents.

is 7.0519 Sv, which is slightly higher than in the earlier resolution due to the step-like increase at day 230.

The main changes before and after the step seem to occur in the top layer. Crossing over in the top layer initially occurs at the exit of the channel as it does in the lowest resolution and as time progresses moves towards the sill, at about day 230 it reaches the sill and remains there. Examples of the flow patterns in the top and bottom layers at day 300 are shown in figure 5.4(B) and the bottom layer thickness is shown in the left panel of figure 5.4(A) along with a surface plot of the interface over the topography on the right. Velocities are generally much stronger in the bottom layer than in the top layer and both layers feature a re-circulating gyre downstream of the sill, and boundary currents on the left-hand side of the channel.

Both flow configurations, before and after the step change in the flux, are physically relevant for the flow in the channel, and as we will later see crossing over in the top layer is not necessarily located close to the sill.

In light of the fact that a fully steady flow is not achievable, we will work with flows which are pseudo-steady over the period of the run, meaning that the flow roughly oscillates around a fixed mean value while maintaining the critical flow setup with a difference in layer thickness on either side of the sill.

The overall features for this and the previous resolution are similar and upstream the layer thickness in each experiment exhibits little difference. The main differences occur in the downstream part of the channel in both top and bottom layer. In contrast to the previous resolution the bottom layer becomes very thin and a region of separated flow appears to the left of the boundary current as can be seen in figure 5.4.

Where the boundary current meets the water in the downstream reservoir, a sharp rise in the interface height occurs at the edge of the weakly recirculating gyre. In figure 5.5 the angle, α at which the current meets the reservoir is marked, in this particular case $\alpha = 45^o$ which agrees precisely with the angle of the hydraulic jump measured by Pratt (1987) during some single-layer laboratory experiments, which were strongly rotationally influenced (with a channel width of more than 3 Rossby radii).

Highest resolution

The highest resolution tested was 0.025 degrees, for which we again doubled the number of gridboxes used in both the N-S direction and the W-E direction, giving a domain of 161×481 gridboxes. The channel was situated between $i = 70 - 90$ and $j = 200 - 280$ resulting in a basin width of 369 km and a length of 461 km at the centre, the channel was 55.3 km wide and 184 km long.

Every time the resolution is increased (the gridbox size halved), the timestep also has to be halved in line with the CFL criterion: $\Delta t < \Delta x/|\mathbf{v}|$. Both the increased number of gridboxes and the smaller timestep act to significantly increase the time the model needs to run. Therefore this model was initially run for only 250 days and the resulting flux over

(A)

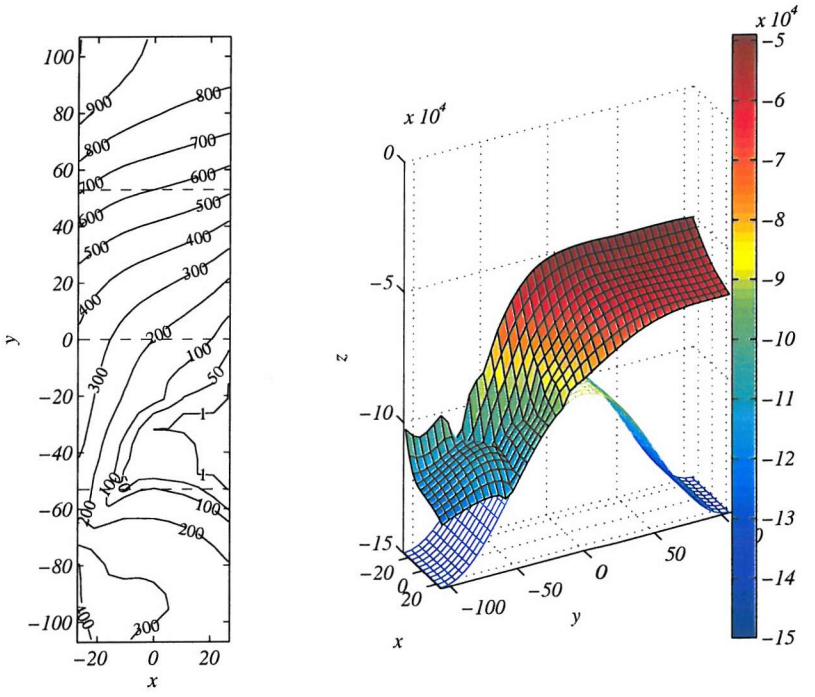

(B)

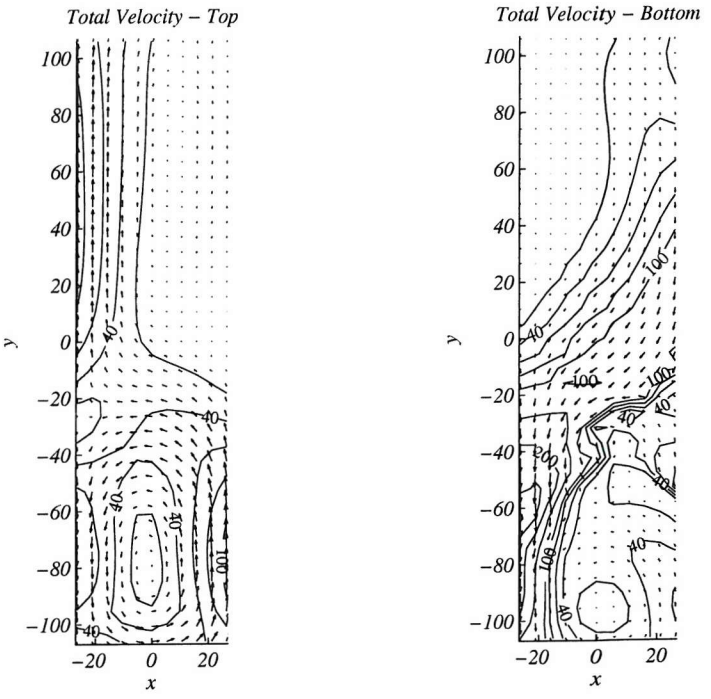

Figure 5.4: Resolution in these plots is 0.05 degrees, all other parameters are as in figure 5.3. **(A)** Contours of the bottom-layer thickness (left) and meshed surface plot of the interface and topography (right). **(B)** Total velocities in the top-layer (left panel) and the bottom-layer (right panel) at day 300.

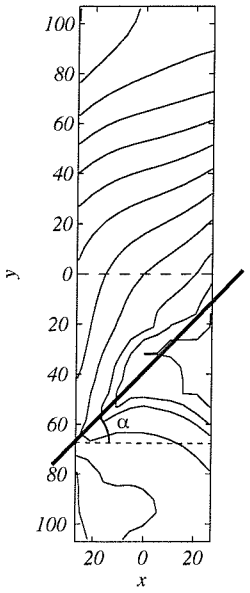

Figure 5.5: The location of the hydraulic jump is marked for the medium resolution experiment. The angle $\alpha = 45^o$ agrees with findings by Pratt (1987) for strongly rotating single layer flows.

the top of the sill is plotted in the bottom panel of figure 5.2. Notice that the flow never seems to settle in a steady state. For the first 100 days it is roughly what we would have expected it to be from the lower resolution experiments, with a flux at day 70 of 7.2715 Sv, but it subsequently increases until at day 200 it has reached a flux that is about twice the flux expected from the lower resolution experiments in the critically controlled state. Contour plots of the velocity at day 100 and 200 in figures 5.6 and 5.7 respectively exhibit marked differences.

The flow on day 100 is comparable in its structure and strength to that of the previous two resolutions. In the bottom layer the current upstream is relatively weak and strongest on the right-hand wall of the channel, on reaching the sill the velocities increase and the flow crosses over to the left-hand side of the channel. Downstream it forms a marked boundary current to the left of a separated region and a mildly re-circulating region. The top layer exhibits a large gyre in the downstream half of the channel, crossing over occurs just downstream of the top of the sill and a boundary current on the left-hand side of the channel flows towards the upstream basin.

At day 200 the velocities in the bottom layer have markedly intensified as can be seen in figure 5.7(B), although the overall structure of the flow including the crossing over and the boundary current are preserved. In the top layer however the usual flow pattern has broken down, crossing over no longer occurs and the layer is occupied by one large re-circulating gyre throughout the entire channel, with net flow towards the upstream basin. From figure 5.7(A) it becomes apparent that the interface structure between the two layers has also markedly changed. Downstream of the sill the interface has risen and flooded the sill. Separation is almost absent, apart from a small region at the right-hand wall of the channel which subsequently also disappears.

(A)

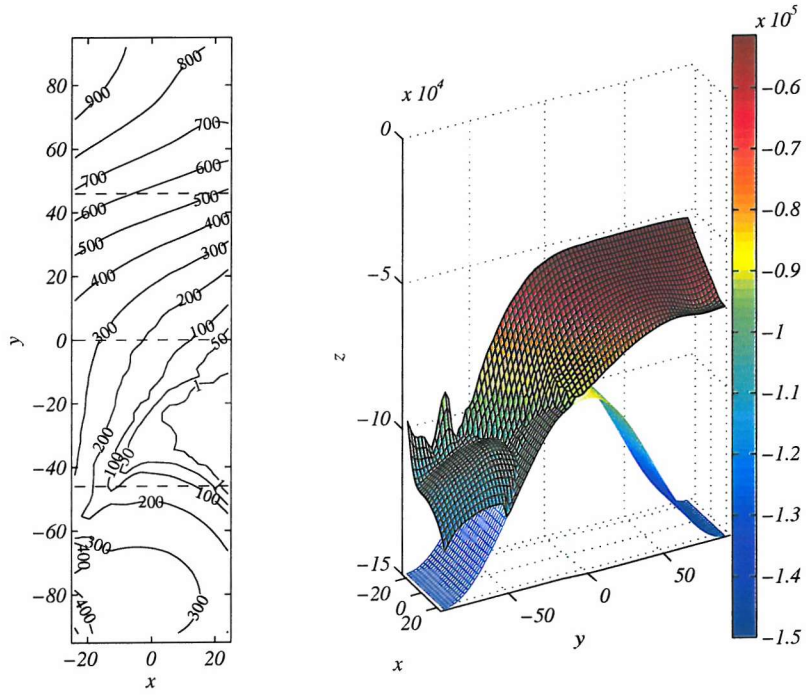

(B)

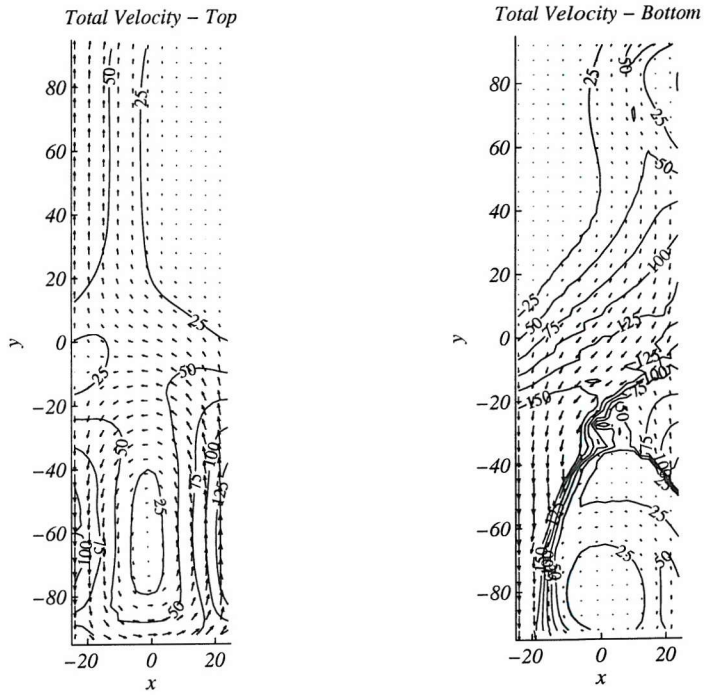

Figure 5.6: Resolution in these plots is 0.025 degrees, all other variables are as in figure 5.3. **(A)** Contour plot of the bottom-layer thickness (left) and meshed surface plot of the interface height and topography at day 100. **(B)** Total velocity at day 100 in the top- (left) and bottom-layer (right) respectively.

(A)

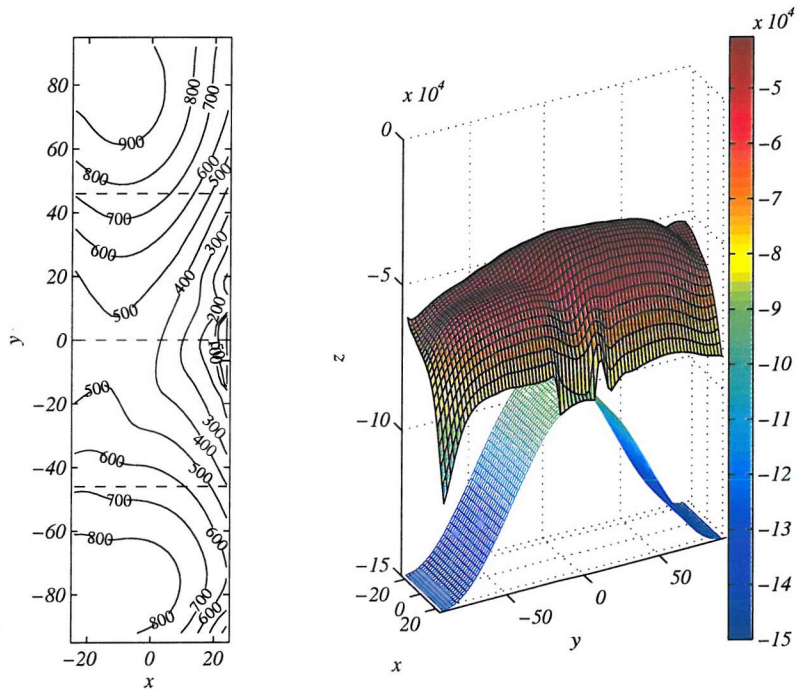

(B)

Figure 5.7: Resolution here is still 0.025 degrees, all other variables are as in figure 5.3. **(A)** Contour plot of the bottom-layer thickness (left) and meshed surface plot of the interface height and topography at day 200. **(B)** Total velocity at day 200 in the top- (left) and bottom-layer (right) respectively.

Another run was carried out at the same resolution but with deeper basins of 4500 m and a down stream relaxation height of 3000 m below the surface. In this setup the flow remained asymmetric along the channel without the sill being flooded. We can conclude therefore that the rise in the flux and the interface downstream of the sill in the case of the shallow basins was due to effects of the circulation in the downstream basin on the flow in the channel.

The 'flooded sill' flow we have seen in this 0.025 degree resolution experiments is not critically controlled in the sense that does not have different layer thicknesses on either side of the sill. It is nonetheless a legitimate and physically realisable state of the flow, which may well be worth studying further, especially since it presents yet another possible flow state through the channel that is not critical yet carries a much larger flow than any of the critical solutions we consider. Our primary interest in this work is to look at critically controlled flows, since these are the most likely to occur in the oceans, therefore we will aim to choose both the resolution and the topography of our experiments in such a way that the flooded-sill state is avoided.

Final Resolution

Comparing all three sets of experiments at the different resolutions we can observe that they all exhibit very similar features up until the flow changes so drastically in the highest resolutions case. The fluxes all lie within 10% of each other and the flow in the medium and high resolution experiments is separated for parts of the experiment, which is a state predicted by the theory and from observations.

From the point of view of the computational expenses a compromise between 0.025 and 0.05 degrees was affordable, and it was decided to adopt 0.04 degrees for all subsequent experiments. Although the fluxes resulting from the three different resolutions did not change significantly, it was felt that in order to look at particular mesoscale features of the flow, such as separation for example, it would be desirable to employ a finer resolution, which would give a larger number of gridboxes covering a Rossby radius.

The run carried out at the final resolution showed a steady gradual increase in flux over the 200 days it was run for, with an average of 7.34 Sv, and had a tendency to also flood the sill. However as the experiment with a deeper basin showed in the high resolution case, this problem may be overcome by adjusting the topography somewhat. To this end a set of runs was carried out to test the topographic effect on the flow to choose the most suitable topography for our purposes.

5.1.4 Topography and relaxation tests

A first test set was run increasing the depth of the basins, another was run to test the effect of making the sill shallower and finally runs were done to test the effect, if any, of the downstream relaxation height on the flow across the sill. Tables C.1 - C.3 in appendix C show details of all these runs and the results are listed in dimensional as well

as non-dimensional form.

We will from now on discuss a lot of the results in non-dimensional terms in order to generalise the results. Let us therefore briefly review the scaling of the parameters we will encounter most frequently. The fluxes are non-dimensionalised using the same expression we employed for the theory:

$$Q_{nd} = \frac{g' H_0^2}{f} \tag{5.6}$$

which is a multiple of a vertical scale H_0, the depth of the channel at the sill, a typical velocity $\sqrt{H_0 g'}$, and a typical horizontal scale $\frac{\sqrt{H_0 g'}}{f}$, the Rossby radius. In general non-dimensionalised variables will be indicated by a (*). Alongside a description of the various flow parameters we also list an estimate for the error Er, in appendix C, for each experiment.

In the top panel of figure 5.8 the non-dimensional fluxes are plotted for varying basin depth and although there are small fluctuations these are within the margin of variability or error of about $Er = 0.005$ estimated for these experiments. We conclude that the depth of the basin has no significant effect on the results of the runs we propose to carry out and will use basins of 4500m depth in most of the subsequent runs. This depth is also closest to the zero potential vorticity assumption we make in the theory.

Similarly we have tested the effects of a shallower sill on the flux and the middle panel in figure 5.8 shows the non-dimensional flux results as a function of the width of the channel in Rossby radii, which changes as we change the depth of the sill. It can be seen that varying the depth of the sill does change the non-dimensional flux appreciably, even beyond the estimated error of ~ 0.006. Notice that in these runs we have kept the ratio of $\frac{\Delta H}{H_0} = \Delta H^*$ constant. Following these experiments, we decided to initially use a sill of minimum depth 500 m, and later carried out a few runs with a deeper sill of 900m, to investigate how the flows differ in their behaviour.

Finally the effect of the downstream interface height relaxation, $\Delta H_D^\star = \frac{\Delta H_D}{H_0}$, was tested and the results are plotted in the bottom panel of figure 5.8. Again it has no effect on the flux across the sill and the difference in flux results lies within the error of ~ 0.006. It should be noted however that if we relax the interface too close to the depth of the sill, the flux across the sill will be affected. The result is that the interface downstream of the sill keeps rising, the flux increases drastically and the sill is essentially being flooded in the same manner we observed at the highest resolution used. We therefore decided to keep ΔH_D low enough in all experiments to avoid a flooded sill state.

5.2 Non rotating channel experiments

Before outlining the non-rotating experiments and comparing them with the theory developed by Armi (1986) let us first briefly recap the theory.

The novelty of the work by Armi (1986) was the new formulation of the governing

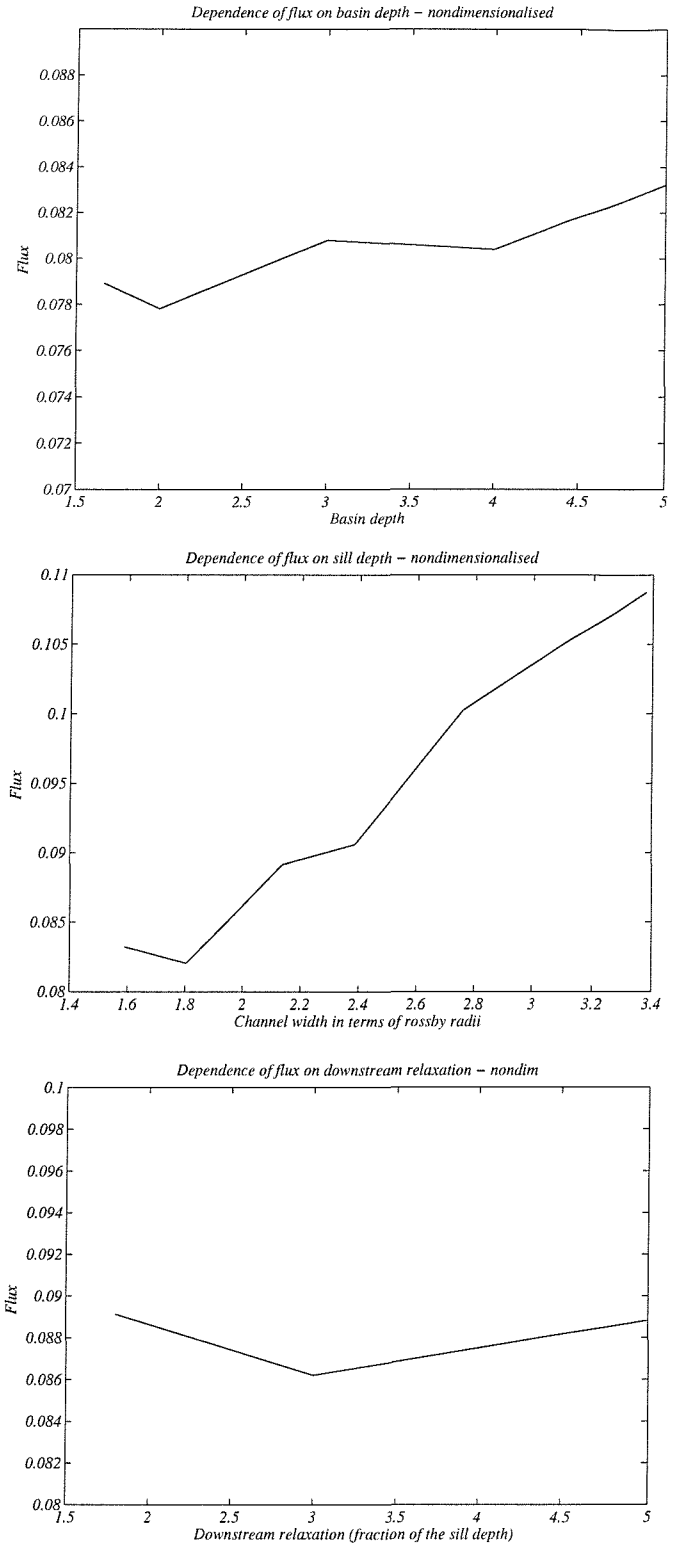

Figure 5.8: **(Top)** Variation of the flux with basin depth, both expressed non-dimensionally. $Er \sim 0.005$. Details of the runs are listed in table C.1 in appendix C. **(Middle)** Variation of the flux with sill depth, expressed non-dimensionally against the width of the channel in terms of Rossby radii, which increases as the sill becomes shallower. $Er \sim 0.006$. Details of the runs are listed in table C.2 in appendix C. **(Bottom)** Variation of the flux with change in the downstream relaxation height, $\Delta H_D^\star$. $Er \sim 0.006$. Details of the runs are listed in table C.3 in appendix C.

equations, continuity and momentum, in terms of Froude numbers. The following expression for the flux per unit width in a channel with a sill or narrow results from the continuity equation:

$$\frac{q_2'}{b'(1-h')^{3/2}} = \left[q_r^{2/3} F_1^{-2/3} + F_2^{-2/3}\right]^{-3/2} \tag{5.7}$$

where q_r is the ratio of the flux in the top-layer divided by the flux in the bottom layer, q_1/q_2 which is always 1 in the cases we consider here. F_1 and F_2 are the Froude numbers in top- and bottom-layer respectively, b' is the width of the channel and h' the height of the topography. The ($'$) indicates non-dimensionalised variables and the non-dimensionalisation of the flux is as follows:

$$q_i' = \frac{q_i}{g'^{\frac{1}{2}} b_0 (y_1 + y_2)_0^{\frac{3}{2}}}. \tag{5.8}$$

Here b_0 is the width of the channel at the narrowest point and $(y_1 + y_2)_0$ is the basin depth. For further details of the non-dimensionalisation Armi (1986) can be consulted.

The difference of the Bernoulli equations $\Delta H''$, can be expressed as follows in the Froude number notation used by Farmer and Armi (1986):

$$\Delta H'' q_1'^{-2/3} = F_1^{-2/3} + \frac{1}{2} F_1^{4/3} - \frac{1}{2}\left[\frac{F_2^2}{q_r}\right]^{2/3}. \tag{5.9}$$

An example of the Froude number plane diagrams used by Farmer and Armi (1986) to trace the flow over a sill is shown in figure 5.9. The thin continuous lines are lines of constant $\frac{q_2}{b'(1-h')^{3/2}}$, from equation (5.7), and the thicker solid lines the solutions lines given by expression (5.9). Note that in the case of a constant width channel $b' = 1$ all along the channel. Along the dashed line the total Froude number $G = 1$ and the flow is controlled.

Farmer and Armi (1986) find that the maximal two-layer exchange flow over a sill occurs for $\Delta H'' q_1'^{-2/3} = 1.5$, with $q_1 = 0.208$, and for this type of flow the thickness of the bottom layer at the sill, given as a fraction of the total sill depth, is equal to 0.375. This is also where the primary control occurs.

In figure 5.9 the maximal solution line is drawn and like all maximal flows it consists of a regions of subcritical flow separated by two regions of supercritical flow. The solution line starts with large F_2^2 downstream, where the bottom layer is very active and the top layer almost stagnant, at the sill the line crosses $G = 1$ and then moves into a subcritical region upstream where the top layer becomes increasingly active as F_1^2 increases and the bottom-layer becomes thick and sluggish. The transition into the second supercritical region upstream relies on the fact that the channel exits into a basin that is deep enough for the bottom-layer to become essentially stagnant at that point, we will see that none of the modelled flow quite reach this point since we have basins of finite depth.

In total five runs were carried out with $f = 0$ using the resolution and basin setup for the 0.1 degree resolution experiment described in section 5.1.3. Downstream the interface

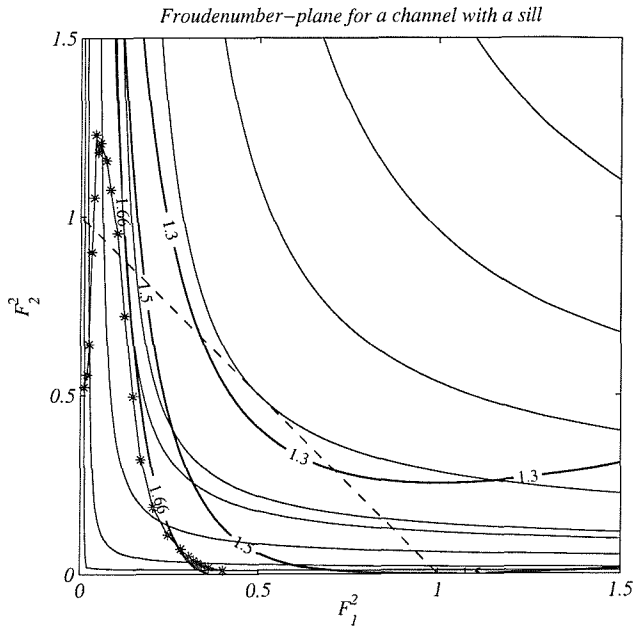

Figure 5.9: Froude number plane for flow over a sill with $q_r = 1$. The thin continuous lines are results of the continuity equation for $\frac{q_2}{b'(1-h')^{3/2}}$, and the thick solid lines the results of the Bernoulli equation for $\Delta H''$. Along the dashed line $G = 1$ and along $\Delta H'' = 1.5$ the maximal flow can be traced. The solid line maked by the stars is the solutions line for the experiment with $\Delta H = 800$ m. Note that in the region where F_1^2 is small this line turns back on itself and crosses $G = 1$ again, this point corresponds to a second control downstream in the form of an hydraulic jump.

ΔH	F_1	F_2	$\Delta H'' q_1'^{-2/3}$	$\Delta H''$	q_1
100	0.0132	0.6998	17.5949	0.9177	0.0119
200	0.0454	0.7915	7.4997	0.8309	0.0369
400	0.1510	0.8333	3.1747	0.6819	0.0995
700	0.3425	0.8496	1.7666	0.5579	0.1775
800	0.3783	0.8273	1.6603	0.5450	0.1881
850	0.3760	0.8235	1.6693	0.5459	0.1870

Table 5.3: Mean Froude numbers are listed taken from the top of the sill of the different non-rotating MICOM experiments. Using $F1$ and F_2, $\Delta H''$ and the flux q_1 are estimated using the expressions derived by Farmer and Armi (1986).

ΔH	Q_1	$\frac{Q_1'}{(1-h')^{3/2}}$	y_{20}
100	1.8941	0.0128	0.0697
200	5.4439	0.0368	0.1319
400	14.5395	0.0983	0.2464
700	26.0159	0.1760	0.3530
800	27.6246	0.1868	0.3730
850	27.7527	0.1877	0.3720

Table 5.4: Table of the actual flux results from MICOM, Q_1 in Sv. They are non dimensionalised to match the results from the theory and as expected column 4 in this table and column 6 in table 5.3 are almost identical. y_{20} is the average height of the interface at the top of the sill, as a fraction of the sill depth, derived from MICOM.

was relaxed to 1400 m below the surface and upstream the relaxation was varied from run to run spanning the following set of $\Delta H = [100, 200, 400, 700, 800, 850]$ m above the sill, which has a minimum depth of 900 m.

For each experiment we derived the average Froude number in the top- and bottom-layer at the top of the sill and these are listed in table 5.3, from these we found the flux using the continuity equation from Armi and Farmer, as well as the values of the solutions lines and $\Delta H''$, the difference in Bernoulli potential between the two layers. It is apparent that even for a setup in which the top layer almost vanishes upstream, as for example in the case of $\Delta H = 850$ m, the maximal value of $\Delta H'' q'^{-2/3} = 1.5$ is not quite approached, with the minimum value being about 1.66, as a result the maximal flux, determined to be 0.208 by Farmer and Armi (1986), is not reached. We find the maximum flux to approach 0.187.

The actual dimensional fluxes Q_1, resulting from the MICOM runs are listed in table 5.4 along with the non-dimensionalised flux Q_1', derived using equation (5.8). These should and are almost identical to those derived from the Froude numbers of the flow listed as q_1 in table 5.3.

For all the runs listed above we have also taken the average of the thickness of the bottom layer at the sill, y_{20}, across the channel and then averaged it from day 40 to 100, the results are listed in table 5.4. The values get very close to the 0.375 given by Armi and Farmer, when the thickness of the top layer becomes very thin upstream.

A further comparison between theory and MICOM is shown in figure 5.10 where we have plotted the non-dimensionalised fluxes against the non-dimensional upstream relaxation height in MICOM, $\Delta H^\star$, as well as against $1 - \Delta H''$ (since $\Delta H''$ is a measure of the thickness of the top-layer) derived from the Froude numbers at the top of the sill.

The analytically derived $1 - \Delta H''$ agree very well with the Armi & Farmer theory. Although the maximal flux of 0.208 at $1 - \Delta H'' = 0.5$ is never quite reached, the fluxes for the three highest relaxation heights $\Delta H = 0.78$, 0.89 and 0.94 tend towards a maximum flux of about 0.188. The ΔH derived from the MICOM results (dashed line) is clearly not the same as that computed at the sill, which suggests a loss of energy between the

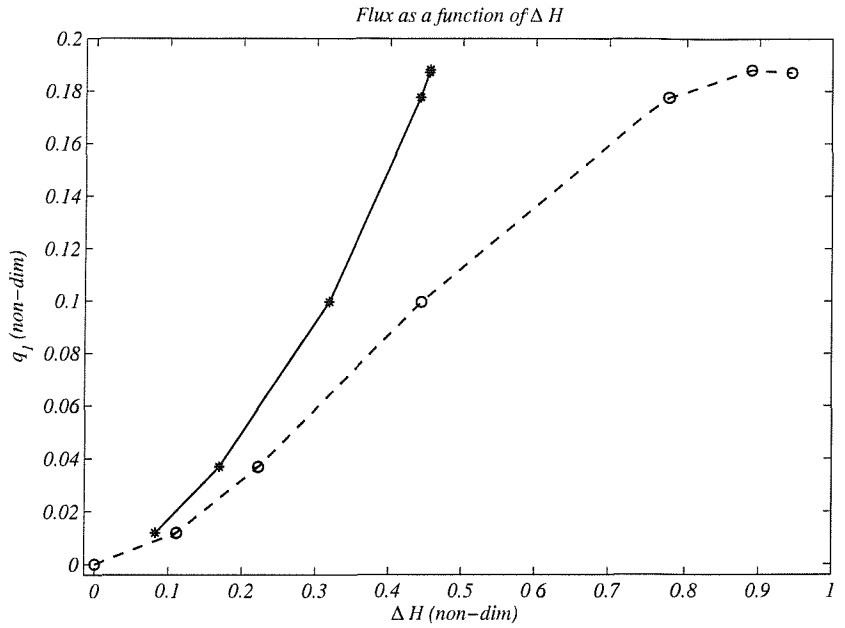

Figure 5.10: Non-dimensional fluxes plotted against $1 - \Delta H''$ (solid line), see table 5.3, and against $\Delta H^\star = \frac{\Delta H}{900}$ (dashed line).

basins and the channel. We can infer from this that the Armi & Farmer theory is correct locally but looses its validity globally.

The question is which measure is more useful, when considering real oceanic flows and deriving a flux for these in terms of external parameters such as the upstream interface height. We believe that it is unlikely for an hydraulic jump to occur upstream of the sill. In the real ocean these hydraulic jumps are 'eroded' by the effects of viscosity and the flow gradually approaches a maximal state as the upstream interface height becomes close to the surface of the water column, however the maximal state is never fully realised.

We will come across the same problem of matching the theoretical measure of basin stratification from the rotating theory, ΔE, with the measure of the upstream interface in MICOM in the next chapter when we outline the results from the rotating experiments.

Flow Structure

In figures 5.11(A) and 5.11(B) the Froude number fields in the channel are shown for the runs with $\Delta H = 100$ and $\Delta H = 800$ respectively. In the former is can be seen that the total Froude number $G = \sqrt{F_1^2 + F_2^2}$ is almost the same as the Froude number in the bottom layer F_2. This indicates that the top-layer is dynamically inactive. The primary control is located away from the sill crest in the downstream direction which is analogous to the effects of friction described by Pratt (1986). He determines that the control lies where the slope of the topography is equal to $-C_d$, where C_d is the drag coefficient. The slope at this point is referred to as the 'critical slope'. Notice that his estimate was done for a single layer flow however the same conditions apply for two-layer flows according to Zhu and Lawrence (2000).

In the model we use $C_d = 0.003$ and we find that the critical slope is 0.0046 for the

(A)

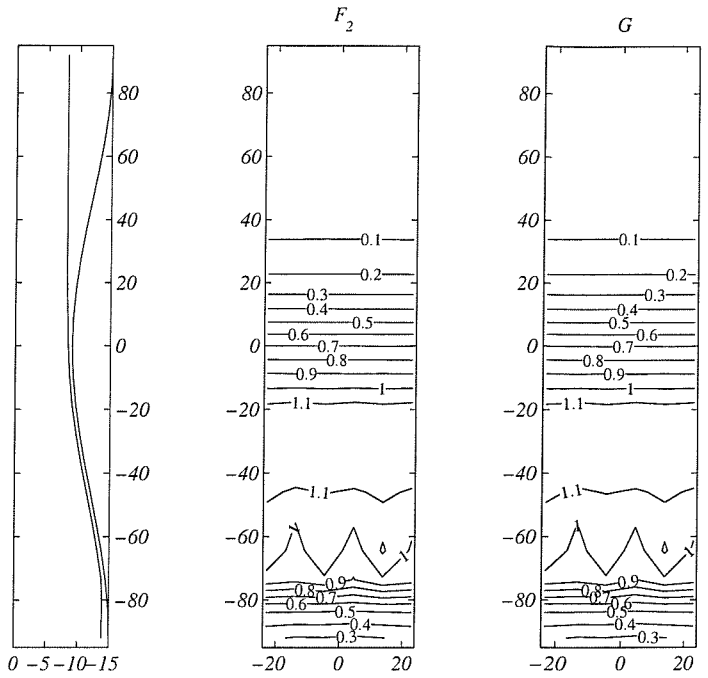

(B)

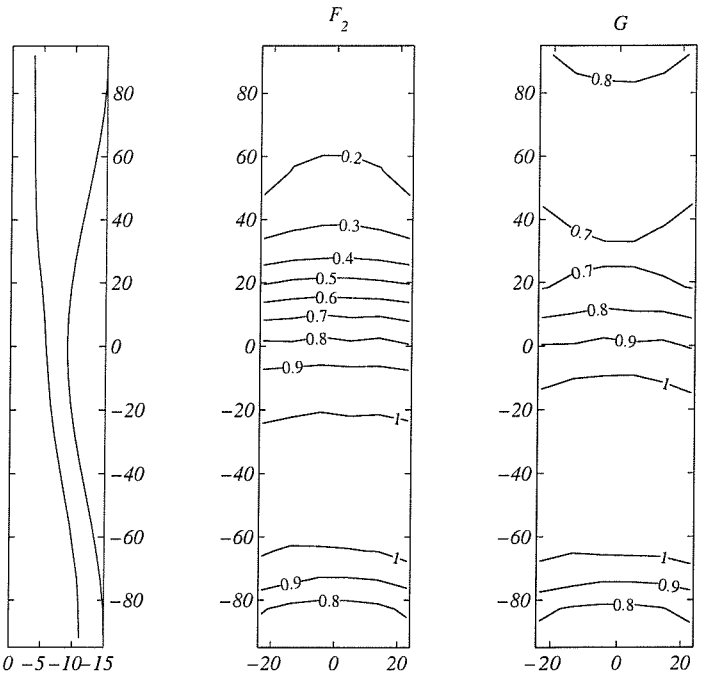

Figure 5.11: **(A)** The small panel on the left shows the elevation of the interface above the topography along the centre of the channel with $\Delta H = 100$ m. In the centre the Froude number of the bottom layer, F_2^2 inside the channel is plotted and to on the right the contours of the composite Froude number G are shown. **(B)** Same as in (A) but for a flow with $\Delta H = 800m$.

case where $\Delta H = 100$ m. It should be noted however that any estimate of a bottom slope in MICOM is only approximate. We found that $G = 1$ occurs between the second and third gridpoint downstream of the sill and the slope of the topography will be constant everywhere between these two points. The slope between the two gridpoints closer to the sill is about 0.0016 and thus it is not possible to draw any definitive conclusions about whether the slope is critical or not at the control.

Another critical section occurs further downstream towards the exit of the channel, this is in the form of an hydraulic jump linking the supercritical region in the channel to the subcritical basin conditions.

In the case of the $\Delta H = 800\ m$, presented in figure 5.11, the Froude number field in the bottom layer and the total Froude number are quite different indicating that the top layer is of significant dynamic importance. This case is one we would expect to come close to maximal and approach a second control upstream. In figure 5.9 its path is represented by a single solid line marked with asterisks. It follows the solution line of $\Delta H'' q_1'^{-2/3} = 1.66$ quite closely and $G = 1$ is approached upstream. However it does not pass through the second control and neither does the experiment with $\Delta H = 850$ which should be even closer to the maximal solution. There is a region of $G > 1.0$ in the upstream basin, where the top layer features a large gyre, but it only distorts the physics related to the overflow.

5.3 Conclusions

After carrying out extensive tests on the optimum resolution and topography for the experiments, an initial setup was chosen with two basins of depth 4500 m and sill with depth 500 m. The resolution was taken to be 0.04 degrees which leads to a grid size of about 3.4 km on average.

The topography tests tell us that the basin depth has only a small effect on the flux through the channel and the equally the downstream relaxation height is of no effect provided it is low enough not to flood the sill.

The resolution experiments already show us some flow features which compare well with the kind of features we would expect from our theoretical knowledge of hydraulic flows as well as from observations in the laboratory. In particular the bottom layer crosses over at the top of the sill and separates from the right-hand wall downstream of the sill. This separation is however only modelled at sufficiently high resolution. As the overflow enters the downstream reservoir of dense water at the bottom a hydraulic jump occurs that is similar in its features to the rotating hydraulic jump observed by Pratt (1986).

As series of non-rotating experiments carried out shows us that in general the model captures the range of possible flows very well and the maximum flux achieved in the model is only about 10% less than the flux predicted by the theory.

The major difference between model and theory is the absence of the hydraulic jump upstream with respect to the sill. It is a feature only of the frictionless and ideal theory. In the model friction modifies the flow in such a way that the hydraulic jump upstream

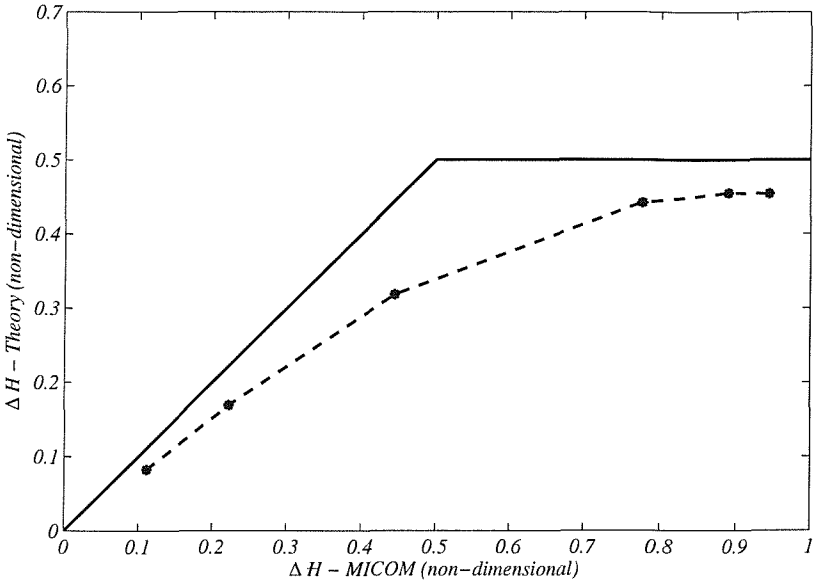

Figure 5.12: Comparison between the $\Delta H^{\star}$ as it is used in MICOM and $\Delta H''$ as it appears in the theory. For $\Delta H'' = 0.5$ the maximal flux is attained in the theory, and for larger $\Delta H''$ there will be not change in flux. The MICOM results are plotted with the dashed line.

is 'eroded'. In addition it is not surprising that we do not see a second hydraulic jump in the channel. Theory suggests it should occur at the entrance to the channel, with respect to the bottom layer, however this part of the domain is strongly influenced by the basin dynamics in our case due to the abrupt transition from channel to basin in our set up, which may be one reason why this control is absent. Another reason already mentioned are the viscous effects in the model.

Figure 5.12 illustrates the resulting difference between the usage of $\Delta H^{\star}$ and $\Delta H''$ in MICOM and the theory well. Whereas the theory assumes that for $\Delta H'' = 0.5$ the flow is maximal and there is no increase in the flux beyond this value, the flux in MICOM increases gradually and only approaches the maximum flux for $\Delta H^{\star} \sim 1$. This we believe is due to the effects of friction and dissipation of energy upstream which prevent a second hydraulic jump from occurring. We should also point out that the ΔH we use upstream in the channel might not be the best parameter to fit the flux against, as it is altered due the viscous effects of the flow just mentioned and by the time the flow enters the basin ΔH may have already changed enough to give a significantly different flux we would expect for the high ΔH set in the basins.

In figure 5.11(B) for example we set ΔH to 800 m in the upstream basin, however on entering the channel this height has reduced to $\sim$ 600 m. Taking this into account the data points on the dashed line in figure 5.10 for the lager ΔH will move closer to the theoretically predicted solid line and agreement is probably much better than initially thought.

Chapter 6

Rotating two-layer flows in MICOM

In this chapter we will outline the results from the rotating experiments with 0.04 degree resolution and the topography described in the previous chapter. The aim is to investigate the dependence of the flux through the channel on the external parameters already referred to, in particular the Coriolis parameter f, the reduced gravity g', and the upstream interface height between the two layers, denoted by ΔH. The changes in f and g' manifest themselves in a changing magnitude of the Rossby radius and hence a widening or narrowing of the channel in terms of Rossby radii. We will therefore concentrate on the flux dependence on L, the width of the channel in terms of Rossby radii, as well as ΔH.

In section 2.1 we will first of all briefly describe the experiments and how they were analysed. Then in section 2.2 we will give a description of the kind of flow features which were observed for a shallow channel and a deep channel example. This will illustrate that although we like to assume the flow is steady, several distinct oscillatory patterns are observed in both cases. In section 2.3 we will present a method to find where in the flow the control sections are located. In section 2.4 a proposed parameterisation will be developed for the fluxes in terms of L and ΔH and finally in 2.5 we will draw conclusions.

6.1 The experiments

In total 71 experiments were run at 0.04 degree resolution, a full list of which is given in appendix C. Having carried out the tests of the effects of the basin depth, sill depth and downstream relaxation on the flux, outlined in the previous chapter, (see tables C.1 - C.3 in the appendix), it was decided to initially use a sill depth of 500 m and basin depth of 4500 m. A set of experiments was carried out varying f and g', see tables C.4 - C.6, as well as a set of experiments varying ΔH listed in tables C.7 - C.9. Finally, because we observed flow features through the shallow sill, which were distinctly different from those we had seen in the resolution test runs, another set of experiments was run with a deeper sill of 900 m and shallower basin depth of 3000 m, see tables C.10 and C.11.

Each experiment was initialised with a horizontal interface extending from the far walls of the basins to 10 gridpoints away from the channel entrance and exit, and the

height of the interface was set to the same value as the interface was relaxed to during the experiments. Within the channel the initial interface was extended linearly from the downstream basin to a point 100 m above the sill and then from there again linearly toward the upstream basin. This initial configuration was then spun up and run for 200 days with diagnostic variables being saved every 10 days.

Generally the flow adjusts to a pseudo steady state within the first 100 days and the final flux is taken to be an average of the fluxes from day 100 to 200. We will refer to the flow as 'pseudo steady' rather than steady, as we will see later that only very few - if any - of the flows are steady in the strictest meaning of the word. By pseudo steady we mean a state of the flow that may not be steady on short time scales of a few days, but that exhibits more or less uniform oscillations about a mean flux. If the flux did not settle to a pseudo steady state, and kept increasing or decreasing over the duration of the run, the model was restarted and run for a further 200 days. If the flux still did not settle down the experiment was treated with caution but they were still included in the analysis, in tables C.1 to C.11 they can be identified by very large errors. In the cases which were rerun, the average flux from day 200 to 400 was used.

The primary diagnostic variables used were the velocity fields for both u and v-velocity components, the interface-height field p, in pressure units, and the v-fluxes along the channel for computing the transport across the sill. In addition the Montgomery potential was diagnosed in some of the runs in order to look at the surface elevation of the flows.

Hydraulic theory has frequently been applied to investigate the dependence of the flux on the width of the channel in terms of Rossby radii, which is generally defined as follows:

$$a = \frac{\sqrt{g' H_0}}{f}. \tag{6.1}$$

To analyse the behaviour of the MICOM result with varying a we have expressed the width of the modelled channel in terms of Rossby radii. Its dimensional width is $W = 55.4$ km for all experiments and $L = \frac{W}{a}$. The range of L covered in the experiment can be assessed from the list of experiments in appendix C. Most lay in the range of L = 1 - 5 with some exceptions. Since the channel is modelled by 15 gridboxes this means that for most cases the Rossby radius is resolved by 3 - 15 gridboxes, so most mesoscale features should be very well resolved.

6.2 Flow features

While analysing the experiments we discovered some intriguing features in the flow fields both in the channel and the basins, which we feel are worth outlining briefly and comparing with previously observed patterns. Such comparisons may be enlightening to others and spur interest in investigating the arising questions further.

Some flow features in the channel have already been discussed in the previous chapter when testing for the appropriate resolution. In particular we discussed the occurrence of a

rotating hydraulic jump downstream of the sill, the features of which closely match those found by Pratt (1987) and observed a separated region of flow which is predicted from the theory. However, these features are not as clearly distinguished in any of the subsequent experiments. We believe this is due to the fact that by changing the topography in the manner we did, we considerably steepened the slope the overflow descends and as a results the flow features in this part of the channel look different to those we saw previously.

Because the characteristics of the flow vary somewhat from experiment to experiment we have chosen two representative examples to focus on. The other experiments can be expected to behave similarly.

The first flow we will describe is taken from the shallow channel experiments (Set I) with a Coriolis parameter $f = 1.0 \times 10^{-4} s^{-1}$, $g' = 9.806 \times 10^{-3} m/s^2$ and $\Delta H = 278.5$ m. It has a channel width of 2.5 Rossby radii and can thus be considered wide. The mean flux observed at the sill is $2.226 Sv$.

Secondly a flow through a deep channel (Set VII) with $\Delta H = 700$ m will be described. It has $f = 1.4 \times 10^{-4} s^{-1}$ and $g' = 2.942 \times 10^{-3} m/s^2$, while its mean flux was observed to be 2.098 Sv and its width is 4.77 Rossby radii.

We shall see that contrary to assumptions made in the analysis of the model data the flows are not actually steady. There are no conspicuously large increases or decreases in the fluxes over the usual 200 day interval and the flows are pseudo steady, but some variation about the mean may be seen in most runs (given as the error in tables in appendix C). The diagnostic frequency of 10 days we used initially did however not allow the study of oscillations on smaller time scales.

In this section we will describe both the overall time invariant features seen in the experiments and the time variability discovered when observing the experiments at higher diagnostic frequencies.

Results will be compared to flow features observed in laboratory experiments by Dalziel (1988) and Borenäs and Whitehead (1998) of channel flows as well as to the theoretical results in the first half of the thesis. The basin circulation will be compared to the circulation in the Western Mediterranean described by Herbaut et al. (1996) and Herbaut et al. (1998), which is to a large extent forced by the exchange flow through the Strait of Gibraltar.

6.2.1 Shallow Channel

Figure 6.1 shows a snapshot of the absolute velocities and current directions in the bottom layer (left panel) and the top layer (right panel). Upstream the bottom layer is thick and slow and only starts to speed up when it approaches the sill. As it does so it turns away from the right-hand wall towards the left-hand side of the channel, which is referred to as 'crossing-over' of the bottom layer, a typical feature in rotating exchange-flows. Typical velocities in the first 10 km after the sill are between 0.4 and 0.5 m/s before the current splits into the much faster finger like currents. Once the overflow has entered the

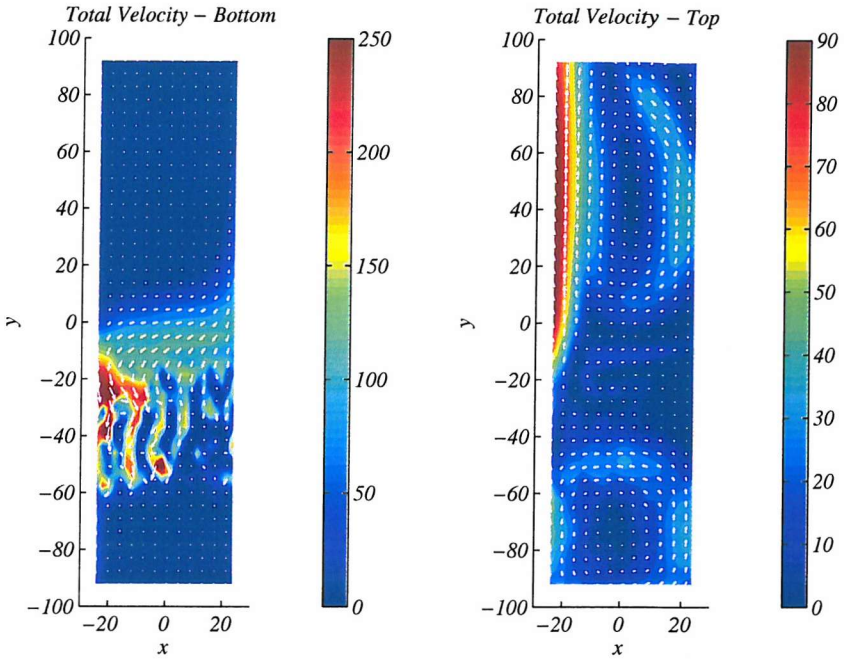

Figure 6.1: Snapshot of the velocity field in the bottom layer (left) and the top layer (right) inside the shallow channel, the velocity is scaled in cm/s. The x and y-axis are given in km. The finger-like instabilities in the bottom layer overflow can be made out clearly just downstream of the sill. The dominant feature in the top layer is the boundary current on the left-hand side transporting the majority of the flow across the sill. (From first diagnostic timestep in figure 6.3).

downstream basin it again become a sluggish and thick subcritical flow.

The characteristic finger-like mesoscale flow pattern downstream of the sill in the bottom layer, which has been observed in several of the shallow channel experiments, attracted our particular attention. In the 0.04 degree resolution experiments these features were only just larger than gridsize ($\sim$ 4 km) and it was therefore decided to rerun this particular experiment at a higher resolutions of 0.025 degrees to investigate the possibility that it might simply be noise. In addition the diagnostic interval was set to $\frac{1}{128}^{th}$ of a day (= 11.25 mins) to determine the direction and speed of propagation of the disturbances.

Even at the higher resolution the finger-like structures are clearly present (see figure 6.1, and four to five of them can be made out across the channel. They are concentrated between $y = -20$ to -60 km, are about 20 - 30 km long and 5 km across. The flow inside the fingers is predominantly directed down the slope with the strongest current on the left-hand wall, where velocities exceed 2.5 m/s.

In other experiments these fingers become weaker if the flow is weaker, for example if ΔH is decreased, f is increased or the density difference between the two layers, and hence g' decreases.

The crossing-over of the bottom layer and subsequent formation of the boundary current are well modelled in the theory presented in chapters 3 and 4. The time varying features are obviously not captured since the analytical model is steady.

In the top layer the flow features are less variable than in the bottom layer, stretch over much larger horizontal scales and have smaller velocities. At the far downstream

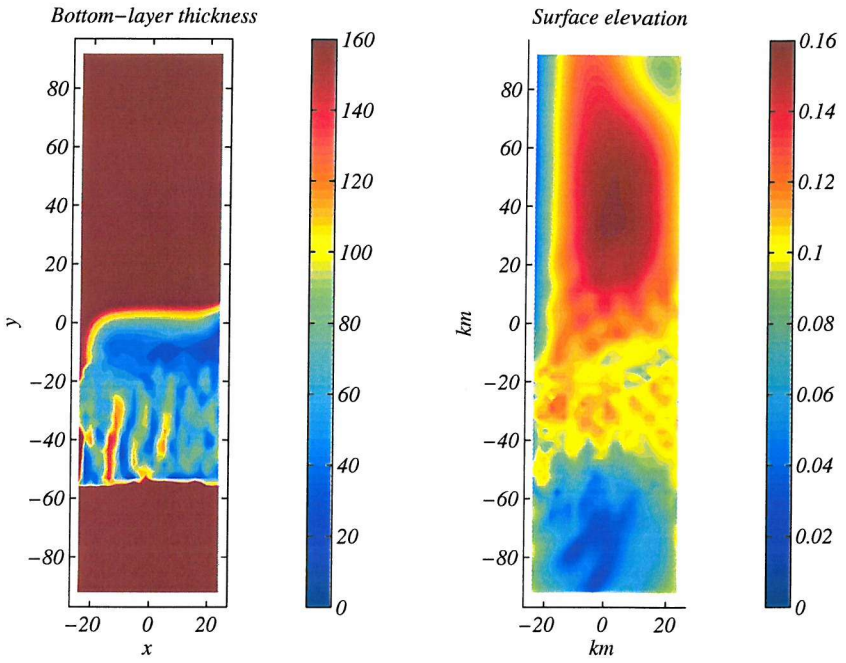

Figure 6.2: Snapshot of the bottom layer thickness (left), scaled in metres, and the surface elevation, also given in metres.

end of the channel a recirculating gyre is formed which extends over the entire width (55 km) of the channel and velocities here only reach up to 0.4 m/s. The gyre is cyclonic and splits at the left-hand wall at about $y = -50$ km into a small boundary current travelling up the channel towards the sill, while the majority of the flow returns within the gyre. As the boundary current approaches the sill it intensifies and velocities increase to about 1 m/s as it approaches the upstream basin.

As well as the boundary current a backflow towards the sill can be observed in the upstream half of the channel originating from the basin. It turns around before reaching the sill and serves to intensify the boundary current. This boundary current will also be affected by changes made to the external parameters for the different experiments. In general it has been observed that it widens as the Rossby radius becomes larger, for example by decreasing f or increasing g'. If ΔH is decreased this will mean a weakening and widening of the boundary current as the flux decreases, the top layer becomes thicker and thus velocities decrease.

This boundary current on the left-hand side of the channel in the upper layer has never been observed in any laboratory experiments because of the main focus on the bottom layer flow. It is however a remarkably consistent feature of all the experiments. While flow features in the downstream part of the channel can take several different forms the upstream circulation will always consist of a crossing over in the bottom layer and a boundary current on the left-hand side of the channel in the top layer. This top layer boundary current is also present in the theoretical model of these flows as is the back flow observed. In the theory however the backflow extends all along the channel whereas in the model it returns before reaching the sill.

The presence of the boundary current in the top layer on the left-hand side of the

channel is contrary to the position we would expect it to have after the Rossby adjustment of a dam-break scenario. In such a case we would expect a crossing-over in the top layer from the left to the right, with Kelvin waves propagating away from the point of the initial discontinuity in the interface height. Hermann et al. (1989) describe lucidly the evolution from the Rossby adjusted flow state to the steady hydraulic solution in a single layer flow.

At the initial layer thickness discontinuity a potential vorticity front is set up which is advected along the channel and eventually the crossing-over feature is 'washed' out of the channel. In the two layer case this is also the case, but only in the top layer. Here the initial crossing over from left to right at the sill due to Rossby adjustment gives way to the steady hydraulic solution with a boundary current only on the left. In the bottom layer the crossing-over remains in the channel only due to the presence of the sill, where the potential vorticity front becomes arrested.

Most of the features we have just described in the flow field of the bottom and top layers can also be observed in the thickness of the bottom layer and the surface elevation of the top layer, shown in figure 6.2 on the left and right respectively. The crossing over in the bottom layer and the increase in velocities goes hand in hand with a rapid decrease in the thickness of the bottom layer from about 160 m to less than 10 m in certain regions. Where the fingers occur in the velocity field a corresponding thickening of the layers is observed. At $y \sim -55$ km a sudden thickening of the bottom layer occurs, as the flow encounters the watermass of the same density in the downstream basin. Because the boundary current is not very steady in time and its width and intensity vary periodically no clear hydraulic jump can be discerned in the plot of the bottom layer thickness as it could be for the experiments in the previous chapter.

Equally the surface elevation of the top layer gives some indication of the circulation in the top layer. A steep gradient at the left-hand side of the channel upstream of the sill coincides with the boundary current while downstream the gyre can be made out by a large blue patch indicating low surface elevation. This results in a pressure gradient between the centre of the gyre and the outside giving rise to the cyclonic geostophic flow. Between the sill and this gyre small disturbances can be seen which probably result from the rapid and quickly changing currents in the bottom layer.

In comparison with theory and previous experimental and observational work the most remarkable feature of the circulation in the channel, which as far as we are aware, has not been reported before, is the occurrences of the mesoscale 'fingers' seen in the overflow. Recirculation on the other hand has attracted substantial attention in the past especially concerning laboratory studies, however these were mostly limited to single layer flows. Borenäs and Whitehead (1998) investigated the pattern of recirculation in a single layer upstream of a sill, and compared results to two theories, one postulating a stagnant region and one a region of recirculation. The experiments they carried out matched neither theory perfectly, but seemed to resemble the stagnant example more closely. Dalziel (1988) observed the flow in the bottom layer upstream of the sill to be largely stagnant

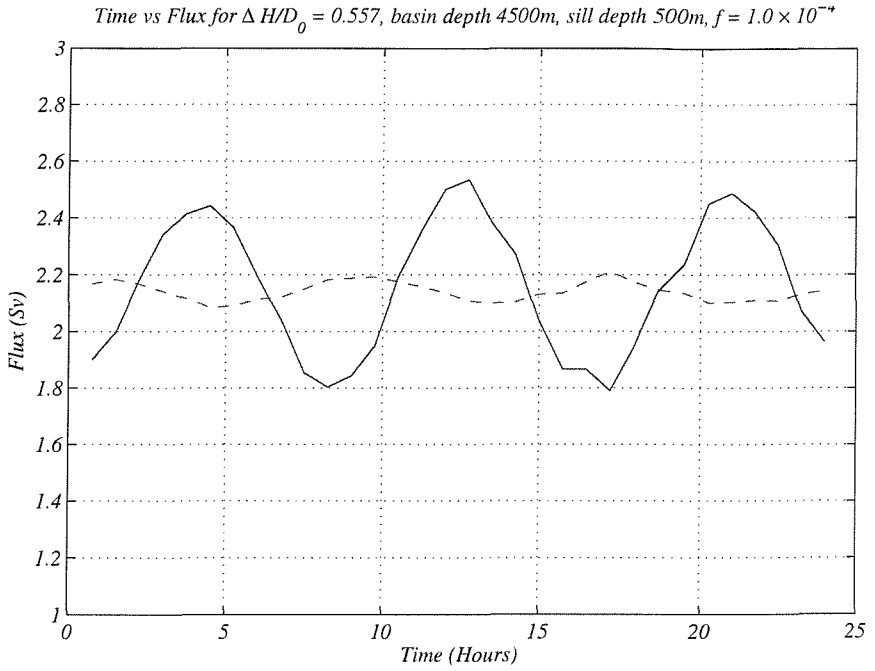

Figure 6.3: Flux across the sill in the top layer (solid line) and the bottom layer (dashed line), for the shallow channel experiment plotted at a diagnostic frequency of 11.25 mins over a period of 24 hours. The frequency of the oscillations in both layers is about $0.3 \times 10^{-4} s^{-1}$.

as well, apart from a boundary current on the left-hand side approaching a contraction (his channel had a flat bottom). He shows no results regarding the circulation in the top layer. We can confirm previous assumptions and observations that upstream of the sill the bottom layer is mostly stagnant. In addition we have been able to describe a large pool of additional observations in the other regions of the channel and in particular in the top layer which may be worth further investigation.

Time variability of the flow in the channel

In figure 6.3 the variability of the transport across the sill in the bottom and top layer over a 24 hour period is shown. The variability is striking and regular, and with a diagnostic frequency of 128 per day (equal to an interval of 11.25 mins) it can be clearly distinguished. The magnitude of the oscillations is about 0.5 Sv in the top layer (solid line), but only about 0.1 Sv in the bottom layer (dashed line). The period is about 9 hours and hence its angular frequency about $1.94 \times 10^{-4} s^{-1}$ which is roughly equal to $2f$.

Visual inspection of the boundary current in the top layer has shown that pulses of fluid travel along the left-hand wall of the channel constituting the oscillations in the flux. However the forcing mechanisms of these pulses is unclear. There is a temptation to link them to the variability of the flow in the bottom layer downstream, but the characteristics of the disturbances in the gravity current down the slope, to be discussed next, and hydraulic theory lead us to conclude that these two time dependent phenomena are not linked. Hydraulic theory, in particular, says that any feature of the flow which occurs in a supercritical region does not affect the flow upstream of that region. Here it means that,

because the instabilities occur downstream of the sill and most likely downstream of the primary control close to the sill, the flow in this supercritical region will not affect flow conditions at the sill. Let us take a closer look at the finger-like oscillations downstream of the sill.

To obtain a clearer picture of the behaviour of the instabilities in the overflow three Hovmöller diagrams, figures 6.4 - 6.6, were plotted at three locations downstream of the sill, $y \sim -23$, -34.5 and -41.4 km, respectively. They illustrate the variations of bottom layer thickness and surface elevation with time. The top panel of figure 6.4 shows a clear signal of an interface height perturbation originating at the right-hand wall of the channel propagating to the left and increasing along the way. The perturbation weakens further down the channel but retains its speed of propagation, as seen in figures 6.5 and 6.6. It travels roughly 20 km in the 6 hours and thus crosses the channel in a little more than 12 hours, which gives it a speed of propagation of about 0.9 m/s, its magnitude reaches up to 100 m and its period is 2.0 hours (frequency $2\pi/7200\ s^{-1} = 0.87 \times 10^{-3}$). We see that the period of this oscillation is much smaller than the 9 hour period of the flux oscillations at the sill, which is the second indicator that they are most likely not linked.

A test experiment was run with a channel that was twice as long at the channel in the experiment just described and as a result the slope has roughly halved. Figure 6.7 shows a Hovmöller plot at a section downstream of the channel that is at the same height, of 3500 km, above the basin depth as the data shown in figure 6.4. We find that the finger like oscillations are still present but much weaker in magnitude, which does not exceed 40 m even as they close in on the left-hand wall. Their period has doubled to about 4 hours and hence the frequency has halved to $\omega = \frac{2\pi}{T} = 0.44 \times 10^{-3} s^{-1}$. This suggest that the frequency of these oscillations scales with the slope of the topography $\frac{dH}{dy}$. The waves in the long channel also increase across the channel as in the short channel experiment and we therefore conclude that they are a type of topographic instability wave.

In the surface elevation (bottom panels) no across channel propagating features can be seen, instead a rising and falling of the surface of 6 cm amplitude and period of a little less than 1 hour is seen and may be attributable to sloshing motion in the channel.

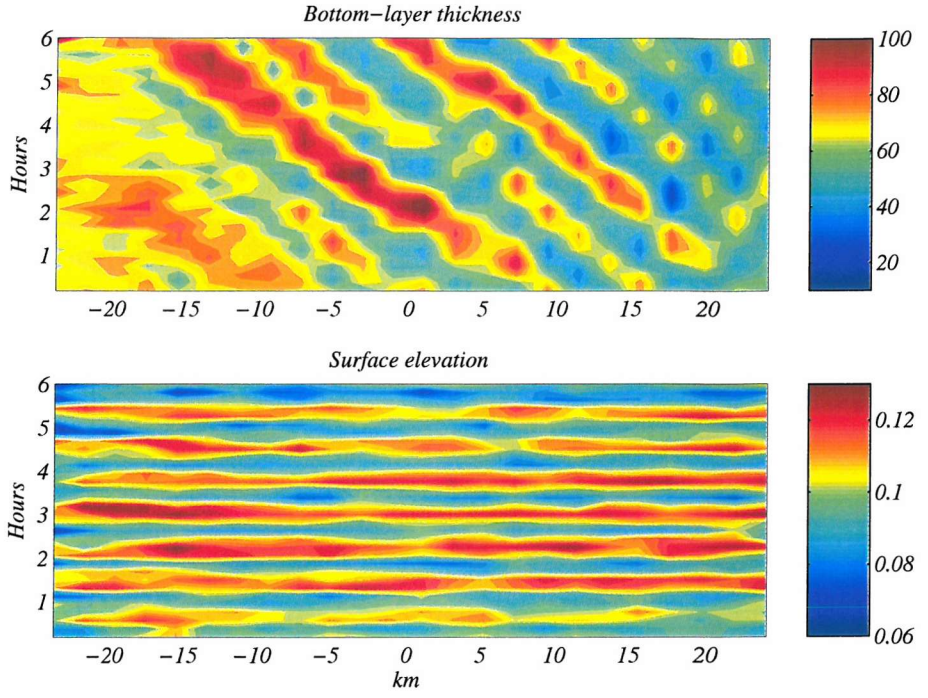

Figure 6.4: Hovmöller plot of the bottom layer thickness in metres (top) and the surface elevation also in metres (bottom) for a section across the channel at $y \sim -23$ km.

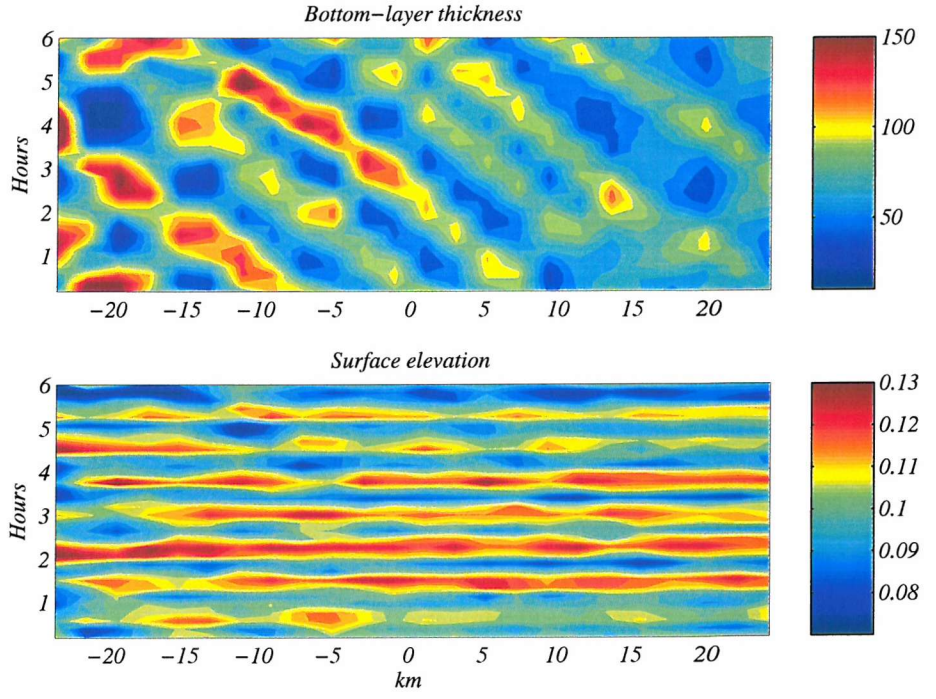

Figure 6.5: Hovmöller as in figure 6.4 at $y \sim -34.5$ km.

Basin circulation

The circulation in the basins is plotted in figure 6.8, showing the bottom and top layer on the right and left respectively. The colours indicate flow speeds while the small superimposed arrows illustrate the direction of the currents.

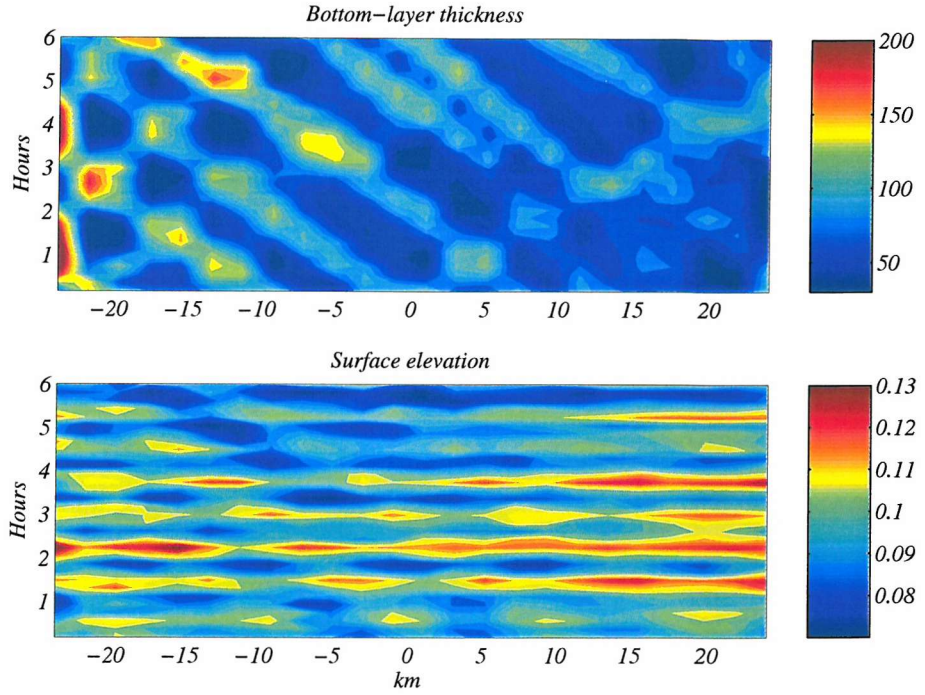

Figure 6.6: Hovmöller as in figure 6.4 at $y \sim -34.5$ km.

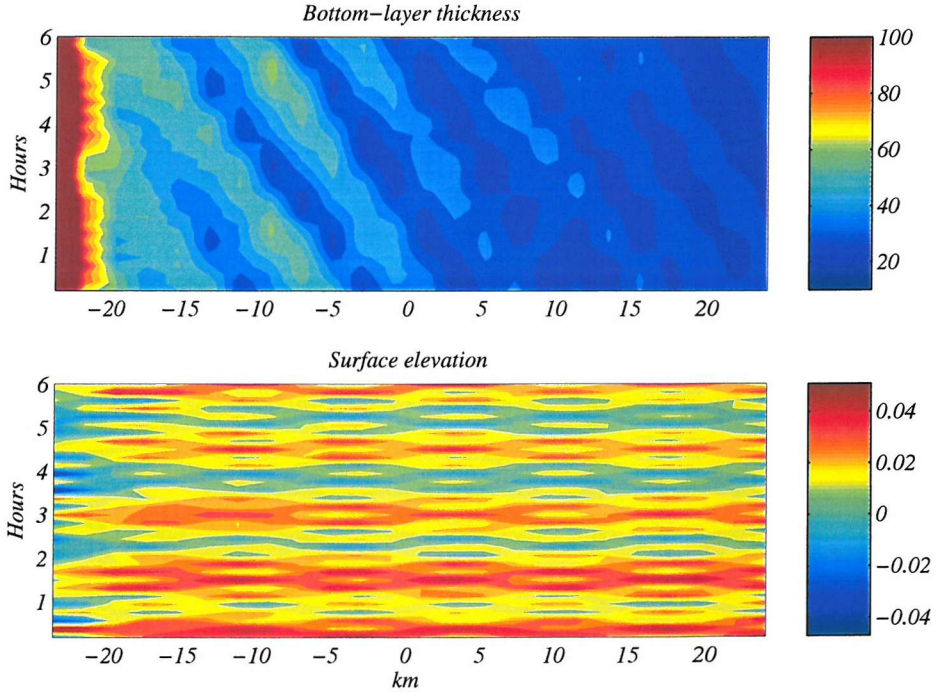

Figure 6.7: Hovmöller plot for a longer channel. The location of this section is equivalent to that in figure 6.4 in that both of there are taken at a height of 3500 m above the basin floors downstream of the sill.

In the upstream (eastern) basin, at the top of the plots, the circulation in the top layer is dominated by a strong anticyclonic gyre which exhibits speeds exceeding 0.8 m/s. This is reminiscent of the surface gyre observed in the Alboran Sea which is driven by fresh Atlantic surface water entering the western Mediterranean. This gyre has been observed

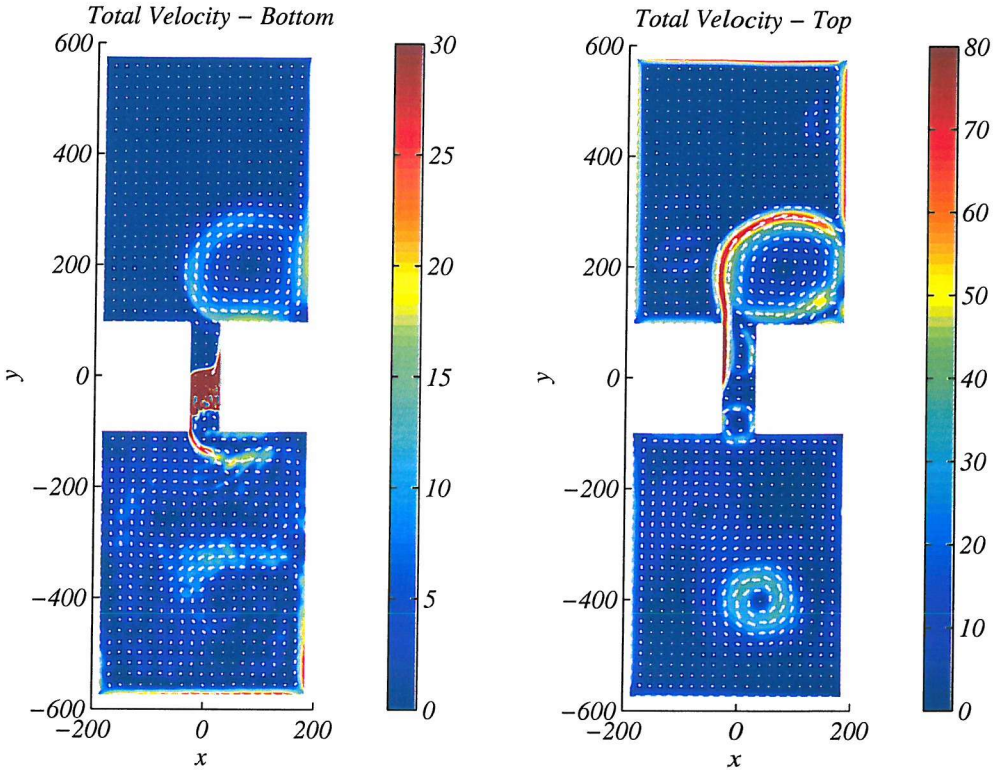

Figure 6.8: Snapshot of the basin circulation during the shallow channel experiment after 0.0625 days (90 minutes). Bottom layer on the left and top layer on the right. The basin at the top is the dense (eastern) reservoir and the lower basin the lighter (western) basin, left therefore corresponds to north and right to south.

during field observations and in numerical experiments by Herbaut et al. (1996) who investigate the response of the circulation in the Western Mediterranean to the forcing of the inflow through the Strait of Gibraltar. In the Alboran Sea the horizontal extent of the gyre is restricted due to the surrounding land masses. Herbaut et al. (1996) report gyres of 80 km to 150 km for different types of experiments, while field observations by Gascard and Richez (1985) report similar dimensions. The gyre in our upstream basin is roughly 200 km in diameter but it is not restricted by land masses since the channel opens sharply into a basin that is 400 km wide.

The gyre splits at the southern wall and part of it continues east as a boundary current, much like the boundary current observed along the African coast in the simulations by Herbaut et al. (1996). They find however that this current, in agreement with observations, develops meanders with horizontal scales reaching 80 km as it travels east, which we do not find here. The part of the gyre which does not split of as a boundary current eastward, continues to circulate and eventually comes back to the entrance of the sill where some of the flow splits again re-enters the channel.

The bottom layer in the upstream basin is thicker and therefore less dynamic than the top layer. The anticyclonic gyre of the top layer penetrates down into the bottom layer forced by the transfer of momentum through the hydrostatic pressures at the interface, but velocities do not exceed 0.15 m/s.

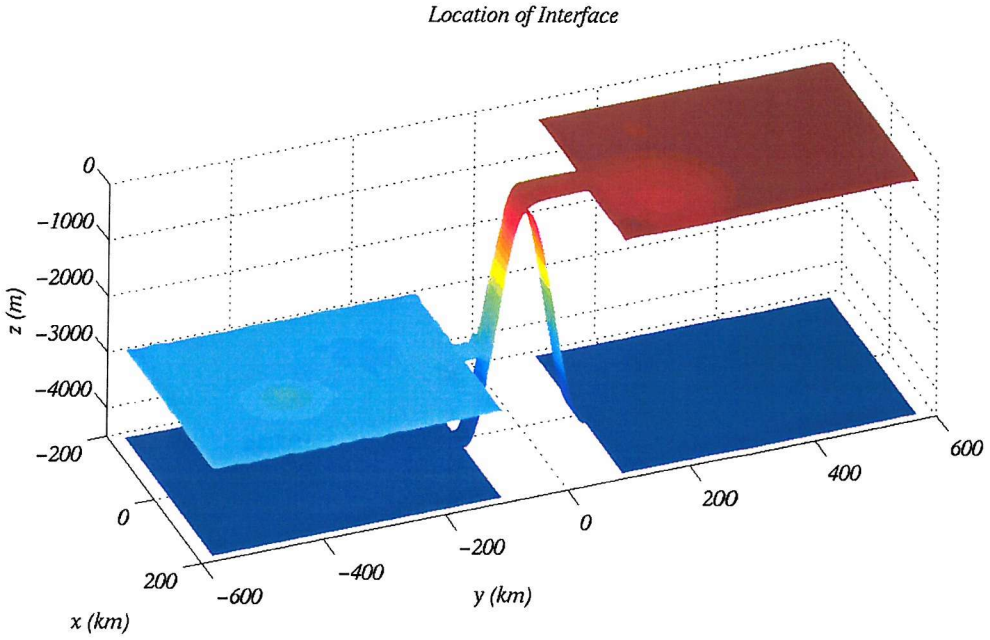

Figure 6.9: Instantaneous surface plot of the interface height in the shallow channel and the adjacent basins above the topography. Upstream relaxation is -212.5 m and downstream -3000 m.

In the downstream basin the top layer is much thicker and thus significantly less active. The only striking feature here is a much weaker cyclonic gyre of about 150 km across which is stationary close to the centre of the basin, velocities in the gyre reach no more than 0.4 m/s; the process giving rise to this gyre is not obvious.

The bottom layer circulation in the downstream basin on the other hand is driven by the boundary current which developes on the left-hand wall of the channel and enters the basin as a jet. This jet turns sharply to the right and forms a boundary current on the southern wall travelling west, analogous to the boundary current in the top layer of the upstream basin but much less dynamic. After travelling about halfway along the southern boundary of the basin the current separates from the wall and continues to flow towards the centre of the basin.

The effectiveness of the relaxation in the two basins is illustrated in figure 6.9, showing a snapshot of the interface height in the channel and both basin above the topography. Relaxation upstream is set to 212.5 m below the surface and downstream to 3000 m below the surface. The level of the interface is remarkably constant at the far end walls of both basins and is maintained during the entire experiment. Even at the points of entry into the channel the interface height has reduced only slightly compared to the relaxation height upstream. The most notable feature disturbing the upstream interface level is due to the gyre forming in the top layer as the surface water enters the upstream basins.

6.2.2 Deep Channel

The circulation pattern in the deep channel experiment is quite different from the one we observed in the shallower channel, however there are some fundamental feature that remain. The bottom layer velocities, shown in figure 6.10 are as usual very small upstream and as the flow approaches the sill it speeds up while the fastest velocities are along the right-hand side of the channel, as expected. At the top of the sill the current separates from the right-hand wall and crosses the channel forming a boundary current on the left-hand side. As the flow enters the subcritical downstream basin it becomes thick and sluggish again. The top layer circulation pattern shown in figure 6.11 again exhibits the remarkably consistent boundary current on the left hand wall with a mild recirculation to its right.

Downstream of the sill however the flow is much different to that seen in the shallow channel. We do not observe a large recirculating gyre that encompasses the whole channel, but rather we find a very sluggish flow over most of the downstream half of the channel. At the sill, between $y = 0$ and -30 km, we find time varying flow features in both the bottom and the top layer. In the top layer small eddies from in this region and propagate across the channel, while the overflow in the bottom layer pulsates periodically across the channel. No finger-like instabilities are observed in this experiment.

Time variability in the channel

The time variable features in the bottom is dominated by a periodic meandering and spreading of the current crossing over at the top of the sill, while in the top layer the crossing-over of the flow takes the form of cyclonic eddies separating from the right-hand wall and moving toward the left-hand side of the channel, where they merge with the boundary current and intensify it. This periodic behaviour which is easily observed, can be directly linked to the flux oscillations at the top of the sill. Figure 6.12 gives an indication of the changes in flux across the section at the top of the sill and an oscillation of magnitude 0.5 Sv and period 4 days is observed. In contrast to the previous example the magnitude of the oscillations are the same in both layers but they are less smooth. We will outline the detailed changes in the flow features associated with the flux oscillations with figures 6.10 and 6.11 for the bottom and the top layer respectively.

In the left panel of figure 6.10, which is a snapshot of the flow at day 1.25, the bottom layer exhibits a jet which meanders across the sill from the right-hand wall to the left-hand wall and then picks up speed down the slope before entering the downstream basin. The top layer shows patterns which can to some extent be matched to those in the bottom layer (first panel in figure 6.11). Overlying the jet initially separating from the right-hand wall is a jet of top layer fluid crossing the sill in the same direction as the bottom layer, that is against the net flow in the top layer. This jet is fed from another jet further across the channel directed upstream and overlaying the second meander in the bottom layer and this second jet in turn merges with the boundary current along the left-hand wall.

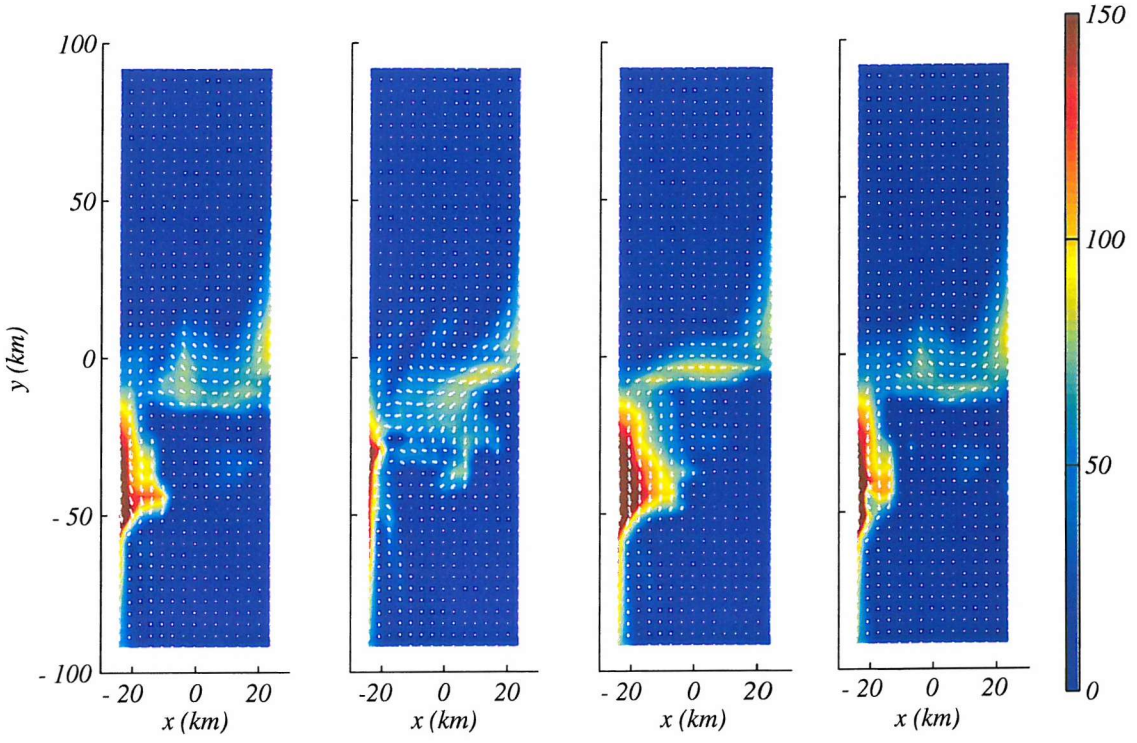

Figure 6.10: Snapshot of the velocity field from the deep channel experiment in the bottom layer at day 1.25, 2.5, 3.75 and 4.74, from left to right.

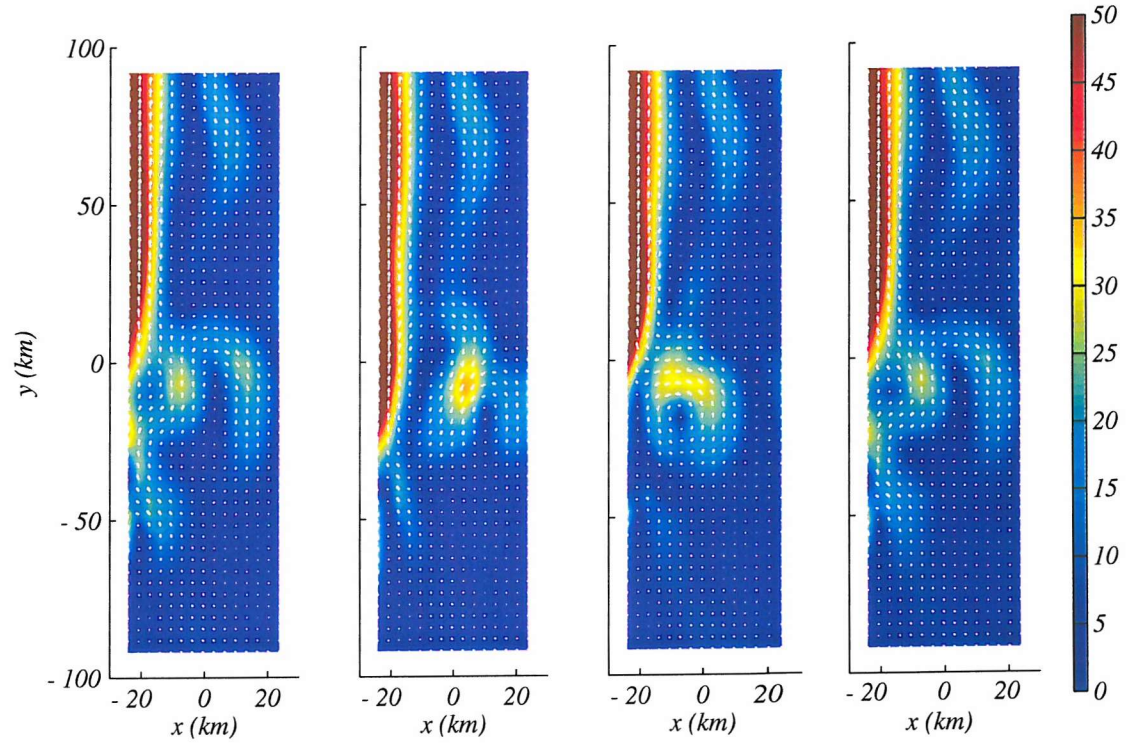

Figure 6.11: Same as figure 6.10 for the top layer.

This flow configuration corresponds to the first peak in flux across the sill present in figure 6.12.

The second panel in figures 6.10 and 6.11 captures the flow-field at day 2.5 where the flux across the sill is almost at its lowest point. The top layer jet which was previously in

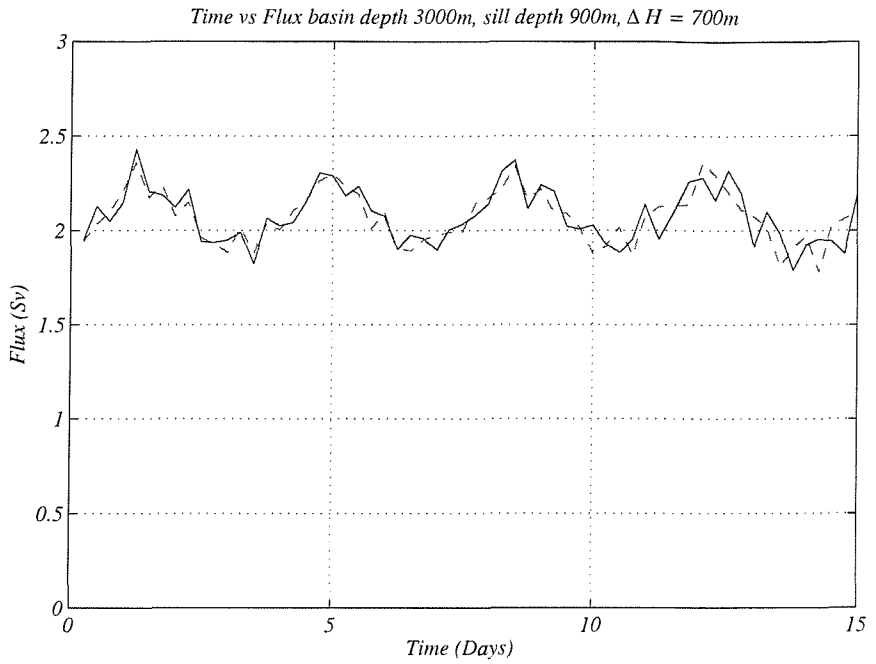

Figure 6.12: Flux through a section at the top of the 900 m sill as a function of time. The oscillations in the top layer (continuous line) have the same magnitude - 0.5 Sv - as those in the bottom layer (dashed line). Both have a period of about 4 days.

the process of merging with the boundary current has now merged fully and as a result the boundary current extends well beyond the crest of the sill and starts at $y \sim -30$ km on the downstream side of the sill.

The current which separated from the right-hand wall in the bottom layer has broadened and parts of it are now moving straight down the slope. Overlying this part of the flow at the right-hand wall a new eddy is forming in the top layer about to move across the channel towards the boundary current.

At day 3.75, shown in panel three of both figures the flow is starting to recover its peak value. The separated current in the bottom layer has become pinched off at the wall and leads into a jet moving straight across the channel without any meander forming. The downstream flow which was previously spread over the entire slope is now confined to a strong boundary current about 20 km wide.

In the top layer the eddy is moving gradually towards the left-hand boundary and the boundary current has retreated again towards the sill, where it now starts at $y \sim 0$.

At day 4.75, the last panel in figures 6.10 and 6.11, the flow pattern has returned to the same state as on day 1.25 and the flow across the sill has reached a peak again.

Figures 6.13 and 6.14 show the bottom layer thickness and surface elevation at the same times as the velocity fields shown. On inspection one observes that the flow patterns in both layers can be associated with regions of strong gradients in the plots of bottom layer thickness and surface elevation.

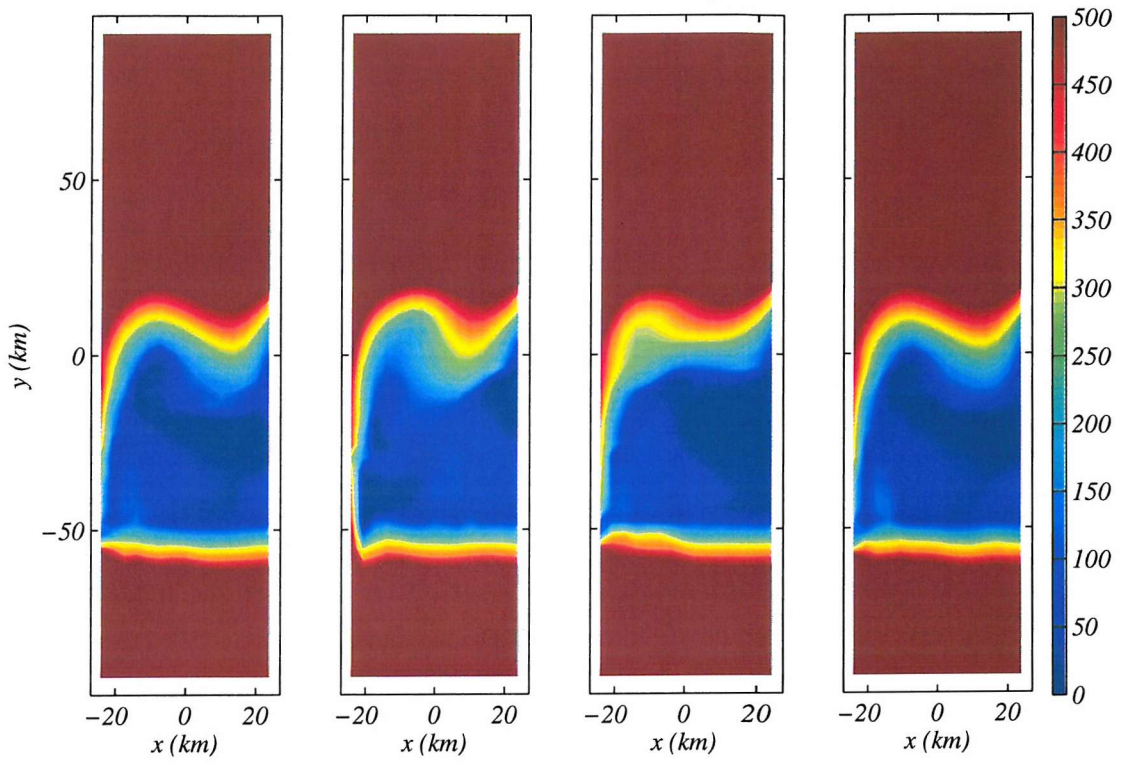

Figure 6.13: Snapshot of the bottom layer thickness from the deep channel experiment at day 1.25, 2.5, 3.75 and 4.74, from left to right.

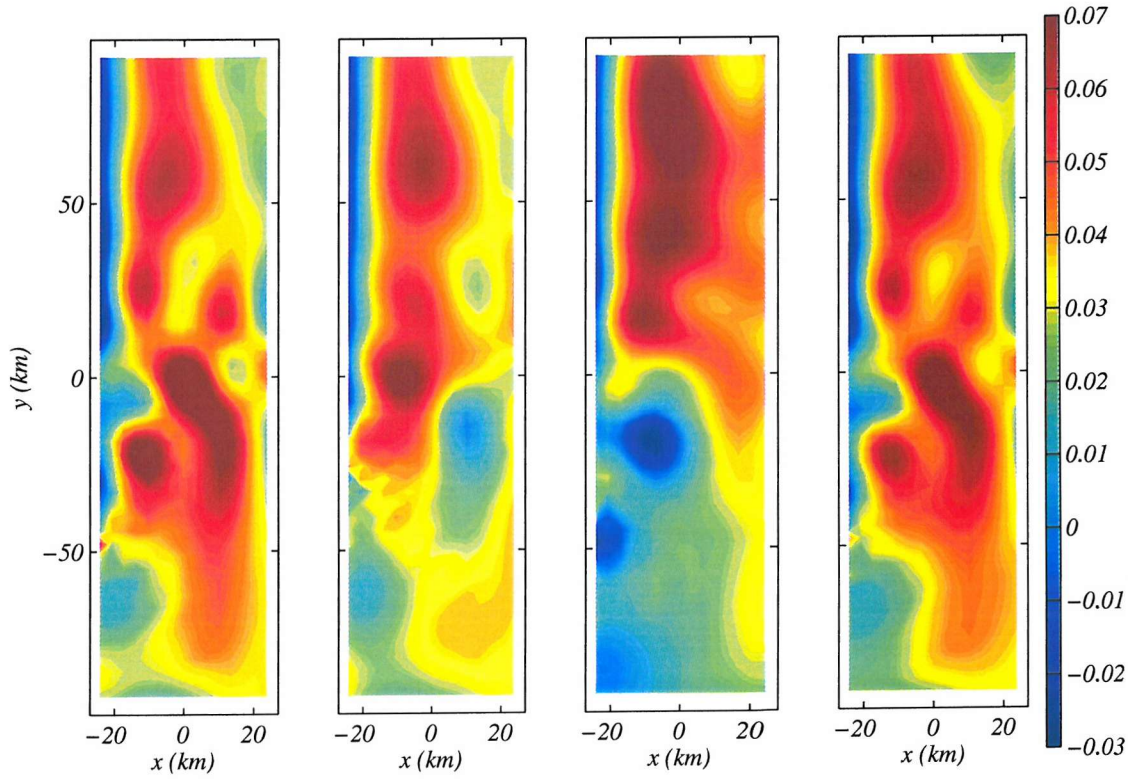

Figure 6.14: Same as figure 6.13 for the top layer.

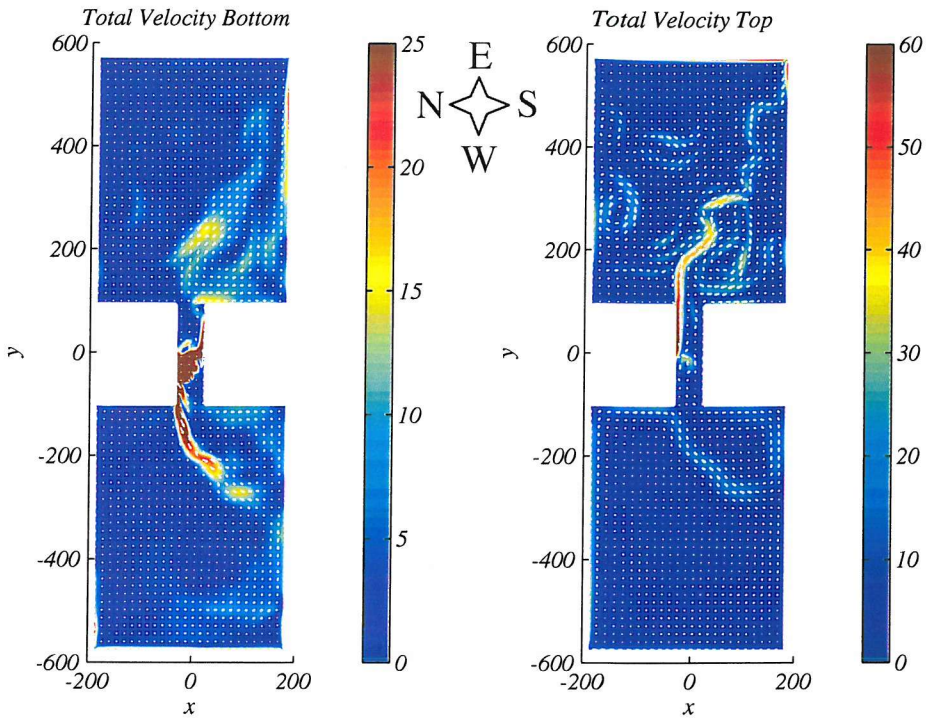

Figure 6.15: Same as figure 6.8 but with a 900 m deep channel and basins of depth 3000 m. Snapshot taken from day 3.75. The compass rose between the plots illustrates the orientation of the channel and the basins.

Basin circulation

The basin circulation for this experiments is shown in figure 6.15. It exhibits a lot more variability than that in the shallow-channel example. This may be partly because the basins are set to 3000 m depth here as opposed to 4500 m in the previous example; this means that the layers will on average be thinner and more dynamic since they carry roughly the same amount of flux.

In the top layer of the upstream basin we do not observe one neat and non-variable gyre and boundary current on the southern wall, but rather the jet entering the upstream basin meanders gradually towards the southern wall. The circulation in the top layer is therefore characterised by a highly variable flow field dominated by meanders and eddies, a pattern more akin to the meandering Algerian current modelled by Herbaut et al. (1996).

In the bottom layer a boundary current along the southern wall flows west towards the channel opening, some of it enters the channel but the bulk of the flow turns eastward and recirculates.

The downstream basin is dominated by the jet in the bottom layer which enters the basin from the left-hand wall of the channel and proceeds south-west towards the southern wall of the basin, where it splits into a westward and an eastward boundary current. The eastward current recirculates towards the channel entrance where some of it enters the channel but most joins the jet exiting the channel and continues recirculating.

Figure 6.16, analogous to figure 6.9, shows an instantaneous snapshot of the interface between the two layers above the topography for a channel with a deep sill and shallower

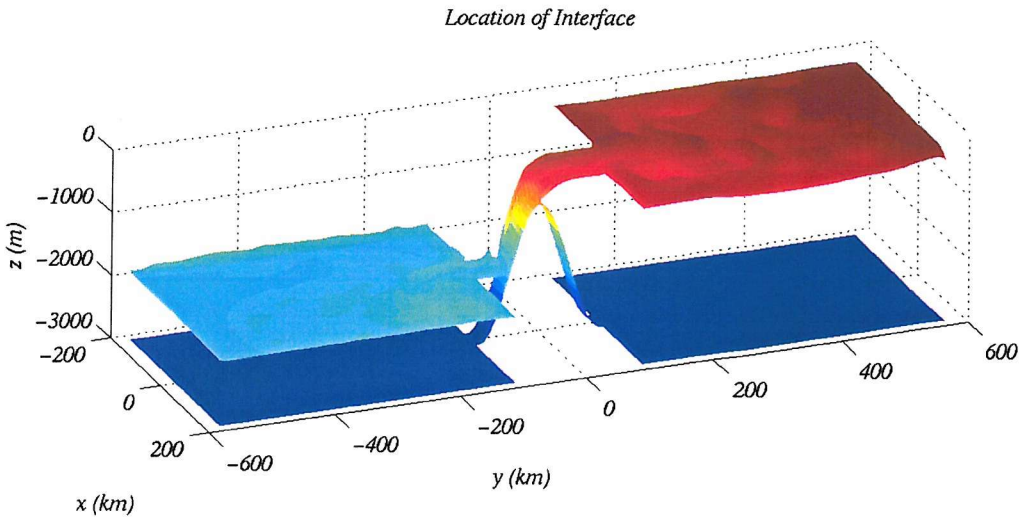

Figure 6.16: Same as figure 6.9 but with a 900 m deep channel and basins of depth 3000 m.

basins. The relaxation heights are set to -300 m and -2000 m in the upstream and downstream basins respectively and are maintained well during the experiment. In comparison to the interface in the shallow channel experiment there is a lot more variability seen in the interface of this experiment. By the time the flow enters the channel the interface will have reduced somewhat from its relaxation value and there is a very distinct tilt across the channel with the interface being lower on the right-hand side of the channel than on the left.

6.3 Locating the controls

From hydraulics we know that the control sections are vital in determining the flow elsewhere in the channel. Therefore we have adapted the method outlined in chapter 3.3, for deriving the wave-speeds in the analytical study of two-layer rotating hydraulic flows, to derive the speed of free long-waves from the MICOM results. As before it basically involves expressing the velocity, layer thickness and pressure fields in the flow in terms of a mean flow and a perturbation about the mean, for example: $u_1 = \bar{u}_1 + u_1'$. The momentum and continuity equations can then be rewritten as functions of several unknowns, the perturbations, with coefficients determined from the mean state of the flow. Finally, the perturbations can be expressed as a wave: $u_1'(x,y) = u_1'(y)e^{ik(x-ct)}$ and so the problem can be formulated as an eigenvalue problem in the following matrix form:

$$\mathbf{AX} = c\mathbf{BX} \tag{6.2}$$

where $\mathbf{A}$ and $\mathbf{B}$ contain the coefficients of the mean fields determined from the MICOM results, $\mathbf{X}$ is the eigenvector consisting of the unknowns (the perturbations) and c is the

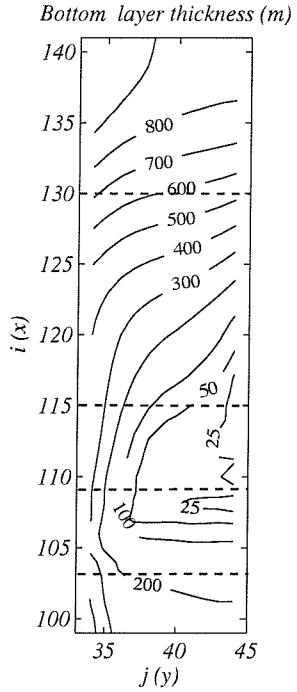

Figure 6.17: Contour plot of the bottom layer thickness at day 20 from the resolution test experiment with a gridsize of 0.05 degrees.

characteristic wave speed associated with each perturbation. More details of the analysis are given in appendix D and a successful test carried out for one of the non-rotating experiments is described.

Applying the method to a rotating example is not as straightforward and the results are less conclusive. Nonetheless we feel it is worthwhile to show the results and discuss their applicability. We intend to try and refine the process in the future in order to apply it to other examples of rotating flows and achieve more conclusive results.

We chose data from day 20 of the medium-resolution test, described in section 5.1.3, to apply the analysis to. It was decided not to use either of the two cases outlined in the previous section for two reasons, firstly because they have a higher resolution leading to a much larger number of possible wave-speeds (eigenvalues) to filter and the decision process to find the right eigenvalue is thus much trickier. Secondly, both experiments show a lot of time varying features, which compromises the clarity of the wave-speed analysis.

The medium resolution experiment exhibited less time variability and also had fewer grid points across the channel, making it easier to analyse and interpret. The choice to use the data from day 20 was somewhat arbitrary, however it should be noted that it is not possible to apply the method to a flow that is separated like the one at day 30, which we discuss in reference to the resolution. This is because the analytical problem changes if only one layer is present and thus the analysis presented does not apply.

In figure 6.17 the thickness of the bottom layer at day 20 of the aforementioned experiment is shown. The sill is located at $i = 120$ and as usual the downstream basin (light reservoir) is at the bottom of the plot while the upstream (dense reservoir) is at the

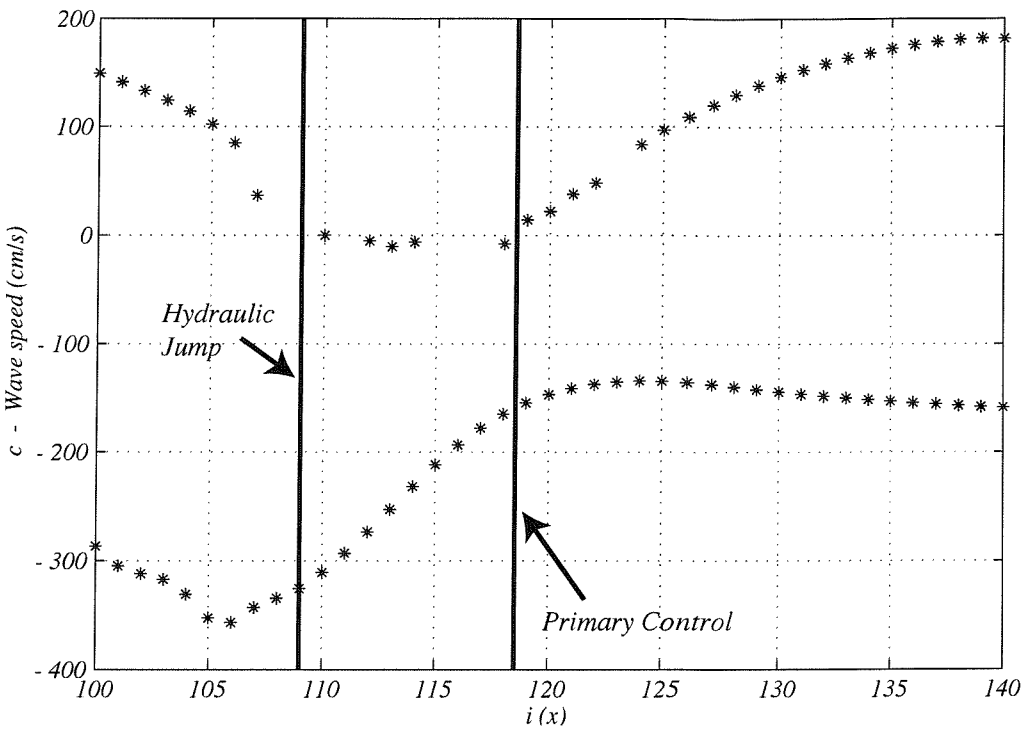

Figure 6.18: Wave-speeds for each section along the channel corresponding to the zeroth mode wave. Determining the right eigenvalues is difficult, hence there are some gaps in the series. The critical sections due to the primary control and the hydraulic jump are indicated by vertical lines.

top. The dashed lines mark the sections along the channel for which we have included the eigenvectors in figures 6.19 to 6.22.

The typical flow features of the crossing-over and the boundary current can be made out in figure 6.17. To the right of the boundary current the bottom layer becomes very thin but never much less than 25 m, and does not separate completely anywhere along the channel.

In this example, a submaximal case, we expect to see two critical regions. The first one, associated with the primary control, will be located close to the top of the sill. We know that friction will displace this control somewhat downstream and thus we expect it to lie somewhere between $i = 115 - 120$. The second critical region will be in the form of an hydraulic jump where the overflow comes in contact with the layer of dense water in the downstream basin. In this case we would expect to find it between $i = 105 - 110$.

Figure 6.18 shows the wave-speeds along the channel, which have been computed and selected by the methods outlined in appendix D. There are two wave-speed for each section along the channel and, as expected, upstream of the sill ($i > 120$) one speed is positive and one negative, the flow is subcritical. Just after the sill, between $i = 119$ and $i = 118$ one of the wave-speeds passes through zero and it is between these two point that control occurs. The flow is then supercritical until $i = 110$, indicated by both wave speeds having values less than $c = 0$. At $i = 110$, $c = 0$ and confirms our claim that the second control would lie close to the hydraulic jump. For $i < 107$ the second wave-speed is clearly positive again and the flow is subcritical.

Unfortunately there are several gaps in the plot making a continuous tracing of the wave-speeds difficult. The reason for the omissions is the difficulty in deciding on and picking the right eigenvector that corresponds to the first mode of the perturbation of the long-wave. In the non-rotating case we chose the most uniform and constant eigenvectors of v_1' across the channel and picked the corresponding eigenvalues. The choice was unambiguous in this case. Here we have chosen to base the decision process first of all on the monotonic character of the eigenvectors of the interface height perturbation h_1'.

In figure 6.19 some of the eigenvectors are shown for the section $i = 130$ and the smoothest are quite clearly the first two, which are also monotonic. The eigenvalues plotted in figure 6.18 at $i = 130$ are those corresponding to these two eigenvectors.

Figure 6.20 illustrates the difficulty in choosing the right eigenvector at section $i = 115$. The first one can again be picked using the monotonic criterion, and the associated eigenvalue links nicely with the prior negative wave speeds close to the sill. However none of the other vectors are monotonic or very smooth and it is difficult to tell which one we would expect to be the appropriate second vector to chose.

Figure 6.21 shows the eigenvectors at $i = 109$. In this case using simply the monotonic criterion will pick out the first two eigenvectors. However, experience suggests that we want to trace one eigenvector with a maximum on the left hand side of the channel and one with a maximum on the right hand side. For this reason we need another criterion which will select vector one, the smoother one, over vector two. We therefore introduced a second criterion for filtering the vectors, which is that the second derivative should not change sign anywhere along the profile of the vector. This will eliminate the second vector. It still leaves us short of the other appropriate eigenvalue which should lie close to zero. Vector 14 seems the most likely candidate, but our selection mechanisms are not refined enough to select this value.

The eigenvectors at $i = 103$ are shown in figure 6.22 and here the flow is in the subcritical region downstream of the hydraulic jump. The two smoothest monotonic curves without any sign changes in the second derivatives are the first and third, again one has a maximum on the right and the other one has a maximum on the left. At this section the criteria we employed to choose the vectors work well and the corresponding eigenvalues are plotted as the wave speeds in figure 6.18.

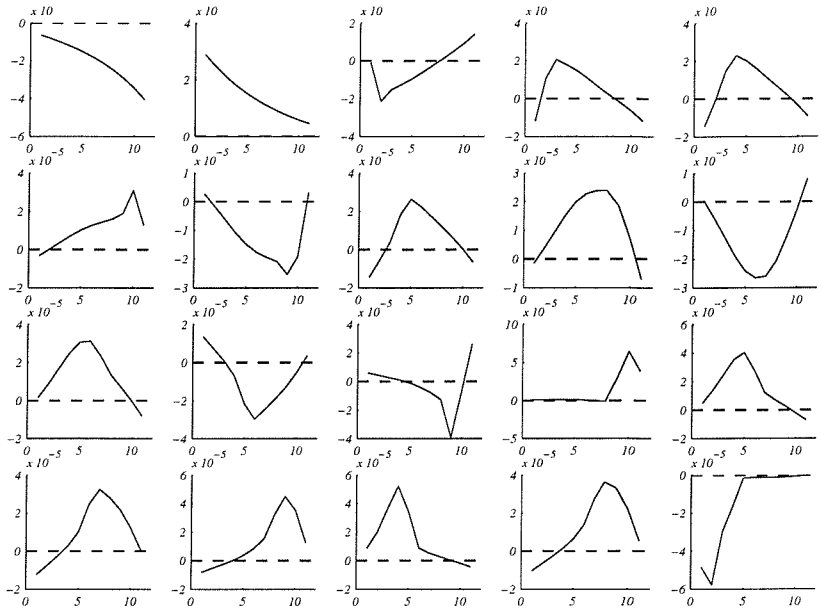

Figure 6.19: Eigenvectors for h_1', the perturbation at the interface, at $i = 130$. The dashed line indicates $h_1' = 0$ for reference.

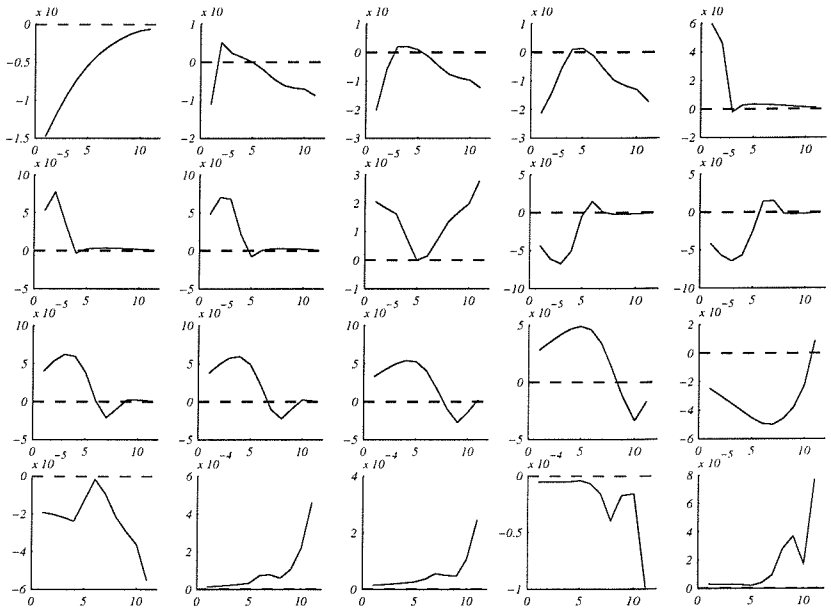

Figure 6.20: Same as figure 6.19, at $i = 115$.

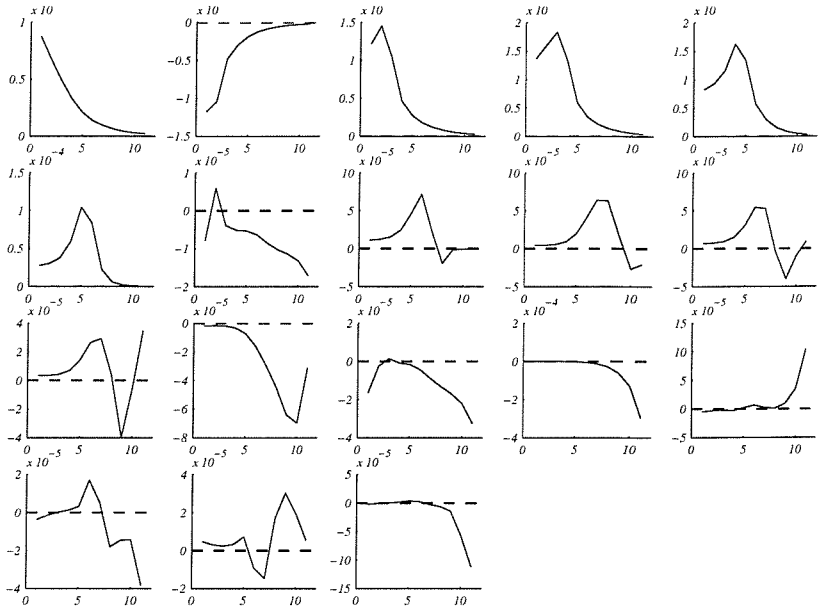

Figure 6.21: Same as figure 6.19, at $i = 109$.

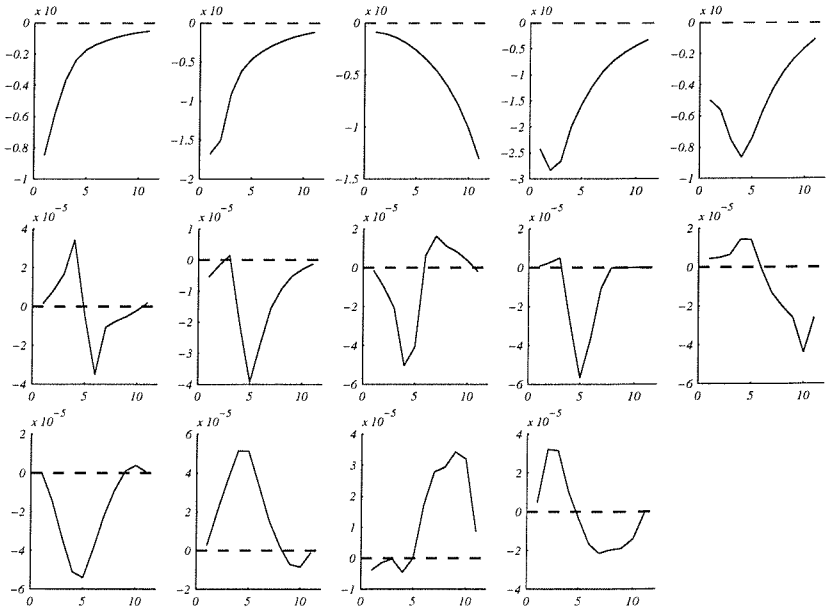

Figure 6.22: Same as figure 6.19, at $i = 103$.

6.4 Parameterisation of the flux results from MICOM

The primary aim of this modelling study was to develop a parameterisation of the flux in a two-layer exchange through an idealised channel. In this section we will use the MICOM results to derive such a parameterisation in terms of the upstream interface height $\Delta H^\star$ and the non-dimensional width L; the asterisk (*) here denotes a non-dimensionalised parameter from MICOM and the non-dimensionalisation used is analogous to the one used in chapter 3 for the rotating hydraulic theory and recapped in the previous chapter. This work presents the first attempt, as far as we are aware, to use results from a numerical model to derive a parameterisation for two-layer exchange flows; previous estimates have primarily been derived from theoretical studies.

6.4.1 Flux dependence on ΔH

A statistics package was used to perform a least squares fit of the log of the flux data against the log of $\Delta H^\star$ in order to find a power law relationship between the primary variable ($Q^\star$) and the subsidiary variable ($\Delta H^\star$).

All MICOM results are plotted in figure 6.23 on a log scale and it can be seen that the relationship between them is linear to a good approximation, with the solid line indicating the least squares linear fit. The slope of the fit is given as 1.48016 ± 0.03805 and we can therefore say that it is 1.5 to a good approximation. The results have an $r^2 = 0.957$, which means that 95% of the variations in the data are accounted for by this relationship, and the p-value which is $\ll 0.05$ tells us that the resulting fit is highly significant and not merely a chance result.

Thus the non-dimensional expression for the flux in terms of $\Delta H^\star$ may be written as follows

$$Q^\star = 0.2\,(\Delta H^\star)^{3/2} \tag{6.3}$$

or dimensionally:

$$Q = 0.4\frac{g'\Delta H^2}{2f}\left[\frac{\Delta H}{H_0}\right]^{-1/2}. \tag{6.4}$$

How well this fit reproduces the non-dimensional fluxes can be seen in figure 6.24 where all MICOM fluxes are plotted using different symbols to distinguish between the experiments and the solid line is the fit we derived above. Although the fit is very good for small $\Delta H^\star$, as the upstream interface height increases the scatter about the fit becomes larger and towards $\Delta H^\star \sim 1$ overestimates the flow with respect to all the model results. For some of the experiments an error bar has been added to give an indication of the uncertainty as well as the possible variability in time of the modelled fluxes. A full set of errors of all experiments is listed in the tables in appendix C.

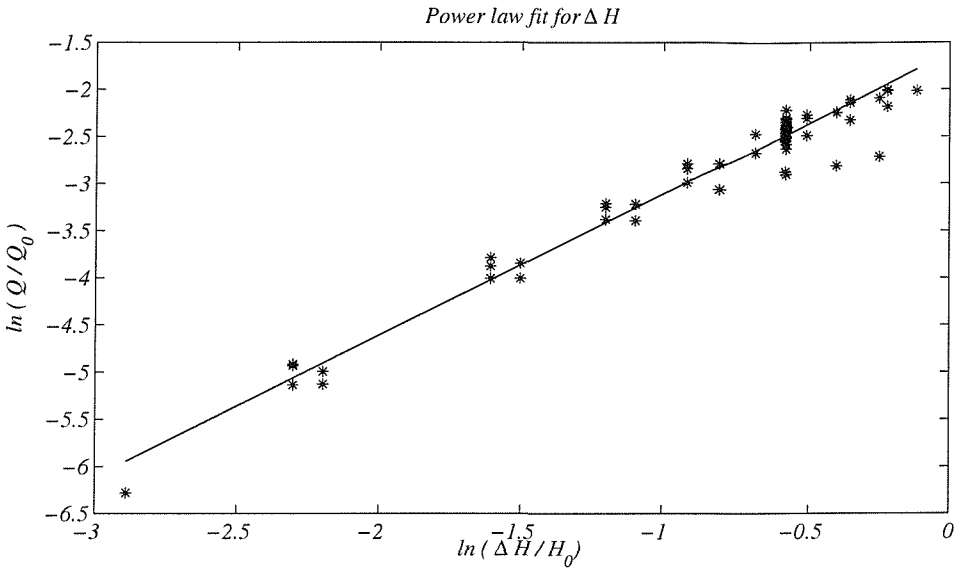

Figure 6.23: Logarithmic plot of all nondimensionalised MICOM flux results against the nondimensional upstream relaxation height. The slope of the linear fit is about 1.5 suggesting a dependence of the flux on $\Delta H^{3/2}$. $r^2 = 0.957$ for this fit.

The dependence of the flux on $\Delta H^{3/2}$ is unexpected for the rotating case. It does apply for non-rotating flows and has been observed in a recent study by Hansen et al. (2001) for the flux through the Faroe Bank Channel, but the physics giving rise to this dependence is not well understood.

6.4.2 Flow dependence on channel width

Notice that the previous analysis implicitly assumed that the dependence of the flow on f, the Coriolis parameter, and g', the reduced gravity, were as we would expect them from theory, namely $Q \sim f^{-1}$ and $\sim g'$. In order to ascertain how the flux responds to changes in f and g' it seems sensible to explore the flux dependence on L. In order to find a relationship for the flux in terms of the width of the channel, $\Delta H^\star$ has to be fixed, since the flux will vary with L as well as with $\Delta H^\star$. The largest set of results we have for a fixed $\Delta H^\star$ are those with $\Delta H^\star \sim 0.557$ and we used these to explore the dependence of the flux on L.

The general notion is that the flux ceases to increase after the width of the channel exceeds a certain width in terms of Rossby radii, or put differently, an increasing rotation rate will act to limit the flow and ultimately serve to prescribe an upper limit on the flux through a channel.

The theoretical analysis carried out by Dalziel (1988) (excluding the possibility of back flow in the top layer) and his laboratory experiments confirm that the flux in terms of the channel width behaves like an inverse exponential, it increases initially with L and then asymptotically approaches an upper limit. We assume this behaviour applies for the experimental data too and propose a fit to the MICOM data in the form of $c_1(1-e^{-L/c_2})$,

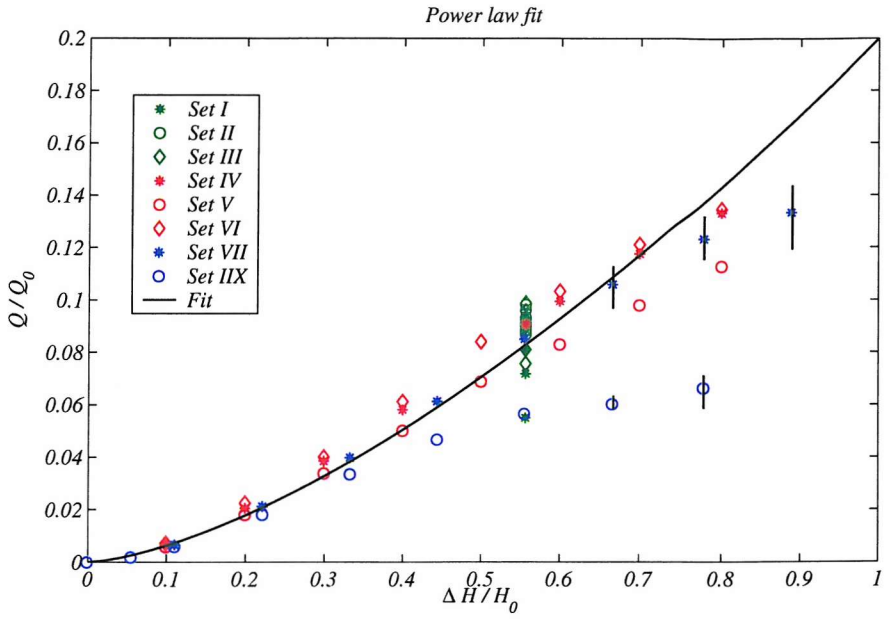

Figure 6.24: Illustration of the goodness of the fit given by expression (6.3). The various symbols mark the fluxes obtained from the various MICOM experiments, and the solid line is the described fit to the data in terms of $\Delta H^\star$. An error bar on some of the results gives an indication of the uncertainty and variability to be expected from the results. For most experiments the estimated non-dimensional error is encompassed by the size of the symbol presenting it.

where c_1 and c_2 are constants to be determined such that they minimise the sum of the squares of the difference between the actual data and the proposed fit:

$$\min \sum_{i=1}^{n} \left[Q_i^\star - c_1(1 - e^{-L_i/c_2}) \right]^2 . \tag{6.5}$$

c_1 and c_2 were numerically determined to be 0.09465 and 0.74706 respectively.

The resulting equation in non-dimensional variables is:

$$Q^\star = 0.095(1 - e^{-L/0.747}) \tag{6.6}$$

or again dimensionally:

$$Q = 0.095 \frac{g' H_0^2}{f} (1 - e^{-\frac{W}{0.747} \frac{f}{\sqrt{g' H_0}}}) \tag{6.7}$$

The flux results for all experiments with $\Delta H^\star \sim 0.557$ are plotted in figure 6.25 along with the above non-dimensional expression for the flux in terms of L (solid line). Since the flow we have modelled here is submaximal the maximum flux of 0.095 approached by the flow is less than the estimate of 0.16 made for maximal flow by Dalziel (1988) and Whitehead et al. (1974) and which we also derived from the theory.

6.4.3 Complete parameterisation

To derive an expression for the flux in terms of both $\Delta H^\star$ and L, we multiply (6.4) and (6.7) and approximate c_2 by 0.75 to get:

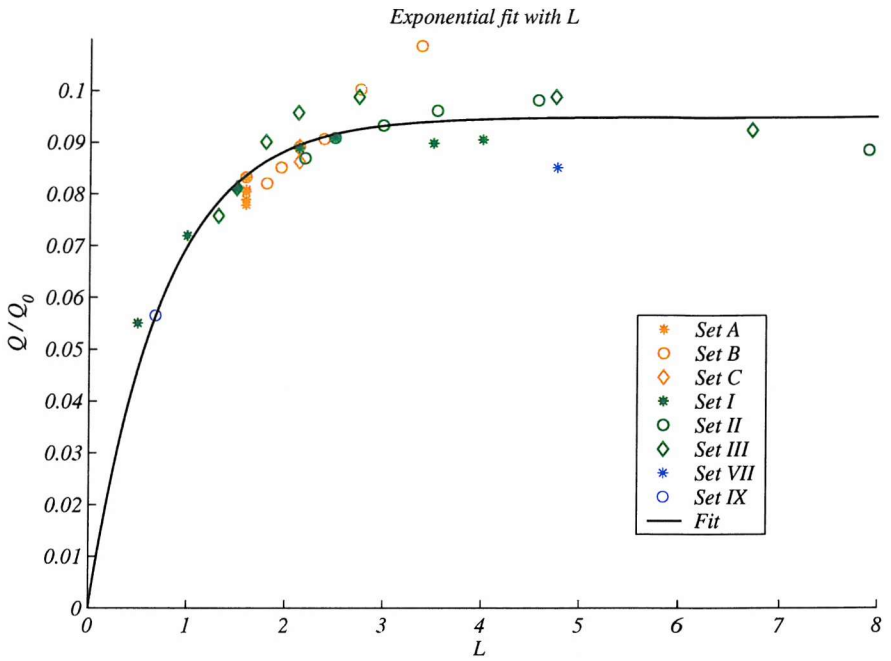

Figure 6.25: Illustration of the goodness of the fit given by expression (6.7). The various symbols mark the fluxes obtained from the different MICOM experiments and the solid line is the described fit to the data in terms of L.

$$Q^{\star} \sim \Delta H^{\star 3/2}(1 - e^{-L/0.75}) \tag{6.8}$$

A fit of the non-dimensionalised flux results from MICOM against the estimates using this new expression tells us that the constant factor by which (6.8) needs to be multiplied to approximate a 1:1 correspondence between the MICOM data and the estimated fluxes is ~ 0.22. We therefore arrive at the following final parameterisation:

$$Q = 0.22\frac{g'\Delta H^2}{f}\left[\frac{\Delta H}{H_0}\right]^{-1/2}(1 - e^{-\frac{Wf}{0.75\sqrt{g'H_0}}}) \tag{6.9}$$

If we use a Taylor expansion for $e^{-L/0.75}$, we find that as $L \to 0$ the flux reduces to $Q = 0.29\sqrt{\Delta H g'}\Delta HW$ to first order (after eliminating terms containing L^2 or larger powers). This estimate is an approximation of the limit as rotation goes to zero and should therefore agree with the non-rotating theory. Farmer and Armi (1986) determine the two layer exchange over a sill to have a transport of $Q = 0.208\sqrt{H_0 g' H_0}W$. The limit we find by equating $\Delta H = H_0$ is therefore almost 50% larger than predicted by the theory. The main reason for this is most likely that we have only a very limited number of experiments which approach the non-rotating limit in the sets used to derive the empirical formula. We have shown in the previous chapter that purely non-rotating channels approach the limit derived by Farmer and Armi (1986) well.

A plot of the non-dimensional MICOM fluxes against the estimated fluxes from equation (6.9) is shown in figure 6.26 and for most of the results which lie around the fitted line the approximation is remarkably good. As the flux approaches the maximal limit,

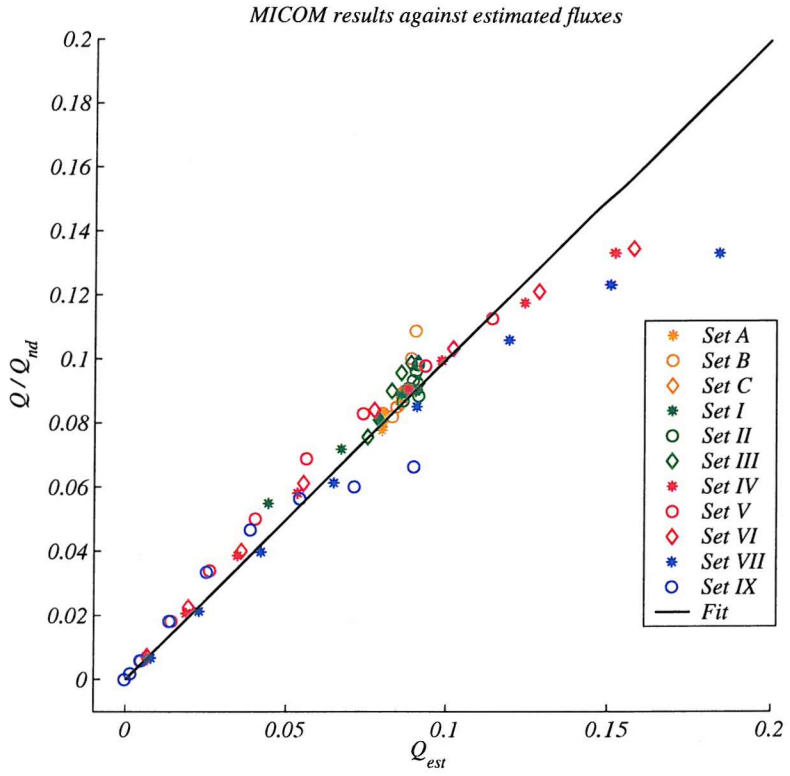

Figure 6.26: Plot of the non-dimensional MICOM fluxes against the estimated fluxes from equation (6.9). This fit has an $r^2 = 0.97$.

however, and ΔH approaches 1 the expression we derived overestimates the flow. Flows with larger ΔH are typically more time dependent than other flows, which may be one reason why a slightly different flow regime applies in this parameter space. We have already seen evidence for this in the results from the non-rotating experiment, there too the flux levelled off as ΔH approached sill depth.

How good and appropriate this fit is to examples of real oceanic straits will be discussed in chapter 7. First, in the next section, we will test the fit using results for $\Delta H^\star$ other than 0.557, which where not used to derive the dependence on L and also compare the fit with theoretical results.

6.4.4 Testing the fit and summary

There are limitations of the fit we have developed both in relation to the dependance of the flux on $\Delta H^\star$ and on the width L of the channel.

When investigating the dependence on $\Delta H^\star$ we have seen clear evidence that as $\Delta H^\star$ approaches 1 a different physical regime applies. As the top layer becomes thinner upstream it also becomes increasingly dynamic and where previously only the bottom layer was taking energy out of the system especially downstream of the sill, here the top layer becomes energetic and 'drains' energy out of the system upstream of the sill thus reducing the flow.

The limitation associated with the dependence on L arises because we deduced it using

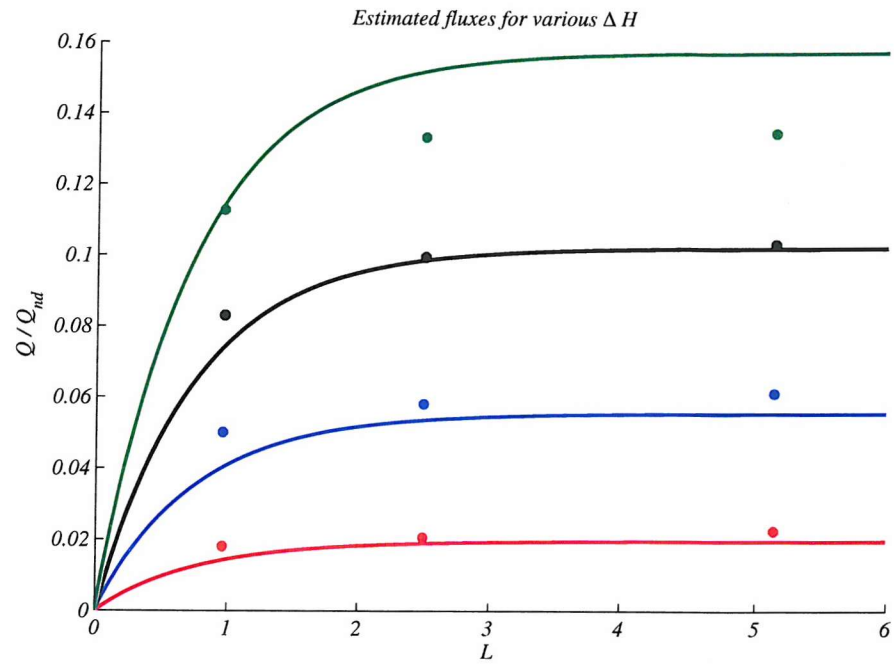

Figure 6.27: The solid lines are estimates of the flux for $\Delta H^\star = [0.2, 0.4, 0.6, 0.8]$ in red, blue, black and green respectively. The dots represent the actual results from the MICOM experiments for the corresponding $\Delta H^\star$ from Sets IV, V and VI.

a single fixed value of $\Delta H^\star \sim 0.557$, this means that the fit reproduced the fluxes with that $\Delta H^\star$ quite well but may be less representative for the dependence on L for different upstream interface heights.

We have some results amongst the experiments for other fixed values of ΔH and varying L, but we feel that these are too limited to derive detailed expressions for each. So we will simply use those results to test the parameterisation. To this end we have taken a sample from Sets IV, V and VI for $\Delta H^\star = [0.2, 0.4, 0.6, 0.8]$ and plotted them together with the corresponding curve for $Q^\star$ from equation (6.9) against the width of the channel in figure 6.27. The colours are red, blue, black and green for $\Delta H^\star = [0.2, 0.4, 0.6, 0.8]$ respectively.

$\Delta H^\star$ here correspond to interface heights in the upstream basin without the presence of any hydraulic jumps, and therefore the maximal case is approached as $\Delta H^\star \to 1.0$.

As predicted the estimates of the fluxes are very good for experiments with $\Delta H^\star < 0.6$ and for channels with $L > 2$, while it clearly overestimates the fluxes for larger $\Delta H^\star$. For narrow channels the agreement is better for larger $\Delta H^\star$ than for $\Delta H^\star < 0.6$, where the empirically derived formula underestimates the kind of fluxes which occur in MICOM.

In summary, we have found a fit for the fluxes in terms of $\Delta H^\star$ and L which works best for submaximal flows through wide channels. The maximal flow for a very wide channel with $\Delta H^\star = 1$ would be 0.22 which is higher than any theoretical estimate and (probably) overestimates most flows observed in the real ocean. The general behaviour of the transport across a sill is well reproduced in MICOM; in particular the characteristic effect of rotation of imposing an upper limit on the flux is emulated.

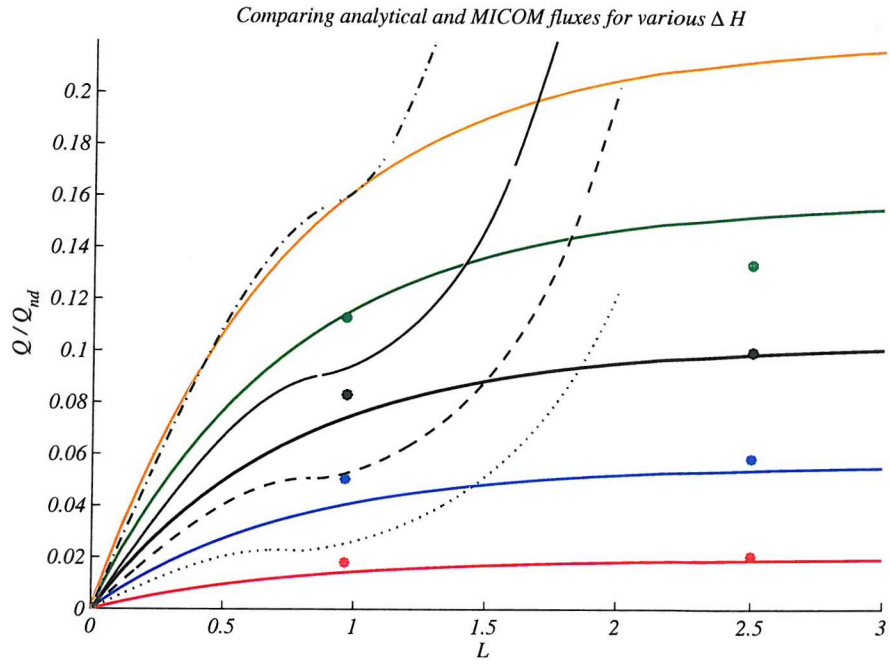

Figure 6.28: The solid lines are estimates of the flux for $\Delta H = [0.2, 0.4, 0.6, 0.8, 1.0]$ in red, blue, black, green and orange respectively. The dots represent the actual results from the MICOM experiments as in figure 6.28. The dashed-dotted, solid, dashed and dotted lines in black are the theoretical results for the flow as presented in figure 4.20 for $1 + \Delta E = [0.5, 0.4, 0.3, 0.2]$ respectively.

6.4.5 Comparison with the theory

A remaining question is how well do the results we have found here compare with the theory we developed in the first part of the thesis. In order to answer this question figure 6.27 has been merged with figure 4.20 and the comparison is shown in figure 6.28.

At first glance there seems to be little agreement between the predicted flux values from MICOM and the theoretical predictions of the fluxes. In that context however it also has to be said that the theoretical predictions hardly apply for channels wider than one Rossby radius.

As already outlined for the non-rotating experiments the ΔE we use in the theory as a measure of upstream interface height and the $\Delta H^\star$ derived from MICOM cannot be compared directly, since the former will have a value of 0.5 in the maximal case and the latter will be 1.0. For values in between there is no direct comparison.

The results for $1 + \Delta E$, which measure the interface height above the sill, are plotted in black with a dotted, a dashed, a solid and a dashed-dotted line for $1 + \Delta E = [0.2, 0.3, 0.4, 0.5]$ respectively. The colours for the MICOM estimates are as described in figure 6.27, with an added line for $\Delta H^\star = 1.0$, the maximal case.

If we consider the maximal case only then the agreement between the theory and the parameterisation we derived is very good up until a channel width of one Rossby radius. Equally on the lower end of the spectrum of results the theoretical estimate of the flux for $1 + \Delta E = 0.2$ at $L = 1$ agrees roughly with upper limit achieved by MICOM with $\Delta H^\star = 0.2$.

6.5 Conclusions

We have presented an extensive process study of two-layer rotating exchange flows, from which a range of interesting results emerged. The most enlightening discovery is that the exchange flows modelled are inherently unsteady and may exhibit a variety of time varying features, whose physical characteristics seem to depend crucially on the slope of the topography.

In terms of the flow features comparison between the theory and the flows modelled in MICOM is difficult, since we assume the theory to be steady which is clearly not true for the flows in MICOM. In general it can be said that the bottom layer in the upstream part of the channel is a much less active than has been observed in laboratory experiments for example or has been predicted from the zero potential vorticity theory. We see hardly any evidence of recirculation or back flow upstream. This is mainly due to the fact that we use very deep basins in MICOM and thus the bottom layer upstream of the sill is characteristically very thick and sluggish. Downstream of the sill the flow patterns are a lot more variable than any theoretical model of such flows, with instabilities forming that so far have not been observed in the field or the laboratory and are ignored by the steady theory.

The top layer also exhibits quite unique and little studied features. Qualitatively some of these can be compared to the flow patterns seen in the theoretical study. The main boundary current upstream of the sill is confined to the left-hand side of the basin and to the right we have back flow towards the down-stream basin, which is also modelled by the theory. However the backflow never extends along the entire channel as it does in the theoretical flows.

We have seen evidence for a topographic instability wave on the slope in the shallow channel experiment which occurs in a region that is often associated with intense mixing in oceanic overflows and which could be of interest for this reason.

To compare the fluxes quantitatively is not straightforward, especially because we assume zero potential vorticity and include back-flow in the analysis. As a result it seems the theoretical fluxes become unrealistically large as the channel widens. The opposite has been observed in both laboratory experiments Dalziel (1988) and our MICOM simulations. The flow here levels off as the channel widens and may even decrease slightly possibly due to a larger topographic area over which friction can act on the flow.

In saying that however we should point out that the behaviour of the flux with increasing ΔH follows a pattern that is similar to what we would expect from theory. Rotating hydraulics, like non-rotating hydraulics, predicts that the flow increases as ΔH increases. At $\Delta H = 0.5$ it reaches a maximum and then levels of, meaning that for all $\Delta H > 0.5$ the flux will be maximal. For different L the maximum will be different. We find that the dependence of the MICOM fluxes on ΔH follows a similar pattern, first the flux increases with ΔH and then approaches a maximum value as $\Delta H \to 1$.

This is in part the reason why the $\Delta H^{3/2}$ fit works well for $\Delta H < 0.5$ but less so

for larger ΔH. It would be worth in a future extended study of this problem to try and reproduce the theoretically predicted behaviour of the flux in the fit to the data, bearing in mind that any transition to a maximum flux will be less sharp than expected from theory.

Another way to improve the fit may be to take a measure of the interface within the channel close to the entrance to fit the fluxes against. A measure here will be independent of the variability and dissipation that occurs in the basins and essentially distorts the ΔH far upstream in the basin. A recent numerical study by Helfrich (2004) for a single layer case supports the fact that a measure closer to the control is necessary to capture the flow that is least influenced by the basin circulation.

Finally, in order to find the control sections in the MICOM experiments, we have developed a method for determining the wave-speeds at each section along the channel (see also appendix D for details). It allows us to test modelled as well as observed flows for the control section, and we have demonstrated that it gives conclusive results in a non-rotating example. In this chapter we have tentatively shown that computing the wave-speeds from the MICOM results for a rotating case can equally give us an idea where the controls lie, and the findings agree with the results we predict from the theoretical understanding of the flows.

It is realised that these results are not as clear and conclusive as we had hoped and some further work is needed to refine the process of determining the true wave-speeds at each section. It should however be noted that this may be very difficult indeed. We find that at certain sections, particularly in the region which we suspect is supercritical, several eigenvalues have very similar value and lie very close to zero. It could prove difficult if not impossible to distinguish them with absolute certainty.

A way forward may be to limit the number of eigenvalues by working with lower resolution experiments or to only use the results at every second gridpoint in the higher resolution experiment and apply the analysis to those.

Chapter 7

Modelling of the Denmark Strait and Faroe Bank Channel

The purpose of the work presented so far was to improve our understanding of flows through straits in the ocean and it is therefore appropriate to simulate one or two specific examples of exchange flows and outline what we have learned that can add to the present understanding of these flows.

We have chosen to set-up two experiments that approximately resemble the conditions of flow through the Denmark Strait, located between Greenland and Iceland, and the Faroe Bank Channel (FBC), between the Faroe Islands and the Faroe Bank, south-west of the Islands. These two channels constitute the major passageways through which the deep waters formed in the GIN Seas find their way into the North Atlantic as North-Atlantic-Deep-Water (NADW). For a brief specific review of the observed characteristics of these dense overflows from the Nordic Seas see Bacon (2002). Several of the references therein and other numerical and observational studies of these overflows have already been mentioned in the introduction.

The conditions of the bathymetry and watermass conditions for the Denmark Strait experiment were taken from Whitehead (1989) and Käse and Oschlies (2000), while those for the Faroe Bank Channel stem from Hansen et al. (2001), and they are listed in table 7.1.

Let us first describe the flow through the Denmark Strait and then the Faroe Bank Channel.

7.1 Denmark Strait

The basic set-up of the model was kept as it has been described in chapters 5 and 6, with two box oceans, here with a depth of 3000 m, separated by a rectangular channel, that deepens from 650 m down to 3000 m over 92 km, which is half the length of the channel. In reality the topography is much gentler in slope and decreases from 650 m down to 2000 m over more than 200 km. As a result it will be difficult and probably not quite appropriate to compare the flow pattern in the overflow plume to the observations,

Parameter	Denmark Strait (1)	Denmark Strait (2)	Faroe Bank Channel
$\Delta\rho$	0.3	0.5	0.5
ΔH	550 m	380 m	350 m
f	$1.3 \times 10^{-4} s^{-1}$	$1.3 \times 10^{-4} s^{-1}$	$1.3 \times 10^{-4} s^{-1}$
D_0	650 m	650 m	850 m
W	151 km	151 km	29 km
$Length$	184 km	268 km	184 km
D_{inf}	3000 m	2500 m	3000 m
a	10.6 km	13.7 km	15.7 km

Table 7.1: List of parameters for three runs set-up specifically to simulate the flows through the Denmark Strait and the Faroe Bank Channel. The values for the Denmark Strait in column 1 are taken from Whitehead (1989), those in column 2 from Käse and Oschlies (2000). The set-up for the Faroe Bank Channel is adapted from Hansen et al. (2001).

we will therefore only make approximate and qualitative comparisons and primarily focus on the time variable aspects of the flow at the top of the sill, which we assume are less affected by slope changes up and downstream of the sill.

The true cross-section of the Denmark Strait at the sill is roughly v-shaped and has a width of 350 km. In order to preserve the cross-sectional area of the channel we have set the width in MICOM to 151 km. However we will show that the width has only a small effect on the transport across the sill which remains about the same as the width of the channel decreases.

The resolution was as usual 0.4 degrees. For the Denmark Strait, where the Rossby radius is roughly 11 km, this meant a resolution of about 3 gridpoints per Rossby radius.

Initially the model was spun up for 200 days and it was found to settle after about 100 days to a uniform flux of 1.4 Sv. A continuation of the run for another 100 days at diagnostic frequency of 2 days revealed oscillations of the flow on a time-scale of about 5 days. To study these closer the model run was continued at a diagnostic frequency of 0.5 days for another 25 days. A regular pulsation like this has also been described from observations in particular by Ross (1984) and we will describe them in more detail in the following section where we will outline the flow features in the channel.

Flow features and time-variability

The three dimensional surface plot on the left in figure 7.1 gives an idea of the topography and the approximate positioning of the interface between the two layers. A trough in the interface can be seen at the left-hand side of the channel in the three dimensional plot on the left. It is present throughout the experiment. After the dense watermass spills over the sill it forms a thin bottom current that never separates, but most of the transport is concentrated in a narrow boundary current at the left hand side of the channel. The right plot in figure 7.1 is a contour plot of the bottom layer thickness which also illustrates the thin bottom current between the sill and $y \sim -60$ km.

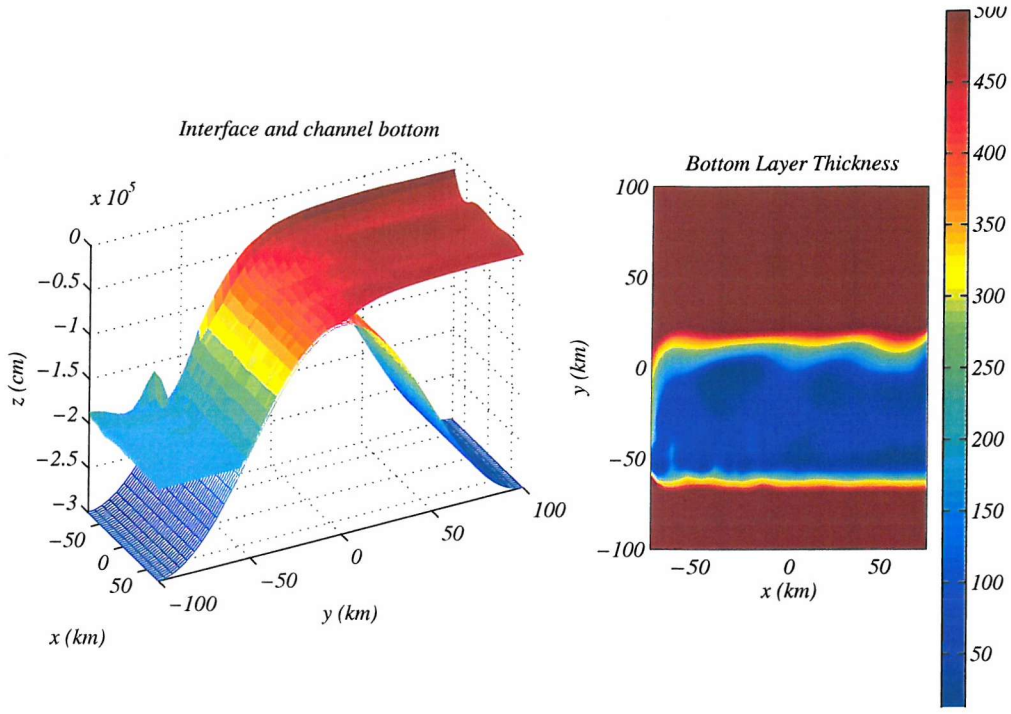

Figure 7.1: The panel on the left shows a snapshot of the location of the interface and topography on day 11.5 for the first Denmark Strait simulation. On the right the thickness of the bottom layer is contoured.

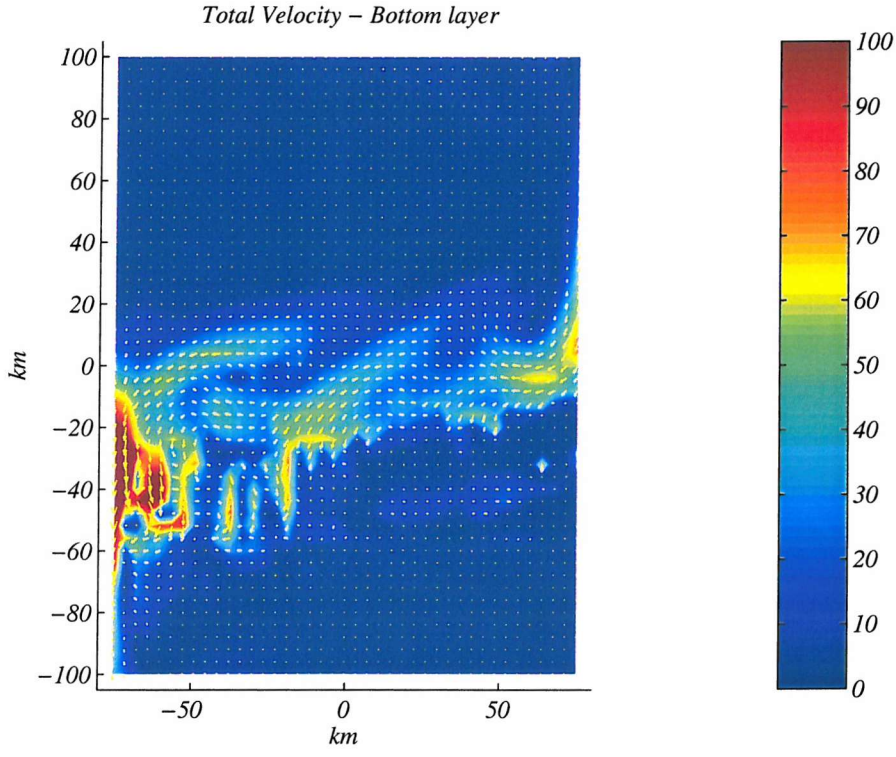

Figure 7.2: Snapshot from day 11.5 of the velocity field in the bottom layer of the first Denmark Strait simulation.

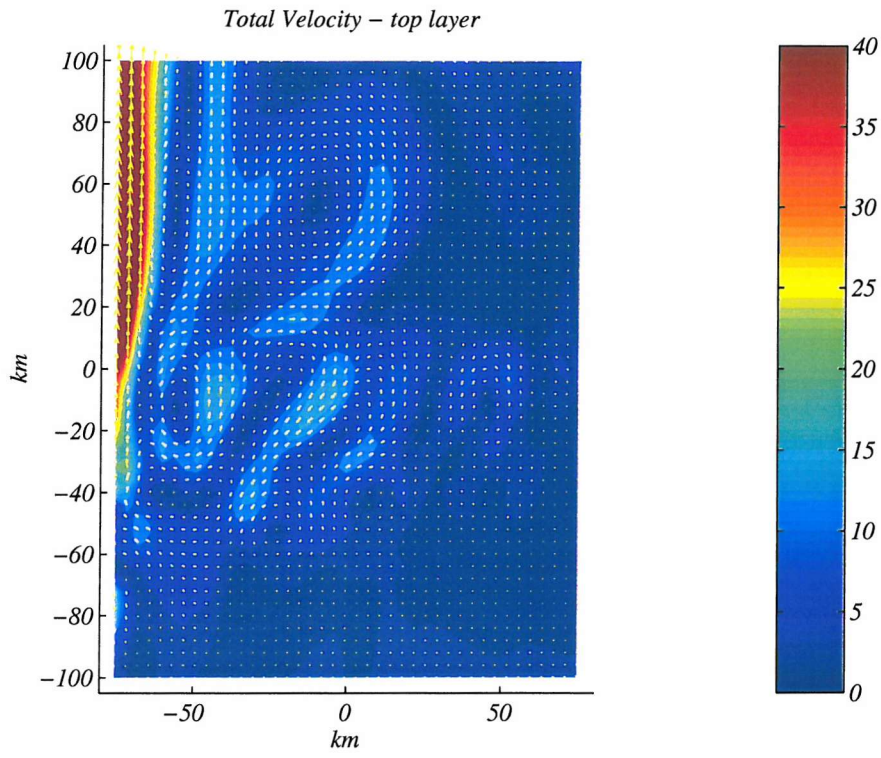

Figure 7.3: Snapshot from day 11.5 of the velocity field in the top layer of the first Denmark Strait simulation.

In figure 7.2 a snapshot of the bottom-layer velocities in the channel on day 11.5 (see figure 7.4) is shown. At the right-hand side of the channel a jet-like current develops at the top of the sill and periodically releases a 'pulse' of water which then travels across the channel in a region between $y \sim 0$ and -20. Two of the pulses can still be seen in the plot, one in the centre of the channel and one merging into the boundary current at the left-hand wall. In the other regions of the channel the bottom-layer does not show any prominent dynamical features.

Figure 7.3 shows the velocity field in the top-layer at the same timestep as figure 7.2. The consistent feature that is present again in this experiment is the boundary current on the left-hand side of the channel which in this particular snapshot extends to $y \sim -20$. To the right of the current is a weak backflow that merges with the boundary current at $y \sim 20$ and further to its right an even weaker gyre can be made out. The back flow has also quite consistently been observed in previous experiments and it arises within the basin. Again a lot of meandering can be seen between the top of the sill and $y \sim -20$ and close to the boundary current an eddy can be made out that is just about to merge with the current.

All of the features described here are very similar to those already discussed in the deep channel case in chapter 6 and the time evolution of the pulsating jet in the bottom layer is analogous. But how do they compare to the flow observed in the Denmark Strait?

The flow features in the top-layer are quite unlike any that have been seen at the surface in the region of the Denmark strait. In fact the observed flows do quite the

opposite. At the western side of the Strait, the Greenland current flows south at the surface, in place of the boundary current that should be moving north according to the model predictions. In the rotating runs simulating the flow through the Denmark Strait with a somewhat smoother topography Käse and Oschlies (2000) also find a northward flow in the surface layer concentrated on the western side of the channel, in our case the left-hand wall of the channel. However this flow occurs over the shelf region which we do not include in our topography. It is well known that the Denmark Strait overflow is much more complex than then simple two-layer structure with which we try to model it here, which is why there are such distinct differences in the flow features. We impose a pure exchange, i.e. zero net flow, which is not the case in the Denmark Strait. Also wind forcing and the shelf regions play a major role in determining the surface currents and neither of these is modelled in our experiments

One aspect however that has consistently reoccured in a set of our experiments is the pulsating nature of the overflow. This can be clearly seen in the top panel of figure 7.4 showing the transport across the sill over a 25 day period in the top and bottom layer. The fluctuations in the two layers are in phase and have the same magnitude of about 0.4 Sv and a period of 5 days. This agrees with observations by Ross (1984), who reported 'pulsating' variations in the transport at the sill, on time scales of 2 to 5 days. It should be noted however that his observations are based on measurements taken a distance 55 km downstream of the actual sill.

If we look at a section about 26 km upstream the same oscillations in transport can be observed with a period of about 5 days, seen in the bottom panel of figure 7.4. There the magnitude has decreased somewhat to only about 0.2 Sv and they occur about 2 - 3 days earlier than at the sill which gives them a speed of propagation of about 0.1 m/s.

The processes giving rise to these pulses at the sill may be similar to those occurring in the ocean and we will look at them more closely.

In figure 7.5 changes of the interface structure at the sill with time are shown in a Hovmöller plot and they can be directly linked to the oscillations seen in the transport across the sill. At the right-hand side of the channel at $x \sim 60$ km the bottom layer thickness is slightly higher (around 180 m) than to either side. At intervals of about 6 days a pulse of water mass is released from this part of the flow, propagates across the sill and joins the boundary current on the days it peaks in figure 7.4. It travels across the channel in about 16 days giving it a propagation speed of 0.11 m/s. The period at which they occur is roughly 6 days, i.e. at a frequency of $1.2 \times 10^{-5} s^{-1}$. These oscillations compare well with those we described in at the sill of the deep channel in chapter 6. There we find they have a slightly smaller period of 4 days.

Figure 7.6, a Hovmöller plot of the v-component of the velocity field at the sill, shows that the primary thrust of the pulses released is initially in the upstream direction, as centred around $x \sim 50$ there is a band of flow which is directed upstream at all times. However after separating from the right-hand wall the regions of increased bottom-layer thickness correspond to regions of negative, thus downstream, velocities.

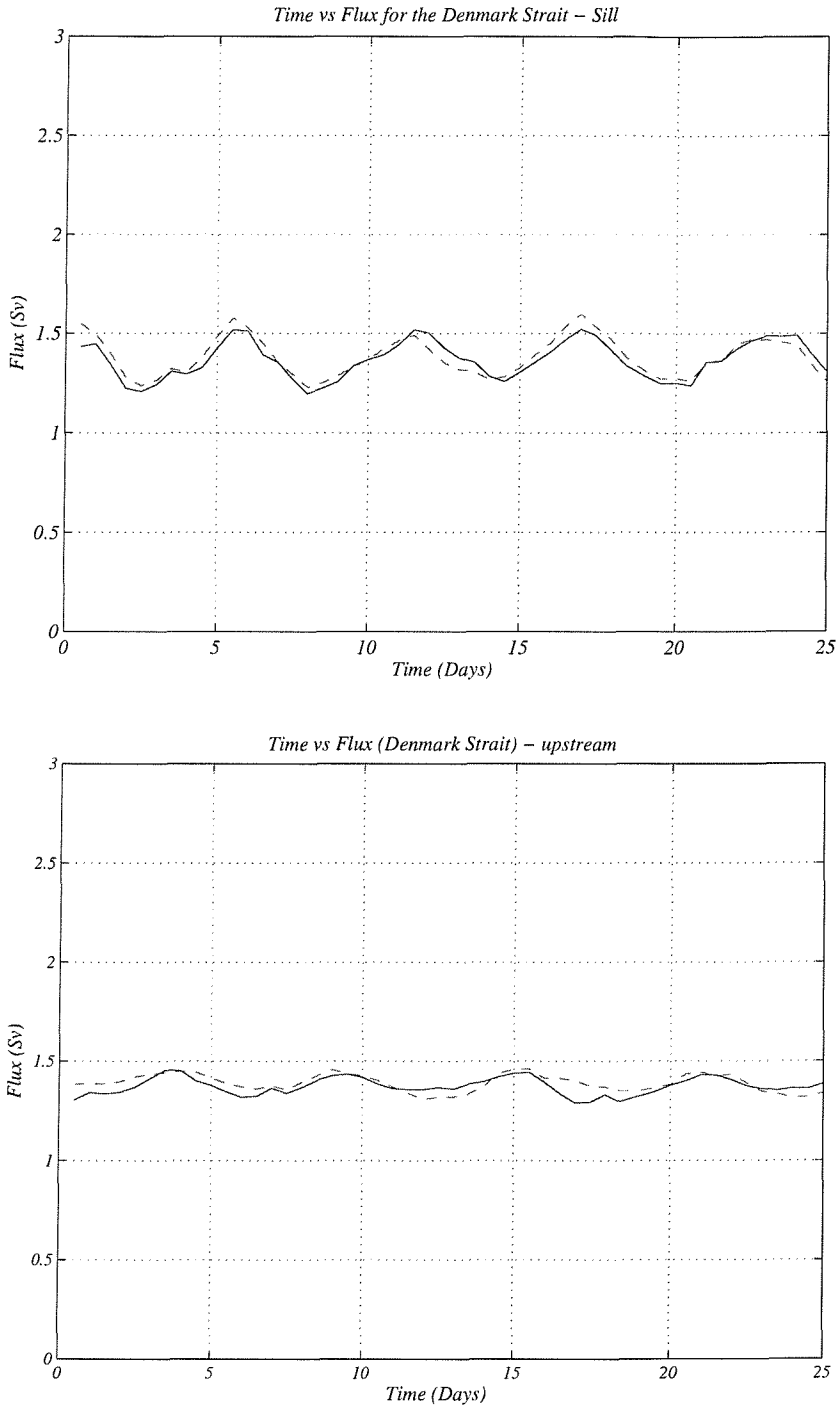

Figure 7.4: (**Top**) Flux in Sv versus time in days at the top of the sill. (**Bottom**) Flux in Sv versus time in days at a section about 26 km upstream of the sill. The dashed line is the flow in the top-layer and the solid line that of the bottom layer.

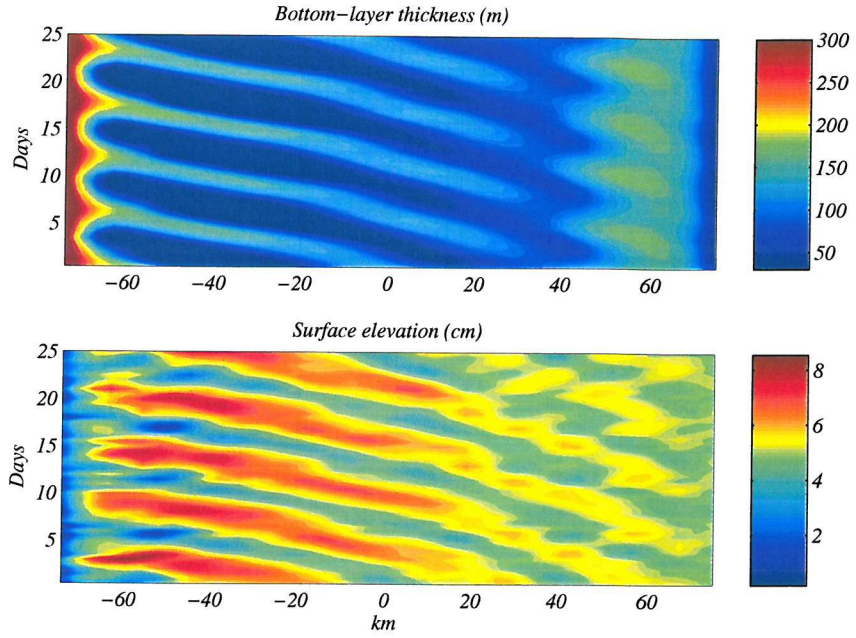

Figure 7.5: The top panel shows a Hovmöller plot of the bottom layer thickness given in m at the top of the sill and the bottom panels shows the surface elevation given in cm at the top of the sill.

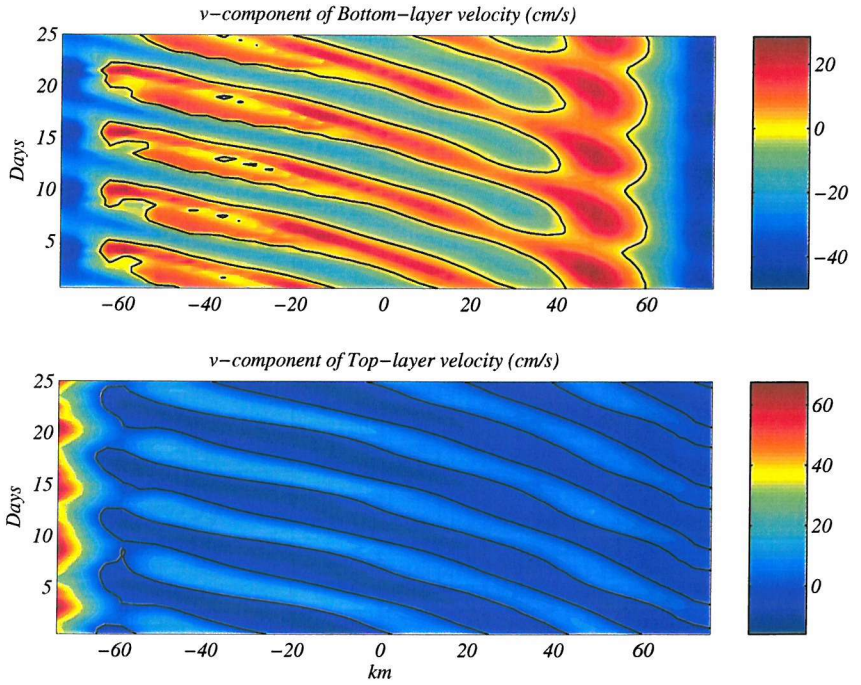

Figure 7.6: The top panel shows a Hovmöller plot of the v-component of the velocity in the bottom layer and the bottom panel shows the equivalent plot for the top layer at the top of the sill. The solid black contour is the line where $v = 0$.

The plots clearly show the flow patterns associated with the oscillations in the transport at the sill and we can conclude that they go hand in hand with an increased bottom-layer thickness and acceleration of the flow. However the exact mechanism by which the 'pulses' separate from the right-hand wall cannot be deduced from the plots.

At a second section $\sim$ 26 km upstream of the sill the interface height and surface elevation have been extracted over the 25 day period of the run as well as the v-component of the velocity field. The results are shown in the Hovmöller plots 7.7 and 7.8 respectively. In the top panel of figure 7.7 a distinct thickening of the bottom-layer can be observed at the left-hand side of the channel, this does not however go hand in hand with any distinctive dynamics of the bottom-layer, as can be seen in the velocity plot of the bottom layer in the top panel of figure 7.8. The surface layer is the driving force in this part of the channel and the boundary current can be clearly discerned on the bottom panel in the figure. Its peaks in velocity coincide with the peaks in the transport seen in the bottom panel of figure 7.4.

The flow in the bottom-layer is concentrated on the right-hand side of the channel in a boundary current noticeable in the top panel of figure 7.8.

It is worth noting that in neither layer are there any features that propagate across the channel and the flow at this section is clearly divided into regions of along channel flow which do not communicate.

A final point that needs to be addressed here is that of control. We will show at the end of this section when discussing the flux resulting from this experiment, that the amount of flow crossing the sill does not seem to be constrained by the width of the channel, however it most likely determined by the depth of the sill. It is expected that any hydraulic control will lie, as we have shown in chapter 6, some distance downstream of the sill, due to frictional effects.

We would expect a second critical section to occur in the region around $y \sim -50$ where the overflow encounters the dense water reservoir in the downstream basin. Since the flow is not maximal we do not expect any other controls upstream of the sill.

Determining the exact location of the control by determining the wave-speeds of a small perturbation to the mean flow field is made difficult by the fact that the flow itself is highly variable in time, but also due to the large number of gridpoints across the channel. We have not attempted to find the controls in this particular experiment, but we will apply the method outlined in the previous chapter in the case of the Faroe Bank Channel.

Fluxes

We have already mentioned that the magnitude of the mean transport across the sill is found to be 1.4 Sv in this experiment as can be seen in figure 7.4, this is only half of that expected from observations and modelling studies. Ross (1984) estimate the mean flux of water below 2^oC to be about 2.9 ± 0.4 Sv and Käse and Oschlies (2000) confirm

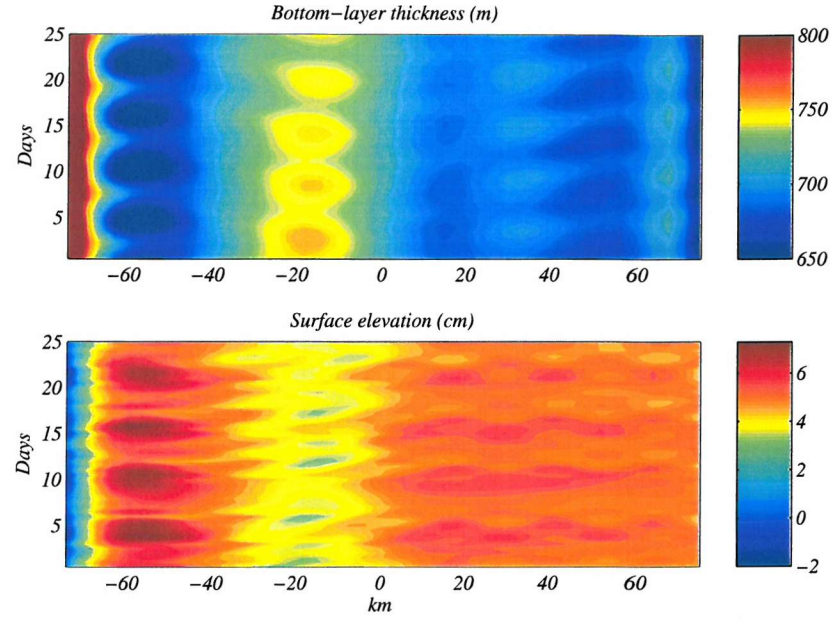

Figure 7.7: As figure 7.5 for a section at $y \sim 26$ km upstream of the sill.

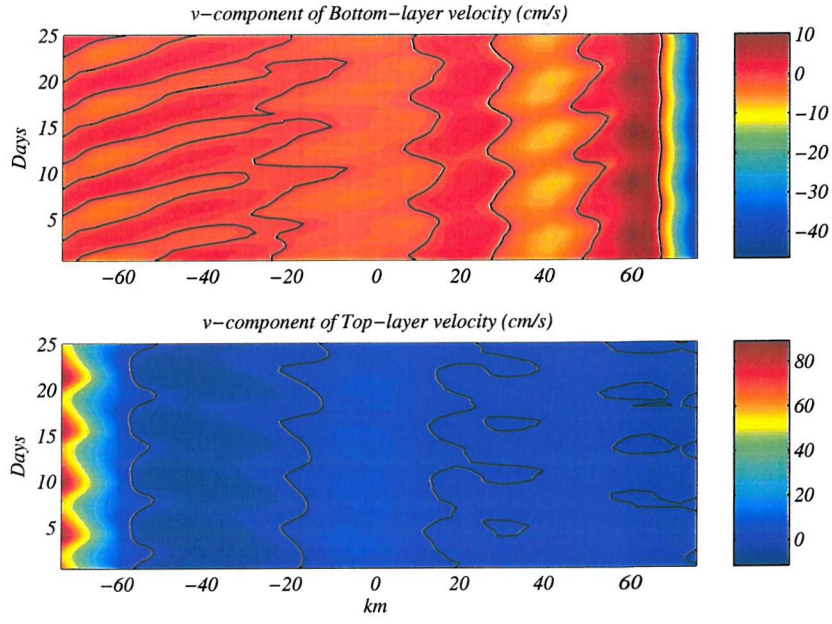

Figure 7.8: Same as figure 7.6 for a section at $y \sim 26$ km upstream of the sill.

Width (km)	Transport (Sv)
177	1.42
151	1.40
100	1.28
55	1.25

Table 7.2: Fluxes through a channel of varying width. The general set-up for each of the runs is as for the Denmark Strait (1) in table 7.1.

a transport of about 2.5 Sv with their modelling studies, while finding that the upstream interface height settles into equilibrium at only about 380 m above the sill. The flux in MICOM would probably reduce further if we were to use this height as a target for the relaxation in the upstream basin. On the other hand the density difference used by Käse and Oschlies (2000) was $\Delta\rho = 0.84$ which would increase the flux somewhat.

This large discrepancy between the modelled flow and the observed one is an indicator that the flow through the Denmark Strait is maybe more complex than the simple two-layer exchange which we are simulating. This has been observed and argued before as making theoretical predictions of transport through the channel difficult and challenging, often with a large margin of error.

We have run a second test experiment with the approximate values from Käse and Oschlies (2000) (but notice a still slightly lower density difference), which are also listed in table 7.1. However there is no significant change in the characteristics of the flow. The mean transport at the sill is found to be 1.48 Sv, an increase of less than 6% compared to the original value. The magnitude of the oscillations also increased to about 0.5 Sv while the period stayed the same at 5 days.

If applying the parameterisation for the flux given by equation (6.9) in chapter 6 we find that it predicts the flux to be 1.636 Sv for experiment (1) and 1.566 Sv for experiment (2). These again underestimate the flow observed but are a good approximation of the mean flows resulting from the MICOM runs. They overestimate the mean flow from the MICOM run by 17% and 6% respectively, while the observed flow of 2.9 Sv is underestimated by 44% and 46% respectively.

A final set of experiments was carried out to test the sensitivity of the flux to the dimensional width of the channel. As expected when the channel becomes narrower the transport of dense water across the sill changes only very little as shown in table 7.2.

7.2 Faroe Bank Channel

As described before the general set-up for this experiment too is kept very similar to those of the previous runs, with changes only to the watermass conditions and the depth and width of the channel, listed in table 7.1.

We have set the channel width to roughly 29 km with 8 gridpoints across the channel.

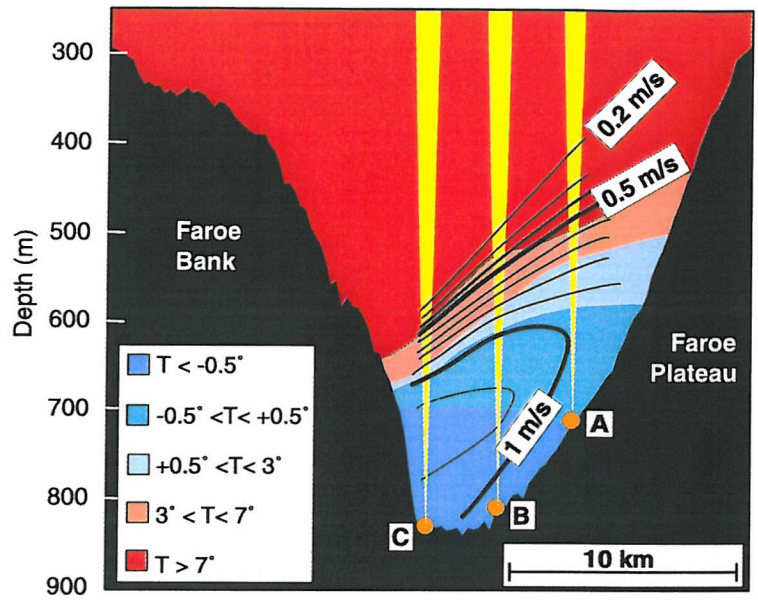

Figure 7.9: Section across the Faroe Bank Channel at the sill showing the temperature and velocity of the water below 250 m depth. Colour shading indicates the temperature distribution (in $.^{o}C$). Contours show the average distribution of the along-channel velocity towards the northwest. Yellow cones illustrate sound beams. The figure was provided by Bogi Hansen, and was published in Hansen et al. (2001).

The true width of the Faroe Bank Channel is estimated from the cross-section plotted in figure 7.9, which has been reproduced from Hansen et al. (2001), to be about 30 km at 300 m depth and narrowing to 13 km at 600 m depth. In order to preserve the cross-sectional area a width of about 15 km would have been most appropriate, however this would reduce the number of grid points across the channel to a maximum of 4 which we felt was not enough to represent the flow adequately and we thus choose a wider channel of 29 km.

The experiment was run for 200 days and was found to settle after about 60 days to a pseudo-steady state, with a mean transport of 2.24 Sv, this value is in much better agreement with observed fluxes of 1.9 ± 0.4 Sv given by Saunders (1990).

Flow features

Figure 7.10 shows on the left a three dimensional surface plot of the interface height and topography in the channel on day 200 while the plot on the right contours the bottom-layer thickness on the same day. The tilting of the interface due to rotation is evident in both plots and downstream the flow in the bottom layer concentrates in the usual boundary current on the left-hand side of the channel. To its right the bottom layer is thin, but never separates. As the flow enters the basins, a sharp increase in the bottom layer thickness can be seen in particular on the side of the boundary current and this feature can be interpreted as an hydraulic jump, although the contours do not match quite so neatly with the features predicted for such hydraulic jumps by Pratt (1987).

The velocity fields in bottom and top layer are shown in figure 7.11. The top layer

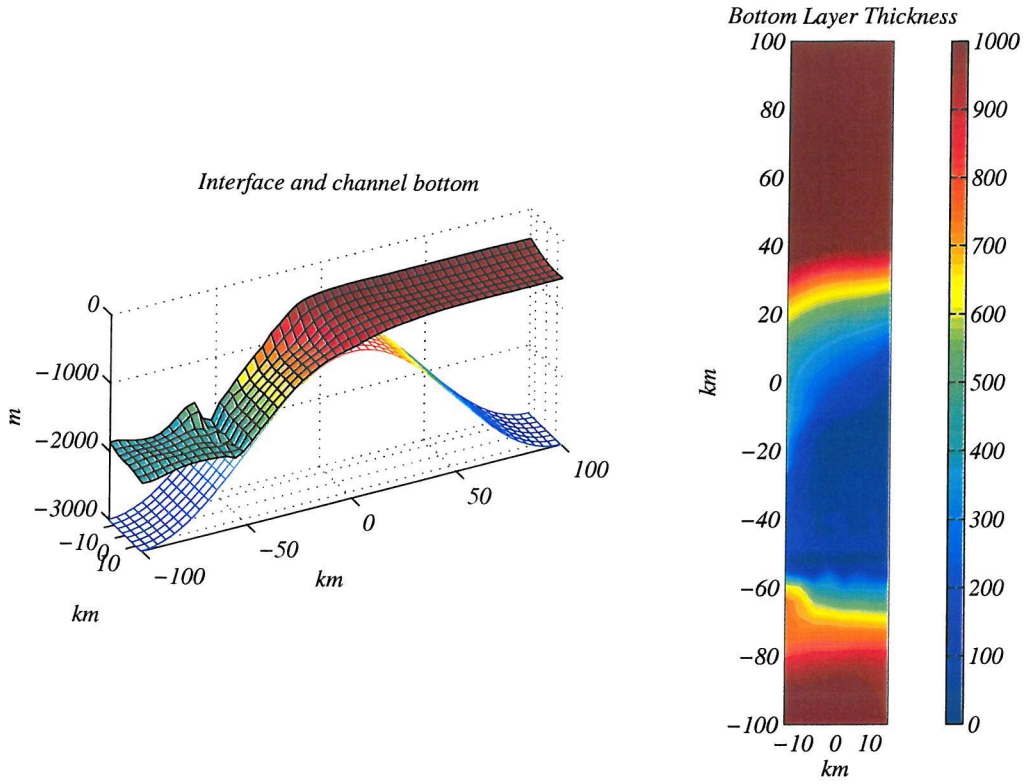

Figure 7.10: The panel on the left shows a snapshot of the location of the interface and topography on day 200 of the Faroe Bank Channel simulation. On the right the thickness of the bottom layer is contoured.

on the right shows the features that have been observed before in virtually all other cases we discussed. A recirculating gyre occupies most of the downstream part of the channel and at $y \sim -40$ a boundary current splits away from the gyre at the left-hand side of the channel. From here it proceeds towards the upstream basin intensifying to maximum velocities of about 0.7 m/s. In the bottom layer the features closely resemble those previously observed with crossing over occurring close to and after the flow passes the sill. In this case the crossing over is straight forward and does not show prominent time varying features like meanders or eddies. At around $y \sim -20$ the current encounters the left-hand wall and forms a boundary current towards the downstream basin with velocities up to 2.5 m/s. It is noticeable that the flow spreads out somewhat as it descends down the slope, which is a feature that is present throughout the run.

In figure 7.12 cross-sections of the interface in the channel are shown for the sill (left), a section about 12 km downstream (middle) and a section about 24 km downstream (right). These sections can tentatively be compared to those shown in figure 1.2 in the introduction and in figure 7.9. The tilt of the interface can be observed clearly at the sill with a rise of about 200 m over a 20 km distance this is comparable to that of the watermasses which have $T < 3$ in the figure 7.9. Further along the channel the bottom layer becomes thinner at the right-hand side of the channel, while the interface around the boundary current becomes steeper. Because we have a rectangular cross-section of the channel, it is difficult to directly compare the flow features in the overflow plume here

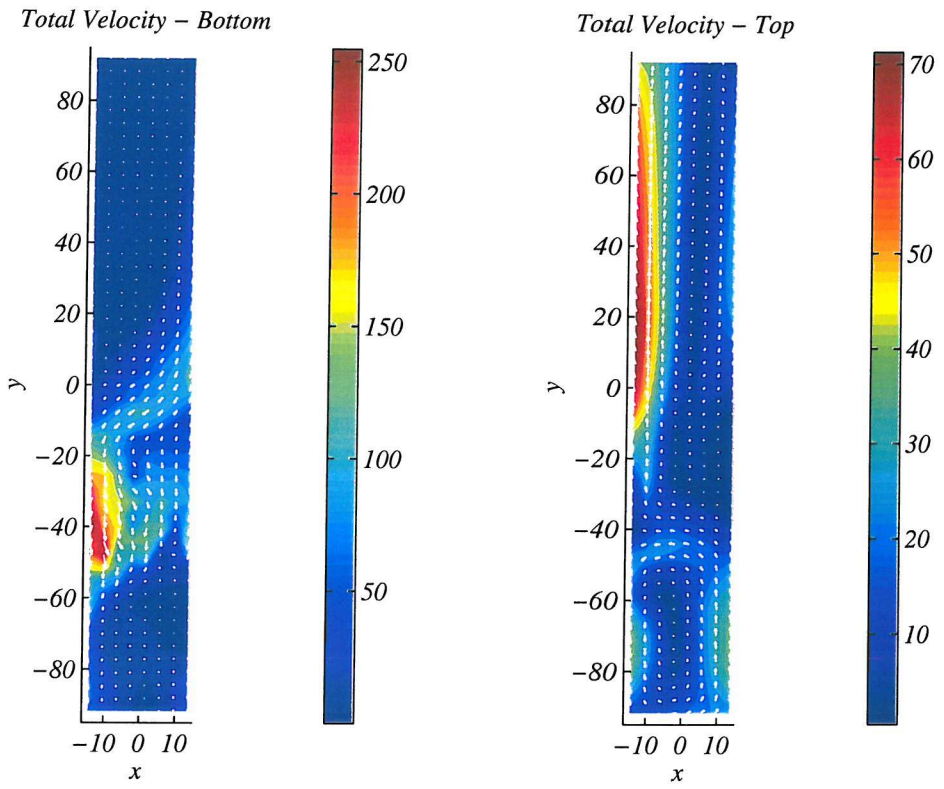

Figure 7.11: Contour plot of the bottom layer velocities (left) and top layer velocities (right) in the Faroe Bank Channel simulation on day 200. The arrows give an indication of the direction of the flow.

with those shown in the introduction, but the increased slope of the plume might suggest that the current become more and more pushed towards the right-hand side of the plot and would follow isobaths as a thin spread-out bottom current were we to use a smoother topography.

No distinct time varying features were observed in this overflow and so we will move on to briefly show the results we got when trying to locate the control points for the flow on day 200, by applying the method of finding the wave speed for a small long-wave disturbance, outlined and tested in appendix D.

From the contour plot of the bottom layer thickness on the right in figure 7.10 and from previous experience, we would expect a control to occur somewhat downstream of the sill around $y \sim -20$ km. A second critical section associated with the hydraulic jump is expected to lie in the region of $y = -50$ km.

In figure 7.13 the wave speeds are plotted for all sections along the channel. These have been selected by choosing only the eigenvectors which monotonically increase or decrease across the channel. For $i > 0$ km and $i < -50$ km, there is no ambiguity in choosing the right vectors and the two associated eigenvalues of the zeroth mode are clearly of opposite sign and the flow regions are subcritical as a result. In the regions between $-50 < i < 0$ picking the right vector is more tricky for the same reasons that were outlined in chapter 6. Within this part of the channel one of the wave-speeds is close to zero, yet only for a small region between $-45 < i < -35$ is it clearly less than zero and thus supercritical.

As before the results are not conclusive and the process will need, if possible, to be

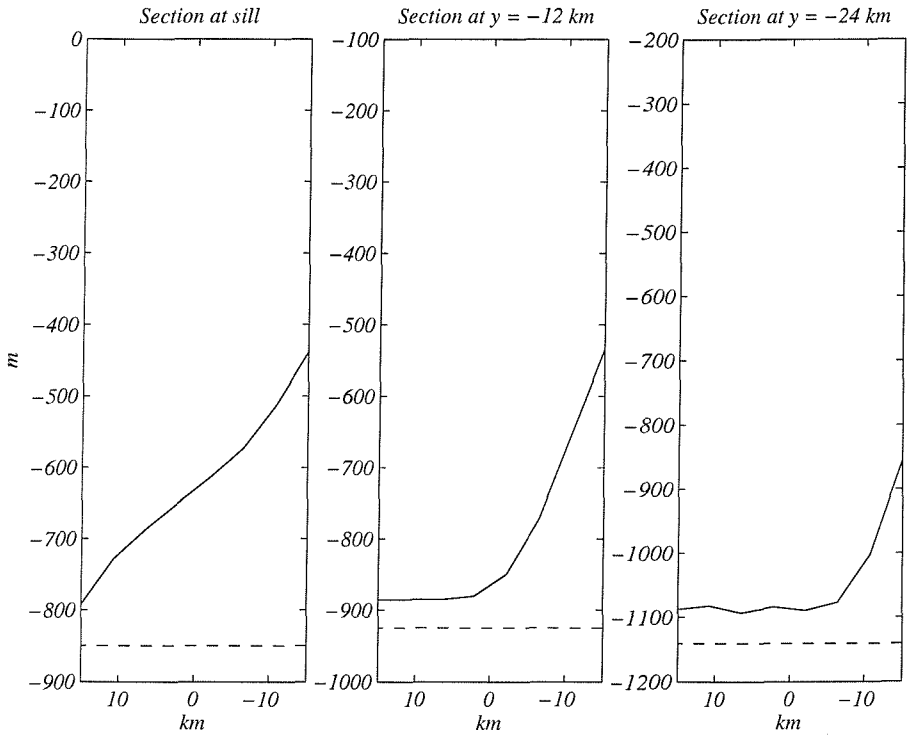

Figure 7.12: Three cross-sections from the Faroe Bank Channel simulation showing the location of the interface (solid line) and the bottom of the channel (dashed line). On the far left a section at the top of the sill is shown, in the middle a section at $y \sim 12$ km and on the right a section at $y \sim -24$ km. The vertical axis marks meters below the surface and the horizontal axis marks km across the channel with the Faroe Bank to the left and the Faroe Plateau to the right (see figure 7.9).

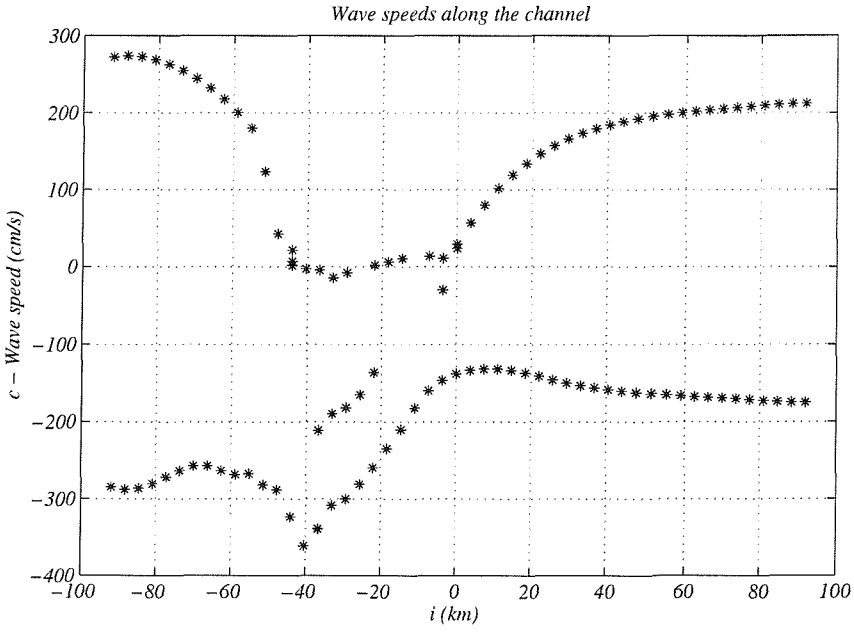

Figure 7.13: Long-wave speeds along the Faroe Bank Channel derived from the MICOM results on day 200.

refined to make sure the right values are selected. However they do show clearly that the control sections are roughly located where we expect them to be from hydraulic theory.

Finally, let us apply and compare the estimate from the empirical formula (6.9) to the model result. From the numbers listed in table 7.1 the parameterisation predicts a flux of 1.448 Sv, which underestimates both the observed and the modelled flux, by 23% and 35% respectively. When testing the parameterisation in the previous chapter we did find that fluxes for channels with $L < 2$ and small ΔH tend to be underestimated by the formula derived, see figure 6.27. The Faroe Bank Channel is one of those examples for which this limitation applies.

7.3 Conclusions

The experiments carried out to simulate the flow through the Denmark Strait and the Faroe Bank Channel have, together with the observations from the experiments outlined in chapters 5 and 6 given us a better understanding of some interesting aspects of these flows.

In the case of the Denmark Strait we have for the first time numerically shown the existence of the time dependent nature of overflows and in particular we find pulses in the transport across the sill, which have also been shown to exist from observations.

In this particular case we have also reiterated the difficulties involved in trying to estimate the flux through a complex channel such as the Denmark Strait and have seen that a simplistic two-layer approach is possibly not appropriate in this case. It underestimates the flow quite considerably and in addition predicts a circulation in the top layer that does not agree with the circulation observed in the strait itself. This is most likely due to the complex nature of the processes, such as wind forcing and the effects of the shelf region for example, determining the circulation in this region of the ocean which are not represented in the model.

The simulations of the Faroe Bank Channel have shown a picture of the flow that is in somewhat better agreement with the observations. The flux agrees in the first place and so do the general features of the interface across the channel at the sill and further along the channel.

These new insights gained from the experiments suggest that there is great potential in further experimental work using the model in order to take a closer look at some of the points that have emerged.

It would for example be of tremendous interest to include a more realistic topography in say the Faroe Bank Channel experiment possibly with a slightly higher resolution and investigate the behaviour of the plume downstream of the sill. In the Denmark Strait case, it might be of interest to devise a model that runs with a very thick, almost stagnant upper layer as well as a more realistic topography and see if the resulting fluxes compare better to observations. It would also be interesting to see if the pulsating transport persists in a channel with a smoother cross-section.

Chapter 8

Conclusions

In this final chapter we shall recap some of the major results of the thesis in section 8.1 and discuss how they have helped us achieve the motivation and aims we set out in the Introduction. In section 8.2 we will recap some of the new interesting questions that have arisen from this work and that may be worth a closer look and further investigation in the future.

8.1 Summary of the main results and achievements

We have tried to draw the main conclusions to each part of the work within the chapters already presented, so this section serves just to briefly recap and point out what we feel are the major new contributions to the present understanding of rotating hydraulics and the behaviour of two-layer rotating exchange flows that have come out of this work.

In chapter 3, firstly, we started developing a new analytical way of looking at two-layer rotating exchange flow by building on the approach used by Dalziel (1988) for the zero potential vorticity case. To do so we cast the problem into a set of equations dependent just on two variables Δu and $\bar{u}$. Using Armi-Farmer like Froude number diagrams we were able to determine the controlled flows for submaximal as well as maximal flows through a channel with rectangular cross-section.

We extended the theory fully to include all possible flow regimes along the channel, by that we mean the different states of the separation of the interface from either or both side walls of the channel due to the effect of rotation.

Furthermore we have shown that the Armi-Farmer like Froude number plane can be used to trace hydraulically controlled flows not only in the non-rotating case but equally in a rotating case for a channel whose width changes like the square root of its depth, $L \propto \sqrt{D}$. A plot for which this property applies is shown in figure 3.13 in chapter 3.

Finally we apply a long-wave analysis to a selection of flows and show that the wave speeds divide the flow into super- and subcritical regions exactly as expected from the hydraulic control arguments.

In chapter 4 the zero potential vorticity problem solved in chapter 3 is cast into a yet more concise set of equations depending on only one variable, h_s, the slope of the interface

across the channel. These are solved using a method analogous to the functional approach developed by Gill (1977). We discuss flows through a variety of channels in this chapter, including flat bottom channels with a constriction and channels of constant width and varying bottom topography, that is with a sill, at the centre of the channel.

Also in extension to the work by Dalziel (1988) we extensively discuss submaximal as well as maximal flows for each of the different channels and show the maximal flows to be a natural limit to the submaximal flows. As usual we can identify maximal flows by finding a primary and a virtual control which border a subcritical regions in the middle, with two supercritical region either side. We find that for each supercritical flow upstream there exists a solution branch that is subcritical which the flow can equally follow. This flow carries the same maximal flux as the supercritical branch and also passes through both controls, it is therefore another possible maximal solutions to the flow.

The controlled fluxes are given for a comprehensive range of channel widths ($L = 0 \rightarrow 2$), and Bernoulli potentials ($\Delta E = 0 \rightarrow -1$) in figure 4.19. We have described the occurrence of a second control for a small domain of specific pairs for L and ΔE, which have not been described previously. We believe that this is due to the fact that in previous theories, such as that by Dalziel (1988) for example, the possibility of backward flow has been excluded. Not all of the flows shown in figure 4.19 are necessarily traceable along any type of channel. For a flat bottom channel the domain of non-traceable flows is marked by the grey shaded region on the plot. For channels with a sill there is no unique way for excluding the non-traceable flows, but as a general rule of thumb, flows with $-0.5 < \Delta E < 0$ are not traceable, and for $-1 < \Delta E < -0.5$ most are traceable. In table 4.1 the ΔE for three channels of width $L = 0.6$, 0.8 and 1.0 is listed at which the flow over the sill becomes maximal. In previous studies it has always been argued that the virtual control in a depth changing channel is located at the exit of the channel where the depth becomes constant and the channel widens; we show that this does not have to be the case, but that in the examples listed, the depth can continue decreasing while the flow become supercritical beyond the virtual control. Examples of maximal flows which have the virtual control at the entrance to the channel are also discussed.

In part two of the thesis, comprising chapters 5, 6 and 7, we have undertaken a modelling study of two-layer rotating exchange flows. We have taken a primitive equation model MICOM and used it in an idealised setting to simulated exchange flows through a rectangular constant width channel with a sill.

Chapter 5 focuses on the set-up of the model and some initial test runs to establish the sensitivity of the model and the flow to parameters such as the depths of the basins, the relaxation heights in the channel and the resolution of the model. Also in this chapter, some interesting observations are presented such as a rotating hydraulic jump in agreement with laboratory experiments by Pratt (1987) and separated regions predicted from the theory.

In addition a set of non-rotating two-layer experiments is carried out and results are compared with the well established Armi-Farmer theory for such flows. The major find

here was that maximal flows as predicted by Armi and Farmer are approached by the MICOM results as an upper limit but are never equalled. The control points of the flow are shown to be where we might expect them to be from hydraulic theory, with friction moving the primary control a small distance downstream of the sill, analogous to Pratt (1986), while no secondary (virtual) control is ever observed upstream, hence no maximal flows are observed. However, a second critical region is confirmed downstream in the vicinity of the hydraulic jump.

In chapter 6 an extensive set of rotating experiments using MICOM is presented. Firstly, we describe in detail the specific flow features observed for a deep channel of 900 m, and a somewhat shallower channel of 500 m. In particular we discover that the flows through the channels are inherently unsteady and we describe particular time dependent features in both channels. In terms of a parameterisation of the fluxes over long time scales such short-time scale variations, which are of the order of days, are not significant as long as the mean flux remains the same over long time periods. However, the presence of time variability in the flow maybe one reason why so far analytical estimates have usually overestimated the mean fluxes as they assumed the flow to be steady. Our simulations have shown that the time variability may be an important part of the flow the effects of which need to be investigated further.

The experiments were primarily designed to allow us to study the dependence of the flux through the channel on parameters such as the density difference between the two layers and hence the reduced gravity g', the Coriolis parameter f, and the level of the interface in the upstream basin, ΔH. Drawing together all the flux results from the experiments an empirical formula is derived for the flux in terms of L, the non-dimensional width of the channel, which depends on g' as well as f, and the upstream interface height ΔH, given in equation (6.9). This is then tested and compared to the results from the analysis.

In an attempt to relate the results achieved to observed flows in the ocean we have modelled the flow through two specific straits, the Denmark Strait and the Faroe Bank Channel. In the case of the former agreement in terms of the amount of the transport across the sill have been found to be poor supporting the notion that the flow through the Denmark Strait is more complex than the simplistic two-layer version we have tried to simulate. However the flow features in the channel have revealed a time dependency in the form of a pulsation of the flux with a period of about 5 days and a magnitude of about 0.4 Sv, which may explain the pulsation of the transport observed by Ross (1984).

The flux through the idealised Faroe Bank Channel agrees better in terms of the flux, and the features along the channel are tentatively compared to the observations of features in the overflow beyond the sill. Similarities are evident and with the introduction of a more realistic topography for example there is scope for more detailed study of the flow features in the channel. We have also attempted to identify the control sections for the flow in this particular experiment with some success.

In this final chapter the parameterisation derived in chapter 6 was put to the test for

the two straits. It was found to underestimate the observed fluxes as well as the results from the MICOM runs. However in the Denmark Strait case, that is for a very wide channel, the agreement between the empirical estimate and the results from MICOM were remarkably good.

This comparison to some observed flows of importance rounded off the work presented here.

8.2 New and interesting questions

Clearly exchange flows through channels continue to be an important topic of research as climate and global circulation models are moving towards the improvement of the representation of processes which have been found to play a profound role in determining the ocean circulation. We feel that a few areas have been touched upon that may well be worth further study in the future.

On the theoretical side of the study it would firstly be interesting to see what kind of flows and fluxes are achieved if the backflow is to be excluded, as has been done in several previous studies. Furthermore other, smoother cross-sections could easily be used and equally the analysis could be extended to investigate flows with non-zero net transport. More complex issues such as non-zero potential vorticity, additional layers and time dependence are less straight forward to solve but might make the comparisons with observed flows and model results more appropriate.

Another question which has only been touched upon briefly in this thesis is, what role the circulation in the basins plays in determining the flow in the channel. A particular problem here for the analytical solutions is that of linking the flow in the basins, particularly the upstream basin, to the flow solutions in the channel. Both of these questions are currently being studied and the results will also help us to compare analytical solutions with observations.

On the whole, theory can give valuable insights into the fundamental processes which set-up exchange flows and control them, such as by allowing us to determine the control sections and find upper bounds on the flow. It has become clear however, from the observed flows in MICOM, that other factors such as time variability, for example, can have crucial limiting effects on the overflows, which cannot be ignored. A comprehensive theory encompassing the time dependent aspect of the flow, might prove to be quite a challenge.

A prominent example of time dependent features are those we described in the deep channel, which are clearly linked to the time variable behaviour of the flux at the sill. A similar oscillation has been observed for the shallow channel although it is simply the result of a periodic intensification of velocities and thickening of the bottom layer and no conspicuous transient flow patterns are observed.

However, in the flow through the shallow channel we also find distinct time variable instabilities downstream of the sill. We argued that these are not linked directly to the

variability of the flux across the sill as they occur in the supercritical region of the flow. They may nonetheless be interesting in their own right as they form in an area where intense mixing takes place along the slope and hence they may contribute or prevent entrainment of surrounding fluid into the bottom layer and influence the formation of deep water.

So the time variable features of the flow, we feel, should be studied further to assess their role and importance in the overflows. Numerical models such as MICOM are a good tool to run idealised set-ups at high resolution in order to resolve them.

In conjunction with further analytical work it would also be quite straightforward to initialise MICOM with a variety of different, smoother topographies as well as with realistic topographies to study their effects on the flow. Extensions could be made to include more layers and with some thought barotropic flows could be set up.

So there is clearly a wealth of simple studies that could be done and will hopefully be done, by ourselves or with others in the future, and that may lead to new insight and further questions to look at.

Appendix A

Determining the separated cases

When solving the no-net flux condition in the two variable case expressions for h_{10} can be derived in terms of u_{10} and u_{20}, or alternatively $\Delta u = \frac{1}{2}(u_{10} - u_{20})$ and $\bar{u} = \frac{1}{2}(u_{10} + u_{20})$, which we frequently use throughout the theory. The expressions for h_{10} will differ depending on the regime the flow is in and we list all those for regimes 2 - 8 below. A cross-sectional representation of all the regimes is shown in figure 3.2. Regimes 1 and 9 are not included in our analysis, since in both only one layer is present, implying that the other layer has completely vanished. Mass conservation and the fact that we do not allow for any mixing between the layers, means that these two cases can never occur.

Regime (2,1) - 2

$$h_{10} = -L\Delta u + \sqrt{-2LD(\bar{u} - \Delta u)} \tag{A.1}$$

Regime (3,1) - 3

$$h_{10} = \frac{1}{2}D - L\bar{u} \tag{A.2}$$

Regime (1,2) - 4

$$h_{10} = L\Delta u + \sqrt{2LD(\bar{u} - \Delta u)} \tag{A.3}$$

Regime (2,2) - 5

$$h_{10} = -\frac{D(\bar{u} - \Delta u)}{2\Delta u} \tag{A.4}$$

Regime (3,2) - 6

$$h_{10} = D + L\Delta u - \sqrt{2LD(\bar{u} + \Delta u)} \tag{A.5}$$

Regime (1,3) - 7

$$h_{10} = \frac{1}{2}D + L\bar{u} \tag{A.6}$$

Regime (2,3) - 8

$$h_{10} = D - L\Delta u - \sqrt{-2LD(\bar{u} + \Delta u)} \tag{A.7}$$

In order to transform these expressions into those applicable for the single-variable reduction we need to replace u_{10} and u_{20} by the following expressions in terms of h_s which are derived in chapter 4:

$$u_{10} = \frac{h_{10} - \Delta E - D}{h_s} - \frac{h_s}{2} \tag{A.8}$$

$$u_{20} = \frac{h_{10} - \Delta E - D}{h_s} + \frac{h_s}{2}, \tag{A.9}$$

or alternatively:

$$\Delta u = -\frac{1}{2}h_s \tag{A.10}$$

$$\bar{u} = \frac{h_{10} - \Delta E - D}{h_s} \tag{A.11}$$

and solve for h_{10}.

A.1 Regime numbering scheme

The numbering of the regimes may seem somewhat arbitrary, but in order to allow for an easy way to test the regimes numerically we devised the following, very simple numbering scheme.

The channel cross-section is divided into three regions, the first one is the region above the surface of the water, labelled 3, region 2 contains the flow and finally the region below the channel is labelled 1. Depending on the point of intersection of the interface with the sidewalls (and/or the extended lines of the sidewalls above and below the channel) the regimes is labelled using the numbers of the regions of intersection. In figure (A.1) the regions are indicated and an example is shown. Here the interface intersects the right-hand side of the channel and the surface, which if extended leads to an intersection with the left-hand wall above the surface, hence this regime is labelled (2,3). In order to simplify the process of determining the regimes especially in the numerical code each regime was then assigned a single number by the following expression:

$$K = I_R + 3(I_L - 1). \tag{A.12}$$

Here K, denotes the case (or regime), I_L the index of intersection along the left-hand wall and I_R the index of intersection along the right-hand wall. So the example in our figure has $I_R = 2$ and $I_L = 3$ and hence $K = 8$.

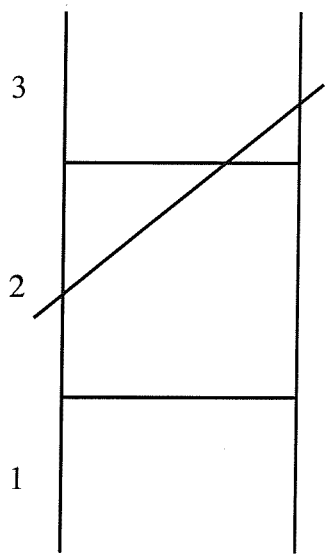

Figure A.1: Illustration of the numbering scheme. The region above the channel is labelled 3, that below the channel 1, and the channel itself 2. According to where the interface intersects the sidewalls (and/or extended sidewalls) the flow is assigned a regime number.

A.2 Validity of the cases

Here we will briefly describe the general outline of the algorithm used to determine the physical realisable solutions for the across channel profile of the flow. As has been discussed in section 4.1 the aim is to find the flux across the sill for a range of u_{10} and u_{20} (or alternatively h_s), which are physical and may occur somewhere along the channel. At the outset however, we do not know which h_{10} to use as we cannot be sure what case a particular combination of channel geometry and values of u_{10} and u_{20} will result in. So the following procedure is followed to determine the relevant case:

1. For a particular geometry and range of u_{10} and u_{20}, the h_{10}'s are computed for all 7 cases we consider.

2. Together with the parameters chosen at the outset, namely the values for D and L describing the channel geometry and u_{10} and u_{20}, h_{10} will describe all the physical characteristics of the flow. We therefore determine the points of intersection of the interface, given by $h_1 = (u_{20} - u_{10})y + h_{10}$, with the side walls of the channel.

3. If these points of intersection agree with the assumptions made about the intersection points when finding h_{10} in the first place (see formulae above) then the solution is valid.

4. If on the other hand the intersection points do not agree with the initial assumptions the case is dismissed.

For some cases h_{10} is the result of a quadratic equation to which there will be two solutions (roots). Therefore the expression for h_{10} will involve a term including $\pm\sqrt{(\ldots)}$. On analysis of the roots as described above it was found that one of these roots never lead to any valid cases and was therefore excluded as a possible solution for h_{10}.

Appendix B

Long-wave speeds

As usual, the non-dimensional semigeostrophic shallow water equations are as follows:

$$\begin{aligned} u_1 &= -P_y - h_{1y} \\ u_{1t} + u_1 u_{1x} &= -P_x - (h_{1x} - D_x) \\ u_{1y} &= 1 \\ h_{1t} + (u_1 h_1)_x + (v_1 h_1)_y &= 0 \\ u_2 &= -P_y \\ u_{2t} + u_2 u_{2x} &= -P_x \\ u_{2y} &= 1 \\ h_{2t} + (u_2 h_2)_x + (v_2 h_2)_y &= 0. \end{aligned} \tag{B.1}$$

We seek long-wave perturbations to the mean field of the velocities in both layers, the height of the interface and the pressure, denoted by $\bar{u}_i(y)$, $\bar{h}_i(y)$ and $\bar{P}(y)$ respectively. The mean values of the flow depend only on the across stream direction, y, since the geometry along the channel varies on scales much larger than its width. As a result changes in the physical parameters are also gradual in the downstream direction. The perturbations to the mean fields are functions of the form $u_i' = u_i e^{ik(x-ct)}$, and similar expressions for $h_i'(y)$ and $P'(y)$, where k is the wave number and c the wave speed.

In order to find the equations for the long-wave perturbations the following expressions are substituted into equations (B.1):

$$u_i = \bar{u}_i + u_i', v_i = \bar{v}_i + v_i', h_i = \bar{h}_i + h_i', P = \bar{P} + P'. \tag{B.2}$$

We assume that variations in the mean flow in the downstream direction are zero and so several terms involving $(\bar{\cdot})_x$ cancel. Terms involving the product of two perturbation terms are ignored as they are assumed to be small and because the flow is parallel in the channel all terms including $v_i(y)$ of any form will also be disregarded. Furthermore, the expressions describing the mean state are subtracted. The equations above thus rearrange to give expressions describing the perturbations to the mean flow:

$$
\begin{aligned}
u_1' &= -P_y' - h_{1y}' \\
u_{1t}' + \bar{u}_1 u_{1x}' &= -P_x' - h_{1x}' \\
u_{1y}' &= 0 \\
h_{1t}' + \bar{u}_1 h_{1x}' + u_{1x}' \bar{h}_1 &= 0 \\
u_2' &= -P_y' \\
u_{2t}' + \bar{u}_2 u_{2x}' &= -P_x' \\
u_{2y}' &= 0 \\
h_{2t}' + u_{2x}' \bar{h}_2 + \bar{u}_2 h_{2x}' &= 0.
\end{aligned}
$$

Now that we have reduced the equations, the perturbation terms in the expressions containing a time derivative will be replaced by expressions for the waves: $u_i' = u_i e^{ik(x-ct)}$, $v_i' = v_i e^{ik(x-ct)}$, $h_i' = h_i e^{ik(x-ct)}$ and $P' = P e^{ik(x-ct)}$.

After substitution and some manipulation, we arrive at the following equations:

$$
\begin{aligned}
(c - \bar{u}_1)(P' + h_1')_y + (P' + h_1') &= 0 \qquad \text{(B.3)} \\
(c - \bar{u}_2) P_y' + P' &= 0 \qquad \text{(B.4)}
\end{aligned}
$$

from the two momentum equations. From the mass conservation in both layers we find:

$$
\begin{aligned}
c h_1' + h_1'(\bar{P} + \bar{h}_1)_y + \bar{h}_1 (P' + h_1')_y &= 0 \\
c h_2' + h_2' \bar{P}_y + \bar{h}_2 P_y' &= 0. \qquad \text{(B.5)}
\end{aligned}
$$

Noting that $h_1' + h_2' = 0$ and $\bar{h}_1 + \bar{h}_2 = D$ and adding the two equations (B.5) gives

$$
D P_y' + (\bar{h}_1 h_1')_y = 0. \qquad \text{(B.6)}
$$

From now on primed terms, (.'), denote the amplitude of the perturbations to the particular physical variable. From layer 2 we know that $P_{yy}' = 0$ and from layer 1 $P_{yy}' + h_{1yy}' = 0$, hence $h_{1yy}' = 0$. We therefore take $h_1' = \alpha^\star + \beta^\star y$ and $(P' + h_1') = \alpha + \beta y$ which yields $P' = (\alpha - \alpha^\star) + (\beta - \beta^\star) y$.

We can substitute these into (B.3) and (B.4),

$$
(c - u_{10})\beta + \alpha = 0 \qquad \text{(B.7)}
$$

$$
(c - u_{20})(\beta - \beta^\star) + (\alpha - \alpha^\star) = 0 \qquad \text{(B.8)}
$$

and eliminating α from the second expression we find:

$$
-\alpha^\star + \beta(u_{10} - u_{20}) - \beta^\star (c - u_{20}) = 0. \qquad \text{(B.9)}
$$

This equation is the same for all regimes. The other two equations (B.5) and (B.6) will be different depending on the regime the flow is in. They are not independent of y when substituting for the above expressions for h_1' and P', and they therefore need to be integrated across the channel. If the flow is fully attached we integrate as follows:

$$c\int_{-L/2}^{L/2} h_2' dy + \int_{-L/2}^{L/2} h_2'\bar{P}_y + \bar{h}_2 P_y' dy = 0 \tag{B.10}$$

and

$$\int_{-L/2}^{L/2} DP_y' + (\bar{h}_1 h_1')_y dy = 0. \tag{B.11}$$

The velocity field and interface height for the different regimes are defined in section 3.1.2 and of course they apply here also.

Determining the pressure term, P', in the regions where only one layer is present, we find that $P'_{(2)} = B(\bar{u}_2 - c)$ if only layer 2 is present, and $P'_{(1)} = A(\bar{u}_1 - c)$ if only layer 1 is present. From $u_2' = -P_y'$ and $u_{2y}' = 1$ it follows that P_y' has to be continuous across the transition from one layer to two layers, meaning $P'_{(2)y-} = P'_{y+}$ and $(P' + h_1')_{y-} = P'_{(1)y+}$ and hence we find that $A = \beta$ and $B = \beta - \beta^\star$.

Finally, equations (B.9), (B.10) and (B.11) are three equations in three unknowns and may be written in matrix form:

$$\mathbf{MB} = \mathbf{0}$$

where

$$\mathbf{B} = \begin{pmatrix} \alpha^\star \\ \beta^\star \\ \beta \end{pmatrix}$$

$$\mathbf{M} = \begin{pmatrix} a_{11} & a_{12x} + ca_{12c} & a_{13} \\ a_{21x} + ca_{21c} & a_{22x} + ca_{22c} & a_{23} \\ a_{31} & a_{32x} + ca_{32c} & a_{33} \end{pmatrix}$$

$\mathbf{M}$ contains the coefficients of equations (B.9), (B.10) and (B.11).

$$\begin{aligned}
a_{11} &= -1 \\
a_{12x} &= u_{20} \\
a_{12c} &= -1 \\
a_{13} &= u_{10} - u_{20} \\
a_{21x} &= \tfrac{y_s^2 - y_b^2}{2} + u_{20}(y_s - y_b) \\
a_{21c} &= y_b - y_s \\
a_{22x} &= \tfrac{y_s^3 - y_b^3}{3} + \tfrac{y_s^2 - y_b^2}{2}(2u_{20} - u_{10}) - (D - h_{10})(y_s - y_b) - D(y_b + \tfrac{L}{2}) \\
a_{22c} &= -\tfrac{y_s^2 - y_b^2}{2} \\
a_{23} &= D(y_b + \tfrac{L}{2}) + (D - h_{10})(y_s - y_b) - (u_{20} - u_{10})\tfrac{y_s^2 - y_b^2}{2}
\end{aligned}$$

where y_s and y_b are as usual determined by the intersection of the interface with the bottom or surface respectively and are given in section 3.1.2. If the interface is attached at one or both of the walls, y_b and y_s are set to $-\frac{L}{2}$ or $\frac{L}{2}$ depending on the regime. Equation (B.11), which can be rewritten as

$$[DP' + \bar{h}_1 h_1']_{-L/2}^{L/2} = 0, \tag{B.12}$$

cannot be generalised in the same way as the other expressions, and each coefficient in the matrix $\mathbf{M}$ has to be determined individually. Therefore a_{31}, a_{32x}, a_{32c} and a_{33} are listed below for each regime we consider.

Regime 4

$$\begin{aligned} a_{31} &= -D + h_{10} + \tfrac{L}{2}(u_{20} - u_{10}) \\ a_{32x} &= D(u_{20} - L) + \tfrac{L}{2}(h_{10} + \tfrac{L}{2}(u_{20} - u_{10})) \\ a_{32c} &= -D \\ a_{33} &= D(L + u_{10} - u_{20}) \end{aligned}$$

Regime 5

$$\begin{aligned} a_{31} &= u_{20} - u_{10} \\ a_{32x} &= h_{10} - D \\ a_{32c} &= 0 \\ a_{33} &= D \end{aligned}$$

Regime 7

$$\begin{aligned} a_{31} &= 0 \\ a_{32x} &= u_{20} - \tfrac{L}{2} \\ a_{32c} &= -1 \\ a_{33} &= u_{10} - u_{20} + L \end{aligned}$$

Regime 8

$$\begin{aligned} a_{31} &= D - h_{10} + \tfrac{L}{2}(u_{20} - u_{10}) \\ a_{32x} &= \tfrac{L}{2}(h_{10} - D - \tfrac{L}{2}(u_{20} - u_{10})) \\ a_{32c} &= 0 \\ a_{33} &= DL \end{aligned}$$

Writing out the determinant of $\mathbf{M}$ we find a quadratic equation in the wave-speed c and solving $det(\mathbf{M}) = 0$ results in the speeds of the two wave modes. This applies to every regime a flow may pass through along the channel. Results for a selection of topographies are shown in chapter 4.

Appendix C

MICOM Experiments

In this appendix all results from the MICOM experiments are listed explicitly for reference. The variables in the header of each table are kept constant for all runs listed in that table. In the first column of each table the varying parameter is listed and in order from left to right, the dimensional flux Q, the Rossby radius a, the width for the channel in terms of Rossby radii L, the non-dimensional upstream relaxation height $\Delta H^{\star}$, the non-dimensional flux $Q^{\star}$, and the non-dimensional error to the flux Er.

The error is estimated from the difference between the maximum and minimum value of the flux in the bottom layer for any given run, after the initial adjustment process is finished. So it is not only a measure of the error in the sense that it gives an interval within which the flux is certainly to be found, but it is also an indictor of the variability of the flow, which in some experiments manifests itself as regular oscillations. One such example is discussed in chapter 6.

The fluxes given are those determined for the bottom layer only. On average the flux in the top layer will be the same, however generally the fluxes in the top layer are more variable and hence the errors will be somewhat larger.

The first section here contains the results for the topography experiments, in section 2 the experiments in which we vary f and g' are listed, and in the third section the ΔH varying experiments are listed.

C.1 Topography experiments

Table C.1: **Set A** H_0 = 900 m, ΔH = 500 m, ΔH_d = 500 m and g' = 9.8060 × 10^{-3} m/s^2, f = 8.5319 × 10^{-4} s^{-1}, W = 55.416 km.

$D_{inf}(m)$	Q (Sv)	a (km)	L	$\Delta H^\star$	$Q^\star$	Er
1500	7.346900	34.819413	1.591523	0.078917	0.555556	0.010742
1800	7.244000	34.819413	1.591523	0.077812	0.555556	0.003051
2700	7.521800	34.819413	1.591523	0.080796	0.555556	0.004383
3600	7.484300	34.819413	1.591523	0.080393	0.555556	0.008303
4500	7.747200	34.819413	1.591523	0.083217	0.555556	0.004801

Table C.2: **Set B** D_{inf} = 4500 m, g' = 9.8060 × 10^{-3} m/s^2, f = 8.5319 × 10^{-4} s^{-1} and W = 55.416 km. We kept the downstream relaxation at 1400 m below the surface and hence ΔH_D = (1400 − H_0) changed with changing H_0

H_0	Q (Sv)	a (km)	L	$Q^\star$	$\Delta H^\star$	Er
900	7.747200	34.819413	1.591523	0.083217	0.555556	0.004801
700	4.620000	30.707836	1.804618	0.082035	0.557143	0.005682
600	3.521000	28.429931	1.949210	0.085098	0.556667	0.006526
500	2.561100	25.952858	2.135252	0.089133	0.556000	0.005429
400	1.666000	23.212942	2.387285	0.090596	0.559500	0.006199
300	1.036700	20.102997	2.756599	0.100222	0.557000	0.004350
200	0.499900	16.414029	3.376130	0.108737	0.557000	0.010223

Table C.3: **Set C** H_0 = 500 m, ΔH = 278.5 m, g' = 9.8060 × 10^{-3} m/s^2, f = 8.5319 × 10^{-4} s^{-1}, W = 55.416 km.

ΔH_D	Q (Sv)	a (km)	L	$Q^\star$	$\Delta H^\star$	Er
900	2.561100	25.952858	2.135252	0.089133	0.556000	0.005429
1500	2.477200	25.952858	2.135252	0.086213	0.557000	0.006856
2500	2.552400	25.952858	2.135252	0.088831	0.557000	0.007204

C.2 Experiments varying f and g'

Table C.4: **Set I** $H_0 = 500$ m, $D_{inf} = 4500$ m, $\Delta H = 278.5$ m, $\Delta H_d = 2500$ m and $g' = 9.8060 \times 10^{-3}$ m/s^2, $W = 55.416$ km.

f (s^{-1})	Q (Sv)	a (km)	L	$\Delta H^\star$	$Q^\star$	Er
1.6×10^{-4}	1.387000	13.839199	4.004271	0.557000	0.090524	0.0052
1.4×10^{-4}	1.572800	15.816228	3.503737	0.557000	0.089819	0.0057
1.0×10^{-4}	2.225800	22.142719	2.502669	0.557000	0.090793	0.0061
0.853×10^{-4}	2.552400	25.952858	2.135252	0.557000	0.088831	0.0072
0.6×10^{-4}	3.313100	36.904531	1.501602	0.557000	0.081087	0.0041
0.4×10^{-4}	4.406400	55.356797	1.001068	0.557000	0.071897	0.0038
0.2×10^{-4}	6.743800	110.713594	0.500534	0.557000	0.055018	0.0023
0.0	7.438200	na	na	0.557000		

Table C.5: **Set II** $H_0 = 500$ m, $D_{inf} = 4500$ m, $\Delta H = 278.5$ m, $\Delta H_d = 2500$ m and $f = 1.0 \times 10^{-4}$ s^{-1}, $W = 55.416$ km.

g' (ms^{-2})	Q (Sv)	a (km)	L	$\Delta H^\star$	$Q^\star$	Er
12.7478×10^{-3}	2.768900	25.246584	2.194986	0.557000	0.086882	0.0078
9.8060×10^{-3}	2.225800	22.142719	2.502669	0.557000	0.090793	0.0061
6.8642×10^{-3}	1.600800	18.525928	2.991262	0.557000	0.093284	0.0064
4.9030×10^{-3}	1.178800	15.657267	3.539309	0.557000	0.096170	0.0106
2.9418×10^{-3}	0.722200	12.128067	4.569228	0.557000	0.098198	0.0109
0.9806×10^{-3}	0.216900	7.002143	7.914135	0.557000	0.088476	0.0204

Table C.6: **Set III** $H_0 = 500$ m, $D_{inf} = 4500$ m, $\Delta H = 278.5$ m, $\Delta H_d = 2500$ m and $f = 0.6 \times 10^{-4}$ s^{-1}, $W = 55.416$ km.

g' (ms^{-2})	Q (Sv)	a (km)	L	$\Delta H^\star$	$Q^\star$	Error
12.7478×10^{-3}	4.023300	42.077640	1.316992	0.557000	0.075746	0.0032
9.8060×10^{-3}	3.313100	36.904531	1.501602	0.557000	0.081087	0.0042
6.8642×10^{-3}	2.576300	30.876546	1.794757	0.557000	0.090078	0.0070
4.9030×10^{-3}	1.955100	26.095444	2.123585	0.557000	0.095701	0.0064
2.9418×10^{-3}	1.210600	20.213444	2.741537	0.557000	0.098764	0.0090
0.9806×10^{-3}	0.403800	11.670238	4.748481	0.557000	0.098829	0.0147
0.4903×10^{-3}	0.188900	8.252104	6.715366	0.557000	0.092466	0.0245

C.3 Experiments with varying ΔH

Table C.7: **Set IV** H_0 = 500 m, D_{inf} = 4500 m, ΔH_d = 2500 m, g' = 9.8060 × 10^{-3} m/s^2 and f = 1.0 × 10^{-4} s^{-1}, W = 55.416 km.

ΔH (m)	Q (Sv)	a (km)	L	$\Delta H^\star$	$Q^\star$	Er
50	0.176400	22.142719	2.502669	0.100000	0.007196	0.0020
100	0.507900	22.142719	2.502669	0.200000	0.020718	0.0012
150	0.948600	22.142719	2.502669	0.300000	0.038695	0.0024
200	1.427200	22.142719	2.502669	0.400000	0.058217	0.0020
278.5	2.225800	22.142719	2.502669	0.557000	0.090793	0.0061
300	2.439300	22.142719	2.502669	0.600000	0.099502	0.0065
350	2.882800	22.142719	2.502669	0.700000	0.117593	0.0073
400	3.265600	22.142719	2.502669	0.800000	0.133208	0.0073

Table C.8: **Set V** H_0 = 500 m, D_{inf} = 4500 m, ΔH_d = 2500 m, g' = 5.8836 × 10^{-3} m/s^2 and f = 0.3 × 10^{-4} s^{-1}, W = 55.416 km.

ΔH (m)	Q (Sv)	a (km)	L	$\Delta H^\star$	$Q^\star$	Error
50	0.287700	57.172254	0.969280	0.100000	0.005868	0.0004
100	0.891200	57.172254	0.969280	0.200000	0.018177	0.0010
150	1.665900	57.172254	0.969280	0.300000	0.033977	0.0008
200	2.461900	57.172254	0.969280	0.400000	0.050212	0.0024
250	3.381700	57.172254	0.969280	0.500000	0.068972	0.0047
300	4.071400	57.172254	0.969280	0.600000	0.083039	0.0039
350	4.798500	57.172254	0.969280	0.700000	0.097869	0.0053
400	5.526000	57.172254	0.969280	0.800000	0.112707	0.0086

Table C.9: **Set VI** H_0 = 500 m, D_{inf} = 4500 m, ΔH_d = 2500 m, g' = 3.9224 × 10^{-3} m/s^2 and f = 1.3 × 10^{-4} s^{-1}, W = 55.416 km.

ΔH (m)	Q (Sv)	a (km)	L	$\Delta H^\star$	$Q^\star$	Error
50	0.055200	10.772527	5.144188	0.100000	0.007318	0.0027
100	0.170300	10.772527	5.144188	0.200000	0.022577	0.0027
150	0.302900	10.772527	5.144188	0.300000	0.040156	0.0053
200	0.462500	10.772527	5.144188	0.400000	0.061315	0.0080
250	0.634800	10.772527	5.144188	0.500000	0.084157	0.0080
300	0.779300	10.772527	5.144188	0.600000	0.103313	0.0106
350	0.913600	10.772527	5.144188	0.700000	0.121118	0.0146
400	1.015500	10.772527	5.144188	0.800000	0.134627	0.0186

Table C.10: **Set VII** $H_0 = 900$ m, $D_{inf} = 3000$ m, $\Delta H_d = 1100$ m, $g' = 2.94179 \times 10^{-3}\ m/s^2$ and $f = 1.4 \times 10^{-4}\ s^{-1}$, $W = 55.416$ km.

ΔH (m)	Q (Sv)	a (km)	L	$\Delta H^\star$	$Q^\star$	Er
100	0.115000	11.622487	4.767990	0.111111	0.006757	0.0012
200	0.363200	11.622487	4.767990	0.222222	0.021339	0.0029
300	0.679100	11.622487	4.767990	0.333333	0.039899	0.0029
400	1.045200	11.622487	4.767990	0.444444	0.061409	0.0047
500	1.448700	11.622487	4.767990	0.555556	0.085116	0.0194
600	1.803600	11.622487	4.767990	0.666667	0.105967	0.0253
700	2.098200	11.622487	4.767990	0.777778	0.123276	0.0223
800	2.268300	11.622487	4.767990	0.888889	0.133270	0.0300

Table C.11: **Set IIX** $H_0 = 900$ m, $D_{inf} = 3000$ m, $\Delta H_d = 1100$ m, $g' = 2.94179 \times 10^{-3}\ m/s^2$ and $f = 0.2 \times 10^{-4}\ s^{-1}$, $W = 55.416$ km.

ΔH (m)	Q (Sv)	a (km)	L	$\Delta H^\star$	$Q^\star$	Error
0	0.0	81.357406	0.681141	0.0	0.0	0.0
50	0.223000	81.357406	0.681141	0.055556	0.001872	0.0001
100	0.705600	81.357406	0.681141	0.111111	0.005922	0.0001
200	2.165300	81.357406	0.681141	0.222222	0.018174	0.0012
300	3.997600	81.357406	0.681141	0.333333	0.033553	0.0024
400	5.569200	81.357406	0.681141	0.444444	0.046744	0.0020
500	6.731400	81.357406	0.681141	0.555556	0.056499	0.0080
600	7.170800	81.357406	0.681141	0.666667	0.060187	0.0065
700	7.901800	81.357406	0.681141	0.777778	0.066322	0.0157

Appendix D

Control in modelled and observed rotating flows

When describing hydraulic flows an important aspect of the flow which one would like to determine is where the control point of the flow occurs. This applies for analytically derived solutions, modelled and observed flows. For non-rotating cases the Froude number can be used to find the control points, however in the rotating case the Froude number is not well defined as the flow exhibits considerable variation in its structure across the channel. For this reason we computed the long-wave speeds for the analytical solutions which are described in section 3.3 and appendix B.

The same principle can be applied to the model data and could equally be used to determine the control in observed flows. However there are some differences to the analytical analysis and hence we will review the method to derive the wavespeed for the model data in this appendix.

Unlike in the analytical solutions, where we used the non-dimensionalised shallow water equations under the assumption of zero potential vorticity, we will use the full dimensional Navier-Stokes equations (without friction) as the model solves them.

$$u_t + uu_x + vu_y - fv = -\frac{1}{\rho}P_x \tag{D.1}$$

$$v_t + uv_x + vv_y + fu = -\frac{1}{\rho}P_y \tag{D.2}$$

$$h_t + (uh)_x + (vh)_y = 0 \tag{D.3}$$

The first two equations are the momentum equations in the x- and y-directions respectively, while equation three is the continuity equation.

(Note that at this point the notation and axis setup is the same as for the analytical results, with x aligned with the channel and y denoting the across channel direction, we will change the notation later to correspond to that used in MICOM.)

Analogous to the method outlined in appendix B the flow parameters in the equations, u, v, h and p are separated into a mean state and a perturbed state, for example $u = \bar{u}+u$,

and replaced in the equations. Subsequently all terms containing only mean terms will cancel to leave expressions which can be solved for the perturbations. In addition several simplifying assumptions are made: $\bar{v} = 0$, i.e. there is no mean flow across the channel (in the rotating case this may cause problems since, especially at the sill, there can be considerable cross-flow), $\bar{u}_x = 0$ as we assume the flow is stretched to infinity at each section, so there are no variations of the mean values in the along channel direction and finally v'_t and v'_x are assumed to be very small and can be set to zero.

The resulting simplified equations for the perturbations of the flow are:

$$u'_{(k)t} + \bar{u}_{(k)}u'_{(k)x} + v'_{(k)}\bar{u}_{(k)y} - fv'_{(k)} = -\frac{1}{\rho}P'_{(k)x} \tag{D.4}$$

$$fu'_{(k)} = -\frac{1}{\rho}P'_{(k)y} \tag{D.5}$$

$$h'_{(k)t} + (u'_{(k)}\bar{h_{(k)}} + \bar{u}_{(k)}h'_{(k)})_x + (v'_{(k)}\bar{h}_{(k)})_y = 0 \tag{D.6}$$

where $k = 1$ for the top layer and 2 for the bottom layer. In addition we have use the assumption of a rigid lid:

$$h'_1 + h'_2 = 0 \tag{D.7}$$

and from the hydrostatic equation $\frac{\partial p}{\partial z} = -\rho g$ we get

$$P'_1 - P'_2 - g'h'_1 = 0 \tag{D.8}$$

So we finally have eight equations: the momentum equations in x-direction in layers 1 and 2, which reduce to geostrophy, the momentum equations in the y-direction for each layer, the continuity equation for each layer, the rigid lid assumption and hydrostatic balance.

As before, we write the perturbation terms as wave-like solution, such as $u'_1 = u'_1 e^{ik(x-ct)}$ and substitute these into the above equations. This leads to the following expressions from (D.4) and (D.6):

$$u'_{(k)}(\bar{u}_{(k)} - c) + v'_{(k)}(\bar{u}_{(k)y} - f) = -\frac{1}{\rho}P'_{(k)} \tag{D.9}$$

$$h'_{(k)}(\bar{u}_{(k)} - c) + u'_{(k)}\bar{h}_{(k)} + (v'_{(k)}\bar{h}_{(k)})_y = 0 \tag{D.10}$$

while (D.5), (D.7) and (D.8) remain the same.

Now the notation of the axes has to be convert to the notation used in MICOM, listed in table D.1. This leaves the rigid lid (D.7) and hydrostatic expression (D.8) again unchanged, but the momentum (D.9), geostrophy (D.5) and continuity (D.10) equations become:

$$v'_{(k)}(\bar{v}_{(k)} - c) + u'_{(k)}(\bar{v}_{(k)x} - f) = -\frac{1}{\rho}P'_{(k)} \tag{D.11}$$

Analytical	$\rightarrow$	MICOM
u	$\rightarrow$	$-v$
v	$\rightarrow$	u
$\frac{\partial}{\partial x}$	$\rightarrow$	$-\frac{\partial}{\partial y}$
$\frac{\partial}{\partial y}$	$\rightarrow$	$\frac{\partial}{\partial x}$

Table D.1: Conversion from the co-ordinates used in the theory and those used in MICOM.

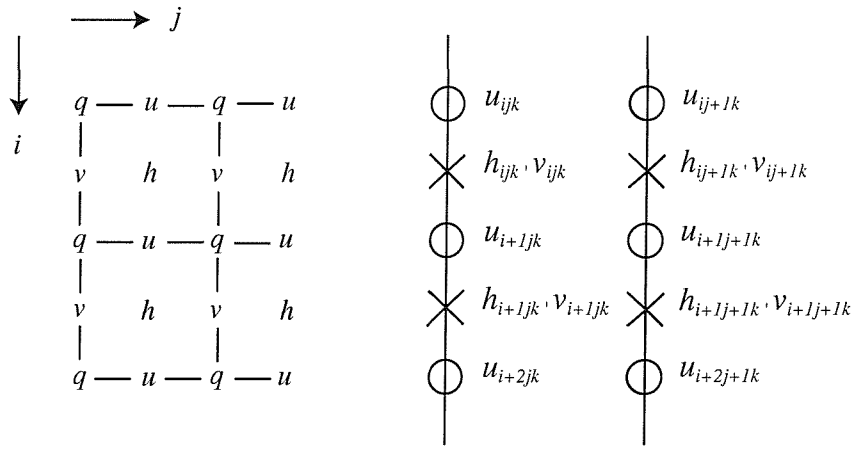

Figure D.1: (Left) C-grid as used in MICOM. (Right) The v values are averaged to fall onto the u-gridline for the wave analysis.

$$fv'_{(k)} = \frac{1}{\rho}P'_{(k)x} \tag{D.12}$$

$$h'_{(k)}(\bar{v}_{(k)} - c) + v'_{(k)}\bar{h}_{(k)} + (u'_{(k)}\bar{h}_{(k)})_x = 0 \tag{D.13}$$

These now need to be converted into an eigenproblem of the form:

$$\mathbf{AX} = c\mathbf{BX} \tag{D.14}$$

which we can solve for the wavespeeds c and the corresponding eigenvectors $\mathbf{X}$. Let us describe how best to go about achieving this.

MICOM uses a C-grid as is shown on the left in figure D.1. In all the experiments we align the channel in the j-direction and to find the location along j where the control occurs the wave speeds have to be found at discrete j. We will be computing them along the gridlines containing u_{ijk} and h_{ijk}, and to bring v onto that line, the values of v_{ijk} and v_{ij+1k}, from either side of u_{ijk}, are averaged and we denote $v_{ijk} = \frac{v_{ijk}+v_{ij+1k}}{2}$. The channel is located between $i = 1$ and $i = N$ and the boundaries are located at along the u-gridlines u_{1jk} and u_{N+1jk} where $u = 0$. The channel therefore consists of N wet boxes each with a h-point at the centre.

At each grid-point i we can derive the above expressions using the v, u and h fields resulting from MICOM. $\mathbf{X}$ can therefore be written as:

$$X = (v'_{1j1}, v'_{1j2}, u'_{1j1}, u'_{1j2}, h'_{1j1}, h'_{1j2}, p'_{1j1}, p'_{1j2},$$
$$v'_{2j1}, v'_{2j2}, u'_{2j1}, u'_{2j2}, h'_{2j1}, h'_{2j2}, p'_{2j1}, p'_{2j2}, \cdots, p'_{Nj1}, p'_{Nj2}), \tag{D.15}$$

and both **A** and **B** will be $8N \times 8N$ matrices. To find the entries in these matrices we rewrite the equations as follows:

Momentum @ v-pts (i = 1 to N)

$$v'_{ijk}\bar{v}_{ijk} + \frac{u'_{ijk} + u'_{i+1jk}}{2}\left[\frac{\bar{v}_{i+1jk} - \bar{v}_{i-1jk}}{2\Delta x} + f\right] + \frac{1}{\rho}P'_{ijk} = cv'_{ijk} \tag{D.16}$$

$\left[\frac{\bar{v}_{i+1jk}-\bar{v}_{i-1jk}}{2\Delta x} + f\right]$ can be replaced by $\left[\frac{(q_{ijk}+q_{i+1jk})h_{ijk}}{2}\right]$, the absolute vorticity at i if it is available. We us this expression when analysing the MICOM results, but in real observations it will most likely not be available.

At the far end of the channel, where $i = N$ the term for u'_{i+1jk} does not exist and is there simply not included in the equation.

Continuity @ v-pts (i = 1 to N)

$$h'_{ijk}\bar{v}_{ijk} + \bar{h}_{ijk}v'_{ijk} + \frac{u'_{i+1jk} - u'_{ijk}}{\Delta x}\bar{h}_{ijk} + \frac{u'_{ijk} + u'_{i+1jk}}{2}\left[\frac{\bar{h}_{i+1jk} - \bar{h}_{i-1jk}}{2\Delta x}\right] = ch'_{ijk} \tag{D.17}$$

$\left[\frac{\bar{h}_{i+1jk}-\bar{h}_{i-1jk}}{2\Delta x}\right]$ can be rewritten in terms of the velocities $\bar{v}_{ij1}$ and $\bar{v}_{ij2}$ from the thermal wind expressions:

$$\bar{h}_{(ij1)x} = \frac{f\rho}{g'}(\bar{v}_{ij1} - \bar{v}_{ij2}) \tag{D.18}$$

and

$$\bar{h}_{(ij2)x} = -\frac{f\rho}{g'}(\bar{v}_{ij1} - \bar{v}_{ij2}) \tag{D.19}$$

this makes computation easier at the boundaries where $\bar{h}_{i-1jk}$ and $\bar{h}_{i+1jk}$ do not exist.

Geostrophy @ u-pts (i = 2 to N)

$$f\frac{v'_{ijk} + v'_{i+1jk}}{2} = \frac{1}{\rho}\frac{P'_{i+1jk} - P'_{ijk}}{\Delta x} \tag{D.20}$$

Rigid lid @ v-pts (i = 1 to N)

$$h'_{ij1} + h'_{ij2} = 0 \tag{D.21}$$

Hydrostatic Balance @ v-pts (i = 1 to N)

$$P'_{ij1} - P'_{ij2} - g'h'_{ij1} = 0 \tag{D.22}$$

All these equations, with exception of geostophy, fall naturally onto the v-points of the grid and we thus have $6 \times N$ equations taken care of. The geostophy equation is

Row	Equation
1	Geostrophy Layer 1 (i = 2)
2	Geostrophy Layer 2 (i = 2)
3	BC $u'_{1j1} = 0$
4	BC $u'_{1j2} = 0$
5	Hydrostatic Balance (i = 1)
6	Rigid Lid (i = 1)
7	Continuity Layer 1 (i = 1)
8	Continuity Layer 2 (i = 1)
9	Momentum Layer 1 (i =1)
10	Momentum Layer 2 (i =1)
11	again from top for the next grid point
⋮	leaving out the BCs

Table D.2: Sequence of equations which make up matrix **A**.

evaluated from $i = 2 \rightarrow N$ and thus only give us $2 \times (N - 1)$ equations, we use the boundary conditions $u'_{1j1} = u'_{1jk} = 0$ to make up the remaining two equations.

The beginning of matrix **A** is shown on the following page. We have filled up the rows in the order shown in table D.2. Matrix **B** has the same layout as **A** but contains the right-hand sides, involving c, of the above equations.

$$
\mathbf{A} = \left(\begin{array}{cccccccccc}
v'_{1j1} & v'_{1j2} & u'_{1j1} & u'_{1j2} & h'_{1j1} & h'_{1j2} & p'_{1j1} & p'_{1j2} & \dots \\
\hline
0 & 0 & 0 & 0 & 0 & 0 & 0 & 0 & \dots \\
0 & 0 & 0 & 0 & 0 & 0 & 0 & 0 & \dots \\
0 & 0 & 1 & 0 & 0 & 0 & 0 & 0 & \dots \\
0 & 0 & 0 & 1 & 0 & 0 & 0 & 0 & \dots \\
0 & 0 & 0 & 0 & -g' & 0 & 1 & -1 & \dots \\
0 & 0 & 0 & 0 & 1 & 1 & 0 & 0 & \dots \\
h_{1j1} & 0 & -\frac{h_{1j1}}{\Delta x} + \frac{v_{1j1}-v_{1j2}}{2g'} f & 0 & v_{1j1} & 0 & 0 & 0 & \dots \\
0 & h_{1j2} & 0 & -\frac{h_{1j2}}{\Delta x} - \frac{v_{1j1}-v_{1j2}}{2g'} f & 0 & v_{1j2} & 0 & 0 & \dots \\
v_{1j1} & 0 & \frac{(q_{1j1}+q_{2j1})h_{1j1}}{4} & 0 & 0 & 0 & 1 & 0 & \dots \\
0 & v_{1j2} & 0 & \frac{(q_{1j2}+q_{2j2})h_{1j1}}{4} & 0 & 0 & 0 & 1 & \dots
\end{array}\right.
$$

$$
\left.\begin{array}{cccccccccc}
\dots & v'_{2j1} & v'_{2j2} & u'_{2j1} & u'_{2j2} & h'_{2j1} & h'_{2j2} & p'_{2j1} & p'_{2j2} & \dots \\
\hline
\dots & f/2 & 0 & 0 & 0 & 0 & 0 & 1/\Delta x & 0 & \dots \\
\dots & 0 & f/2 & 0 & 0 & 0 & 0 & 0 & 1/\Delta x & \dots \\
\dots & 0 & 0 & 0 & 0 & 0 & 0 & 0 & 0 & \dots \\
\dots & 0 & 0 & 0 & 0 & 0 & 0 & 0 & 0 & \dots \\
\dots & 0 & 0 & 0 & 0 & -g' & 0 & 1 & -1 & \dots \\
\dots & 0 & 0 & 0 & 0 & 1 & 1 & 0 & 0 & \dots \\
\dots & h_{2j1} & 0 & -\frac{h_{2j1}}{\Delta x} + \frac{v_{2j1}-v_{2j2}}{2g'} f & 0 & v_{2j1} & 0 & 0 & 0 & \dots \\
\dots & 0 & h_{2j2} & 0 & -\frac{h_{2j2}}{\Delta x} - \frac{v_{2j1}-v_{2j2}}{2g'} f & 0 & v_{2j2} & 0 & 0 & \dots \\
\dots & v_{2j1} & 0 & \frac{(q_{2j1}+q_{3j1})h_{2j1}}{4} & 0 & 0 & 0 & 1 & 0 & \dots \\
\dots & 0 & v_{2j2} & 0 & \frac{(q_{2j2}+q_{3j2})h_{2j1}}{4} & 0 & 0 & 0 & 1 & \dots \\
\vdots & \vdots & \vdots & \vdots & \vdots & \vdots & \vdots & \vdots & \vdots & \ddots
\end{array}\right)
$$

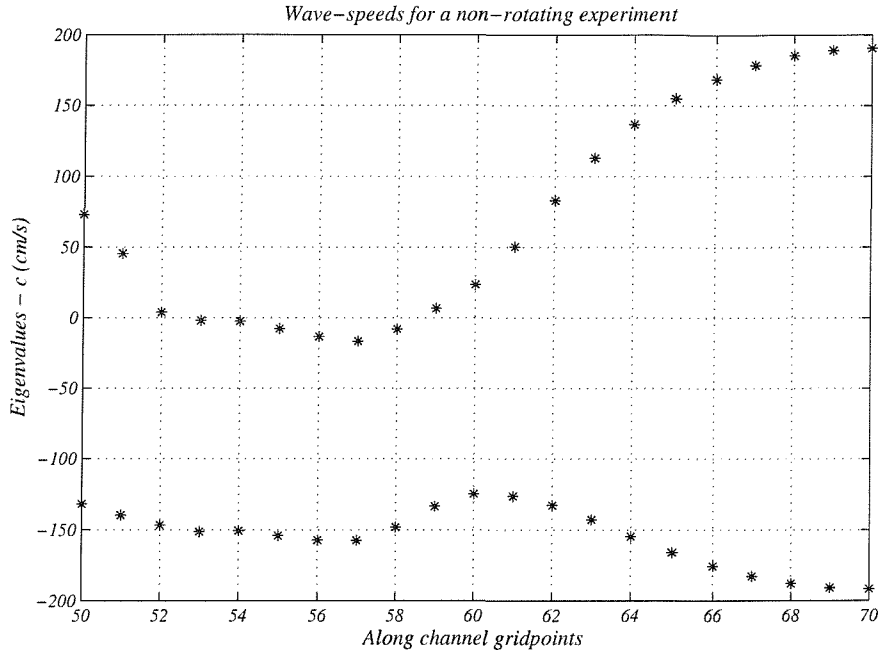

Figure D.2: Wavespeeds along a non-rotating channel with $\Delta H = 100$ m.

D.1 Non-rotating test

Before applying this analysis to the rotating case we test the code on a non-rotating example with $\Delta H = 100$ m described in chapter 5. For this case we know the location of the controls from simply contouring the Froude number along the channel as seen in figure 5.11(A).

The method outlined above to find the wavespeeds is applied at each section along the channel. In this particular case $N = 6$ and thus the matrix is 48×48, which leaves us with 48 eigenvalues. A few criteria are applied to eliminate values that are quite obviously not correct: those that tend to infinity and those that are complex. In addition we find that some eigenvalues are too large to apply and we therefore set an upper limit of 1×10^7 cm/s for the eigenvalues to be chosen, this is an arbitrary value but we do not expect values that are much larger than about 1×10^2 cm/s which means a wavespeed of 1 m/s. After the selection usually a manageable number of about 12 eigenvalues remain.

To distinguish further we go on to plot the eigenvectors corresponding to each eigenvalue. In figures D.3 and D.4 we show the vectors v_1' and v_2' for the 12 remaining eigenvalues at $j = 69$ which is very close to the entrance of the channel.

In the non-rotating case we expect the first mode of both of these vectors to be of the same sign and approximately uniform across the channel, a characteristic, which clearly only applies to the first two vectors. So the final criterion applied to select the primary wavespeeds is that both corresponding eigenvectors v_1' and v_2' must not have any nodes (crossings of the $v_1' = v_2' = 0$ line) anywhere across the channel.

This allows us to extract two wavespeeds at each section along the channel which are plotted in figure D.2. The sill is located at $j = 60$ and to the right ($j > 60$) is the

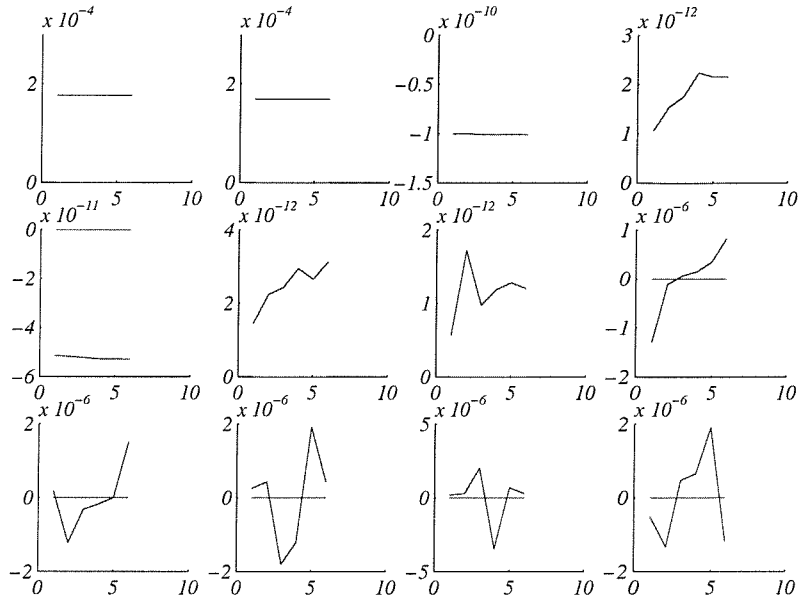

Figure D.3: Eigen-vectors for v_1' at $i = 69$. The solid red line is $v_1' = 0$ for reference.

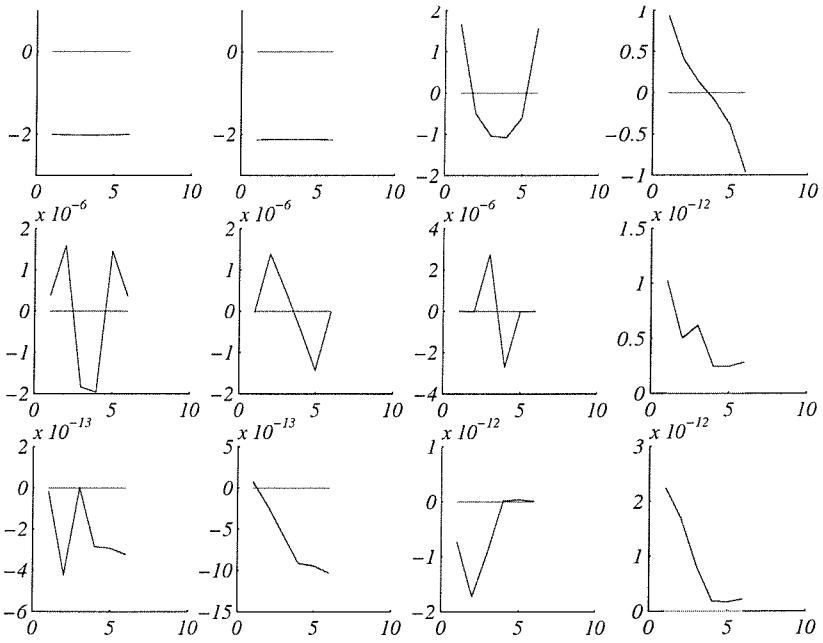

Figure D.4: Eigen-vectors for v_2' at $i = 69$. The solid red line is $v_2' = 0$ for reference.

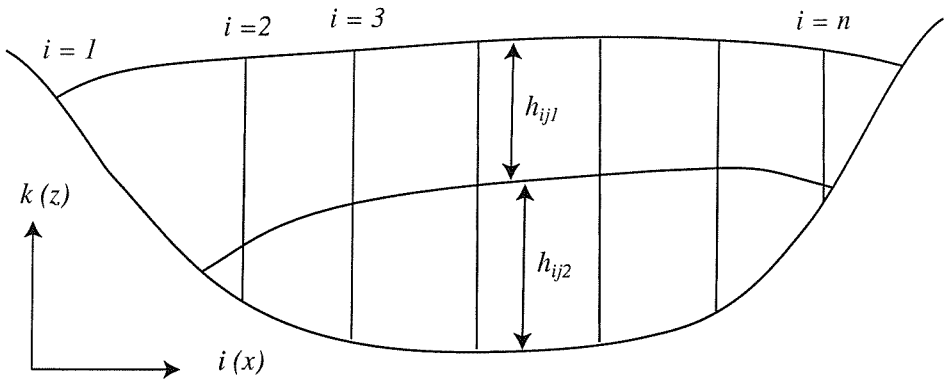

Figure D.5: Cross-section of an observed of modelled two-layer channel flow with n stations or data points along its width.

dense reservoir and to the left ($j < 60$) the light reservoir. Upstream the two wavespeeds are of opposite sign indicating a subcritical flow. Just after passing the sill one of the wavespeeds passes through zero, between $j = 59$ and 58 precisely where $G = 1$ is located in figure 5.11(A). The flow then becomes supercritical for a time and between $j = 53$ and 52 passes back into a subcritical regime, through encountering an hydraulic jump.

We have shown conclusively that the method outlined in the previous section, to derive the wave speeds and hence deduce the location of the controls in non-rotating case, works very well and gives the expected answers which agree with the results we determined from simply plotting the Froude numbers along the same channel. In chapter 6 we apply the analysis to a rotating case, but find that it is much more difficult to get the same kind of conclusive results.

D.2 Application to observed data or laboratory experiments

The application to observed flows, be it in the field or in the laboratory, can be quite straightforward. Let us assume an observational array as shown in figure D.5, with n number of stations across the channel. We need to have observations of the bottom and top layer thickness which can be derived from observed density profiles, as well as the velocity components in the horizontal. Potential vorticity data will not be directly observed but can be computed from the velocity and layer-thickness fields.

These can simply be read into the matrix and the eigenproblem solved. The difficulty lies however in deciding which of the eigenvalues and eigenvectors correspond to the first mode which describes the propagation of the Kelvin waves along the channel, and which is arrested close to the top of the sill.

The method outlined here, is similar to that described for a deep single-layer overflow

by Pratt (2003a). We have extended it to apply to a flow that involved a top layer which is also dynamically important.

Appendix E

List of variables and parameters

E.1 Chapter 2

$G_i(\ldots)$	i^{th} functional (or single functional if it has no subscript)
$L(x)$	Width of the channel
$D(x)$	Depth of the channel
E_i	i^{th} Bernoulli constant (here i usually denotes the number of layers)
Q_i	Flux in the i^{th} layer
$h(x)$	variable of flow structure, usually taken to be the layer thickness, however it could equally be some descriptor of the velocity field or some other variable
x_c	location of the primary control along the channel
x_v	location of the virtual (secondary) control along the channel
G_c	Value of the functional at x_c, $G_c = G(x_c)$
G_v	Value of the functional at x_v, $G_v = G(x_v)$ For all flow we consider $G_v = G_c$
u_i	Velocity field of the i^{th} layer
g'	Reduced gravity
F_i	Froude number in the i^{th} layer

Table E.1: Table of variables as they appear in chapter 2.

E.2 Chapter 3 & 4

u_i	along channel velocities in the bottom layer ($i = 1$) and top layer ($i = 2$)
v_i	cross channel velocities
h_i	layer thickness
u_{10}	velocity at $y = 0$ in the bottom layer
u_{20}	velocity at $y = 0$ in the top layer
h_{10}	thickness of the bottom layer at $y = 0$
h_{20}	thickness of the top layer at $y = 0$
h_s	$(= u_{20} - u_{10})$ slope of the interface
Δu	$= \frac{1}{2}(u_{10} - u_{20})$
$\bar{u}$	$= \frac{1}{2}(u_{10} + u_{20})$
q_i	potential vorticity
ρ_i	layer density
P	pressure at a reference level $z = 0$
g'	reduced gravity
D	depth of the channel
D_0	depth of the sill at the shallowest point
L	non-dimensional width of the channel
L_0	non-dimensional width of the channel at the narrowest point
R	along channel length scale
$a = \sqrt{g'D_0}/f$	Rossby radius of deformation
Q_i	layer transports
E_i	Bernoulli potentials
ΔE	difference in Bernoulli potentials $(E_1 - E_2)$
F_i	layer Froude number
W	dimensional width of the channel
F_{10}, F_{20}	Froude numbers at the centre of the channel
$L^{(1)}$, $D^{(1)}$, $\Delta E^{(1)}$, $W^{(1)}$	Variables describing the topography of the channel and the flow at some section away from the primary control
k	wave number
c	wave speed

Table E.2: Table of variables as they appear in chapter 3 & 4.

E.3 Chapter 5 & 6

$\mathbf{v} = (u, v)$	horizontal velocity field
f	Coriolis parameter
M	Montgomery potential
ζ	relative vorticity
p	pressure
$\alpha = \frac{1}{\rho}$	specific volume
g	gravitational acceleration
$\tau_{x,y}$	Reynolds stresses
ν	eddy viscocity coefficient
λ	Smagorinsky constant
C_D	Drag coefficient
u_d	diffusive velocity for momentum dissipation
$\bar{c}$	residual bottom layer velocity
$\Delta\rho$	density different between the two layers in sigma units
ΔH	upstream relaxation height above the sill (dimensional)
ΔH_D	downstream relaxation height below the sill (dimensional)
D_0 or H_0	depth of the channel at the shallowest point
D_{inf}	depth of the basins
Q_{nd} or Q_0	$= \frac{g' H_0^2}{f}$, scaling of the fluxes
$\Delta H^\star$, $\Delta H_D^\star$	non-dimensionalised parameters
$Q^\star$	non-dimensional flux
q_1'	non-dimensional flux used by Farmer and Armi (1986)
q_r	ratio of fluxes between top and bottom layer flux q_1/q_2
F_i	Froude numbers
b_0	channel width at the narrowest point
b'	non-dimensional width
h'	non-dimensional topography height
y_i	layer thicknesses
$\Delta H''$	Bernoulli potential for flow over a sill from Farmer and Armi (1986)
Er	Error determined for the MICOM fluxes

Table E.3: Table of variables as they appear in chapter 5 & 6.

Bibliography

Adcroft, A., Hill, C., and Marshall, D. (1997). Representation of topography by shaved cells in a height coordinate ocean model. *Monthly Weather Review*, 125:2293–2315.

Armi, L. (1986). The hydraulics of two flowing layers with different densities. *Journal of Fluid Mechanics*, 163:27–58.

Armi, L. and Farmer, D. M. (1985). The internal hydraulics of the Strait of Gibraltar and associated sills and narrows. *Oceanologica Acta*, 8:37–46.

Armi, L. and Farmer, D. M. (1986). Maximal two-layer exchange through a contraction with barotropic net flow. *Journal of Fluid Mechanics*, 164:27–51.

Bacon, S. (2002). The dense overflows from the Nordic Seas into the deep North Atlantic. *ICES Marine Science Symposia*, 215:148–155.

Béranger, K., Mortier, L., Gasparini, G.-P., Gervasio, M., Astraldi, M., and Crépon, M. (2004). The dynamics of the Sicily Strait: A comprehensive study from observations and models. *Deep Sea Research*, II:in press.

Bleck, R. and Boudra, D. (1986). Wind-driven spin-up in eddy-resolving ocean models formulated in isopycnic and isobaric coordinates. *Journal of Geophysical Research*, 91(C6):7611–7621.

Bleck, R. and Smith, L. T. (1990). A wind-driven isopycnic coordinate model of the North and Equatorial Atlantic Ocean, 1. Model development and supporting experiments. *Journal of Geophysical Research*, 95(C3):3273–3285.

Borenäs, K. M. and Whitehead, J. A. (1998). Upstream separation in a rotating channel flow. *Journal of Geophysical Research*, 103:7567–7578.

Bormans, M. and Garrett, C. (1991). The effect of rotation on the surface inflow through the Strait of Gibraltar. *Journal of Physical Oceanography*, 19(10):1535–1542.

Bryden, H. L. and Kinder, T. H. (1991). Steady two-layer exchange through the Strait of Gibraltar. *Deep-Sea Research*, 38:445–463.

Dalziel, S. B. (1988). *Two-layer hydraulics: maximal exchange flows.* PhD thesis, Department of Applied Mathematics and Theoretical Physics, University of Cambridge.

Dalziel, S. B. (1990). Rotating two-layer sill flows. In Pratt, L. J., editor, *The Physical Oceanography of Sea Straits*, NATO/ASI Series. Kluwer.

Dalziel, S. B. (1991). Two-layer hydraulics: a functional approach. *Journal of Fluid Mechanics*, 223:135–163.

Dalziel, S. B. (1992). Maximal exchange in channels with nonrectangular cross section. *Journal of Physical Oceanography*, 22:1188–1206.

Dickson, R. R. and Brown, J. (1994). The production of North Atlantic Deep Water: sources, rates and pathways. *Journal of Geophysical Research*, 99 (C6):12319–12341.

Duncan, L. M., Bryden, H. L., and Cunningham, S. A. (2003). Friction and mixing in the Faroe Bank Channel outflow. *Oceanologica Acta*, 26:473–486.

Farmer, D. M. and Armi, L. (1986). Maximal two-layer exchange over a sill and through the combination of a sill and contraction with barotropic flow. *Journal of Fluid Mechanics*, 164:53–76.

Ferron, B., Mercier, H., and Treguier, A. (2000). Modeling of the bottom water flow through the Romanche Fracture Zone with a primitive model–Part I: Dynamics. *Journal of Marine Research*, 58(6):837–862.

Gascard, J. C. and Richez, C. (1985). Water masses and circulation in the western Alboran Sea and in the Strait of Gibraltar. *Progress in Oceanography*, 15(3):157–216.

Gill, A. E. (1977). The hydraulics of rotating-channel flow. *Journal of Fluid Mechanics*, 80(4):641–671.

Girton, J. B. and Sandford, T. B. (2001). Synoptic sections of the Denmark Strait Overflow. *Geophysical Research Letters*, 28(8):1619–1622.

Girton, J. B. and Sandford, T. B. (2003). Descent and modification of the overflow plume in the Denmark Strait. *Journal of Physical Oceanography*, 33(7):1351–1364.

Griffies, S. M., Böning, C., Bryan, F. O., Chassignet, E. P., Gerdes, R., Hasumi, H., Hirst, A., Treguier, A., and Webb, D. (2000). Developments in ocean climate modelling. *Ocean Modelling*, 2:123–192.

Griffies, S. M. and Hallberg, R. W. (2000). Biharmonic friction with a Smagorinsky-like viscosity for use in large-scale eddy-permitting ocean models. *Monthly Weather Review*, 128(8):2935–2946.

Hansen, B., Turrell, W. R., and Ø sterhus, S. (2001). Decreasing overflow from the Nordic seas into the Atlantic Ocean through the Faroe Bank Channel since 1950. *Nature*, 411:927–930.

Helfrich, K. R. (1995). Time-dependent two-layer hydraulic exchange flows. *Journal of Physical Oceanography*, 25:359–373.

Helfrich, K. R. (2004). Upstream and downstream effects of rotating hydraulic control. In *Preceedings of the Ocean Science Meeting, Portland, Oregon.*

Herbaut, C., Cordron, F., and Crépon, M. (1998). Separation of a coastal current at a strait level: Case of the Strait of Sicily. *Journal of Physical Oceanography*, 28:1346–1362.

Herbaut, C., Mortier, L., and Crépon, M. (1996). A sensitivity study of the general circulation of the Western Mediterranean Sea. Part I: The response to density forcing through the strait. *Journal of Physical Oceanography*, 26:65–84.

Hermann, A. J., Rhines, P. B., and Johnson, E. R. (1989). Nonlinear Rossby adjustment in a channel: beyond Kelvin waves. *Journal of Fluid Mechanics*, 205:469–502.

Hogg, A. M., Ivey, G. N., and Winters, K. B. (2001). Hydraulics and mixing in controlled exchange flows. *Journal of Geophysical Research*, 106(C1):959–972.

Käse, R. H., Girton, J. B., and Sandford, T. B. (2003). Structure and variability of the Denmark Strait Overflow: Model and observations. *Journal of Geophysical Research*, 108(C6):12.1–12.15.

Käse, R. H. and Oschlies, A. (2000). Flow through Denmark Strait. *Journal of Geophysical Research*, 105(C12):28,527–28,546.

Killworth, P. (1992a). Flow properties in rotating, stratified hydraulics. *Journal of Physical Oceanography*, 22:997–1017.

Killworth, P. (1992b). On hydraulic control in a stratified fluid. *Journal of Fluid Mechanics*, 237:605–626.

Killworth, P. (1994). On reduced-gravity flow through sills. *Geophysical and Astrophysical Fluid Dynamics*, 75:91–106.

Killworth, P. (1995). Hydraulic control and maximal flow in rotating stratified hydraulics. *Deep-Sea Research*, 42(6):859–871.

Killworth, P. and McDonald, N. R. (1993). Maximal reduced-gravity flux in rotating, stratified hydraulics. *Geophysical and Astrophysical Fluid Dynamics*, 70:31–40.

Lacombe, H. and Richez, C. (1982). The regime of the Strait of Gibraltar. *Harvard University Division of Applied Sciences, Reports in Meteorology and Oceanography*, 41:57–114.

Lane-Serff, G. F., Smeed, D. A., and Postlethwaite, C. R. (2000). Multi-layer hydraulic exchange flows. *Journal of Fluid Mechanics*, 416:269–296.

Marsigli, C. L. F. (1681). Osservazioni intorno al Bosforo Tracio o vero Canale di Constantinopoli rappresentate in lettera alla Sacra Real Maesta di Cristina Regina di Svezia. *Bolletino di Pesca Piscicoltura e Idrobiologia (Reprint 1935)*, pages 734–758.

Mauritzen, C., Sanford, T., and Price, J. (2004). Circulation and mixing in the Faroese Channels. *to be submitted.*

Nikolopoulos, A., Borenäs, K., Hietala, R., and Lundberg, P. (2003). Hydrographic estimates of Denmark Strait Overflow. *Journal of Geophysical Research*, 108(C3):40.1–40.12.

Pratt, L. J. (1986). Hydraulic control of sill flow with bottom friction. *Journal of Physical Oceanography*, 16:1970–1980.

Pratt, L. J. (1987). Rotating shocks in a separated laboratory channel flow. *Journal of Physical Oceanography*, 17:483–491.

Pratt, L. J. (2003a). Generalized conditions for hydraulic criticality of oceanic overflows. *submitted to Journal of Fluid Mechanics.*

Pratt, L. J. (2003b). Notes on two-layer zero potential vorticity theory. *unpublished.*

Pratt, L. J. (2003c). Recent progress on understanding the effects of rotation in models of sea straits. *in preparation.*

Pratt, L. J., Helfrich, K. R., and Chassignet, E. (2000). Hydraulic adjustment to an obstacle in a rotating channel. *Journal of Fluid Mechanics*, 404:117–149.

Pratt, L. J. and Lundberg, P. A. (1991). Hydraulics of rotational strait and sill flow. *Annual Review of Fluid Mechanics*, 23:81–106.

Price, J. and Baringer, M. O. (1994). Outflow and deep water production by marginal seas. *Progress in Oceanography*, 33:161–200.

Price, J. and Yang, J. (1998). Marginal sea overflows for climate simulations. *Ocean Modeling and Parameterisation*, pages 155–170.

Rabe, B., Smeed, D. A., and Bryden, H. (2002). Rotating exchange flows through straits with multiple channels: Preliminary results of laboratory sudies. *Proceedings of the 2nd Meeting on the Physical Oceanography of Sea Straits*, pages 185–188.

Roberts, M. J. and Wood, R. A. (1997). Topographic sensitivity studies with a Bryan-Cox-Type ocean model. *Journal of Physical Oceanography*, 27:823–836.

Ross, C. K. (1984). Temperature-salinity characteristics of the "overflow" water in Denmark Strait during "OVERFLOW '73". *Rapp. P. V. Reun. Cons. Int. Explor. Mer.*, 185:111–119.

Saunders, P. M. (1990). Cold outflow from the Faroe Bank Channel. *Journal of Physical Oceanography*, 1:29–43.

Smagorinsky, J. (1963). General circulation experiments with the primitive equations: I. The basic experiment. *Monthly Weather Review*, 91:99–164.

Smeed, D. (2000). Hydraulic control of three-layer exchange flows: Application to the Bab al Mandab. *Journal of Physical Oceanography*, 30:2574–2588.

Whitehead, J. A. (1989). Internal hydraulic control in rotating fluids–applications to the oceans. *Geophysical and Astrophysical Fluid Dynamics*, 48:169–192.

Whitehead, J. A. (1998). Topographical control of oceanic flows in deep passages and straits. *Reviews of Geophysics*, 36(3):424–440.

Whitehead, J. A., Leetman, A., and Knox, R. A. (1974). Rotating hydraulics of strait and sill flows. *Geophysical Fluid Dynamics*, 6:101–125.

Whitehead, J. A. and Salzig, J. (2001). Rotating channel flow: Control and upstream currents. *Geophysical and Astrophysical Fluid Dynamics*, 95:185–226.

Willebrand, J., Barnier, B., Böning, C., Dieterich, C., Killworth, P. D., Le Provost, C., Jia, Y., Molines, J., and New, A. L. (2001). Circulation characteristics in three eddy-permitting models of the North Atlantic. *Progress in Oceanography*, 48:123–161.

Wood, I. R. (1970). A lock exchange flow. *Journal of Fluid Mechanics*, 42:671–687.

Zhu, D. Z. and Lawrence, G. A. (2000). Hydraulics of exchange flows. *Journal of Hydraulic Engineering*, 12(126):921–928.